Hardware and Software Interfaces Design for Multi-Panel Electrochemical Sensors

Thèse n. 8725
présentée le 3 décembre 2021
à la Faculté informatique et communications
Laboratoire des systèmes intégrés (IC-IINFCOM-LSI1)
Programme doctoral en microélectronique et microsystèmes
École polytechnique fédérale de Lausanne

pour l'obtention du grade de Docteur ès Sciences
par

Mandresy Ivan NY HANITRA

acceptée sur proposition du jury :

Prof. Catherine Dehollain, présidente du jury
Prof. Giovanni De Micheli, directeur de thèse
Prof. Sandro Carrara, co-directeur de thèse
Prof. David Atienza, rapporteur
Prof. Alena Simalatsar, rapporteur
Prof. Pantelis Georgiou, rapporteur

Lausanne, EPFL, 2021

Success is sweet,
but the secret is sweat.
— General Norman Schwarzkopf

To my beloved sister Adriana that was my source of inspiration and motivation throughout this Ph.D. journey, and to my always supporting family.

Acknowledgements

This Ph.D. journey has been a roller-coaster emotionally. I will keep all the good memories and experience that helped me grow up as a person and as a scientist. I am grateful to all the people that helped me and always supported me throughout these last five years.

First of all, I would like to express my most sincere gratitude to Prof. Giovanni De Micheli for giving me the opportunity to pursue my doctoral studies and research at the Integrated Systems Laboratory. I have been fortunate to have available all technological resources allowing me to undertake thrilling and innovative projects. I am grateful for his attentive supervision, guidance, and support, above all during the pandemic period. I would also like to thank my thesis co-supervisor Prof. Sandro Carrara for sharing all his expertise on biosensors, and for always giving me relevant comments to improve the quality of my manuscripts and presentations. I will remember our endless conversations. I am grateful to my jury committee, Prof. Catherine Dehollain, Prof. David Atienza, Prof. Alena Simalatsar, and Prof. Pantelis Georgiou, for reviewing my thesis and providing precious feedback to meliorate it. I would like to extend my acknowledgments to Prof. Danilo Demarchi that kindly hosted me at the Mines group in Politecnico di Torino, where I had the chance to discuss and interact with top scientists in microelectronics and biomedical engineering.
Then, I would like to give special thanks to my LSI colleagues that set a stimulating research environment at my workplace, and with whom I have shared joyful moments outside the laboratory as well. Big hugs to Bossy Giulia that was always caring for me, cheering me up, and making me happy. You have made my Ph.D. journey brighter. Eleonora, thank you for your authentic friendship and care. I am glad to have shared the office with you. Thank you Francesca C. for your goodwill, energy, and open-mindedness. It has been a pleasure to be co-workers and also teammates. Many thanks to Francesca S., Enrico, and Leo, for your infinite generosity, hospitality, and care. I will remember all memorable dinners and moments we have spent together. Giovanni, you have been a role model to me. I hope to get one day your cooking skills and recklessness in doing mountain activities. Thank you Simone for your kindness and altruism. I am grateful about our fruitful collaboration. I am deeply appreciative to Nadja for sharing her expertise in electrochemistry. I thank you for your sincere affection as well. Thank you Tugba for your contagious positivity and for organizing international dinners. Thank you Fereshte for your company during lunchtime. Thank you Aya for your goodness. I am thankful to my logic synthesis colleagues Zhufei, Cunxi, Mathias, Heinz, Winston, Bruno, Sonia,

Alessandro, Dewmini, and newly arrived Andrea. Thank you for letting me join your LS dinners. I would like to thank as well LSI visitors: my dear friend and hard-working mate Abuduwaili, Sattar, Kate, Sofia N., Nadia, Lucia, Sofia M. I have thoughts for Marine and Francesco that have carried out their semester projects under my supervision. I would like to express my gratitude towards Christina, Carole, Chantal, and Lucie, that have been assisting me with bureaucratic matters, and for supporting me during exam periods.

I can not forget to thank all my VLSI colleagues at Politecnico di Torino. Special thanks to Kristjane that always managed to make me laugh. I am grateful for your deep and sincere care and friendship. I am thankful to Yuri, Rosanna, Umberto, Luca, Carmine, Luciano, Fabio, Maurizio, David, Susanna, Paolo, Amir, and all the Andreas. I will remember all the funny moments I have shared with you during and after labor time. I have thoughts to the nice people I have met during conferences such as Hoda and Diana.

Afterwards, I would like to thank all my friends I have met in Lausanne. I am deeply thankful to Iasy for his care and support, and for the sincere brotherhood we have. Thank you Vanisha for your true care and for helping me grow up spiritually. You always have the right words to comfort and appease me. Thank you Sofia for all the moments we have had together on basketball and soccer courts, or behind a screen. You are an amazing and sincere friend. Thank you Ella for all memorable and very funny moments. Good luck for your ongoing Ph.D. I would like to thank all the Malagasy community at EPFL, specially, Deyllan, Yannick, Sharone, Samuel, Kaourintin, Tiavina, Deborah. Thank you for your support and for making me feel like home for a while. Thank you Boris for your sincere and frank friendship, for your help in maths, for your precious advice, and for all the moments we have shared during these last six years. Thank you Luc and Alessandro for all crazy moments we have had in Lausanne or elsewhere. Many thanks to Chiara for her sincere care, yummy dishes, and contagious happiness. I would like to thank Veronica for her comfort, support, and for her attentive care with me. Thank you Mish, Enrico for your encouragement. I have thoughts to my former LMIS2 friends Gergely, Baris, and Roger. S/O to my DMG dawgs Julien, Thibaut, Mehdi, Clife, Abiola. It is a true pleasure to share passion for basketball, fashion, and music with you. I have thoughts to all my basketball and soccer friends across the student campus.

To close these acknowledgments, I would like to dedicate this thesis to my beloved sister Adriana. You have taught me values of courage, hard-work, and faith. You have always been my main source of inspiration and motivation. I miss you a lot! Then, I would like to thank my parents Gérard and Marie Josée for always believing in me and supporting me in my projects. These ten years far from home have been extremely hard to live through. Even if I am not communicating a lot, you know that you mean everything for me. I am warmly thanking my sister Gaëlle, and David, for always caring for me, and making me feel like home by the other side of the lake.

Lausanne, November 30, 2021 Ivan

Abstract

The exponential growth of wearable healthcare devices market is fostered by the *Internet-of-Things* (IoT) era. Connected smart biosensors enable a decentralized healthcare that does not constrain the user to be in a medical facility to get a real-time insight on his health status and a medical diagnosis from a doctor. Moreover, remote physiological monitoring is appealing in sport applications where athletes need real-time feedback on their level of dehydration and muscle fatigue in order to optimize their performances. Electrochemical sensors play a crucial role in physiology and healthcare monitoring since they provide information at molecular level, where the biosensor is in direct contact with bodily fluids such as sweat. A comprehensive healthcare diagnosis is achieved by continuously monitoring several types of biomarkers because of correlations between biological compounds. Namely, endogenous metabolites such as lactate, or potassium and ammonium ions, enable the quantification of muscle fatigue, hence, preventing muscle cramping. In therapeutic drug monitoring, exogenous compounds are continuously tracked so that the drug is maintained in its therapeutic range, in order to always be effective and not toxic for the patient. Besides multi-sensing and general-purpose capabilities, electrochemical platforms need to be correlated to the health and physiological status of the user, where the large amount of measured biological data must be accurately processed and interpreted by smart data analytic tools.

This thesis covers the design, implementation, characterization, and validation of hardware and software interfaces for multi-panel electrochemical sensing platforms.
A multi-mode hardware front-end enabling voltammetric and potentiometric measurements was designed to provide a continuous and concurrent monitoring of endogenous metabolites, drugs, and electrolytes. The electronic front-end was successfully characterized through lactate, paracetamol, and lithium ions monitoring, with an in-vitro setup. This versatile and multi-sensing platform offers a portable solution for remote and comprehensive healthcare monitoring.
Moreover, a multi-ion-sensing front-end was designed for accurate physiology in sweat-sensing applications. Sodium, potassium, ammonium, and calcium ions were concurrently monitored in artificial sweat, with the developed multi-channel hardware. The latter is proposed as a solution for multiple electrolyte detection in artificial sweat samples. In such complex media, multi-ion-sensors are subject to interference from background electrolytes that considerably distort sensor response. Therefore, a compact and analytical model of ion-sensing transduction mechanism was proposed to understand both qualitatively and

quantitatively the non-linearity induced by these artifacts. The ion-sensor model was implemented at the core of an emulator of synthetic datasets that was built to simulate ion-sensor responses in artificial sweat samples. The emulator addresses the expensive time and chemical resources needed to acquire large database for training multivariate calibration models. Thus, the emulated data was used for the training and optimization of a multi-output support vector regressor that is proposed as an accurate, unbiased, robust, compact, low-complexity, and low-latency estimator for the multivariate calibration of multi-ion-sensors. Then, the multi-ion-sensing array, the analog front-end interface, and the chemometric model deployed on a Raspberry Pi, were seamlessly co-integrated for the monitoring of sodium, potassium, ammonium, and calcium ions in artificial sweat, within an IoT framework for real-time and accurate physiology.

Key-words: *electrochemical sensors*, *internet-of-things*, *ion-sensing modeling*, *machine learning*, *multivariate calibration*, *multi-analyte-sensing*, *remote healthcare monitoring*, *remote physiology*.

Résumé

La croissance exponentielle du marché des dispositifs médicaux portables est encouragée par l'ère de l'internet-des-objets. Les biocapteurs intelligents connectés permettent une décentralisation des services de santé, ne contraignant plus les utilisateurs à être dans un établissement médical pour recevoir un aperçu en temps réel de leur état de santé, ou pour recevoir un diagnostic médical d'un docteur. Par ailleurs, le télésuivi de l'état physiologique est attractif pour les applications sportives, où les athlètes ont besoin d'information en temps réel de leur niveau de déshydratation et de fatigue musculaire afin d'optimiser leurs performances. Les capteurs électrochimiques jouent un rôle crucial en physiologie et pour le suivi médical puisqu'ils fournissent des informations à l'échelle moléculaire, où le biocapteur est en contact direct avec les fluides biologiques tels que la sueur. Un diagnostic médical exhaustif est possible grâce à une mesure en continu de plusieurs types de biomarqueurs étant donné que des corrélations existent entre ces composés biologiques. En effet, des métabolites endogènes tels que le lactate, ou des ions potassium ou ammonium, fournissent une quantification de la fatigue musculaire, permettant ainsi d'éviter des crampes. Pour la détection thérapeutique de médicaments, les composés exogènes sont détectés en continu afin de maintenir le médicament dans sa fenêtre thérapeutique, assurant ainsi une efficacité optimale et pas de toxicité pour le patient. En plus du besoin de mesurer plusieurs molécules appartenant à diverses familles, les plateformes électrochimiques doivent être corrélées à l'état de santé et au statut physiologique de l'usager, où la grande quantité de données biologiques doit être traitée et interprétée précisément par des outils d'analyse intelligents.

Cette thèse couvre la conception, l'implémentation, la caractérisation, et la validation d'interfaces hardware et software pour des plateformes de mesures électrochimiques à détection multiple. Une interface hardware à multiple-mode permettant des mesures voltametriques et potentiometriques a été conçue pour assurer un suivi en continu et simultané de métabolites endogènes, de médicaments, et d'électrolytes. Le circuit électronique a été caractérisé avec succès pour la mesure de lactate, paracétamol, et ions lithium, avec une configuration in vitro. Cette plateforme versatile à détection multiple constitue une solution portable pour un télésuivi médical exhaustif. En outre, une interface à détection multiple d'ions a été conçue pour un suivi physiologique précis dans le cadre d'applications de mesures non-invasives à partir de la sueur. Les ions sodium, potassium, ammonium, et calcium ont été mesurés simultanément dans des solutions de sueur artificielle, avec le circuit à multiple-canaux développé. Cette interface

hardware est proposée comme une solution à la détection multiple d'électrolytes dans des échantillons de sueur artificielle. Dans ces solutions complexes, les capteurs d'ions multiples sont sujets aux interférences des électrolytes intrinsèques à la solution, qui détériorent considérablement la réponse des capteurs. Par conséquent, un modèle compact et analytique des mécanismes de transduction des capteurs d'ions est proposé afin d'avoir une compréhension qualitative et quantitative de la non-linéarité introduite par ces artefacts. Le modèle est implémenté au cœur d'un émulateur de données synthétiques qui est construit pour simuler la réponse de capteurs d'ions dans des échantillons de sueur artificielle. L'émulateur répond aux contraintes en matière de temps de mesure expérimentale et de ressources chimiques nécessaires pour acquérir de grandes bases de données pour entraîner des modèles d'intelligence artificielle assurant la calibration de multiples capteurs d'ions. Ainsi, les données simulées sont utilisées pour la calibration et l'optimisation de machines à vecteurs de support à données de sortie multiple, qui est proposé comme un estimateur précis, non-biaisé, robuste, compact, à faible complexité, et à faible latence, pour la calibration de multiples capteurs d'ions. Ensuite, le réseau de capteurs d'ions multiples, l'interface électronique, et le modèle de calibration déployé dans une Raspberry Pi, sont co-intégrés pour la mesure des ions sodium, potassium, ammonium, et calcium dans la sueur artificielle, dans un environnement d'internet-des-objets, pour un suivi en temps réel et précis de l'état physiologique.

Mots clés : *capteurs électrochimiques*, *internet-des-objets*, *modélisation de capteurs d'ions*, *apprentissage machine*, *calibration multiple*, *multiple détection de molécules*, *télésuivi médical*, *télésuivi physiologique*.

Contents

List of Figures

List of Tables

List of Acronyms

ADC *Analog-to-Digital Converter*

ANN *Artificial Neural Network*

AWS *Amazon Web Services*

BLE *Bluetooth Low Energy*

BSN *Body Sensor Network*

BTC *Bluetooth Classic*

CA *Chronoamperometry*

CE *Counter Electrode*

CV *Cyclic Voltammetry*

DAC *Digital-to-Analog Converter*

DDS *Direct Digital Synthesizer*

DPV *Differential Pulse Voltammetry*

ELU *Exponential Linear Unit*

ET *Electronic Tongue*

FFNN *Feed-Forward Neural Network*

FIM *Fixed Interference Method*

GATT *Generic Attribute Profile*

GUI *Graphical User Interface*

HMF *Hydroxymethylferrocene*

IoT *Internet-of-Things*

IRWLS *Iterative Reweighted Least-Squares*

ISE *Ion-Selective Electrode*

ISM *Ion-Selective Membrane*

IUPAC *International Union of Pure and Applied Chemistry*

LOD *Limit Of Detection*

LOx *L-lactate Oxidase*

LPF *Low-Pass Filter*

LSB *Least Significant Bit*

MCU *Microcontroller Unit*

MLR *Multiple Linear Regression*

MLP *Multi Layer Perceptrons*

MRE *Mean Relative Error*

M-SVR *Multi-output Support Vector Regressor*

NFC *Near-Field Communication*

NIPALS *Non-linear Iterative Partial Least-Squares*

NRMSE *Normalized Root Mean-Squared Error*

OCP *Open Circuit Potential*

OLS *Ordinary Least-Squares*

OpAmp *Operational Amplifier*

PBS *Phosphate Buffer Saline*

PC *Principal Component*

PCA *Principal Component Analysis*

PCB *Printed Circuit Board*

PCR *Principal Component Regression*

PLS *Partial Least-Squares Regression*

RBF *Radial Basis Function*

RE *Reference Electrode*

RMSD *Root Mean-Squared Deviation*

RPi *Raspberry Pi*

RSSI *Received Signal Strength Indicator*

RTD *Resistive Thermal Device*

SNR *Signal-to-Noise Ratio*

SPE *Screen-Printed Electrode*

SSCE *Sodium-Saturated Calomel Electrode*

SSM *Separate Solution Method*

SVD *Single Value Decomposition*

SVM *Support Vector Machine*

SVR *Support Vector Regression*

TIA *Transimpedance Amplifier*

TDM *Therapeutic Drug Monitoring*

UART *Universal Asynchronous Receiver-Transmitter*

VNC *Virtual Network Computing*

WE *Working Electrode*

1 Introduction

Over the last decade, we have witnessed an exponential growth in the biomedical devices market, particularly through wearable healthcare devices that are projected to reach USD 46.6 billion by 2025, from USD 18.4 billion in 2020 (see Fig. 1.1).

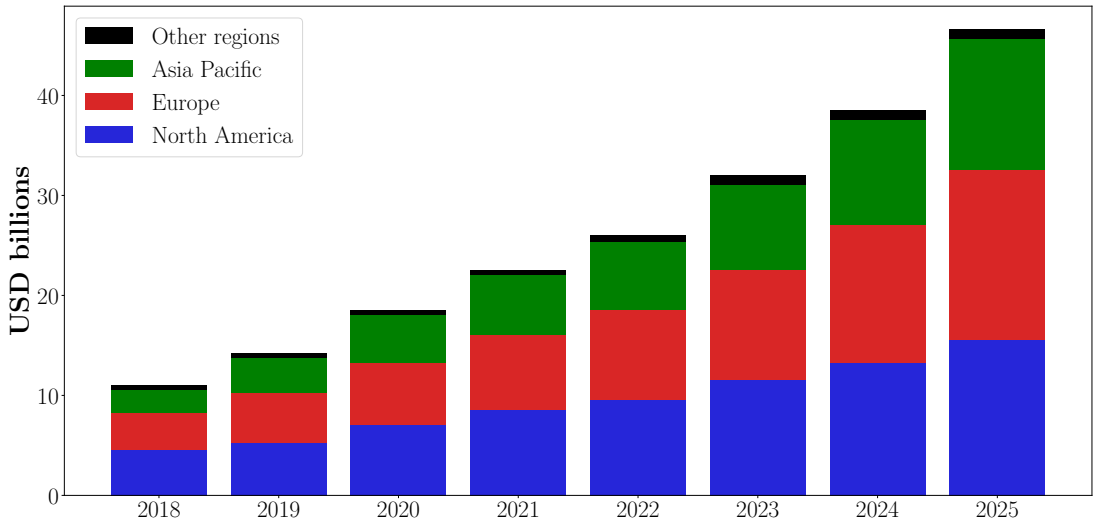

Figure 1.1 – Wearable healthcare devices market by region in USD billion (data: Markets and Markets, 2020).

The growth of this market is fostered by the IoT era in which we are living, where smartphones and connected devices are capable of providing, in real-time, relevant information about the physical activity of the user [**?**, **?**]. For instance, most commercial smartwatches embed heart rate trackers, are able to monitor oxygen saturation, foot steps, and/or sleep cycle. Besides, portable healthcare tools enable fast diagnosis, and could alert the user about potential health hazard such as cardiac abnormal activity [**?**]. Therefore, remote healthcare is appealing to consumers since they are not constrained to be in an hospital environment to get insights on their vital signs [**?**]. Moreover, a decentralized digital healthcare allows doctors to undertake a more exhaustive diagnosis

of their patients since they have access to their physical and physiological parameters that are shared on cloud databases. In the sequel of this chapter, the current trends and challenges in remote healthcare monitoring are discussed. Then, an IoT solution is proposed, where both hardware and software interfaces are designed and optimized for an accurate and real-time healthcare monitoring or for physiology applications. Next, the research contributions and the thesis outline are detailed.

1.1 Trends and challenges in remote healthcare monitoring

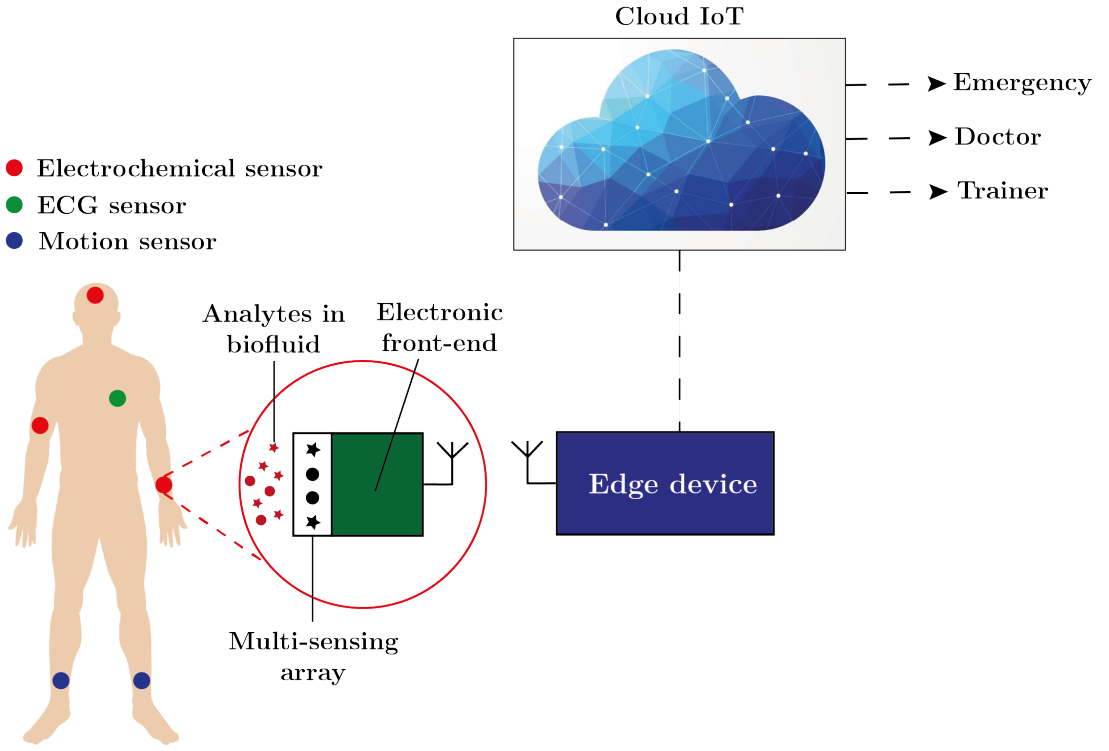

Figure 1.2 – Different modules of a wearable sensor network enabling remote healthcare monitoring.

Novel advances on miniaturized, light-weight, low-power, and intelligent wearable sensors contribute to the development of new network architectures referred as *Body Sensor Network*s (BSNs) [**?**]. Namely, on-body sensors continuously monitor physical (cardiac activity, muscle activity) and physiological (bio-chemical information) status of the user, and convey the biological data wirelessly to a nearby personal server or an edge node, through a local network. Data processing and real-time visualization can be performed on the edge device that is used as a gateway to cloud IoT platforms, where data storage, computation, and sharing to medical databases, doctors, and trainers can be performed. The different modules of a BSN that enable remote healthcare monitoring are highlighted in Fig. 1.2. In this section, some of the main challenges in remote healthcare monitoring

are discussed, considering multi-sensing platforms, electronic front-end interfaces, data analytics, and connectivity.

1.1.1 Electrochemical sensing platforms

Most commercial remote healthcare systems are able to track the user's physical activity such as cardiac activity [**?**, **?**] and body motion [**?**]. Yet, a continuous monitoring of biochemical parameters is essential to obtain a precise information about the user's health and physiological status. Electrochemical sensors are able to provide such insights at molecular level since they are in direct contact with biological fluids. They are appealing since they leverage progress in microtechnology to be miniaturized and integrated into wearable systems, and they enable a non-invasive health monitoring through small sample volume of bodily fluids such as sweat, tears, or saliva. Moreover, they feature excellent sensitivity and *Limit Of Detection* (LOD), high selectivity, fast response time, at a lower cost than other detection techniques that necessitate bulky laboratory instrumentation (e.g. optical transducers) [**?**, **?**, **?**]. The analytes of interest span a wide range of biomolecules, including endogenous metabolites such as lactate or glucose [**?**, **?**], electrolytes like potassium or sodium ions [**?**], exogenous compounds absorbed in the organism as drugs in *Therapeutic Drug Monitoring* (TDM) [**?**], heavy metals [**?**], and toxic gases [**?**]. Glucose monitoring from blood samples is quite mature, and portable devices are present in the market for the treatment of diabetes since many years [**?**]. Nevertheless, the non-invasive detection of the aforementioned family of compounds still presents many challenges and draws a lot of research interest.

First of all, on-body sensing requires soft and stretchable materials able to address mechanical stress and motion artifacts. Research on flexible electronics contemplates innovative materials and techniques for the patterning of the electrode transducers on the substrates. Polymeric or paper-based substrates are commonly used [**?**], and standard printing or lithographic technology should be adapted to the new underlying materials [**?**]. Moreover, biological fluid extraction and management necessitates a custom-designed microfluidic setup [**?**]. Besides, research efforts are typically carried out for improving sensitivity, specificity, LOD, and transduction mechanisms involved in the detection of one specific analyte [**?**]. However, multi-analyte sensing is needed for a more comprehensive health status diagnosis, and because of correlations between the target analytes. For instance, in sport applications, lactate is measured to assess muscle fatigue, while glucose level indicates the energy consumed by the cells. Sodium ions concentration reflects the level of dehydration, and potassium and ammonium ions are monitored to foresee muscle cramping [**?**, **?**]. Furthermore, measuring multiple analytes concurrently helps disambiguating whether the sensor signal fluctuations stem from a change in the concentration of the analytes, or if they are due to sweat rate effects, for instance in sweat sensing [**?**]. As a matter of fact, sweat sodium ions are always monitored simultaneously with potassium ions at least [**?**]. Therefore, multi-sensing

arrays are necessary, but cross-talks and cross-interference between individual sensors should be taken into account carefully during multiplexed or concurrent measurements.

1.1.2 Electronic front-end interface

The electronic front-end interface ensures both correct polarization of the electrochemical sensors, and readout of the transduced electrical signal resulting from the chemical detection. Depending on the type of analyte (e.g. a metabolite, an electrolyte, or an exogenous compound) and the electrochemical sensing technique employed, different front-end circuitry are implemented. Therefore, in a multi-sensing framework with different families of biomolecules to track, a multi-mode hardware front-end is needed, where the sensing channels should be properly decoupled. Moreover, the electronic interface should contain signal conditioning blocks to process and filter the electrical signal sensed without loss, and it should relay the final calibrated biological information to a display interface via a wireless node. Low-noise and low-power circuits are targeted for the design of the hardware front-end in order to ensure a continuous healthcare monitoring. Application-specific integrated circuits can supply ultra low-noise and low-power performances, but they are intended mainly for small form-factor integrated sensors, for instance for saliva monitoring [**?**], or for implantable applications [**?**]. Whereas in wearable sweat sensing, portable devices embedded in headbands or wristbands could be implemented with standard *Printed Circuit Board* (PCB) technology, where the transducers are electrodes of typically 3 mm diameter in size [**?**, **?**]. PCBs can be mass-produced cost-effectively, leveraging mature industrial processes for the manufacturing of flexible and semi-rigid substrates. In addition, low-noise and low-power off-the-shelf components are available to implement the various electronic front-end modules. Regarding the powering of the hardware, small portable and rechargeable coin cell or lithium ions batteries are commonly integrated in wearable systems [**?**, **?**]. Energy harvesting sources such as biofuel cells or supercapacitors are also investigated, but several issues such as long-term stability, bio-compatibility, operational lifespan, and on-body compliance need to be addressed [**?**, **?**]. Battery-free strategies leveraging wireless power transfer through *Near-Field Communication* (NFC) technology is appealing. In addition, it involves a reduced electronic footprint and power consumption. However, it operates at very short-range (less than 5 cm) and features a lower data rate compared to active transceivers [**?**]. Eventually, the co-integration of the sensing front-end with the readout electronics necessitates a careful packaging to insulate properly the hardware from the sample solution.

1.1.3 Examples of fully-integrated remote healthcare monitoring platforms

Some examples of fully-integrated electrochemical sensing platforms for real-time healthcare monitoring are illustrated in Fig. 1.3, highlighting the diverse design choices for the realization of the sensing platform and the electronic interface. In Fig. 1.3 **(a)**,

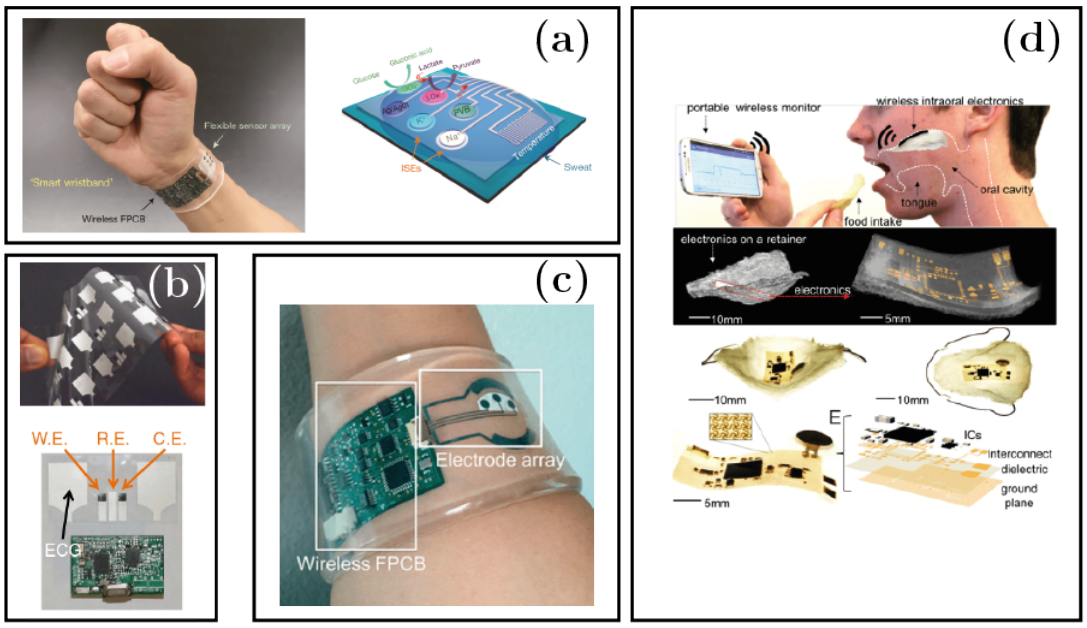

Figure 1.3 – Fully-integrated remote electrochemical sensing platforms for real-time healthcare monitoring: **(a)** multiplexed sensing of glucose, lactate, sodium and potassium ions, and on-body temperature from perspiration analysis in sport applications (reprinted from [**?**]); **(b)** multi-modal chemical and electrophysiological monitoring with sweat lactate and heart rate tracking for fitness applications (reprinted from [**?**]); **(c)** simultaneous detection of chloride, sodium, and glucose from sweat, with an epidermal iontophoretic biosensor (reprinted from [**?**]); **(d)** monitoring of sodium intake through saliva during hypertension management (reprinted from [**?**]).

the sensing front-end was integrated in a wristband for perspiration analysis in sport applications, enabling the monitoring of glucose, lactate, sodium and potassium ions, and on-body temperature. Both sensing platform and hardware were manufactured on flexible substrates. In Fig. 1.3 **(b)**, a multi-modal biosensor is shown, enabling the monitoring of heart rate and sweat lactate for fitness applications. The electrodes were patterned with screen-printed technology on an highly flexible polyester substrate, while the hardware was mounted on a 4-layer PCB. In Fig. 1.3 **(c)**, an epidermal biosensor is displayed for the monitoring of chloride, sodium, and glucose in sweat that was induced by an iontophoretic circuit. In Fig. 1.3 **(d)**, an oral monitoring of sodium intake during hypertension management is shown. An user-comfortable system leveraging an ultra-thin stretchable electronics with miniaturized sensors was proposed for ion-monitoring through saliva.

1.1.4 Smart biosensors

The electrical signals measured at the sensing interface need to be correlated to the health or the physiological status of the user. Smart modules are needed to process, analyze, and interpret these signals so as to provide physiologically relevant information.

The raw electrical signals are first processed and elaborated. Namely, digital filters are implemented to smooth the signals, or data could be standardized (e.g. zero-mean, unit-variance). Next, features are extracted from the measured signals. For instance, in voltammetry, the electrical current is measured as a function of the applied cell voltage. The oxidation and reduction peaks need to be extracted from the voltammograms since the peak currents are related to the concentration of the electroactive species of interest. Generally, electrochemical laws dictate the dependence between the measured signals and the concentration of the analytes, and that dependence is valid in the detection range of the senor [**?**]. A sensor calibration is typically carried out prior to the measurement in order to determine the linear relationship between the measured signal and the corresponding analyte concentration. However, interference from the compounds present in the sample could distort sensor response, necessitating advanced processing techniques. For instance, in voltammetry, when electroactive compounds of similar redox potentials are detected, the resulting RedOx peaks are overlapping, and it is necessary to decompose the contribution of each compound to the observed signal. Even though the Faradaic peaks are not necessarily Gaussian, a Gaussian decomposition of proprofol and paracetamol oxidation peaks enables a robust drug monitoring in anesthesia practice, in [**?**]. In ion-sensing, interference from the background electrolytes in the biological fluid adds an offset to the measured potential, and distorts the logarithmic Nernstian response of the ion-sensor. Another challenge arises from sensor limited selectivity, and cross-interference between individual sensors in multi-ion-sensing systems [**?**]. This effect is even more severe when the analyte of interest is diluted in real samples (e.g. trace metals in sweat are present at µM concentration [**?**]). Therefore, non-linear and advanced models are needed to monitor the electrolytes of interest in these cases. These smart modules are commonly implemented in post-processing pipelines on a laptop [**?**], but this hampers a decentralized and real-time healthcare monitoring. Thus, embedded software solutions are desired. Alternatively, the processing algorithms could be synthesized on a configurable hardware (e.g. automatic peak detection for voltammetry implemented on an field programmable gate array in [**?**]).

Besides data processing and accurate data analysis, data interpretation is another challenge in smart healthcare monitoring. Namely, the large amount of data collected from multiple sensors needs to be analyzed and filtered in order to determine their true physiological relevance. It is necessary to identify correlations between the estimated values of physiological parameters acquired from the sensor array, and the health status of the user. Long-term studies are carried out for this purpose, with comparisons between healthy and unhealthy subjects [**?**]. This allows us to establish some trends and threshold

values of the physiological parameters of interest that could indicate an healthy status. For instance, the therapeutic window of a drug, in personalized medicine, corresponds to the range of concentration for which the drug is optimally effective and not toxic to the patient. Smart closed-loop systems could be implemented to maintain the concentration of the exogenous compound always in its therapeutic window by adjusting its dose with am integrated fluidic bioelectronic system [**?**]. To ameliorate the interpretation of the physiological information acquired from sensor arrays, the current trend in data analytics is to leverage big data and data mining techniques using data fusion, statistical methods, pattern recognition, and advanced machine learning models [**?**, **?**, **?**].

1.1.5 Wireless sensor networks

Remote healthcare monitoring involves wireless technology to transmit the chemical analytical information measured by a sensor array to a remote device for further data processing, elaboration, visualization, and storage. Data is conveyed through a local area network, where the common communication protocols are Bluetooth, NFC, radio-frequency identification, and Zigbee. The biomedical application dictates the choice of the most appropriate protocol, taking into account size constraints of the hardware footprint, power consumption requirements, transmission range, data rate, real-time or event-based monitoring [**?**]. The wireless sensor could be used for a single point-to-point reading on a personal server or mobile device, or it could be used in distributed systems in a wireless sensor network. Indeed, the IoT paradigm intends to create a large network of connected sensors that interact and communicate between themselves and their local users, forming BSNs [**?**]. Cloud services can be exploited for advanced data processing leveraging higher computational and memory resources than on an edge device, and for storage of the big data aggregated from the sensors. Nevertheless, very high data rates are required to satisfy latency requirements for real-time applications. Another paramount challenge concerns data security and user privacy. Innovative cryptographic algorithms and secure authentication procedures are needed to protect big data generated in remote healthcare monitoring.

1.2 Hardware and software interfaces design for accurate and real-time healthcare monitoring

The design of accurate remote healthcare monitoring systems requires a concurrent optimization of:

- **the sensor interface** that should feature high stability, sensitivity, and selectivity towards the target analyte. A large sensor dynamic range is desired for monitoring very small amount of biomarkers present in the biofluid (e.g. drugs, toxic compounds). Moreover, multi-sensing capabilities are needed for a comprehensive health

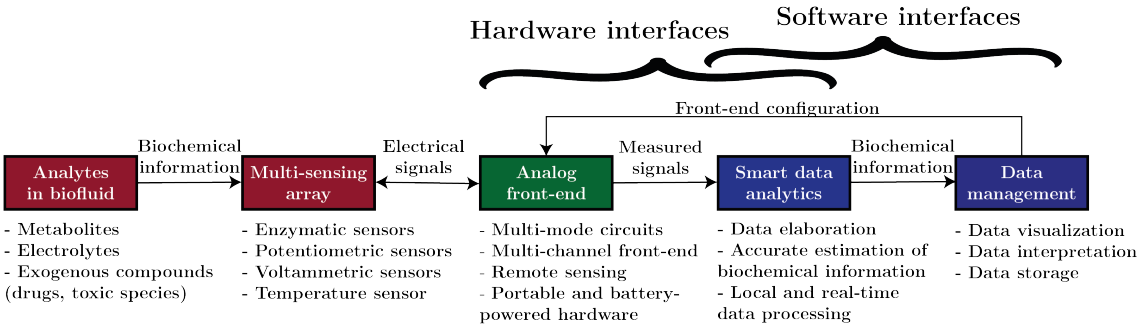

Figure 1.4 – Hardware and software interfaces for multi-panel electrochemical sensing

status diagnosis. Namely, endogenous/exogenous metabolites and electrolytes are monitored through different electrochemical techniques, requiring specific sensor functionalization. In situ temperature is a relevant physiological parameter as well.

- **the analog front-end** that should properly polarize the sensors and accurately measure the electrical signals transduced by the electrode array. Mixed-mode circuits are needed to implement voltammetric, potentiometric, and temperature measurements. Low-noise and low-power circuits are aimed, and a portable and battery-powered hardware is required for wearable sensing applications.

- **the data processing tools** that elaborate and extract features from the raw electrical signals measured, and eventually retrieve the biochemical information contained in the sample. For instance, advanced multivariate calibration models are required for the analysis of low-selective ion sensors subject to interference from the electrolytes inherently present in the biofluid. Such data analytics are implemented locally, in the vicinity of the sensor, in order to ensure a real-time healthcare monitoring.

- **data management unit** enabling a continuous and real-time visualization of the monitored biochemical information. An user interface is typically developed, allowing both data visualization and configuration of the sensing front-end. The storage and maintenance of the biological data should be addressed along with data security.

The main features of multi-panel electrochemical sensors that were optimized in this thesis are summarized in Fig. 1.4, where emphasis is put on the hardware and software modules. In the remainder of this section, two remote healthcare monitoring systems implemented in this thesis are briefly introduced. All further details will be deeply and critically presented in the subsequent chapters of this thesis.

1.2.1 Multi-mode hardware for comprehensive healthcare monitoring

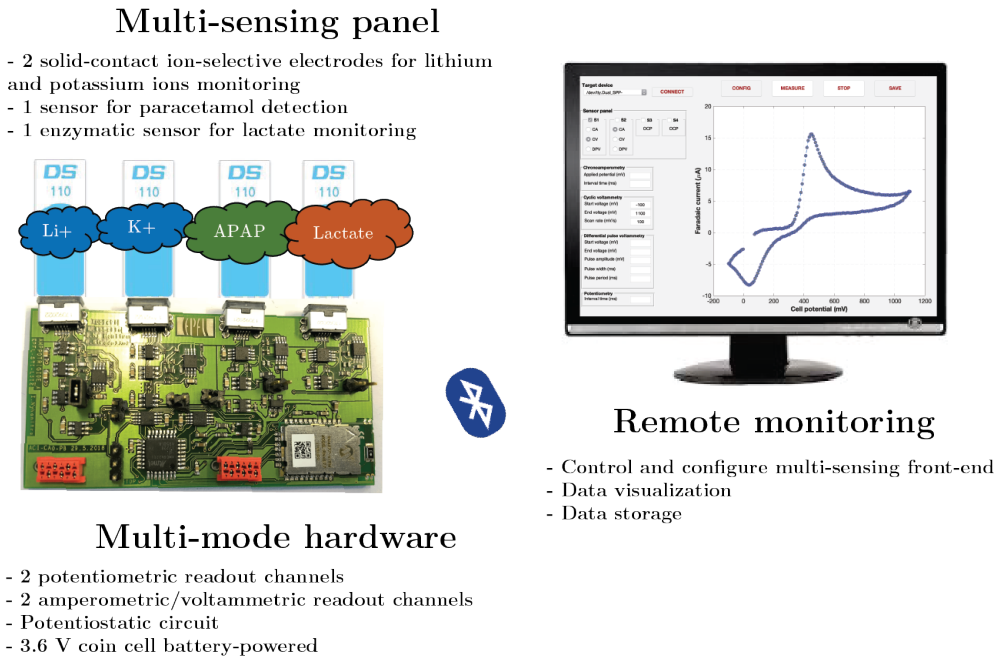

Figure 1.5 – Multi-mode sensing front-end enabling the detection of electrolytes, metabolites, and drugs.

A comprehensive healthcare diagnosis can be achieved by carrying out multi-analyte monitoring, for which endogenous electrolytes and metabolites are relevant biomarkers. The detection and monitoring of exogenous compounds is also desired in TDM. The electrochemical techniques used for tracking these different types of analytes involve specific electronic front-ends. Thus, a multi-mode hardware is proposed in Fig. 1.5, enabling a remote monitoring of electrolytes, metabolites, and drugs. The hardware was manufactured on a flexible or rigid substrate, and was powered by a coin cell or lithium ion battery. A remote *Graphical User Interface* (GUI) was implemented to control and configure the multi-panel electrochemical platform. The measured data was visualized in real-time on the display interface. The system was validated in vitro, through lithium ions, paracetamol, and lactate detection, being typical examples of electrolyte, exogenous compound, and endogenous metabolite, respectively.

1.2.2 Multi-ion-sensing front-end for accurate and real-time physiology

Sweat sensors generate a lot of interest for non-invasive healthcare monitoring and physiology. Indeed, perspiration contains several biomarkers (electrolytes, metabolites, trace metals) providing diagnostic capabilities with good correlation with blood values, making these sensors paramount for preventive medicine [**?**, **?**]. In particular, ions are

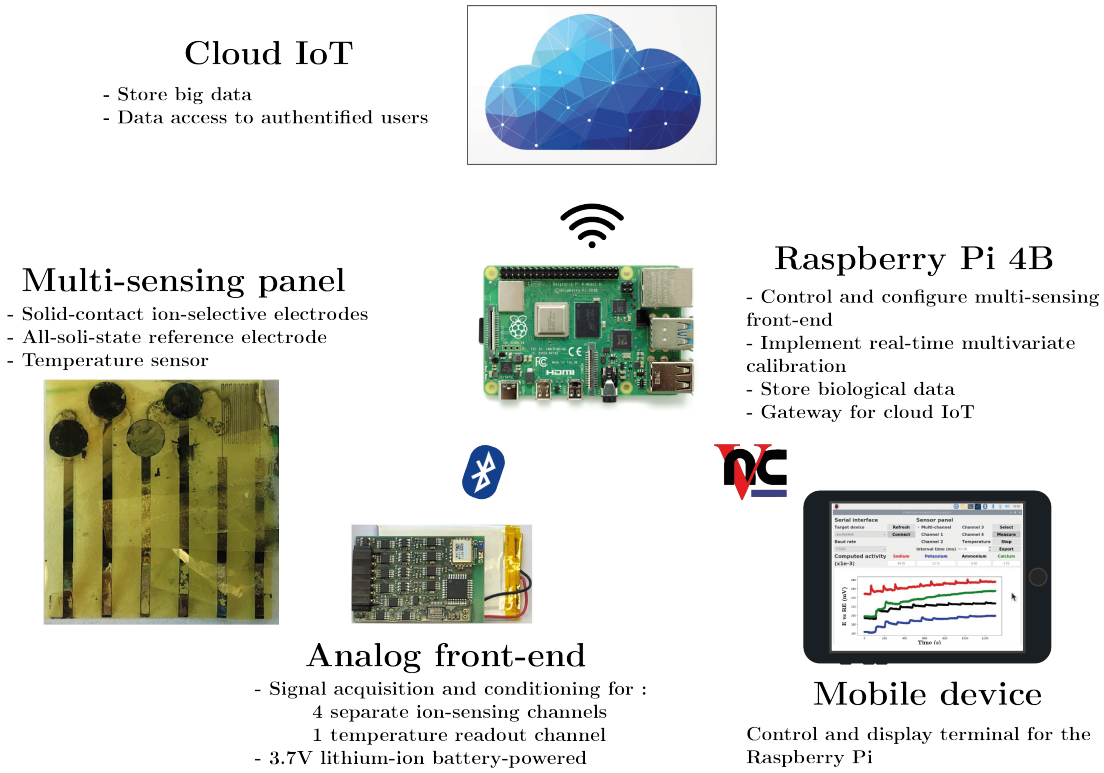

Figure 1.6 – Multi-ion-monitoring front-end for accurate and real-time physiology.

significantly involved in human physiological processes. Namely, certain diseases such as cystic fibrosis, hypo/hyperkalemia, or cardiac arrhythmia could be controlled by the determination of cations and anions (chloride and sodium, potassium, magnesium ions, respectively) [**?**, **?**]. Moreover, physiological status during physical exercise can be assessed by tracking chloride, sodium, potassium, ammonium, calcium, magnesium ions, that indicate level of dehydration, muscle fatigue, aerobic performance, and electrolyte balance [**?**].

Therefore, a complete multi-ion-sensing front-end is proposed and illustrated in Fig. 1.6 for the continuous and real-time monitoring of physiologically relevant ions. Sweat is easily reproducible in laboratory, facilitating the characterization of the electrochemical sensing interfaces with artificial sweat samples. A multi-electrode platform was manufactured on a flexible substrate, and solid-contact *Ion-Selective Electrode*s (ISEs) for sodium, potassium, ammonium, and calcium ions were fabricated. An all-solid-state Ag/AgCl *Reference Electrode* (RE) was built for fully-integrated ion sensing, and a platinum *Resistive Thermal Device* (RTD) was patterned for in situ temperature measurement. The analog front-end interface enables a concurrent measurement of the four analytes, and of in situ temperature. The biological data was wirelessly conveyed to an edge node, where a multivariate calibration model was deployed. As a matter of fact, interference from background electrolytes in the sample and inherent cross-selectivity bounds of

the ion-sensors significantly distort sensor responses, necessitating the use of non-linear models for the prediction of the concentration of the target electrolytes. Unbiased, robust, low-complexity, and low-latency estimators are desired for an accurate and real-time multi-ion-sensing. Data was then visualized on a mobile device, and was stored on cloud databases, leveraging a cloud IoT framework.

1.3 Research contributions

This thesis covers the design, implementation, characterization, and validation of hardware and software interfaces for multi-panel electrochemical sensing platforms. The different modules of a remote healthcare monitoring system are concurrently designed and optimized, including the multi-sensor array, the analog front-end interface, the embedded smart data analytics, and the cloud IoT support for big data storage and healthcare decentralization. The main contributions are summarized hereinafter:

- The design and realization of a **multi-mode hardware front-end enabling potentiometric and voltammetric measurements**. The platform provides a continuous and concurrent monitoring of metabolites, electrolytes, and drugs. A waveform generator was designed to generate potential step, triangular, and pulsed waveforms that stimulate the electrochemical cell in voltammetric measurements. This hardware front-end provides a versatile, programmable, and multi-analyte sensing platform for remote healthcare monitoring.

- The design and realization of a **multi-ion-sensing front-end** able to continuously and simultaneously monitor up to four electrolytes. A precise temperature readout circuit was added for in situ temperature measurement. This hardware front-end is proposed as a solution to support multiple electrolyte detection in complex samples.

- A **compact analytical model of ion-sensing** transduction mechanism through polymeric ISEs. This study provides both quantitative and qualitative understanding of the impact of ion interference in sensor responses. The analytical model was implemented at the core of an emulator of synthetic datasets that was built to simulate the response of polymeric ISEs in complex samples of different electrolytic composition. The sensing performances of fabricated polymeric ISEs (sensitivity, LOD, selectivity) were parameters added to the model in order to produce datasets explaining accurately the experimental response of polymeric ion-sensors. Such emulator addresses the expensive time and chemical resources needed to obtain large database for training complex multivariate calibration algorithms.

- An accurate, unbiased, robust, compact, low-complexity, low-latency *Multi-output Support Vector Regressor* (M-SVR) is proposed and implemented for the **multivariate calibration of multi-ion systems**. The multivariate regressor was

trained and optimized with emulated datasets of different size. The performance of the calibration model was compared with linear and other non-linear models for the compensation of interference in accurate multi-ion-sensing.

- The validation of a **complete electronic tongue system** developed for accurate and real-time multi-ion-monitoring in physiology, within an IoT framework. The different modules (ion-sensor array, analog front-end interface, embedded multivariate calibration model, edge node, and cloud storage) were co-integrated for a real-time monitoring of sodium, potassium, ammonium, and calcium ions in artificial sweat.

1.4 Thesis organization

The thesis is organized as follows:

Chapter 1 has given an overview of the trends and main challenges in remote healthcare monitoring, necessitating a concurrent design and optimization of multi-panel sensors, electronic front-end, smart data analytics, and wireless networks.

Chapter 2 provides a detailed background covering the fundamentals on electrochemical sensing principles for the detection of endogenous metabolites, electroactive compounds, and endogenous electrolytes, that involves voltammetric and potentiometric measurements. The functional blocks of the electronic front-end ensuring a correct biasing and readout of the electrochemical sensor response is also detailed. Moreover, chemometric models are presented for the analysis and treatment of complex electrochemical datasets, in particular in multi-ion-sensing in presence of interference.

Chapter 3 describes the design, implementation, and characterization of a general-purpose electrochemical sensing front-end for comprehensive healthcare monitoring. The proposed four-channel hardware *AmpPot* supports concurrent voltammetric and potentiometric measurements, where a programmable waveform generator supplies different polarization potentials to the potentiostat driving the electrochemical cell in voltammetry. The multi-mode front-end was successfully characterized through lactate, paracetamol, and lithium ions monitoring. The latter are typical examples of endogenous metabolite, drug, and electrolyte, tracked for various healthcare applications.

Chapter 4 describes the design, implementation, and characterization of a multi-ion-sensing front-end for physiology. Solid-contact ISEs were developed for the monitoring of sodium, potassium, ammonium, and calcium ions, that are prevalent electrolytes in sweat, yielding a physiological status insight for physical activity applications and for medical care. In situ temperature was also tracked for calibration purposes. The proposed multi-ion-sensing front-end provides the sensing interface for an electronic

tongue performing a multivariate analysis of complex media such as sweat.

Chapter 5 presents the derivation of a compact model of polymeric ISEs in mixed-ion samples. The impact of ion interference on multi-ion-sensor response was studied from an analytical perspective, and validated through comparison with experimental data. An ion-sensing emulator was developed as an investigation tool to provide both quantitative and qualitative estimation of the influence of sensor properties and sample composition on the distortion of the calibration curves by ion interference. Moreover, the multi-ion-sensing emulator enabled an automatic generation of emulated synthetic datasets for the monitoring of sodium, potassium, lithium, and lead ions, in artificial sweat samples.

Chapter 6 describes the implementation, training, and optimization of machine learning models developed to improve the multivariate calibration accuracy of multi-ion-sensors hindered by ion interference. Linear and non-linear regressors were investigated, and the performance of the proposed M-SVR model was compared to *Multiple Linear Regression* (MLR), single-output *Support Vector Regression*s (SVRs), and MLP models. The multivariate regressors were trained and evaluated on emulated synthetic datasets of sodium, potassium, lithium, and lead ions, of different size, in typical sweat electrolytic mixtures.

Chapter 7 presents a complete electronic tongue system enabling an accurate, continuous, and real-time monitoring of sodium, potassium, ammonium, and calcium ions, for physiology. The co-integration of the multi-ion-sensing panel, the electronic readout interface, and the M-SVR model deployed on an edge node is described. The multivariate calibration model was trained, optimized, and evaluated with an experimental synthetic dataset acquired with the developed polymeric ISEs. An automatic training of the M-SVR with an emulated synthetic dataset is proposed as an efficient solution to avoid re-calibrating the multivariate regressor before each inference phase. The electronic tongue system was then validated through a real-time multi-ion-monitoring task in artificial sweat samples, where data was stored on cloud databases, enabling a decentralized healthcare.

Chapter 8 summarizes the main contributions of the thesis and gives an outlook on possible future works.

2 Background

This chapter introduces the basic electrochemical sensing principles for the detection of metabolites, drugs, and electrolytes, that are the different types of biomarkers considered for healthcare monitoring. The electronic interface circuits enabling such monitoring are then detailed. Next, an overview on the mathematical tools used to process the data collected from chemical sensors is provided.

2.1 Electrochemical sensing

Electrochemical sensing involves charge transfer processes at electrode/electrolyte interfaces of an electrochemical cell. The sensing electrode transduces the bio-chemical recognition event into an electrical signal, enabling the monitoring of the analyte. Different analytical methods are implemented depending on the type of biomarkers to detect. Namely, voltammetry is used for enzyme-mediated detection of metabolites (e.g. lactate or glucose) and for direct detection of electroactive drugs (e.g. paracetamol), while potentiometry is employed for ion-sensing (e.g. sodium or potassium ions). These two analytical methods are described in the sequel.

2.1.1 Voltammetric sensors

Voltammetry is the common analytical method for the characterization of Faradaic processes, where the electrical current is measured in a potential-controlled setup [**?**, **?**].

Electrochemical cell

A three-electrode electrochemical cell is usually implemented (see Fig. 2.1), where the *Working Electrode* (WE) is the sensing electrode at which a redox reaction occurs, the RE is constituted of phases of constant composition so that its potential is fixed, and the

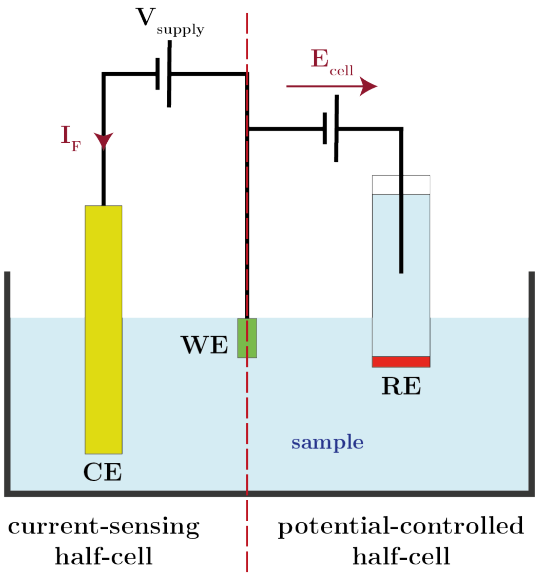

Figure 2.1 – Sensing configuration of a three-electrode electrochemical cell.

Counter Electrode (CE) is an auxiliary electrode that is inert to the analyte in the sample. The system operates by imposing an electrochemical cell potential $E_{cell} = E_{WE} - E_{RE}$, while measuring the current I_F flowing through the WE–CE path. The RE is a high impedance node ensuring that zero-current flows at this node, making E_{RE} independent of Faradaic processes, and the CE is needed to balance the electron transfer observed at the sensing electrode, thus, closing the current path.

By imposing more negative potentials to the WE, the energy of the electrons in the metal raises until reaching a sufficient energy to transfer electrons to vacant electronic states on species in the electrolyte. This results in a **reduction current** (electrons flowing from the metal to the electrolyte). Conversely, an **oxidation current** is observed when the WE is biased to more positive potentials since the energy level of the electrons in the metal is decreasing up to a point that it is lower than the energy level of the highest occupied electronic states in the electrolyte, resulting in an electron transfer from the electrolyte to the electrode. The potential at which these Faradaic processes are triggered is related to the standard potential E_0 of the corresponding electroactive compounds, and if the charge transfer kinetics are fast, the concentrations of the oxidized and reduced form of the electroactive compound at the electrode surface, C_{ox} and C_{red}, are governed by Nernst equation:

$$E_{cell} = E_0 + \frac{RT}{nF} \ln\left(\frac{C_{ox}}{C_{red}}\right), \tag{2.1}$$

where R is the gas constant, T is the absolute temperature, n is the number of electrons

exchanged, and F is the Faraday constant. The observed current is a measure of the rate of reaction of these electroactive compounds at the electrode surface. The latter depends on the charge transfer kinetics at the electrode/electrolyte interface and on the mass transport of the electroactive species to/from the electrode (through convection, migration, and/or diffusion). In the sequel, it is assumed that diffusion is controlling the rate of Faradaic processes.

Besides, non-Faradaic processes systematically occur when the electrode is immersed in the electrolyte. Namely, charge separation and redistribution take place at the metal/solution interface, forming an electrical double layer capacitor C_{dl} which value changes with the potential applied. Once a potential is applied to the cell, charges accumulate at the interface, and a transient **charging current** flows through the electrical double layer. Therefore, the total current measured in voltammetric sensing is the sum of the Faradaic and non-Faradaic processes contributions.

Voltammetric techniques

Several voltammetric techniques can be implemented for the detection of electroactive species, depending on the potential E_{cell} applied to the electrochemical cell.

***Chronoamperometry* (CA)** is a potentiostatic technique for which a potential step is applied to the cell, and the resulting current is measured in time. It is assumed that the species are electroinactive before the potential step, and that the step potential is at a value for which the electroactive species are oxidized/reduced at a diffusion-limited rate. The latter assumption is necessary to observe a diffusion-limited current when the step potential is applied.

More precisely, let us consider the following reduction at the electrode surface:

$$\mathrm{Ox} + \mathrm{ne}^- \rightarrow \mathrm{Red}, \tag{2.2}$$

where Ox and Red are the oxidized and reduced form of the electroactive compound, respectively. After application of the potential perturbation, Ox is instantly reduced at the electrode surface, and a large current flows. This results in a concentration gradient of the reactant, thus a continuous flux of Ox towards the electrode. However, the region at the vicinity of the electrode becomes increasingly depleted with Ox, so its concentration gradient reduces in time, therefore the observed current at the electrode surface decreases. This decaying diffusive current is described by the Cottrell equation:

$$\mathrm{i(t)} = \frac{\mathrm{nFA}\sqrt{\mathrm{D}}}{\sqrt{\pi \mathrm{t}}}\mathrm{C}^*, \tag{2.3}$$

where n is the number of exchanged electrons during the reduction, F is the Faraday constant, A is the active area of the electrode, D is the diffusion coefficient of the reactant, and C^* is the bulk concentration of the reactant.

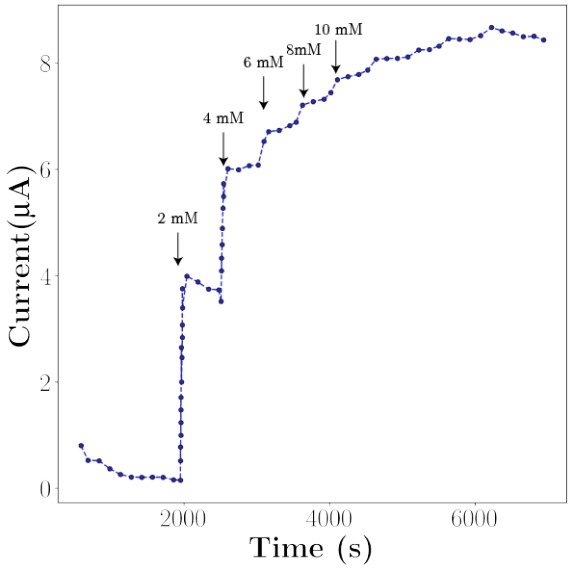

Figure 2.2 – Typical chronoamperometric response of our lactate sensor to successive additions of the analyte in phosphate buffer saline solution.

CA is implemented for continuous monitoring of biomarkers. For instance, enzymatic biosensors are used to track endogenous metabolites such as lactate and glucose. The corresponding oxidases are coated on the sensing electrode and trigger RedOx processes in presence of the analyte. Typical chronoamperometric response of our lactate sensor to successive additions of the analyte in *Phosphate Buffer Saline* (PBS) solution is displayed in Fig. 2.2. Faradaic current steps are observed after injection of the analyte.

Potentiodynamic techniques are generally used for the characterization of electrochemical sensors. The current-time-potential space is exploited where the applied potential E_{cell} is varying in time, and the resulting current is continuously measured. Consequently, electrochemical analysis is performed by analyzing the current-potential plot called voltammograms. Several potential sweep methods are available. A linear potential scan method and a pulsed potential method are described next.

***Cyclic Voltammetry* (CV)** is a linear scan technique for which the cell potential is swept as:

$$E_{cell}(t) = \begin{cases} E_{start} + \nu t, & \text{for } 0 < t \leq t_{switching}, \\ E_{start} + 2\nu t_{switching} - \nu t, & \text{for } t > t_{switching}, \end{cases} \tag{2.4}$$

where E_{start} is the cell potential at the begin of the experiment, ν is the scan rate, and $t_{switching}$ is the instant at which the direction of the scan is switched. The excitation waveform is displayed in Fig. 2.3.

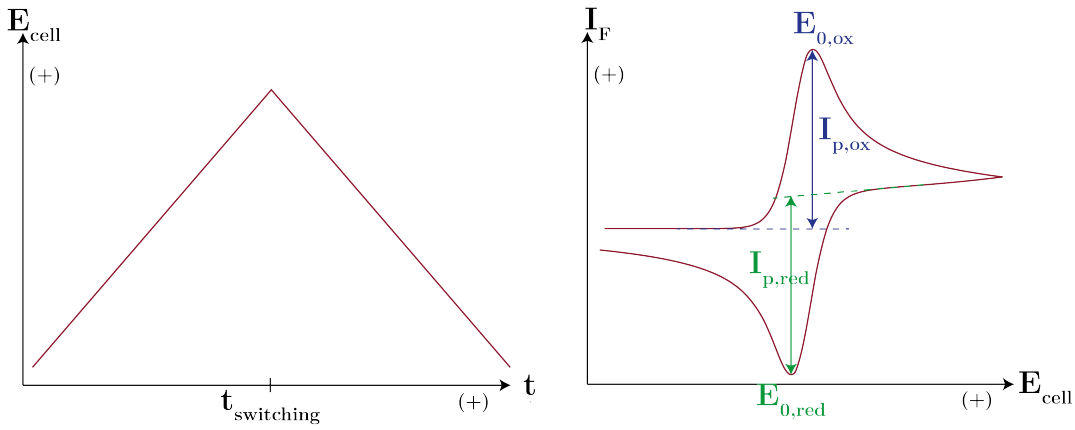

Figure 2.3 – Typical cyclic voltammetry excitation waveform and voltammogram for a reversible Faradaic process.

The potential window should include the RedOx potentials of the electroactive compounds. The recorded voltammogram highlights peak currents at these corresponding potentials. In particular, if both oxidation and reduction peak currents are observed, the Faradaic process is reversible. The peak currents are measured with respect to the extrapolated background baseline, as illustrated in Fig. 2.3. The measured peak currents are related to the concentration of the electroactive compound by Randles-Sevcik equation:

$$I_p = 0.4463 \cdot nFA\sqrt{\frac{nF\nu D}{RT}}C^*. \tag{2.5}$$

The equation implies that a faster scan rate induces larger peak current. This is because a faster potential sweep will cause a larger concentration gradient at the vicinity of the electrode, as stated by Nernst equation (2.1), resulting in a higher Faradaic current.

Moreover, pulsed potential techniques can be used for the characterization of Faradaic processes. In ***Differential Pulse Voltammetry*** **(DPV)**, incremental pulses are applied to the electrochemical cell, as illustrated in Fig. 2.4. The parameters of the potential waveform are the pulse amplitude, width and period, and the step potential added at the end of each pulse period. The electrochemical cell current is sampled twice: a current I_1 is measured before applying the pulse, and a current I_2 is measured after a time T, when the pulse is applied. The differential current $\Delta I_F = I_2 - I_1$ is then plotted against the cell potential. The resulting voltammogram has a symmetric bell-shaped. More precisely, when the base potential is much more positive/negative than the RedOx potential E_0, no Faradaic current flows, and the pulse does not trigger enough Faradaic processes,

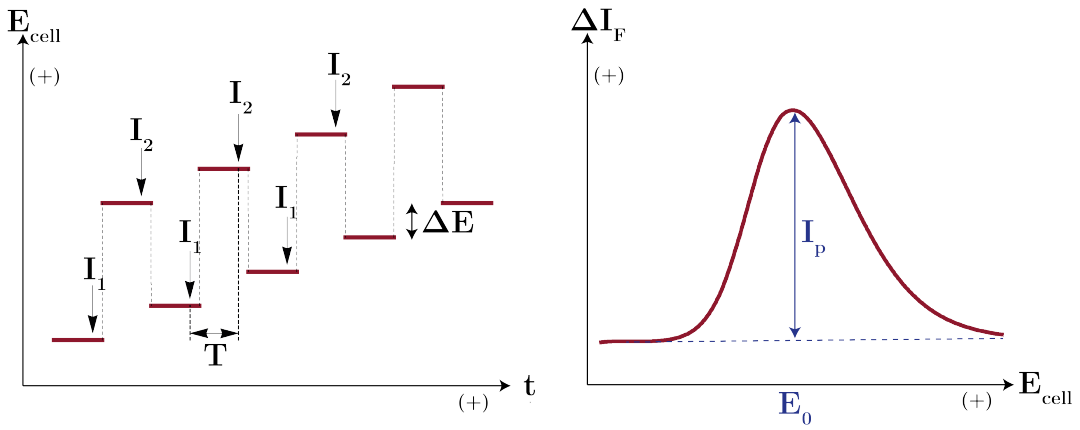

Figure 2.4 – Typical differential pulse voltammetry excitation waveform and voltammogram recorded.

resulting in $\Delta I_F \sim 0$. Moreover, when the base potential reaches the diffusion-limited current region, the electroactive compound is reduced/oxidized at the maximum rate. The application of the pulse does not increase the rate of the Faradaic processes, so nearly equal currents are sampled, resulting in $\Delta I_F \sim 0$. A great differential Faradaic current is observed in the region near the RedOx potential E_0. When the base potential is applied, the compound reacts at a non-maximum rate. The application of the pulse diminishes the concentration of the reactant at the electrode surface, hence increasing the flux of the reactant towards the interface. Therefore the Faradaic current is largely enhanced. The differential peak current can be determined by considering the flux balance of the RedOx compounds at the electrode surface, when a potential is applied [**?**]. The analytical differential current is computed as:

$$\Delta I_F = nFA\left(\frac{1-\sigma}{1+\sigma}\right)\sqrt{\frac{D}{\pi T}}C^*, \tag{2.6}$$

where $\sigma = \exp(\frac{nF}{RT}\frac{\Delta E}{2})$, and ΔE is the incremental potential step. DPV technique yields an higher sensitivity since the charging currents are canceled out by differential measurements.

2.1.2 Potentiometric sensors

Ion-sensing involves different detection mechanisms than the previously described voltammetric measurements. A background on potentiometric sensors is provided in the sequel.

Ion activity

First, a couple of thermodynamic notions are introduced. The thermodynamic equilibrium of a solution containing ionic species depends on the activity of these compounds. The ion activity is defined as $\mathbf{a = \gamma \cdot c}$, where γ is the activity coefficient, and c is the molar concentration of the specie. The activity coefficient is hard to determine experimentally, while the mean activity coefficient of cations and anions of valence z_+ and z_- can be computed as:

$$\log \gamma_\pm = \frac{|z_-|}{|z_+| + |z_-|} \log \gamma_+ + \frac{|z_+|}{|z_+| + |z_-|} \log \gamma_-. \tag{2.7}$$

The mean activity coefficient is obtained with the semi-empirical extended Debye-Hückel theory [**?**]:

$$\log \gamma_\pm = -A \frac{|z_+ z_-| \sqrt{I}}{1 + B\sqrt{I}} + CI, \tag{2.8}$$

with $I = \frac{1}{2} \sum_j z_j^2 c_j$ the ionic strength of the solution containing ions j. A, B, and C are thermodynamic constants that are determined experimentally and tabulated in literature [**?**]. In practice, the single ion activity coefficients are then computed using the simplified Debye-Hückel convention [**?**]:

$$\log \gamma_+ = \left| \frac{z_+}{z_-} \right| \log \gamma_\pm \qquad \text{and} \qquad \log \gamma_- = \left| \frac{z_-}{z_+} \right| \log \gamma_\pm. \tag{2.9}$$

Conventional ion-selective electrode

Potentiometric sensing is carried out with a two-electrode electrochemical cell including an ISE and a RE, as illustrated in Fig. 2.5. The ISE is coated with an *Ion-Selective Membrane* (ISM) that contains an ionophore, that is a neutral compound that binds specifically to the target electrolyte. The inner solution (for instance chloride ions) has a constant electrolytic concentration, and ensures ion-to-electron transduction through RedOx with the internal RE (e.g. $Ag^+(aq) + Cl^-(aq) \rightleftharpoons AgCl(s)$). As for the RE, the liquid junction ensures that the potential at this node is independent of sample composition changes. Potentiometric measurement is performed under zero-current conditions. Therefore, there is no potential drop at the electrode contacts. The measured *Open Circuit Potential* (OCP) is the sum of all interface potentials. All of them are independent of sample composition, except for the ISM/sample boundary, at which a potential difference is induced by ion partitioning between the sample and the membrane phase.

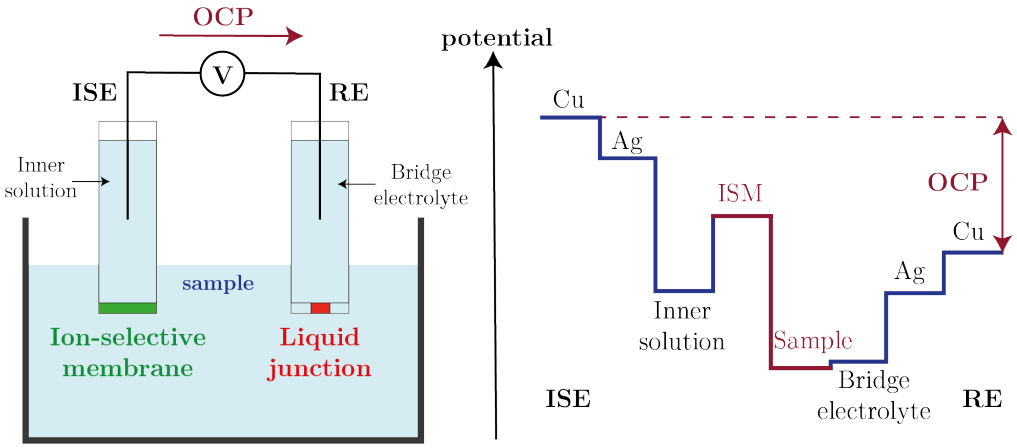

Figure 2.5 – Two-electrodes potentiometric sensing setup and the interface potentials in the cell.

Solid-contact ion-selective electrode

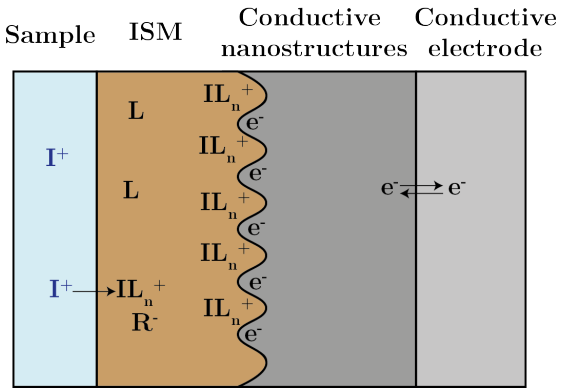

Figure 2.6 – Structure of a solid-contact ISE with conductive nanostructures.

The conventional ISE is bulky, thus not suitable for integrated sensing in wearable applications. All-solid-state ISEs are built by creating a solid-contact between the ISM and the sensing electrode. Different ion-to-electron mechanisms are investigated and summarized in [?]. Solid-contacts based on nanostructured layers are used for this research. The structure of such transducer is displayed in Fig. 2.6. Conductive nanostructures are electrodeposited on top of the conductive substrate, then the ISM is drop-casted on top of the electrode. When the target ion is entrapped by the ionophore L present in the ISM, complexes IL_n^+ are formed, and the counter ions R^- ensure the electroneutrality of the ISM. The charged complexes accumulate in the membrane, inducing the formation of an electrical double layer at the interface between the ISM and the solid-contact nanostructures. The double layer can be seen as an asymmetric capacitor with cations and anions on the side of the ISM, and electrical charge on the side of the nanostructures. The potentiometric measurement is performed under open

circuit conditions, thus, the only change of potential in the electrochemical cell that depends on the analyte concentration takes place at the phase boundary between the sample and the ISM.

2.1.3 Sensing performance criteria

Electrochemical sensors are characterized through a sensor calibration. It consists in measuring the output of the sensing front-end under controlled composition of the sample, by successively increasing the concentration of the target analyte. The calibration curve is then plotted as the measured parameter against the analyte concentration (for voltammetry) or the analyte activity (for potentiometry). The figures of merit enabling the assessment of sensor performance are reported hereunder.

Sensing performance criteria for voltammetric sensors

The **dynamic range** of the sensor is obtained by extracting the range of concentration of the analyte for which the response of the voltammetric sensor is linear. A linear regression analysis is performed to assess the proportion of variance in the measured signal explained by the concentration of the analyte.

Next, the sensor **sensitivity** corresponds to the slope of the calibration curve in its linear range. A large sensitivity allows to discriminate small changes in analyte concentration.

The sensor **LOD** represents the minimum concentration of analyte that the sensor is able to detect. More precisely, it corresponds to the smallest concentration of analyte that gives a response significantly different from the blank signal (background signal measured without the analyte). The LOD is computed following the *International Union of Pure and Applied Chemistry* (IUPAC) definition [**?**]:

$$\mathrm{LOD} = \frac{3\sigma_\mathrm{b}}{\mathrm{S}}, \tag{2.10}$$

where σ_b is the standard deviation of the blank signal and S is the sensor sensitivity. The factor 3 ensures with a confidence level of 99.7% that the measured signal for $\mathrm{c_{analyte}} = \mathrm{LOD}$ is larger than the blank signal plus 3 times the standard deviation of the blank signal. The noise and resolution of the sensing front-end are parameters limiting the sensor LOD.

Sensing performance criteria for potentiometric sensors

For potentiometric measurements, the sensor calibration is carried out and the measured OCP is plotted against the logarithm of the activity of the analyte. As a matter of fact, under ideal conditions, the potential E_I measured at the ISE selective for a target ion I is related to the ion activity a_I of the analyte by Nernst equation:

$$E_I = K_I + \frac{RT}{z_I F} \ln a_I = K_I + \frac{s}{z_I} \log a_I, \tag{2.11}$$

where $s = \ln 10 \cdot \frac{RT}{F}$ is the slope factor, and K_I is a constant offset value. The ion-sensor **sensitivity** ideally corresponds to the slope factor equal to 59.18 mV/decade at 25°C.

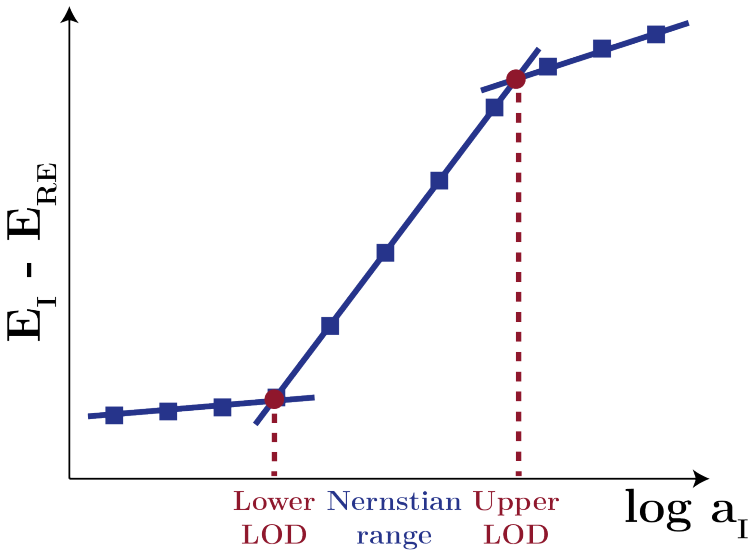

Figure 2.7 – Detection range, upper and lower LOD of a potentiometric sensor.

The sensor **dynamic range** is the range of activity of the analyte for which the sensor exhibits a Nernstian response. The sensor upper and lower **LOD** are extrapolated as the higher and lower bounds of the sensor dynamic range as illustrated in Fig. 2.7. Namely, at lower ion activity, an offset potential due to interference and background electrolytes is observed. The intercept between this flat response and the Nernstian slope of the sensor corresponds to the lower LOD. Moreover, a deviation from the Nernstian slope is observed at very high target ion activity. This is due to a loss of permselectivity of the ISM where counter-ions are co-extracted along with the primary ion [**?**]. The sensor response to the counter-ion is of opposite sign to the primary ion contribution, so the resulting OCP response exhibits a sub-Nernstian sensitivity in this regime. Therefore, the upper LOD is the analyte activity at which this slope deviation is observed.

Sensor **selectivity** is critical in ion-monitoring systems. It is quantified by the selectivity

coefficient $\log K^{pot}_{I,J}$, that measures the ability of the ISE to sense the target ion I instead of an interfering ion J. *Fixed Interference Method* (FIM) and *Separate Solution Method* (SSM) are common experimental methods implemented for the determination of selectivity coefficients. The former method consists in a sensor calibration in presence of an interfering ion at a constant activity, while in the latter method, the selectivity coefficients are determined through separate calibration curves of the interfering ions and the primary ion [**?**]. The experimental methods for the computation of the selectivity coefficients are reported in Section 4.2.

Other sensing performance criteria

Sensor reproducibility, stability, and lifetime are other performance criteria of electrochemical sensors. Reproducibility expresses the ability to obtain identical sensor responses over time, under the same experimental conditions. It is related to sensor stability and drifts. For ion-sensing technology, the nanostructuration of the ISE prevents the formation of a water layer at the ISM/solid-contact interface, that is crucial for potential response stability and reduced sensor drifts [**?**]. Furthermore, sensor lifetime depends on storage and operating conditions, and the nature of the chemicals. The importance of sensor lifetime depends on the sensing application.

2.2 Electronic interface for electrochemical sensing

The functional blocks to drive electrochemical sensors and acquire the transduced electrical responses are described in this section.

2.2.1 Functional blocks to drive and readout electrochemical sensors

The electrochemical sensor is driven by an electronic interface that biases the cell with a stimulus signal that triggers the biochemical recognition events in voltammetry, or ensure open circuit conditions in potentiometry. A readout circuit senses the transduced electrical response of the sensor and processes it. The blocks constituting the electronic interface are illustrated in Fig. 2.8, where a signal generator and a potentiostat produce the control signal, while a readout circuit followed by conditioning and processing circuits enable the acquisition of the sensor signal.

In potentiometric measurements, DC electrical potentials at the ISE and RE are measured in open circuit conditions. Namely, no current should flow through the electrochemical cell. However, a polarization current of few nA is needed to reduce the lower LOD, increase sensitivity and reproducibility of the sensor [**?**, **?**]. This sensor isolation is critical since it induces potential drifts otherwise. Buffering circuits and a differential amplifier enable OCP sensing, where an amplification gain can be added in the signal condition

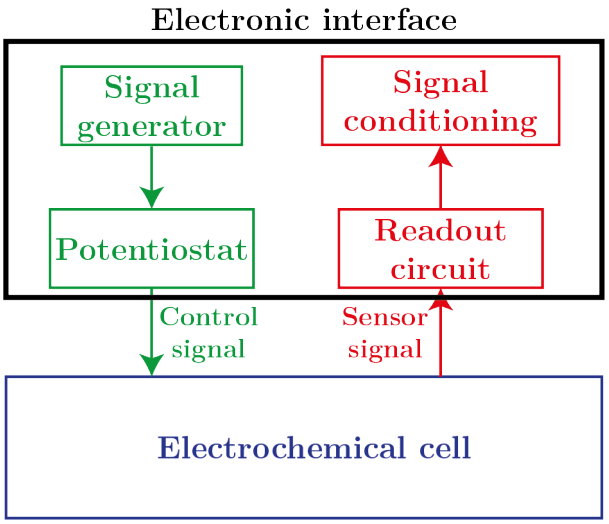

Figure 2.8 – Electronic interface for electrochemical sensing.

path. A low-pass filter is also necessary to remove high frequency noise, where sub-Hz cut-off frequency is implemented to process the DC signal [**?**, **?**].

More emphasis is given to voltammetric sensors in the following.

2.2.2 Front-end interface for voltammetric measurements

The electronic interfaces enabling voltammetric measurements are detailed hereunder.

Equivalent model of the electrochemical cell

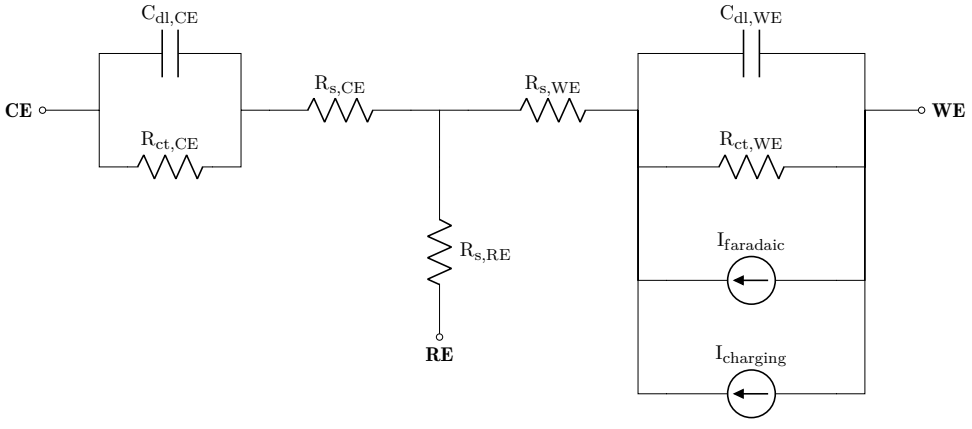

Figure 2.9 – Equivalent circuit of an electrochemical cell.

First, an equivalent circuit of the electrochemical cell is needed to model electrode / electrolyte interfaces during circuit simulations. The equivalent model of a three-electrode

electrochemical cell is displayed in Fig. 2.9. The electrode / electrolyte interface is described by a Randles circuit [?]. Namely, the metal/solution interface is modeled by a solution resistance R_s in series with the parallel combination of a charge transfer resistance R_{ct} and a double-layer capacitance C_{dl}. R_s takes into account the resistvity of the solution, while R_{ct} is associated to the Faradaic processes. Its value depends on the material and geometry of the electrode. Thus, the surface area of the auxiliary electrode should be much larger than the WE area so that the kinetics at CE is not a limiting factor for the analyte detection at the WE. As for C_{dl}, it models the formation of a double-layer capacitor at both WE and CE where Faradaic processes take place. In theory, the double-layer is not an ideal capacitor and it could be modeled by a constant phase element defined as $Z_{CPE} = \frac{1}{(j\omega)^{\alpha} C_{dl}}$, where $\alpha = 1$ in the ideal case [?]. Moreover, the Faradaic and charging current are represented as current sources.

Potentiostat

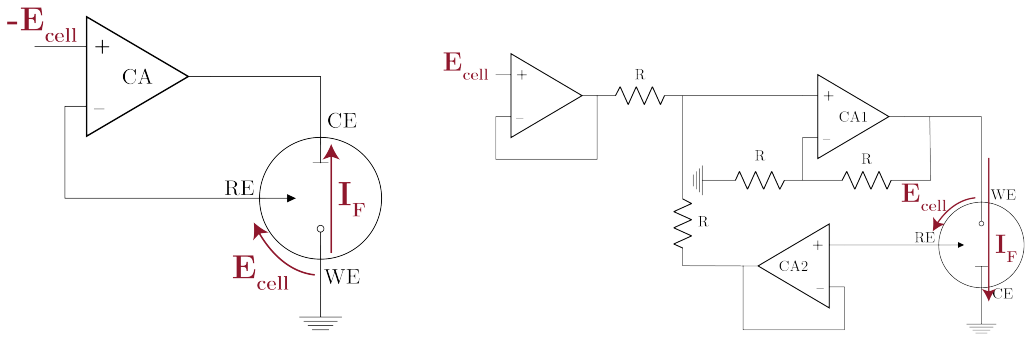

(a) Grounded-WE configuration

(b) Grounded-CE configuration

Figure 2.10 – Potentiostat configurations to drive a three-electrode electrochemical cell.

A potentiostat is required to enforce a controlled potential to the electrochemical cell in order to trigger Faradaic processes. The cell potential needs to be set accurately and should be independent of the chemical reactions in the cell. With a three-electrode cell, the potentiostat can be designed in a grounded-WE or grounded-CE configuration, as shown in Fig. 2.10. The grounded-WE configuration involves one *Operational Amplifier* (OpAmp) at which $-E_{cell}$ is applied. The feedback of the control amplifier forces $E_{RE} = -E_{cell}$, and the WE is tied to the analog ground. Therefore, the cell potential $E_{cell} = E_{WE} - E_{RE}$ is correctly set. Moreover, the RE is a high impedance node since it is connected to the input of the OpAmp, thus, quasi-zero current flows at this node, limiting the voltage drop through $R_{s,RE}$ in Fig. 2.9. The output of the control amplifier is connected to the CE that provides an electrical path to the cell current I_F resulting from biochemical RedOx at the sensing electrode. With a grounded-CE configuration, the cell current is collected at the CE that is tied to the analog ground. The control amplifiers *CA1* and *CA2* force the WE potential to $E_{RE} + E_{cell}$, that is desired. Besides, *CA2* ensures that RE is a high impedance node. The additional OpAmp is a buffer for the generated

controlled potential. It is straightforward that the grounded-CE configuration is more complex and involves more active components. Hence, the grounded-WE potentiostat configuration will be implemented

Readout circuit

The electrochemical cell supplies a DC current related to the Faradaic processes in the cell. An amperometric readout circuit able to sense a wide current range with high resolution in the bandwidth of interest is desired. The circuit should allow the measurement of bi-directional currents (oxidation and reduction currents).

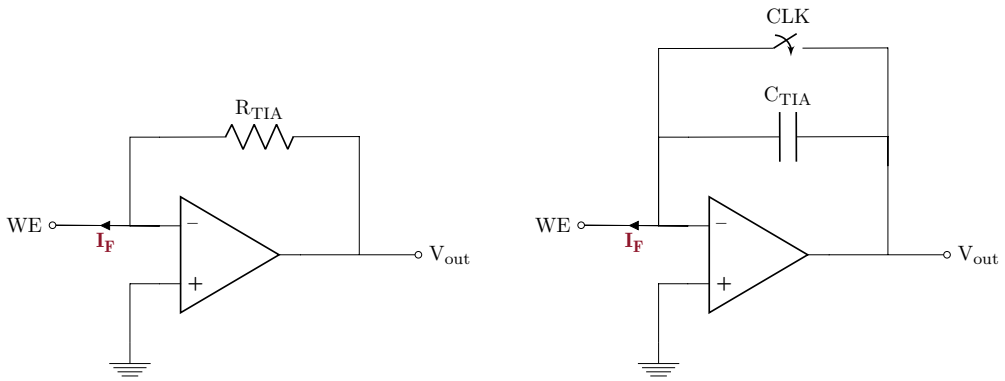

(a) Resistive feedback TIA (b) Switched-capacitor TIA

Figure 2.11 – Current-sensing with a transimpedance amplifier.

Voltage-mode circuits are the most used circuits to acquire RedOx currents [**?**,**?**,**?**,**?**,**?**]. A *Transimpedance Amplifier* (TIA) sets a virtual ground or virtual DC voltage at the WE, and generates an output voltage proportional to the RedOx current. With symmetric power supply, WE is set to the analog ground, otherwise, it is set to half-V_{dd}, in order to measure bi-directional currents. The TIA can be implemented with a resistive or capacitive feedback as illustrated in Fig. 2.11. With a resistive feedback TIA, the dynamic range of the current readout circuit is tuned by R_{TIA} since $V_{out} = R_{TIA}I_F$. A large value should be chosen to decrease the input-referred current noise, but at expense of thermal noise. Switched-capacitor TIAs are also common solutions where the charge resulting from RedOx processes accumulate on C_{TIA}, and discharges through the switch that is controlled by a clock signal. Switches induce offset errors due to clock feedthrough and charge injection that can be compensated at transistor-level design by slow-gating or bottom-plate sampling techniques [**?**], and fully differential circuits. Correlated double sampling technique is often used to compensate the Flicker noise that is critical in bio-sensing applications [**?**, **?**]. Namely, in a first phase, the noise and offset of the amplifier are sampled while the electrochemical cell is disconnected, then in a second phase, the RedOx current is sampled while removing the noise and offset of the amplifier through

feedback. However, the effects of switching noise on the electrochemical sensor are not thoroughly understood.

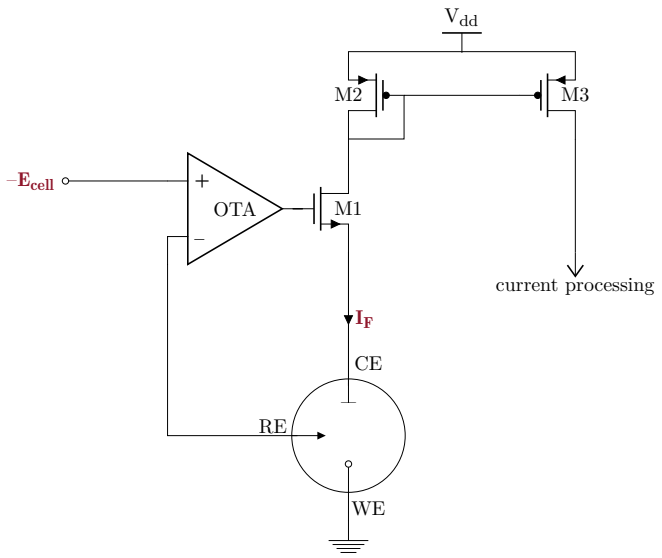

Figure 2.12 – Reduction current-sensing with a current conveyor structure.

Current-mode circuits can also be used, where the current is sensed at the front-end interface without current-to-voltage conversion. A current-conveyor structure is typically used in current-mirror-based potentiostats for amperometric sensing [**?**]. A structure for RedOx current-sensing is displayed in Fig. 2.12, where the amplifier *OTA* and the transistor *M1* constitute the potentiostat that impose E_{cell} to the electrochemical cell through the feedback loop, while measuring I_F that is conveyed from WE to the high impedance drain of *M1*. The current is then mirrored to the other branch for further processing. An analogous circuit can be obtained for sensing bi-directional currents. Current-mode circuits involving full or quasi-digitization of the RedOx current are also reported in literature. A current-to-quasi digital stream of events is proposed in [**?**] for monitoring anesthetics delivery.

In this thesis, a TIA with resistive feedback will be used since it is a simple and flexible technique to measure a wide range of RedOx currents with off-the-shelf low-power and low-noise integrated circuits.

Signal generator

A signal generator is required to produce the stimulus signals to the electrochemical cell. Continuous and programmable waveform generators are needed to support multi-mode waveforms, since CA, CV, and DPV techniques involve step potentials, linear potential scans, and pulsed potentials, respectively. A *Direct Digital Synthesizer* (DDS)

is typically implemented to output periodic waveforms. It comprises a numerically controlled oscillator and a *Digital-to-Analog Converter* (DAC) that are clocked by a reference oscillator. The period of the produced waveform is tuned by the digital word in the frequency controlled register. An example of on-chip DDS is realized in [**?**] to generate triangular waveforms for CV measurements. It comprises a 14-bit digital up/down counter and a 9-bit DAC implemented in a resistor ladder scheme. The slope of the triangular shape is programmed by tuning the step width of the digital counter, yielding high amplitude sub-Hz triangular signals.

2.3 Chemometric tools for electrochemical sensors

Chemometrics is an interdisciplinary field that leverages signal processing, mathematical methods, and statistics, to address problems in analytical chemistry, biochemistry, or medicine [**?**]. A data-driven approach is implemented where the objective is to extract relevant information from sensor responses in order to solve descriptive problems (understanding the properties of chemical systems), or for predictive tasks (predict attributes of components in chemical systems). The application of chemometric tools in multi-analyte-sensing is discussed in this section.

2.3.1 Electronic tongue systems

An *Electronic Tongue* (ET) is a system that couples a sensor array with chemometric models in order to understand the complex structure of the measured data and to predict some attributes of the sensor array. More precisely, it is defined by IUPAC as "a multisensor system, which consists of a number of low-selective sensors, and uses advanced mathematical procedures for signal processing based on Pattern Recognition and/or Multivariate data –*Artificial Neural Network*s (ANNs), *Principal Component Analysis* (PCA), and so forth–." [**?**] Feature extraction methods are often necessary in the pre-processing of complex ET data. PCA, splines or Legendre polynomials fitting, and Wavelet or Fourier transform are typical methods [**?**].

ETs can be applied for qualitative tasks in food, beverage, or environmental applications. Namely, they are used for the identification of species or for the classification of a compound by analyzing the features excerpted from the data. Supervised pattern recognition or classification models such as k-nearest neighbor, PCA, *Partial Least-Squares Regression* (PLS), linear discrimination analysis, classification trees, and ANNs are commonly implemented for the analysis of ET data [**?**]. For instance, in [**?**], 6 ion-sensitive field effect transistors selective to ions and heavy metals are used for the analysis of grape juice and wine samples. PCA and soft independent modeling class analogy are implemented to distinguish the samples according to the grape variety and the vintage year. In [**?**], the combination of 20 ISEs and an ANN used for pattern

recognition enables the discrimination of soils based on chemical components extracted from the soils.

Moreover, chemometric tools can be used for quantitative determination in systems where interfering compounds can distort the response of low-selective sensors. A multivariate calibration model is typically built to bind the sensor array response to the attributes of the chemical compounds in the sample that need to be quantified (e.g. concentration of the compounds, activity of the ions, pH or acidity of the sample) [**?**]. *Principal Component Regression* (PCR), PLS, or non-linear models leveraging ANNs are commonly applied [**?**]. For instance, in [**?**], an ISE array is coupled with a data processing chain including PCA–genetic independent component analysis–back-propagation *Feed-Forward Neural Network* (FFNN), in order to determine accurately up to five ions in water samples, regardless of pH, ionic strength, and interference from background electrolytes.

Besides, most ET systems found in literature use potentiometric sensors since ions are the compounds of interest in food, beverage, and water quality monitoring. Nevertheless, these smart systems can be designed for voltammetric sensors as well. The latter yield voltammograms (I_F vs E_{cell} plots) that are related to the concentration of the compounds in the sample. Therefore, the analysis of the multiple voltammograms output by the sensor array is a high-dimensional task requiring data reduction techniques such as PCA, Fourier or Wavelet transforms [**?**]. An alternative approach is the use of multi-way decomposition methods such as PARAFAC [**?**], but these procedures are more complex to implement in practice. A more suitable approach is to extract features from the voltammograms. Indeed, in [**?**], we have excerpted the peak currents, the corresponding RedOx potentials and the total charge accumulated during the RedOx, from the voltammograms acquired during detection of propofol in anesthesia practice. The features from the voltammograms and the number of consecutive measurements performed with the sensor are fed to a support vector classifier designed for the estimation of the range of concentration of the anesthetic compound hindered by fouling phenomena, for this TDM application.

2.3.2 Multivariate calibration in multi-ion-sensing systems

As mentioned beforehand, ETs can be used for quantitative analysis of low-selective sensors. In this thesis, an ET is designed for multi-ion-sensing in sweat-sensing applications, where interference from the background electrolytes in the sample, the intrinsic cross-selectivity bounds of ISEs, and the presence of highly concentrated and diluted target electrolytes (sodium ions ranging from 10 to 100 mM, while calcium ions ranging from 0.1 to 1 mM [**?**]) distort considerably sensor response. Therefore, traditional calibration procedures are not accurate enough to predict ion activity in samples of unknown composition. An analytical background on multivariate calibration implemented in multi-ion-sensing systems is provided in the following.

Multivariate calibration problem

A multivariate calibration procedure implemented for multi-ion-sensing consists in building a multivariate model from collected OCP/ion activity observations during a training phase, and then predicting the ion activity of the target electrolytes from the sensor responses during an inference phase [**?**]. For N observations, let $\mathbf{X} = \{\mathbf{x_n}\}_{\mathrm{n}=1,\cdots,\mathrm{N}}$, with $\mathbf{x_n} \in \mathbb{R}^{\mathrm{P}}$, denote the matrix of OCP signals output by P ISEs, and $\mathbf{Y} = \{\mathbf{y_n}\}_{\mathrm{n}=1,\cdots,\mathrm{N}}$, with $\mathbf{y_n} \in \mathbb{R}^{\mathrm{M}}$, denote the matrix of activity of M target electrolytes. The multivariate calibration problem can be formulated as

$$\mathbf{Y} = \mathbf{X}\mathbf{W} + \mathbf{E}, \tag{2.12}$$

where $\mathbf{W}$ is the matrix of regression coefficients, and $\mathbf{E}$ is the error made in the prediction of the activity of the analytes. It is an inverse calibration problem since the controlled variables (activity of the target ions) are estimated from the dependent variables (OCP signals).

Linear regression models

Inverse least-squares regressor is the simplest first-order model used in multivariate calibration. Contrary to classical least-squares regression, it is not necessary to know the sample composition during the calibration phase (i.e. the activity of all constituting electrolytes). As a result, the matrix of activity of the target ions $\mathbf{Y}$ can be of any dimension M. The minimization objective is

$$\forall\ \mathrm{m} \in [\![1;\mathrm{M}]\!], \quad \min_{\mathbf{w}_{:,\mathrm{m}}} \quad \left\|\mathbf{X}\mathbf{w}_{:,\mathrm{m}} - \mathbf{y}_{:,\mathrm{m}}\right\|_2^2, \tag{2.13}$$

where $\mathbf{w}_{:,\mathrm{m}}$ and $\mathbf{y}_{:,\mathrm{m}}$ are columns of $\mathbf{W}$ and $\mathbf{Y}$, respectively. Namely, the activity of each target ion is estimated independently, ignoring cross-correlations. Hence, this multivariate calibration model consists of multiple independent *Ordinary Least-Squares* (OLS) regressions also referred as a MLR. $\widehat{\mathbf{W}}$ can be computed by least-squares minimization of (2.13), or in a closed-form solution with the normal equation

$$\widehat{\mathbf{W}} = (\mathbf{X}^{\mathrm{T}}\mathbf{X})^{-1}\mathbf{X}^{\mathrm{T}}\mathbf{Y}, \tag{2.14}$$

where $\mathbf{X}^{\mathrm{T}}\mathbf{X}$ must be invertible. This holds if $\mathbf{X}$ is a full-rank matrix or the columns of $\mathbf{X}$ are uncorrelated. In general, this constraint is fulfilled by applying PCA to $\mathbf{X}$. Namely, OCP signals are decomposed in a set of successive orthogonal components that explain a maximum amount of their variance. The resulting principal component scores, denoted as $\mathbf{T}$, are the new input variables. Combination of PCA and MLR corresponds to PCR.

Nevertheless, the uncorrelated columns of $\mathbf{T}$ are not necessarily correlated to $\mathbf{Y}$. PLS regression is another popular chemometric tool [**?**]. It constructs latent variables for $\mathbf{X}$ and $\mathbf{Y}$, by taking into account the variance of $\mathbf{X}$ and the correlation between factors extracted from both matrices.

Linear regressors are efficient models for univariate calibration systems. However, in multivariate systems, and above all, in presence of non-linearity due to ion interference, non-linear regressors are privileged to increase multivariate calibration accuracy.

Non-linear regression models

Several approaches are possible to cope with an apparent non-linearity in the dataset. Firstly, traditional linear regressors can be extended to non-linear versions, by projection of the input matrix $\mathbf{X}$ onto a non-linear surface, producing a matrix $\mathbf{K}$. Hence, non-linear PLS can be achieved by applying classical PLS methods to the kernel matrix $\mathbf{K}$ and $\mathbf{Y}$. A different approach is to replace the assumed linear relationship between the latent vectors of $\mathbf{X}$ and $\mathbf{Y}$ into a non-linear dependence [**?**]. In general, however, a prior theoretical knowledge of the non-linearity present in the dataset is needed to implement these methods efficiently, i.e. an accurate sensor modeling is necessary.

Other types of regressors can be implemented for multivariate calibration tasks. Indeed, *Support Vector Machine*s (SVMs) are prominent tools for linear and non-linear input/output modeling [**?**]. Non-linear SVRs are obtained by an implicit mapping of $\mathbf{X}$ to a higher dimensional feature space leveraging a kernel function [**?**]. Thus, the regression hyper-plane is constructed in the space induced by the kernel. Standard SVR models perform unidimensional regression of the input matrix $\mathbf{X}$ to each output channel $\mathbf{y}_{:,\mathrm{m}}$, independently. As a matter of fact, SVM implementations use an L_1-based norm loss function that can only consider one output channel at a time [**?**]. Therefore, the model consists of multiple single-output SVRs, where each column of $\mathbf{Y}$ is considered separately, ignoring cross-correlations. Single-output models are usually less robust to noise in the dataset, making these estimators less efficient with scarce datasets.

ANNs are widely used to model non-linear dependencies between multivariate OCP signals and ion activity of multiple target ions. A typical FFNN architecture is displayed in Fig. 2.13. The input layer consists of P pass-through neurons that relay the input features $\mathbf{x}_\mathrm{n}$ to the subsequent layers. The features are either the raw OCP signals, normalized OCP signals, or the PCA scores. Then, the signals are conveyed to the hidden layer that produce a non-linear transformation of the dataset, and the output layer predicts the activity of the M target ions. Formally, let us denote $\mathbf{x}^{(\mathbf{I})}$, $\mathbf{x}^{(\mathbf{H})}$, and $\mathbf{x}^{(\mathbf{O})}$, the vector at the output of each layer. The sequential steps required for the estimation of the activity of the ions $\hat{\mathbf{y}}_\mathrm{n}$ from the input instances $\mathbf{x}_\mathrm{n}$ are

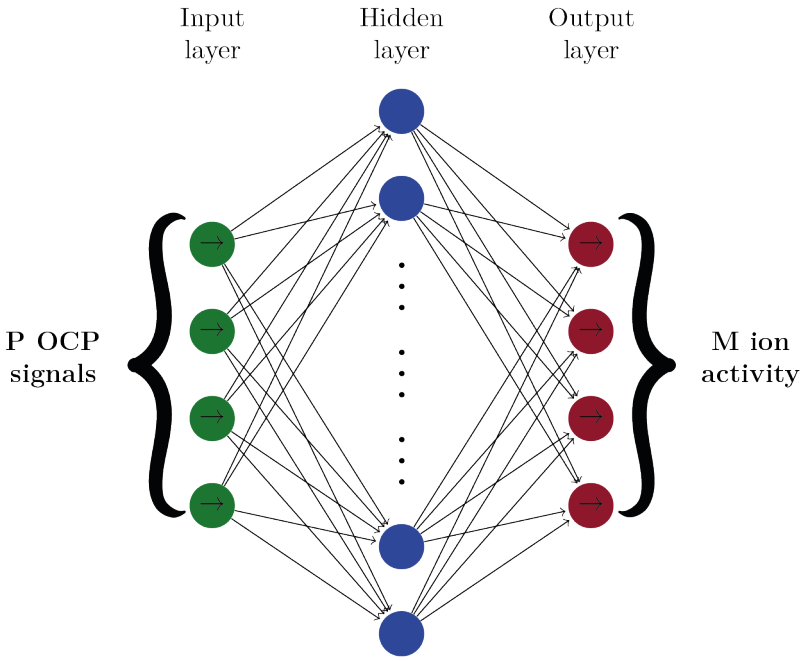

Figure 2.13 – Typical feed-forward neural network architecture for multivariate calibration of potentiometric sensors.

$$\begin{aligned} \mathbf{x}^{(\mathbf{I})} &= \mathbf{x}_{\mathrm{n}} \\ \mathbf{x}^{(\mathbf{H})} &= \sigma\left(\mathbf{w}^{(\mathbf{H})} \cdot \mathbf{x}^{(\mathbf{I})} + \mathbf{b}^{(\mathbf{H})}\right) \\ \mathbf{x}^{(\mathbf{O})} &= \mathbf{w}^{(\mathbf{O})} \cdot \mathbf{x}^{(\mathbf{H})} + \mathbf{b}^{(\mathbf{O})} \\ \hat{\mathbf{y}}_{\mathrm{n}} &= \mathbf{x}^{(\mathbf{O})}, \end{aligned} \tag{2.15}$$

where σ is the non-linear activation function of the hidden layer, and ($\mathbf{w}$,$\mathbf{b}$) are the weights and bias associated to each layer. The model parameters (weights and bias) are usually trained with a back-propagation training algorithm minimizing the mean-squared error loss function [**?**]. ANNs are attractive since they perform an efficient estimation of the activity of the ions of interest without knowledge of the nature of the non-linearity in the dataset, interference, or noise.

In practice, one or two hidden layers are sufficient to perform the multivariate calibration task. Indeed, a FFNN with a single hidden layer is implemented in [**?**] and [**?**] for

the determination of multiple ions in water pollution monitoring. Nevertheless, more complex processing tools can be used as well. In [**?**], potassium, sodium, calcium, and magnesium ions were monitored for agriculture water quality. In the latter work, data pre-processing includes PCA of the input OCP signals, and a fast fixed-point algorithm for independent component analysis that is implemented by a genetic algorithm. Then, a back-propagation FFNN was used to determine the ion activity. Moreover, more complex neural network architectures are also proposed in literature. In [**?**], a back-propagation FFNN constrained with a priori knowledge of charge balance and electrical conductivity of the sample was developed for monitoring of nine electrolytes and pH for environmental monitoring.

2.3.3 Training and optimization of chemometric models

Chemometric tools are data-driven models that are built and optimized following an adaptive methodology. Namely, the algorithms are constructed leveraging a training set, and their performance is assessed with a validation set. An external test set is used to evaluate their generalization prediction capabilities. The training set should be large enough in order to capture most of the variance in sensor response, and thus be representative of the observed dataset. As for the validation set, it should span the whole sample space of interest, but must be independent of the training set. An experimental design of dataset is usually carried out, where synthetic samples of known ion activity (in the case of ion-sensing) are prepared, and the response of the ISEs are collected [**?**, **?**, **?**, **?**, **?**, **?**, **?**, **?**]. The external test set should be independent of the training set as well, and could be obtained from real samples [**?**, **?**]. In general, a large training set is required to achieve accurate results. However, the acquisition of big data is extremely expensive in terms of chemical resources and experimental time. As a matter of fact, the dataset size in works presented in literature consider 15 up to 100 samples. Some approaches have been proposed to cope with this data scarcity. Data fusion techniques were used in [**?**] to extract relevant features from data-limited ion-sensors, and generate synthetic samples from cumulative distribution functions of the concentration of the target ions, before feeding the training set to different machine learning algorithms implemented for ammonium ion measurement. An alternative approach consists in modeling sensor response with an analytical chemical model in order to generate emulated datasets. For instance, in [**?**], a mathematical and its corresponding numerical model based on diffusion equations was used to simulate the response of enzymatic biosensors in presence of a mixture of four analytes in the sample solution. The simulated dataset was pre-processed with correlation coefficients analysis and PCA, then the multivariate calibration of the concentration of the four metabolites was performed by a FFNN.

2.4 Summary

The design of a multi-panel electrochemical sensing platform enabling a remote and accurate healthcare and physiology monitoring requires a deep understanding of the sensing and transduction mechanisms involved in the detection of the biomarkers of interest. The fundamentals on electrochemical sensing and the methods implemented for the acquisition and processing of the multivariate sensor response are detailed in this chapter. The most important information is summarized hereunder:

- Different electrochemical sensing techniques are implemented depending on the type of target biomarker. Namely, **voltammetry** is carried out for the detection of compounds involving Faradaic processes, via a three-electrode electrochemical cell. Enzymatic biosensors are developed for the detection of endogenous metabolites such as lactate, while electroactive compounds are detected directly at the sensing electrode surface. Continuous healthcare monitoring is performed with CA, while the characterization of Faradaic processes is carried out with voltammetric scans through analytical methods such as CV and DPV. With voltammetric techniques, the RedOx current is proportional to the concentration of the analyte.

  As for ion-sensing, it is performed through **potentiometry** with a two-electrode electrochemical cell, where the OCP of the cell is related to the activity of the target electrolyte by a Nernstian law in the detection range of the sensor.

- The electronic interface for electrochemical sensors includes specific circuitry to drive the electrochemical cell and to readout the sensor response. In voltammetry, a **potentiostat** ensures that the electrochemical cell is correctly biased at a cell potential that is generated by a **waveform generator**. Current-readout is typically performed by **TIAs with resistive feedback**. As for potentiometry, **buffering circuits** and **differential amplifiers** enable the readout of OCP signals.

- The accurate determination of biological/physiological information from a multi-panel electrochemical sensor necessitates chemometric models for both qualitative and quantitative analysis of multivariate sensor responses. In particular, in multi-ion-sensing, more complex **multivariate calibration models** than multiple linear regressions are needed to cope with non-linearity induced by interference from background electrolytes and sensor low cross-selectivity. Besides, the training and optimization of such data-driven models necessitates new paradigms for the design of large datasets.

3 General-purpose electrochemical platform for healthcare applications

The design of a multi-mode hardware front-end enabling multi-analyte voltammetric and potentiometric measurements is presented in this chapter. The research motivations are detailed first, then an electrochemical sensing platform is proposed for general-purpose healthcare monitoring. Next, the system architecture and the analog front-end are described. Thereafter, the electrochemical platform is validated by sensing lactate, paracetamol, and lithium ions, that are typical endogenous metabolite, exogenous compound, and electrolyte, monitored for healthcare applications.

3.1 Motivation

Portable electrochemical sensing platforms enable the continuous and real-time monitoring of an individual's physiological biomarkers [**?**]. For instance, endogenous metabolites and electrolytes are tracked in sport applications in order to improve training performance by optimizing hydration and resting cycles, and avoiding muscle cramping or severe physiological dysfunctions [**?**]. Namely, muscle fatigue can be evaluated through **lactate** monitoring. The latter is the basis conjugate of lactic acid, a compound that is produced when the individual's metabolism lacks energy, for example after an intense physical effort [**?**]. Other electrolytes such as potassium and ammonium ions are also indicators of muscle activity and exercise intensity [**?**, **?**].

Moreover, portable electrochemical sensing platforms are increasingly used for fast disease diagnosis, or for drug abuse detection in TDM applications. For instance, **lithium** is the principal mood stabilizer administrated for persons suffering from bipolar disorder [**?**]. The therapeutic window of this compound is very narrow ($0.5 - 1.5\,\mathrm{mM}$ [**?**]), thus, requiring a continuous and accurate follow-up care. Besides, drug abuse is also a vital concern in medical procedures. For example, anesthesia is carried out to keep a patient in an unconscious state during a surgery [**?**]. Namely, a cocktail of anesthetic compounds is administrated to the patient, including an analgesic such as **paracetamol**

(also named **acetaminophen** or **APAP**), an hypnotic such as propofol, and a muscle relaxant midazolam [**?**]. APAP is metabolized by the liver first, and overdose could lead to hepatotoxicity when the drug concentration is beyond 30 mg/L following an APAP intravenous injection [**?**].

The detection of endogenous metabolites such as lactate is performed through an enzymatic biosensor. *L-lactate Oxidase* (LOx) is the most common enzyme used in lactate monitoring since it involves a simple enzymatic reaction and the sensor design is relatively simple [**?**]. The enzyme is coated on the sensing electrode, and in presence of dissolved oxygen, it catalyzes the oxidation of the L-Lactate analyte into pyruvate. Hydrogen peroxide is a side product of the reaction, and the latter electroactive compound is oxidized by biasing the transducer at the corresponding oxidation potential. The chemical and RedOx reactions are summarized as:

$$\mathrm{L-Lactate} + \mathrm{O_2} \xrightarrow{\mathrm{LOx}} \mathrm{pyruvate} + \mathrm{H_2O_2} \tag{3.1}$$

$$\mathrm{H_2O_2} \xrightarrow{\mathrm{E_{cell}}} \mathrm{O_2} + 2\,\mathrm{H^+} + 2\,\mathrm{e^-} \tag{3.2}$$

Therefore, L-Lactate is monitored with an amperometric readout front-end. As for APAP, it is an electroactive compound that could be detected with voltammetric techniques. A direct sensing with carbon electrodes is extensively reported in literature [**?**, **?**, **?**]. Moreover, lithium ion detection relies on a potentiometric readout front-end.

A couple of mixed-mode sensing platforms were proposed in literature to achieve combined amperometric and potentiometric measurements. In [**?**], a four-channel electrochemical sensing front-end enabled a conformal multi-metabolite and electrolyte sensing through a flexible PCB. Yet, it does not offer programmability in the analytical detection techniques since the circuit architecture did not include a potentiostat. This reduces the panel of target biomarkers as well, since the sensing electrodes needed to be functionalized with specific membranes, given that the transducers were not polarized. Besides, a real-time telemetry system enabling amperometric and potentiometric sensing was proposed in [**?**]. It provides programmability, full-flexibility, and real-time processing, but the overall system was bulky (CMOS front-end, field-programmable gate array, transceivers). Furthermore, a wireless system-on-chip for concurrent potentiometry and amperometry was recently proposed in [**?**]. The fully-integrated system included four electrodes (WE, CE, ISE, and a shared RE), the front-end integrated circuit for current and OCP measurement, the power management unit, and the wireless data transmission module to a base station through load-shift keying. The front-end is appealing for ultra-low-power electrochemical sensing but it does not offer programmability for voltammetric measurements, and does not support multi-analyte sensing.

In this chapter, we present a four-channel front-end interface *AmpPot* that is proposed as a versatile, programmable, and portable solution, to enable multi-sensing of different families of analytes, which requires specific electrochemical sensing techniques.

3.2 System overview

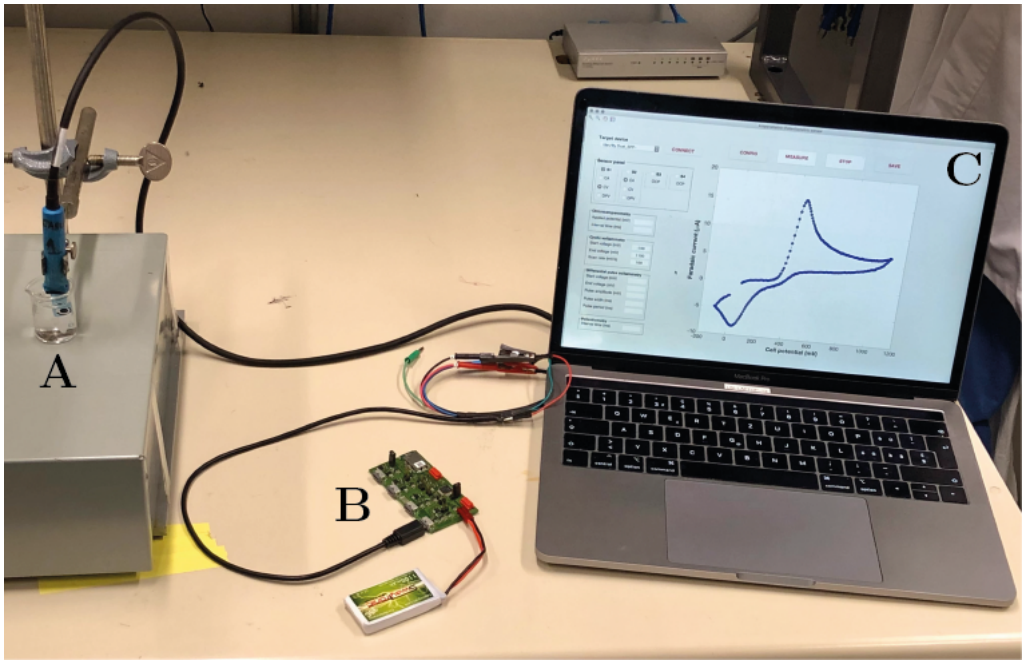

Figure 3.1 – Setup for in vitro characterization of APAP detection: **A** Carbon SPE in a PBS solution where APAP concentration is controlled; **B** hardware front-end *AmpPot* powered by a lithium ion battery; **C** GUI to configure voltammetric measurements and to display real-time voltammograms.

The electrochemical sensing front-end consists of: the sensors functionalized for the specific detection of a target biomarker; the electronic interface ensuring the polarization of the electrochemical cell, and the readout and processing of the sensor response; a remote terminal allowing the user configuration of the electrochemical sensing measurements, and to collect biological data. The typical in vitro electrochemical characterization setup is displayed in Fig. 3.1, where APAP is detected through CV, and the acquired voltammogram is displayed in real-time on a GUI. The features of the mixed-mode electrochemical sensing platform are described in this section.

3.2.1 Electrochemical sensors

The methods implemented for the functionalization of the electrochemical sensors developed for lactate, APAP, and lithium ions detection are detailed hereunder. An enzymatic sensor was built for lactate monitoring where the WE was functionalized with LOx.

L - Lactate sensing was performed in presence of *Hydroxymethylferrocene* (HMF) that acted as a RedOx mediator. The latter compound has a RedOx potential of 0.3 V (versus *Sodium-Saturated Calomel Electrode* (SSCE)) that is lower than the typical potential needed for H_2O_2 oxidation (0.7 V versus SSCE) in (3.1), thus avoiding RedOx from other species that could interfere with L-Lactate detection at these high potentials [**?**]. As for APAP, it is an electroactive compound, so it was detected directly at the surface of the electrode transducer. Moreover, lithium ions were sensed through an ISE which selective membrane contained a lithium ionophore. In this work, the electrochemical sensors were built on commercial ceramic *Screen-Printed Electrode*s (SPEs) purchased from Metrohm (Switzerland).

Electrode functionalization and sample preparation for lactate monitoring

The chemicals included LOx from aerococcus viridans (powder form of 67.6 units/mg), Lithium L - Lactate (salt, 95%), and PBS (tablet form, pH 7.4), that were purchased from Sigma-Aldrich (Switzerland). HMF (crystalline form, 97%) was obtained from Alfa Aesar (Germany). The other solutions were purchased from Sigma-Aldrich.

A stock solution of 10 mM PBS was prepared by dissolving one tablet of PBS in 200 mL of ultra pure water. A stock solution of LOx was prepared by dissolving 0.8 mg of the LOx powder in 160 µL of PBS, and stored at –18 °C. A stock solution of 0.5 M L-Lactate was prepared by dissolving 1.40 g of L-Lactate powder in 0.5 mM HMF dissolved in PBS solution.

Ceramic SPE (carbon WE with an active area of 12.56 mm^2, carbon CE, silver RE) was used as substrate. A conditioning procedure similar to [**?**] was performed. Namely, the WE was activated by applying a fixed potential of +2.0 V for 5 s, in 0.1 M H_2SO_4, followed by a fixed potential of –0.35 V for 10 s. Then, linear potential sweeps from –0.3 V to 1.5 V were applied with a scan rate of 5 $V \cdot s^{-1}$ during 2 min. The cleanliness of the electrode was assessed by CV from –0.3 V to 1.5 V at 0.1 $V \cdot s^{-1}$. After that, the SPE was rinsed with water. A direct adsorption of the enzyme was performed by drop-casting 6.3 µL of the stock solution of LOx on top of the WE. The excess of enzyme was removed by fast dips into ultra pure water. The enzymatic sensor was kept overnight at 4 °C.

The sensor functionalization was performed on gold and platinum WEs as well, but the produced sensors were less sensitive to L-Lactate. Therefore, only the results obtained with carbon SPEs are shown in this thesis.

Sample preparation for APAP detection

The chemicals include Acetaminophen (powder form) and PBS (tablet form, pH 7.4), that were purchased from Sigma-Aldrich (Switzerland).

A stock solution of 10 mM PBS was prepared by dissolving one tablet of PBS in 200 mL of ultra pure water. A stock solution of 30 mM APAP was prepared by dissolving 5 mg of APAP powder in 1 mL of PBS.

Ceramic SPE (carbon WE with an active area of 12.56 mm^2, carbon CE, silver RE) was used as substrate.

Electrode functionalization and sample preparation for lithium ions sensing

All chemicals were purchased from Sigma-Aldrich (Switzerland). Ceramic SPE (platinum WE with an active area of 12.56 mm^2, platinum CE, silver RE) was used as substrate.

First, the sensing electrode was cleaned in 0.1 M H_2SO_4 with CV scans. Then, platinum nanostructures were electrodeposited on top of the WE, following the procedure from [**?**]. Namely, the metal nanostructures were deposited by applying –1 V in 50 mM H_2SO_4 and 25 mM H_2PtCl_6, for 200 s, with a three-electrode setup where an auxiliary SPE was used. Next, the ISM was prepared by dissolving 100 mg of a mixture consisting of 1wt% Li Ionophore VI (6,6-Dibenzyl-1,4,8-11-tetraoxacyclotetradecane), 0.7wt%, Potassium tetrakis(4-chlorophenyl)borate, 28.00wt% Poly(vinyl chloride) high molecular weight, and 70.3wt% 2-Nitrophenyl octyl ether, in 1 mL of Tethraydrofuran. 10 µL of the obtained solution was drop-cast on the platinum-nanostructured WE. Finally, the solid-contact ISE was kept at dark overnight to allow solvent evaporation. Prior to each measurement, the lithium-ISE was conditioned for 24 h in a solution of 10 mM LiCl. During the conditioning period, the hydrophylic counter ion of the ion-exchanger (Potassium tetrakis(4-chlorophenyl)borate) is replaced with the target ion. This is crucial for maintaining a constant activity of the target ion in the ISM in order to ensure a Nernstian sensitivity (see Section 5.2 for the analytical modeling of ISEs).

3.2.2 Hardware front-end

A first hardware prototype was manufactured on a 0.1 mm flexible Kapton polyimide substrate. This material is stable across a wide range of temperatures, has good dielectric properties, and provides mechanical flexibility that is suitable for conformal measurements [**?**]. The FPCB has a size of 97 × 66 mm, but it could be greatly shrunk by removing all probe points placed after each functional analog block. Moreover, the placement and routing of the off-the-shelf components could be more compact since wide trace widths of 150 µm were used to minimize electrical cross-talks. Despite its size, the portable hardware fits into commercial armbands as illustrated in Fig. 3.2.

The FPCB was successfully characterized and validated with lithium ions sensing in [**?**], but it had a short lifespan since the flexible hardware could withstand a limited amount of bending. Indeed, the copper wire connections were crumbly after each

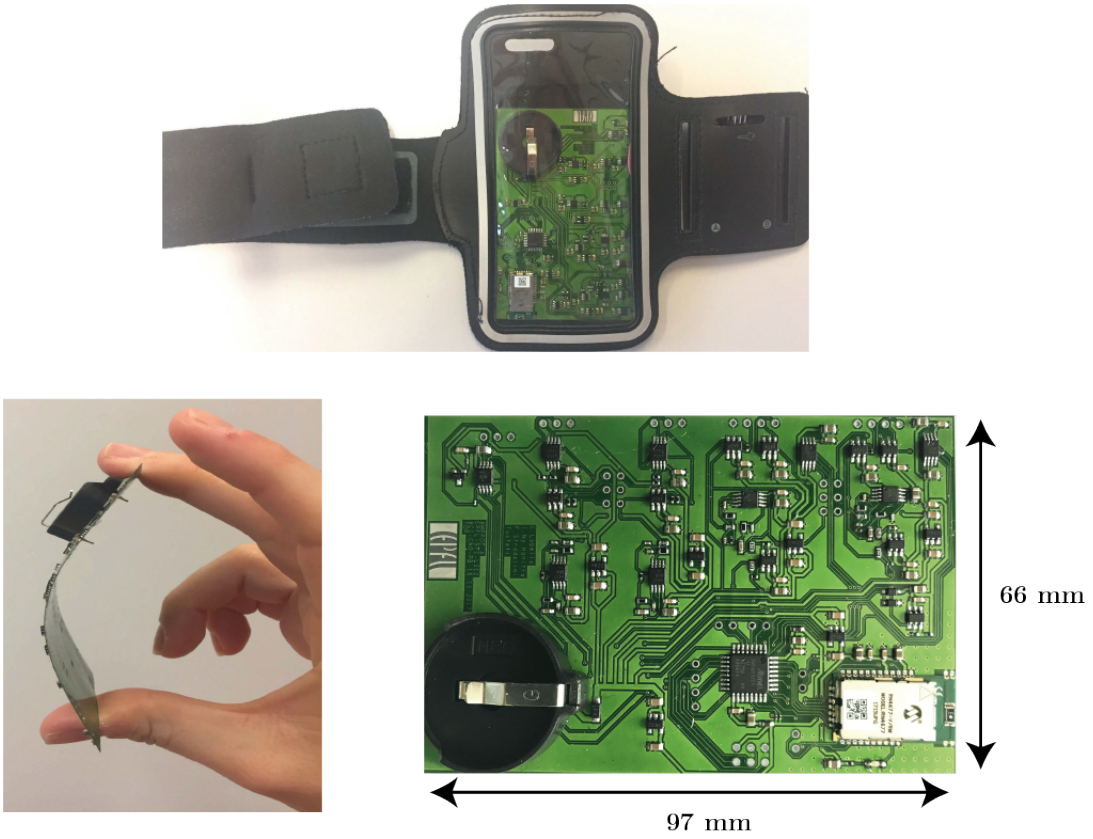

Figure 3.2 – *AmpPot* front-end mounted on a flexible PCB.

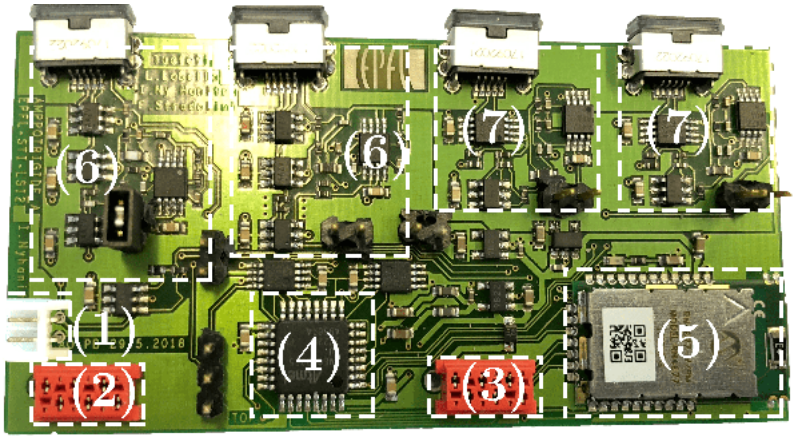

Figure 3.3 – Functional blocks of *AmpPot* front-end: (1) power supply socket, (2) programming/debugging interface, (3) UART/I^2C serial ports, (4) microcontroller unit, (5) Bluetooth module, (6) voltammetric sensing channels, (7) potentiometric readout channels (reprinted from [**?**]).

bending, and they did not provide reliable electrical contacts. Gold PCB traces are investigated in industrial processes for the fabrication of FPCBs. Therefore, the analog

front-end was mounted on a FR4 rigid substrate with a smaller hardware footprint of 38×76 mm. The functional blocks constituting the analog front-end are displayed in Fig. 3.3. It includes two independent voltammetric sensing channels and two independent potentiometric readout channels. A low-power 8/16-bit ATxmega32E5 *Microcontroller Unit* (MCU) is the core processing unit. It mainly embeds three 16-bit timer/counters, a two-channel 12-bit 1 Msps DAC, and a built-in one-channel 12-bit *Analog-to-Digital Converter* (ADC) enabling multiplexed measurements. Concurrent measurements were implemented by scanning and sampling the four sensor channels at 300 ksps. Moreover, the MCU provides two *Universal Asynchronous Receiver-Transmitter* (UART) serial communication interfaces and an I^2C bus. The UART modules feature full-duplex connectivity: one port was used to configure the Bluetooth module via ASCII commands and to relay the acquired and processed data to the wireless node, and in the other direction, it was used to read Bluetooth module status and to receive the user requests for the configuration of the electrochemical measurements. The second UART interface was optionally used to connect the hardware to a personal computer via a RS-232 cable, mainly for prototyping. As for power management, a 3.7 V lithium ion battery with a capacity of 1.1 Ah was powering the hardware. Low-dropout voltage regulators MCP1801 with low quiescent current of 25 µA were used to provide stable 3.3 V to the rail-to-rail operational amplifiers in the analog blocks, to the MCU, and to the Bluetooth module.

3.2.3 Remote configuration and monitoring of electrochemical sensors

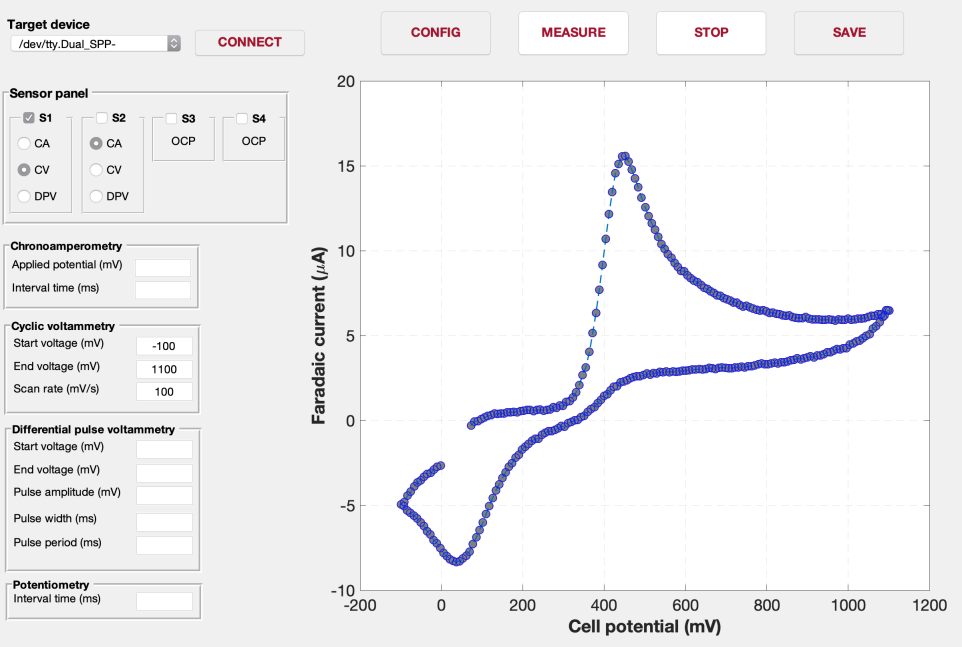

Figure 3.4 – GUI enabling the configuration of the electrochemical measurements and the collection of measured data.

A dual-mode RN4677 *Bluetooth Classic* (BTC)/*Bluetooth Low Energy* (BLE) 4.0 module with an integrated antenna was soldered on the hardware. It establishes a wireless link between the sensing front-end and a personal computer that was used as remote interface. The BTC module ensures a robust wireless continuous data stream, while the BLE technology performs a periodic transfer of small amount of data, thus saving energy. BTC technology leverages a serial port profile protocol, whereas BLE conveys data through a transparent UART *Generic Attribute Profile* (GATT) Profile private service. Either technology could be used for the characterization of voltammetric sensors since fast voltage scans were implemented (applied potential updated and data sampled every 80 ms), but BLE is power-efficient for CA and potentiometry if the interval time chosen between each measurement is large (e.g. one measurement every five seconds). Nevertheless, both technologies emulate a standard RS-232 UART protocol since a data pipe is created between the user interface and the sensing front-end, where data is transferred at 115'200 baud rate, by one-byte packets, with an interval time of 1 ms. A GUI developed in Matlab® was executed on a personal computer nearby the hardware front-end, and enabled the configuration of the electrochemical measurements by the user, and the collection and real-time visualization of the measured data (see Fig. 3.4). The principal features of the GUI include:

- the establishment of a wireless connection with the paired target hardware.
- the selection of the sensing channels and the corresponding electrochemical method.
- the setup of the parameters of the electrochemical measurements.
- the configuration of the sensing front-end with the user's selection.
- the request to start/pause/resume the electrochemical measurement, with a real-time data visualization.
- the request to stop the electrochemical measurement and put the electrochemical cell in its idle state.

Each request from the user was conveyed to the sensing front-end through a configuration byte

Bit	7	6	5	4	3	2	1	0
CONFIG_BYTE	COMM		TECH		ELECTRODE			

- **Bit 7:6 – COMM[1:0] – Command type**
  00: configure electrochemical measurements with the parameters sent subsequently
  01: start measurements
  10: stop measurements and apply 0 V to the voltammetric cell
- **Bit 5:4 – TECH[1:0] – Electrochemical sensing technique**
  00: CA
  01: CV
  10: DPV
  11: potentiometry
- **Bit 3:0 – ELECTRODE[3:0] – WEs considered**
  each bit represent one WE

The configuration parameters of each analytical technique were sent by two-byte packets. The list of parameters are shown in Fig. 3.4. As for the data measured from the sensing platform, with CV and DPV, the cell potential applied and the voltage at the output of the sensing channel were sent by two-byte packets each, whereas with CA and potentiometry, only the voltage at the output of the sensing channel was conveyed. An identification byte containing the type of electrochemical technique and the considered WE was sent prior to each data packet in order to ensure a safe data transmission.

3.3 Circuit architecture

In this section, the analog front-end circuitry enabling voltammetric and potentiometric measurements are described. The electrical characterization of the hardware is also reported.

3.3.1 Voltammetric measurement circuit

The circuit architecture designed for voltammetric measurements is displayed in Fig. 3.5. A potentiostat in a grounded-WE configuration was built around the OpAmp *CA* to control the three-electrode cell potentials. The WE was biased to $\frac{V_{cc}}{2}$ in order to measure bi-directional currents, and the RE was a high impedance node at which $-E_{cell}$ was applied. The cell current I_F was sensed by a resistive feedback TIA. The dynamic range of the electrical current measurement was set by R_{TIA}, where a gain value of 30 kΩ was chosen since typical Faradaic currents observed for the detection of the metabolites and drugs of interest are below 30 µA [**?**]. Resistors of 0.1 % tolerance were used. Next, the

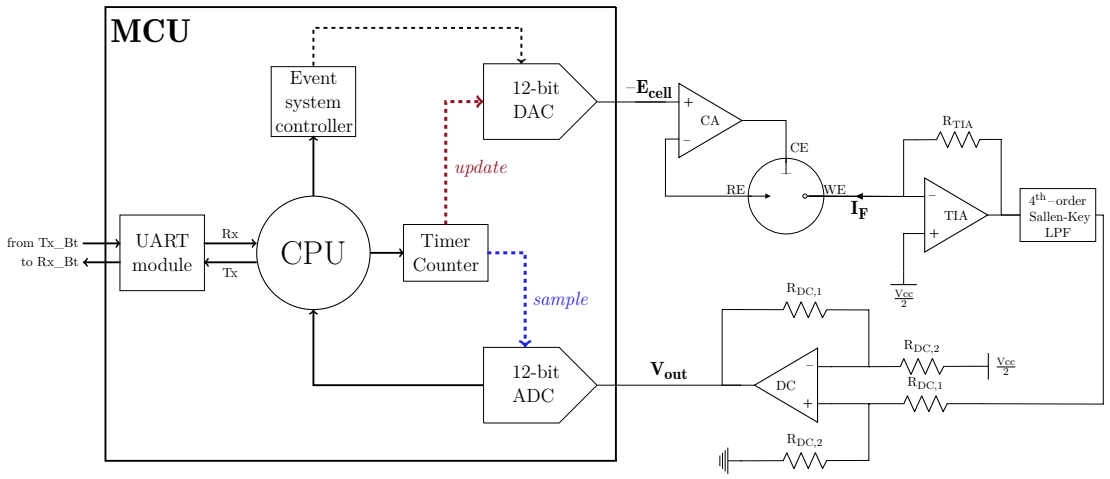

Figure 3.5 – Circuit architecture for polarization of the three-electrode electrochemical cell and sensing of the Faradaic current. The full-duplex UART interface enables both configuration of the electrochemical sensing measurements and transmission of the measured data to the remote terminal (adapted from [**?**]).

signal was filtered through a 4^{th}-order Sallen-Key *Low-Pass Filter* (LPF), with a –3 dB cut-off frequency of 200 Hz. Indeed, we observed that the Faradaic current needed at least 10 ms to stabilize once a potential step was applied to the electrochemical cell. A high-order filter was chosen to attenuate high frequency noise and interference. It was used as anti-aliasing element as well. Furthermore, the differential amplifier around *DC* was designed to compensate the offset of $\frac{V_{cc}}{2}$ introduced by the TIA. An output channel voltage $V_{out} = 1 + R_{TIA} \cdot I_F$ [V] was obtained so as to use the full dynamic range of the ADC $[0; 2.06\,\text{V}]$. Low-noise, low-distortion, rail-to-rail MAX4475 OpAmps were used.

The generation of the cell potential E_{cell} is discussed hereunder. For potentiostatic measurements, the digital code corresponding to the cell potential was merely written to the channel data register of the DAC of the MCU. As for potentiodynamic measurements, a continuous and programmable DDS was implemented to generate the dynamic cell potential. A 16-bit Timer/Counter of the MCU was the time reference for, first, sampling the output voltage V_{out} by the embedded ADC, and then, updating the digital word written to the DAC. The module was clocked at 250 kHz with the peripheral clock. An event system controller was used to trigger DAC conversions every 1 ms, where the converter featured a *Least Significant Bit* (LSB) of 0.8 mV.

The implemented DDS architecture output linear voltage scans through upwards and downwards staircase voltages with a scan rate from $8\,\text{mV} \cdot \text{s}^{-1}$ to $2\,\text{kV} \cdot \text{s}^{-1}$ for CV, while for DPV, pulses with programmable amplitude, width, and period were generated. For the differential technique, the Faradaic current was sampled twice: first, before applying the pulse, secondly, just before applying the subsequent base potential. The base potential and the two measured voltages $V_{out,1}$ and $V_{out,2}$ were sent to the remote

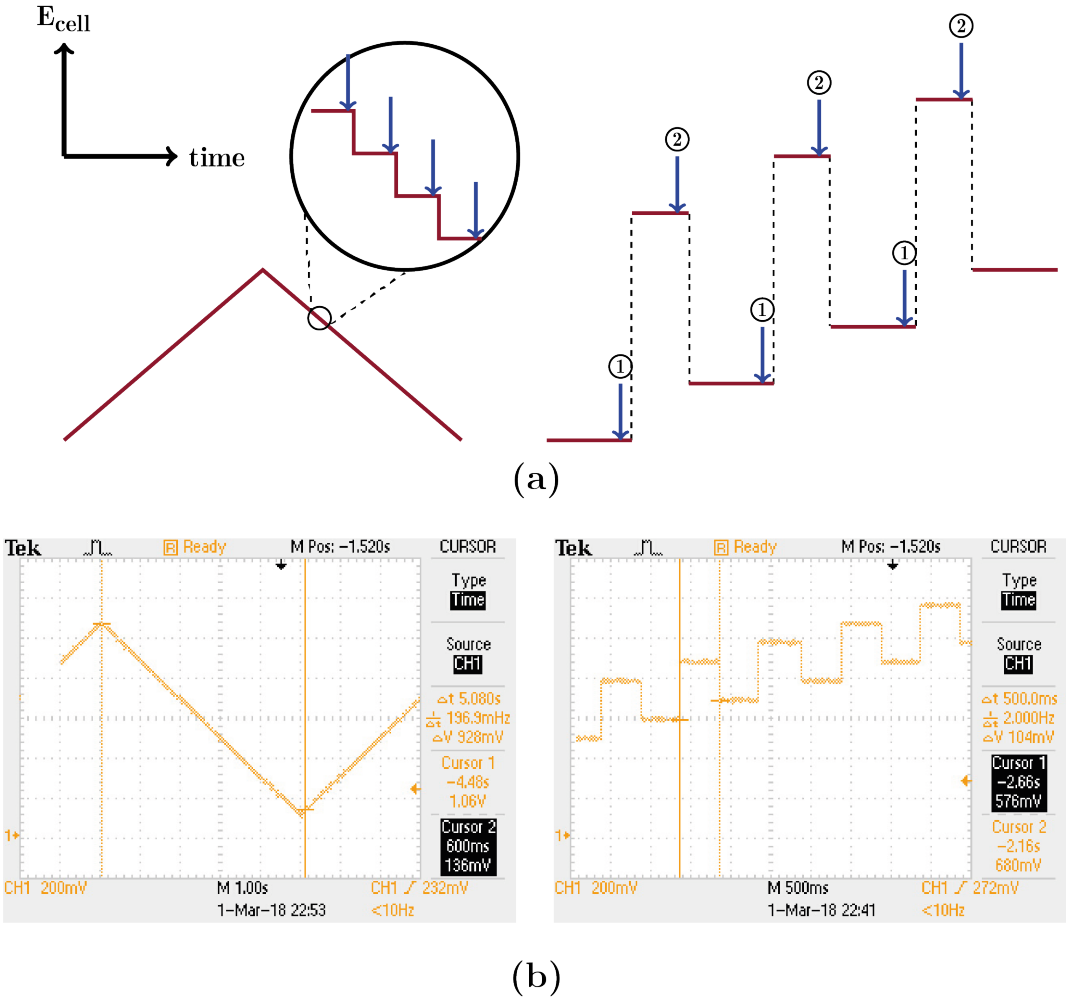

Figure 3.6 – CV and DPV waveforms generated with a DDS architecture: **(a)** typical triangular voltage sweep and pulsed-modulated voltage where the blue arrows indicate the instant when V_{out} is sampled by the ADC, **(b)** signals measured between the WE and the RE.

interface. Typical CV and DPV waveforms are displayed in Fig. 3.6. The signals were measured between the WE and the RE, where a linear voltage scan from 0.1 V to 1.1 V was output at $200\,\mathrm{mV} \cdot \mathrm{s}^{-1}$ for CV, and a 50% duty cycle pulsed-waveform of 1 s period with 300 mV pulse amplitude and 100 mV voltage step was output for DPV.

3.3.2 Potentiometric measurement circuit

The circuit implemented for potentiometric measurements is displayed in Fig. 3.7. The OCP of the two-electrode electrochemical cell was measured by sensing the potential of the sensing electrode ISE against the grounded-RE that was shared for the two

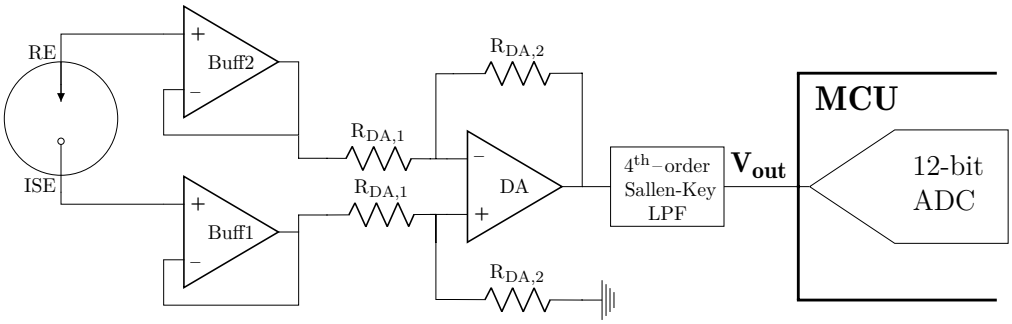

Figure 3.7 – Circuit architecture for potentiometric readout (adapted from [**?**]).

potentiometric channels. High impedance MAX44242 voltage buffers that draw up to 0.5 pA bias current ensured open circuit conditions and sensor isolation. This tiny bias current helps reducing potential drift of the sensor, lowering sensor lower LOD, and increasing sensor sensitivity [**?**]. Next, the differential signal was amplified by the differential amplifier built around *DA* with a gain of 3.9. The latter was chosen in order to use the full dynamic range of the ADC, given that the observed OCPs typically varied in $[0; 525]$ mV. The differential sensing stage reduced common-mode interference as well. Moreover, the signal conditioning path included a fourth-order Sallen-Key LPF in order to attenuate high-frequency noise and to serve as anti-aliasing element prior to the ADC.

3.3.3 Signal conditioning circuit

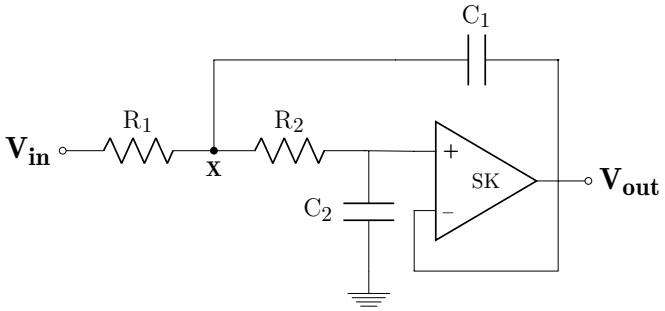

Figure 3.8 – 2^{nd}-order unity-gain LPF implemented with a Sallen-Key topology.

The design of the LPF for attenuating high-frequency noise and interference from measurements, and serving as anti-aliasing element prior to the ADC, is described hereunder. An unity-gain active LPF was implemented with a Sallen-Key topology, that is a degenerate form of voltage-controlled voltage source with high input impedance and low output impedance [**?**]. The 2^{nd}-order LPF is displayed in Fig. 3.8, and its transfer function is obtained through Kirchhoff current laws at node X and at the summing node

of the OpAmp:

$$H(s) = \frac{V_{out}(s)}{V_{in}(s)} = \frac{1}{1 + \omega_c C_2(R_1 + R_2) \cdot s + \omega_c^2 R_1 R_2 C_1 C_2 \cdot s^2}\,, \tag{3.3}$$

where $s = \frac{j\omega}{\omega_c}$ is the Laplace variable normalized to the corner pulsation. A Butterworth filter was implemented in order to achieve a flat response in the passband. The LPF transfer function can be re-written with normalized Butterworth polynomials:

$$H(s) = \frac{1}{1 + a \cdot s + b \cdot s^2}\,, \tag{3.4}$$

where the Butterworth coefficients are tabulated. By identification,

$$\left\{ \begin{array}{ll} a & = \omega_c C_2(R_1 + R_2) \\ b & = \omega_c^2 R_1 R_2 C_1 C_2 \end{array} \right. \Leftrightarrow \left\{ \begin{array}{ll} a & = \omega_c C_2 \left(R_1 + \frac{b}{\omega_c^2 R_1 C_1 C_2} \right) \\ R_2 & = \frac{b}{\omega_c^2 R_1 C_1 C_2} \end{array} \right. \tag{3.5}$$

The system of equations (3.5) leads to the second-order polynomial equation with R_1

$$\omega_c^2 C_1 C_2 R_1^2 - a\omega_c C_1 R_1 + b = 0\,, \tag{3.6}$$

yielding the real solutions

$$R_{1,2} = \frac{aC_1 \pm \sqrt{(aC_1)^2 - 4C_1 C_2 b}}{2\omega_c C_1 C_2}\,. \tag{3.7}$$

As a result, ω_c and C_1 could be fixed, and R_1 and R_2 are computed using (3.7) while complying with $0 \leq \frac{C_2}{C_1} \leq \frac{a^2}{4b}$.

Two 2^{nd}-order Sallen-Key LPFs were put in cascade in order to achieve a 4^{th}-order LPF with a steeper roll-off of 80 dB/decade. A parametric numerical simulation was performed on Wolfram Mathematica® for the sizing of the filter components (see Fig. 3.9). The Bode plots are shown for the first and second stage of the LPF, and the overall response. The corner frequency and the Butterworth coefficients were fixed, while the values of the passive components were chosen according to nominal values from electronic components supplier.

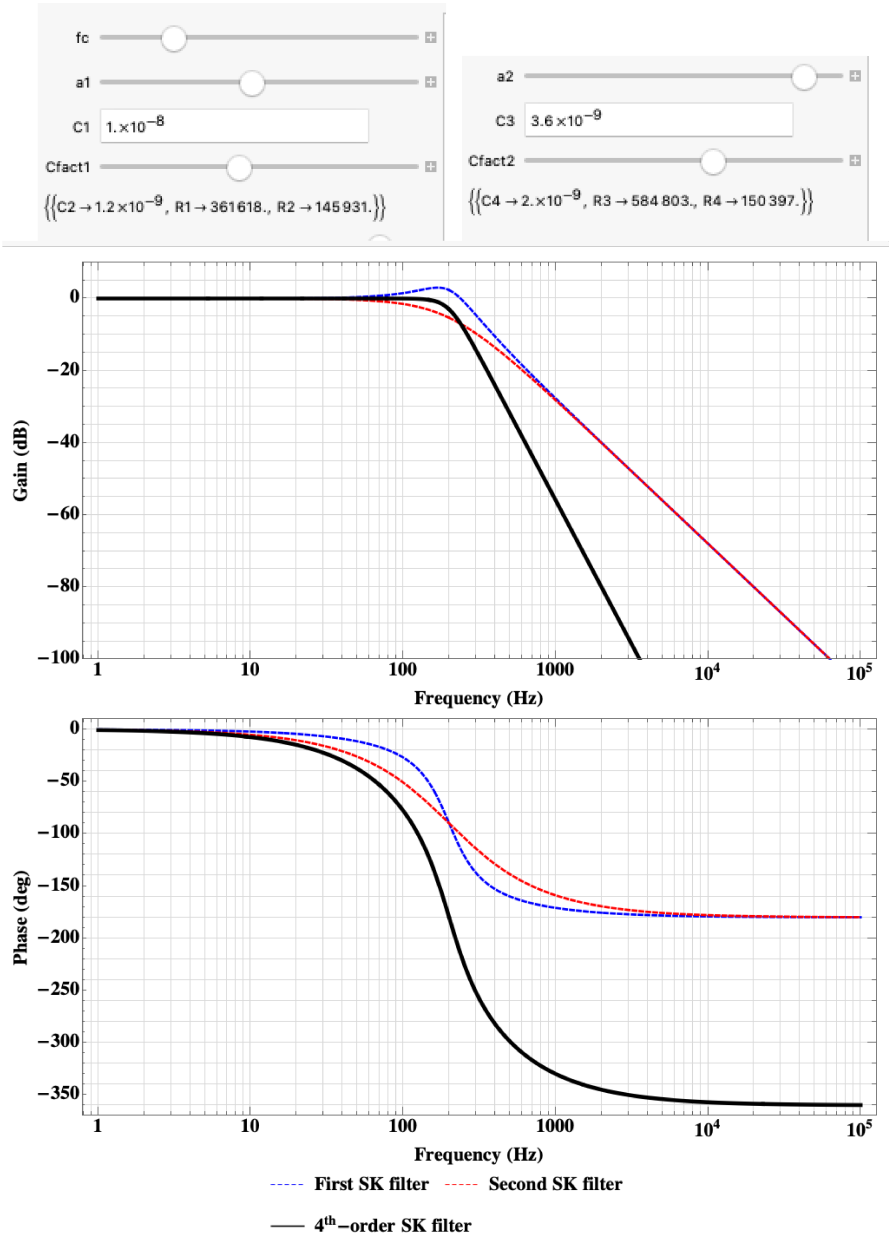

Figure 3.9 – Numerical simulation for the sizing of the fourth-order Sallen-Key LPF.

3.3.4 Front-end electrical characterization

AmpPot front-end was characterized in order to assess the electrical performance of the readout circuitry and the hardware. First, the linearity and sensitivity of the current-readout blocks were evaluated by applying a DC current ranging from –40 µA to 40 µA at the WE. The transduced voltage was measured at the output node and plotted in Fig. 3.10.a. An excellent linearity with a sensitivity of 29.92 mV/µA was observed, corresponding to the gain of the resistive feedback TIA. Moreover, the *Signal-to-Noise*

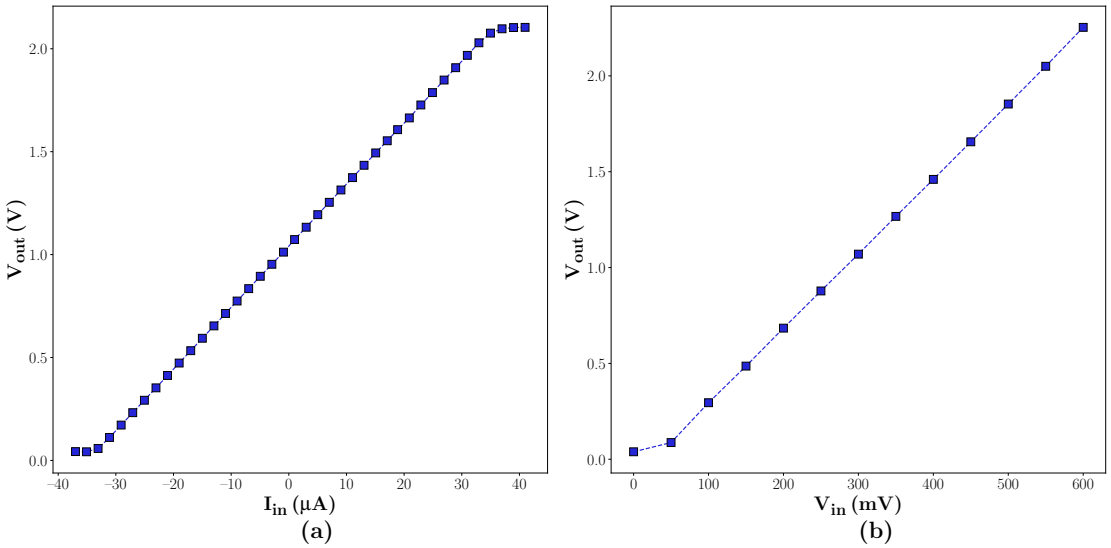

Figure 3.10 – Electrical characterization of **(a)** amperometric and **(b)** potentiometric readout circuits (adapted from [**?**]).

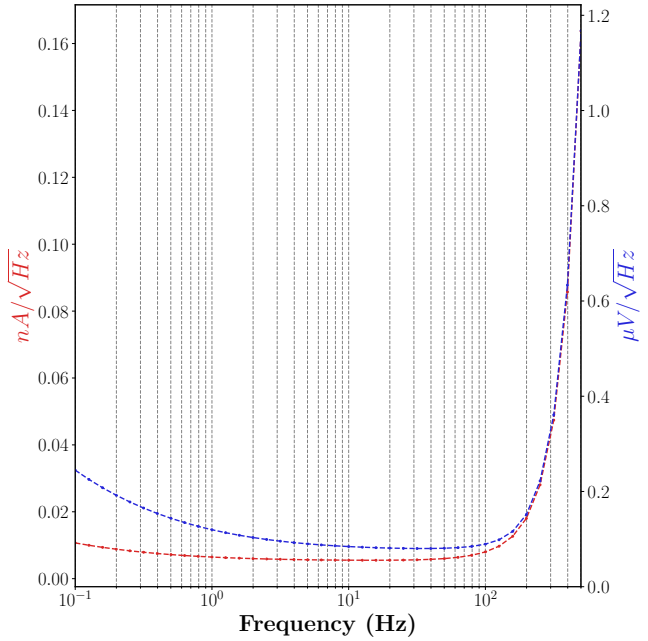

Figure 3.11 – Simulated input-referred noise of amperometric (*red*) and potentiometric (*blue*) readout circuits. The signal bandwidth is of 100 Hz (reprinted from [**?**]).

Ratio (SNR) was measured at the output channel, yielding a resolution of 320 nA by taking into account the noise level.

Regarding potentiometric readout, a DC voltage ranging from 0 mV and 600 mV was applied between the ISE and the RE terminals. The output voltage was measured

and plotted in Fig. 3.10.b, highlighting an excellent linearity. A sensitivity of 3.89 was obtained, corresponding to the gain of the differential amplifier. The simulated input-referred noise spectrum for both amperometric and potentiometric readout circuits are plotted in Fig. 3.11, with the PSpice models of the OpAmps used. An integrated noise of 6.3 nA and 84.2 µV was measured over the signal bandwidth for the amperometric and potentiometric channels, respectively.

Moreover, the power consumption of the hardware front-end was of 150 mW in multi-sensing mode, where 67% was absorbed by the 4 analog front-end channels; 23% was consumed by the voltage regulators, the MCU, and the Bluetooth module; and 10% was due to BLE transactions. The 3.7 V lithium-ion battery used features 1.1 Ah capacity, enabling continuous multi-sensing tasks for 27 h.

The electrical characteristics of *AmpPot* are summarized in Table 3.1.

Table 3.1 – Electrical characteristics of *AmpPot*

	Voltammetric channels	**Potentiometric channels**
Input range	[–33; +33] µA	[50; 530] mV
Sensitivity/Gain	29.92 ± 0.04 mV/µA $R^2 > 0.9999$	3.89 ± 0.05 $R^2 > 0.9999$
Resolution	320 nA	1.3 mV
Integrated noise @ 100 Hz (simulated)	6.3 nA	84.2 µV
Power consumption (2 channels)	66 mW	34 mW

3.4 Electrochemical sensing

After the assessment of the electrical performances of *AmpPot* hardware, the sensing front-end was validated through lactate monitoring, APAP detection, and lithium ion sensing. These are typical examples of endogenous metabolite, exogenous compound, and electrolytes monitored for healthcare applications. An Autolab PGSTAT 302N potentiostat (Metrohm, Switzerland) driven by Nova 1.11 software is a reference laboratory instrument used for the development and characterization of electrochemical sensors. The results achieved for the in vitro characterization of the electrochemical sensors with the proposed hardware *AmpPot* and the laboratory potentiostat are compared and described in this section.

3.4.1 Lactate monitoring

The three-electrode electrochemical cell for lactate monitoring consisted of: the enzymatic lactate sensor built on the carbon WE of a ceramic SPE, the carbon CE of the SPE, and a double junction Ag/AgCl/KCl (3 M)/LiOAc (1 M) RE from Metrohm (Switzerland). The LOx functionalization of the sensor was thoroughly detailed in Section 3.2.1. The detection of lithium L-Lactate salt was performed through HMF RedOx mediator in order to avoid interference from electroactive species that could be oxidized at the high potential required for classical detection involving H_2O_2 (see (3.1)). The reaction pathway for lactate sensing is:

$$\begin{aligned} \mathrm{CH_3-CH-OH-COO^- + 2\,Fc^+ \xrightarrow{LOx} CH_3-CO-COO^- + 2\,Fc + 2\,H^+} \qquad (3.8)\\ \mathrm{Fc \xrightarrow{E_{cell}} Fc^+ + e^-}\,, \end{aligned}$$

where L-Lactate is transformed into pyruvate in presence of ferrocenium. Then, the produced ferrocene is oxidized at the transducer surface that is biased at the proper oxidation potential.

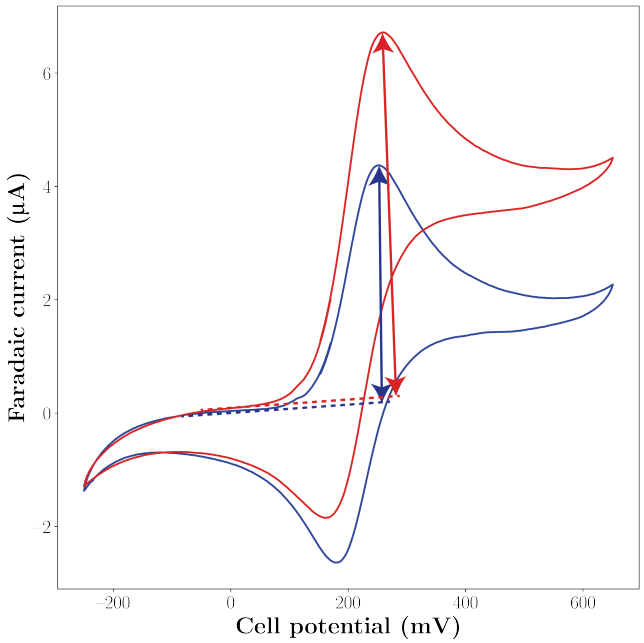

Figure 3.12 – Catalytic activity of developed LOx-C lactate sensor: CV responses at $10\,\mathrm{mV \cdot s^{-1}}$, in 10 mM PBS solution containing 0.5 mM HMF: without L-Lactate (*blue*), and with 4.95 mM L-Lactate (*red*) (adapted from [**?**]).

The first experiment was the evaluation of the catalytic activity of the enzymatic sensor through CV between –250 mV and 650 mV, at a slow scan rate of $10\,\mathrm{mV \cdot s^{-1}}$.

The voltammetric measurement was carried out in a background solution of 10 mM PBS and 0.5 mM HMF, without and in presence of 4.95 mM L-Lactate. The obtained voltammograms are displayed in Fig. 3.12. The blue voltammogram shows the response of $Fc|Fc^+$ RedOx couple in aqueous solution, highlighting a reversible reaction with an oxidation potential around 260 mV, and a reduction potential around 190 mV. In presence of the analyte, the oxidation current increased of 2.8 µA. Similar results were achieved in [**?**], where an anodic current sensitivity of $0.56\,\mu A \cdot mM^{-1}$ was obtained. Therefore, this CV characterization confirms the correct catalytic response of the enzymatic lactate sensor where the LOx was directly adsorbed on the electrode surface.

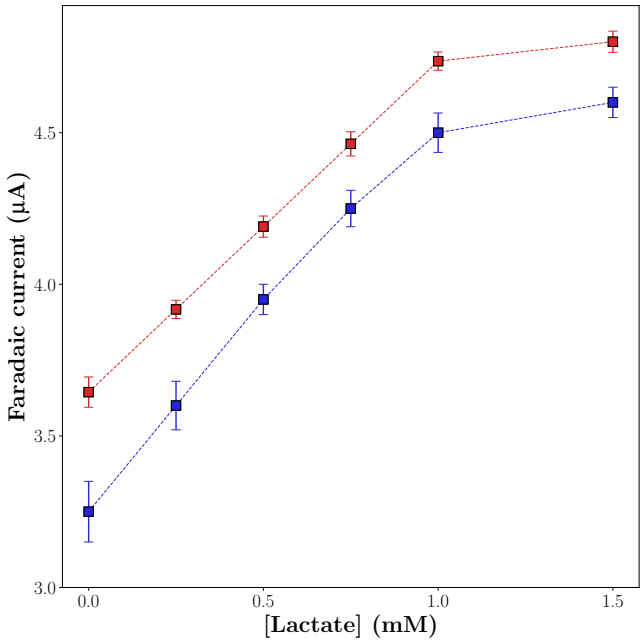

Figure 3.13 – Calibration curves resulting from CA of LOx-C lactate sensor at $E_{cell} = 300$ mV: with *AmpPot* hardware (*blue*), and with an Autolab potentiostat (*red*). The error bars correspond to standard deviations obtained with three measurements, with different sensors (reprinted from [**?**]).

Next, the analytical properties of the lactate sensor were assessed with CA measurements. A static potential of 300 mV was applied to the electrochemical cell, slightly above the oxidation potential of the HMF mediator, and the cell current was continuously measured. The background solution consisted of 10 mM PBS with 0.5 mM HMF. The analyte was gradually injected into the sample while maintaining the concentration of RedOx mediator constant in the sample. The results of lactate calibration with both *AmpPot* hardware and the Autolab potentiostat are displayed in Fig. 3.13. The enzymatic sensor exhibits a linear response up to 1 mM, above which the enzyme starts being saturated. The sensitivity and LOD achieved with both sensing front-ends are reported in Table 3.2. A higher sensitivity of $1.20 \pm 0.30\,\mu A \cdot mM^{-1}$ up to 1 mM was achieved with *AmpPot* hardware, but a larger LOD of 37.0 ± 8.0 µM was obtained compared to the laboratory potentiostat.

Indeed, a higher background current noise was observed with the proposed system. The results are compared with similar work involving lactate detection through HMF RedOx mediator. In [?], LOx was drop-cast on gold electrodes, and lactate calibration was carried out in presence of 0.5 mM HMF like with our experiments. CA was performed with a BAS CV-27 potentiostat connected to a BAS X-Y recorder. A sensitivity of $0.77 \pm 0.08\,\mu A \cdot mM^{-1}$ was achieved with a linear response up to 0.3 M. The sensitivity and linearity obtained with our LOx-C sensing front-end were superior. However, the LOD provided by the BAS CV-27 potentiostat was much lower than with *AmpPot*. This is not an issue since the physiological range of lactate in biofluid such as sweat is above 1 mM [?].

Table 3.2 – Performance of lactate sensing front-ends through HMF RedOx mediator

	AmpPot	Autolab	[?]
Sensitivity ($\mu A \cdot mM^{-1}$)	1.20 ± 0.30	1.08 ± 0.12	0.77 ± 0.08
Linear response (mM)	up to 1	up to 1	up to 0.3
	R=0.99	R=0.99	R=0.98
LOD (μM)	37.0 ± 8.0	20.6 ± 3.6	10

3.4.2 APAP detection

The capability of *AmpPot* sensing front-end to perform potentiodynamic measurements was then assessed through APAP detection. The electroactive compound was sensed with a three-electrode setup leveraging a ceramic SPE (carbon WE with an active area of 12.56 mm^2, carbon CE, silver RE). The measurements were carried out with the bare sensor in a 10 mM PBS solution (pH $\sim$ 7.4). APAP was gradually injected in the sample from 50 to 300 μM, in agreement with the pharmaceutical formulation of the drug [?]. APAP detection was characterized with both CV and DPV. The parameters of the waveforms are reported in Table 3.3, similar to the ones used in [?]. These parameters could be further optimized, in particular, by tuning the sampling frequency in order to reduce the power consumption during voltammetric measurements in energy-constrained systems [?].

Table 3.3 – Parameters of CV and DPV waveforms for APAP detection

Cyclic voltammetry		**Differential pulse voltammetry**	
Lower potential	–0.1 V	Lower potential	0 V
Upper potential	1.1 V	Upper potential	1 V
Step potential	8.1 mV	Step potential	8.1 mV
Scan rate	$0.1\,V \cdot s^{-1}$	Pulse amplitude	80 mV
		Pulse duration	80 ms
		Pulse period	160 ms

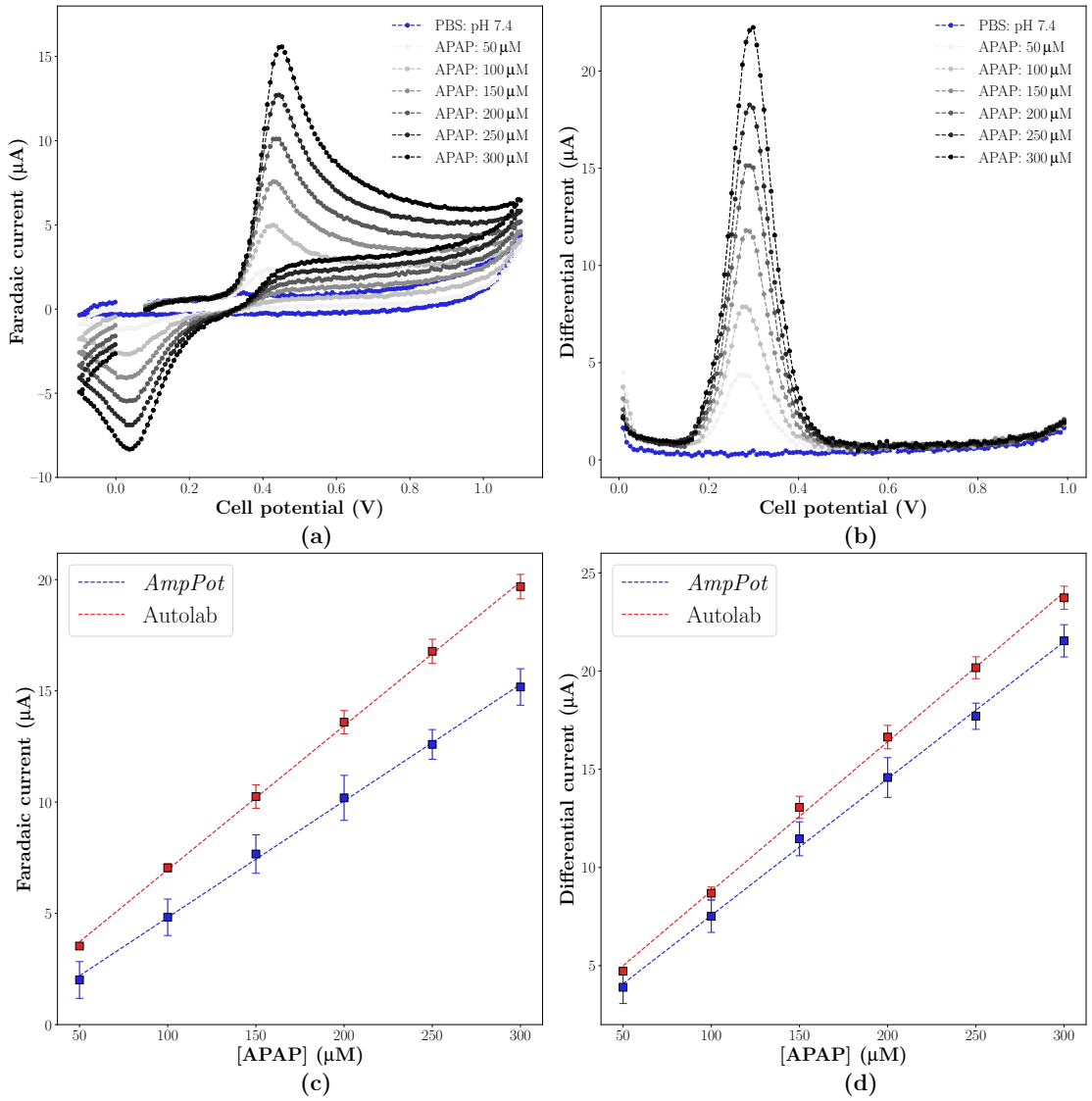

Figure 3.14 – Electrochemical detection of APAP: voltammograms obtained with *AmpPot* hardware through **(a)** CV and **(b)** DPV; APAP calibration curves with *AmpPot* and Autolab potentiostat through **(c)** CV and **(d)** DPV measurements. The error bars correspond to standard deviations obtained with three measurements, with different sensors (reprinted from [**?**]).

The voltammograms acquired for APAP calibration with *AmpPot* front-end are shown in Fig. 3.14.a and Fig. 3.14.b. With CV measurements, the peak oxidation currents are observed around 430 mV, and increase linearly with APAP concentration. A sensitivity of $52.4 \pm 0.15\,\text{nA} \cdot \mu\text{M}^{-1}$ was obtained with an excellent linearity. The sensor LOD was computed as the concentration of APAP providing a Faradaic current three times the standard deviation of the background current in a window centered around the peak oxidation current. A LOD of $2.6 \pm 0.49\,\mu\text{M}$ was obtained, below the concentration

at which toxicity could be detected (20 µM [?]). As for APAP calibration through DPV, the differential cell currents exhibit peaks around 290 mV. A higher sensitivity of $69.6 \pm 2\,\text{nA} \cdot \mu\text{M}^{-1}$ was achieved compared to CV, as expected, since differential measurements reduce the contribution of non-Faradaic background currents arising from interfacial capacitance or transient charging currents flowing through the electrical double layer at the surface of the transducer [?]. The sensor LOD was slightly improved as well with DPV measurements.

Table 3.4 – Performance of sensing front-ends for APAP detection

	AmpPot		Autolab		[?]	
	CV	DPV	CV	DPV	CV	DPV
Sensitivity ($\text{nA} \cdot \mu\text{M}^{-1}$)	52.4 ± 0.2	69.6 ± 2.0	64.7 ± 2.8	76.0 ± 5.8	47.5 ± 5.0	57.6 ± 5.6
RMSE (µA)	0.146	0.226	0.149	0.269	n.a.	n.a.
R^2	>0.99	>0.99	>0.99	>0.99	>0.99	>0.99
LOD (µM)	2.6 ± 0.49	2.1 ± 1.22	0.75 ± 0.42	0.5 ± 0.15	5.43 ± 0.57	5.08 ± 0.49

RMSE: Root Mean-Squared Error, R^2: Coefficient of determination

Next, the calibration results obtained with *AmpPot* and the Autolab potentiostat are compared, and the sensing performances are reported in Table 3.4. The calibration curves are displayed in Fig. 3.14.c and Fig. 3.14.d, for CV and DPV, respectively. Both front-ends exhibit an excellent linearity with the two voltammetric techniques. Slightly lower sensitivities are observed with the proposed hardware, that might be due to a higher background current noise arising from the cabling of the electronic interface to the sensor in such in vitro measurement setup. Nevertheless, the developed system provides much higher sensitivity than in [?], where sensitivities of $40\,\text{nA} \cdot \mu\text{M}^{-1}$ and $22\,\text{nA} \cdot \mu\text{M}^{-1}$ were obtained, or in [?], where sensitivities of $47.5 \pm 5.0\,\text{nA} \cdot \mu\text{M}^{-1}$ and $57.6 \pm 5.6\,\text{nA} \cdot \mu\text{M}^{-1}$ were obtained, with CV and DPV, respectively. Regarding the LOD, the Autolab potentiostat provides a much lower LOD since the laboratory instrument features a finer current resolution and a lower background current noise. Nevertheless, LODs achieved with *AmpPot* are more that seven times below the detectable APAP concentration toxicity [?], and it outperforms LODs achieved with state-of-the art APAP sensing platforms [?].

3.4.3 Lithium sensing

The characterization of the ion-sensing channels of *AmpPot* was performed with lithium ion sensing. The fabrication of lithium solid-contact ISEs was thoroughly described in Section 3.2.1. Sensor calibration was carried out in pure water samples, where LiCl was gradually injected from 10^{-8} M to 10^{-1} M, every 50 s. The OCP between the lithium-ISE and a double junction Ag/AgCl/KCl (3 M)/LiOAc (1 M) RE from Metrohm (Switzerland) was continuously measured. A typical lithium ion calibration curve is

displayed in Fig. 3.15, where the corresponding OCP time trace is reported in the inset. Two operating regimes could be distinguished: in diluted analyte, the OCP response is almost flat and increases slightly; above a certain lithium ion concentration, the OCP increases with clear potential steps at every analyte injection. A quasi-Nernstian slope of 55.6 ± 1.16 mV/decade was obtained. The sensor lower LOD was computed as the intersection of the extrapolated linear portions of the calibration curve (IUPAC [**?**]). As a result, a lower LOD of 11 ± 3.5 µM was obtained. This value is well below the minimum effective concentration of lithium drug (0.5 mM [**?**]). Likewise, lithium ion calibration was performed with the Autolab potentiostat. The obtained calibration performances are reported in Table 3.5. The measurements with *AmpPot* yield lower sensitivity but very good linearity. Besides, the LODs are comparable.

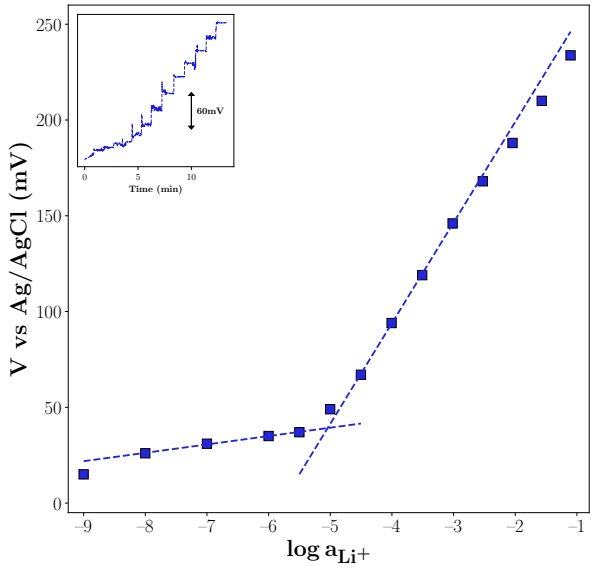

Figure 3.15 – Lithium ion-sensor calibration in water background electrolyte (reprinted from [**?**]).

Table 3.5 – Performance of sensing front-ends on developed lithium ion-sensors

	AmpPot	Autolab
Sensitivity (mV/decade)	55.6 ± 1.16	61.9 ± 0.48
RMSE (mV)	0.5	0.1
R^2	0.9994	0.9993
LOD (µM)	11.0 ± 3.50	12.4 ± 2.40

RMSE: Root Mean-Squared Error, R^2: Coefficient of determination

3.5 Summary and main contributions

A comprehensive health status monitoring is achieved by tracking several types of biomarkers, including endogenous metabolites and electrolytes, and exogenous compounds ingested as drugs in TDM applications. In this chapter, we have presented the co-design of a general-purpose electrochemical sensing front-end enabling voltammetric and potentiometric multi-analyte sensing. The system was characterized with lactate, APAP, and lithium ions, that are typical examples of metabolite, drug, and electrolyte monitored in healthcare applications. The sensing front-end consists of:

- the **electrochemical sensor array** built on ceramic SPEs. An enzymatic sensor was developed on a carbon SPE for lactate monitoring, the detection of APAP was carried out on a bare carbon SPE, and a solid-contact ISE was built on a platinum SPE for lithium ion-sensing.
- the **electronic interface *AmpPot*** enabling both voltammetric and potentiometric measurements. For voltammetric sensing, the hardware ensures the polarization of the electrochemical cell through a potentiostat, the generation of programmable electrochemical cell potential waveforms (potential step, linear potential scan, pulsed-potential) with a DDS circuit, and the acquisition and processing of the electrochemical cell current through a resistive feedback TIA and a fourth-order Sallen-Key LPF. As for potentiometry, *AmpPot* enables the monitoring of the two-electrode cell OCP transducing the detection of the target electrolyte through buffered and differential circuitry. The electronic front-end was mounted on a rigid FR4 PCB which size complies with portable applications. The power consumption of the overall front-end allows continuous measurements with 27 h autonomy, with a 1.1 Ah 3.7 V lithium ion battery.
- the **remote monitoring interface** that was executed on a personal laptop. The terminal allows the user to configure the parameters of the electrochemical measurements and the sensing channels to activate, and to visualize in real-time the data collected form the sensors (time traces or voltammograms).

The main features of *AmpPot* are reported in Table 3.6, with comparison to hardware front-end enabling multi-channel voltammetric/amperometric and potentiometric sensing. The proposed multi-mode electrochemical sensing interface is a versatile, programmable, portable, and power efficient solution for remote healthcare monitoring. The front-end provides an excellent linearity, a slightly lower sensitivity, and comparable LODs for the detection of lactate, APAP, and lithium ions, compared to a bulky laboratory Autolab potentiostat. Moreover, *AmpPot* supplies improved sensing performances for APAP detection compared to state-of-the art voltammetric front-ends [**?**, **?**], where identical measurement conditions were implemented for a fair comparison.

Table 3.6 – Hardware front-ends enabling multi-channel voltammetric/amperometric and potentiometric sensing

	[?]	[?]	***AmpPot***
Sensing techniques	Voltammetry (2), potentiometry (2)	Amperometry (2), potentiometry (2)	Voltammetry (2), potentiometry (2)
Target biomarkers	Nitrite and pH	Lactate, glucose, sodium, and potassium	Lactate, APAP, and lithium
Hardware size (mm)	$58 \times 87 \times 30$	fits in wristband	$38 \times 76 \times 1.6$
Technology	0.18 µm CMOS FE[1] and FPGA	Flexible PCB	Rigid FR4 PCB
Potentiostat	Control amplifier and feedback resistor	None	Control amplifier
Waveform generator	None	None	DDS architecture
Current readout	DDA[2]	Resistive feedback TIA	Resistive feedback TIA
OCP readout	DDA[2]	Buffered and differential circuit	Buffered and differential circuit
Power consumption	157.25 mW (3.3 V)	n.a.	150 mW (3.7 V)

[1] CMOS front-end [2] Differential difference amplifier

4 Multi-ion-sensing front-end for physiology

The design of a multi-ion-sensing front-end aiming at physiology applications is presented in this chapter. The motivations driving this research are discussed first. Then, the experimental methods implemented for the development of solid-contact ISEs enabling sodium, potassium, ammonium, and calcium ions monitoring are described. Besides, in situ temperature needs to be tracked as well for calibration purposes. Next, the electronic front-end interface ensuring remote potentiometric measurement of the ion-sensors, and temperature readout through a RTD are detailed. Furthermore, the characterization of the multi-ion-sensing platform in artificial sweat samples is presented.

4.1 Motivation

Recent studies indicate that endogenous electrolytes are significantly involved in several human physiological processes for both healthcare quality monitoring and high-performance sport practice [**?**]. Namely, the monitoring of specific ions enables the control of diseases or physiological dysfunctions like hypo/hyperkalemia, hypo/hypernatremia, cystic fibrosis, or cardiac arrhythmia [**?**, **?**, **?**]. Moreover, many electrolytes are indicators of the physical activity of subjects undergoing intense training or physical exercise. A continuous tracking of the relevant biomarkers helps optimizing training intensity, hydration and resting cycles, thus reducing risks of severe muscle cramping or injuries [**?**, **?**, **?**, **?**, **?**]. Besides, ions can be monitored through non-invasive perspiration analysis, where the biomarkers are present at relatively high concentrations ($\sim$ mM range) [**?**, **?**]. As a matter of fact, wearable sensing platforms can be embedded into sweatbands in several parts of the body (e.g. forehead [**?**], wrist [**?**], tight and calf [**?**]). The most relevant electrolytes for healthcare monitoring and physical exercise applications through sweat analysis are reported in Table 4.1, along with the typical concentration range of the analytes. The electrolytes span a wide range of concentration since the latter is influenced by several factors including sweating rate, environmental temperature and humidity, heat stress, diet, gender, and inter-subject variability [**?**].

Table 4.1 – Relevant ions enabling physiology through sweat analysis

Ion	Concentration (mM)	Medical application	Physical exercise	Ref.
Na^+	10–100	Hypo/hypernatremia, cystic fibrosis	Dehydration	[?, ?, ?]
K^+	5–25	Hypo/hyperkalemia	Muscle fatigue	[?, ?]
Cl^-	10–100	Cystic fibrosis	Dehydration	[?, ?, ?]
NH_4^+	0.5–8	Liver dysfunction	Muscle fatigue	[?, ?]
Ca^{2+}	0.5–3	Bone mineral loss	Homeostatis	[?, ?]
Mg^{2+}	0.04–0.7	Cardiac arrhythmia	Aerobic performance	[?, ?]

As a result, a multi-ion-sensing platform is needed to obtain a comprehensive insight of the physiological status of an athlete undergoing intense physical activity, or a person suffering from physiological dysfunctions, since correlations exist between the several biomarkers present in sweat. Moreover, ion interference is significantly hampering detection accuracy, mostly at lower concentration levels, because of the background ions constituting sweat samples that distort sensor responses. Thus, the monitoring of both target ions and interfering agents through a multi-sensing array could help mitigating this sensor artifact by feeding the multivariate sensor response to complex processing models [?]. Nevertheless, most of reported wearable ion-sensing platforms are specific to one or two target electrolytes, that are often sodium and potassium ions, given that they are the prevalent electrolytes in sweat [?, ?, ?, ?].

Therefore, a multi-ion-sensing front-end is proposed to address the lack of multi-sensing capabilities in current electronic interfaces developed for potentiometric ion-sensors. A concurrent monitoring of sodium, potassium, ammonium, and calcium ions was implemented and characterized in artificial sweat samples, given that sweat biofluid is easily reproducible in laboratory with standard electrolytic, metabolite, and organic compounds composition. Besides, in situ temperature is a crucial parameter for sensor calibration, thus a temperature readout module was included in the sensing front-end. The proposed remote sensing front-end will be used for the dataset acquisition involving the training and optimization of the multivariate calibration models described in the subsequent chapters of this thesis.

4.2 Experimental methods

The experimental methods implemented for the development of sodium, potassium, ammonium, and calcium ions solid-contact ISEs are presented in this section. The ion-sensors were built on commercial rigid ceramic SPEs for intensive sensor characterization. Moreover, a custom micro-fabricated sensing platform enabling ion-sensing and temperature measurement was developed, targeting wearable sweat sensing.

4.2.1 Solid-contact ion-selective electrodes

The fabrication of solid-contact ISEs on ceramic SPE is described hereunder.

Chemicals and material

All chemicals were purchased from Sigma-Aldrich (Switzerland) unless otherwise stated. These include H_2PtCl_6, H_2SO_4, 4-tert-Butylcalix[4]arene-tetraacetic acid tetraethylester (Sodium ionophore X), Valinomycin (Potassium ionophore I), Nonactin (Ammonium ionophore I), N,N-Dicyclohexyl-N',N'-dioctadecyl-diglycolic diamide (Calcium ionophore IV), Potassium tetrakis(4-chlorophenyl)borate, 2-Nitrophenyloctylether (o-NPOE), bis(2-ethylhexyl)sebacate (DOS), Poly(vinyl chloride) (PVC), and Tetrahydrofuran (THF).

Ceramic SPEs (platinum WE with 12.56 mm^2 active area; platinum CE; silver RE) were purchased from Metrohm (Switzerland), and were used for the extensive characterization of the ion-sensors.

Electrode nanostructuration

The electrode nanostructuration was carried out with a three-electrode setup, where an auxiliary SPE was used to provide the CE and RE of the electrochemical cell. The experiments were performed with an Autolab PGSTAT 302N potentiostat driven by Nova 1.11 software.

First, the WE was cleaned by CV cycles in 0.5 M H_2SO_4. Then, platinum nanostructures were electrodeposited by applying –1 V in (25 mM H_2PtCl_6, 50 mM H_2SO_4) solution, following the procedure from [**?**]. Next, the sensor was cleaned with pure water and dried.

Ion-selective membrane fabrication

The nanostructured electrode was then functionalized by 10 µL of a polymeric ISM that was drop-cast on top of the electrode. The composition of the different ISMs for sodium, potassium, ammonium, and calcium-ISEs are reported in Table 4.2. Thereafter, the ion-sensor was left to dry for 24 h in dark conditions, enabling solvent evaporation.

The structure of the fabricated solid-contact ISE on a ceramic SPE is displayed in Fig. 4.1.

Measurement setup

The ion-sensors were conditioned with a solution of the corresponding target ion at least one day before the measurements. Namely, sodium and potassium-ISEs were

Table 4.2 – ISM compositions for 100 mg mixture

Sodium-selective membrane		
Ionophore	Sodium Ionophore X	0.7 mg
Lipophilic anionic site	Potassium tetrakis(4-chlorophenyl)borate	0.2 mg
Plasticizer	2-Nitrophenyloctylether (o-NPOE)	64 µL
Polymerizer	Poly(vinyl chloride) (PVC)	33 mg
Potassium-selective membrane		
Ionophore	Potassium Ionophore I	1 mg
Lipophilic anionic site	Potassium tetrakis(4-chlorophenyl)borate	0.5 mg
Plasticizer	bis(2-ethylhexyl)sebacate (DOS)	72 µL
Polymerizer	Poly(vinyl chloride) (PVC)	33 mg
Ammonium-selective membrane		
Ionophore	Ammonium Ionophore I	1 mg
Lipophilic anionic site	Potassium tetrakis(4-chlorophenyl)borate	0.5 mg
Plasticizer	bis(2-ethylhexyl)sebacate (DOS)	73.1 µL
Polymerizer	Poly(vinyl chloride) (PVC)	32.2 mg
Calcium-selective membrane		
Ionophore	Calcium Ionophore IV	1 mg
Lipophilic anionic site	Potassium tetrakis(4-chlorophenyl)borate	0.28 mg
Plasticizer	2-Nitrophenyloctylether (o-NPOE)	63.3 µL
Polymerizer	Poly(vinyl chloride) (PVC)	32.9 mg

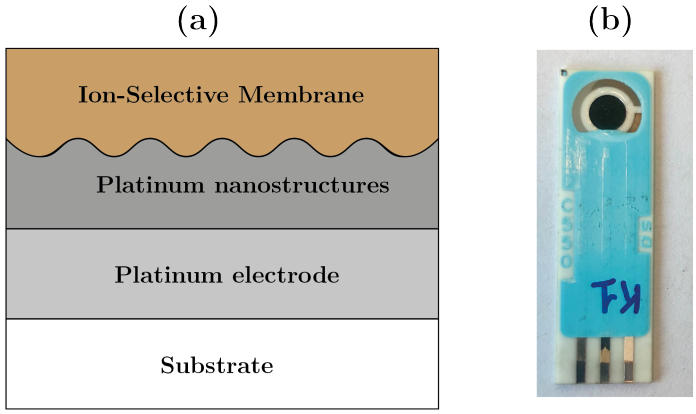

Figure 4.1 – Solid-contact ISE: **(a)** sensor cross-section, **(b)** ion-sensor fabricated on a platinum SPE.

immersed in solutions of 10 mM NaCl and KCl, respectively, while ammonium and calcium-ISEs were conditioned in solutions of 1 mM NH_4Cl and $CaCl_2$, respectively. A lower conditioning concentration tends to reduce sensor lower LOD, but the values were chosen taking into account the typical detection range of these ion-sensors. Moreover, an

artificial sweat stock solution was prepared considering the nominal concentration of the electrolytes and organic compounds typically constituting sweat samples. The artificial sweat composition is detailed in Table 4.3, where all chemicals where purchased from Sigma-Aldrich (Switzerland).

Table 4.3 – Artificial sweat composition

Compound	**Concentration**
NaCl	40 mM
KCl	5 mM
NH_4Cl	3.5 mM
$CaCl_2$	0.4 mM
$MgCl_2$	55 µM
Urea	5 mM
L-Lactic acid	5 mM
D-Glucose	100 µM
L-Ascorbic acid	10 µM

4.2.2 Fully-integrated multi-sensing platform

Moreover, a fully-integrated multi-sensing platform was manufactured on a flexible substrate, targeting wearable sweat sensing. The multi-electrode platform was fabricated in the Center of MicroNanotechnology cleanroom facilities at EPFL by Dr. Francesca Criscuolo. The electrodes were patterned on a flexible polyimide substrate, leveraging standard lithography process. A diameter of 4 mm was designed in order to get the same active area as commercial SPEs. Three platinum sensing electrodes and a silver shared-RE were built for multi-ion-sensing. Besides, a platinum RTD was patterned for in situ temperature monitoring. The fabrication process flow was fully described in [**?**], and the multi-sensing platform is shown in 4.2.

The cleaning, nanostructuration, and polymeric membrane preparation of solid-contact ISEs built on a flexible polyimide substrate are identical to the experimental methods described for SPEs. Therefore, only the description of the fabrication of an all-solid-state RE and a RTD are detailed in the following.

All-solid-state reference electrode fabrication

A shared all-solid-state Ag/AgCl RE was built in order to achieve fully-integrated measurements, avoiding the use of a double junction RE. Thus, the liquid junction of conventional REs was replaced by a polymer impregnated with an ionic liquid. An ionic liquid-doped Poly(vinyl chloride) (PVC) was used in this work.

The all-solid-state RE fabrication was carried out following the procedure from [**?**].

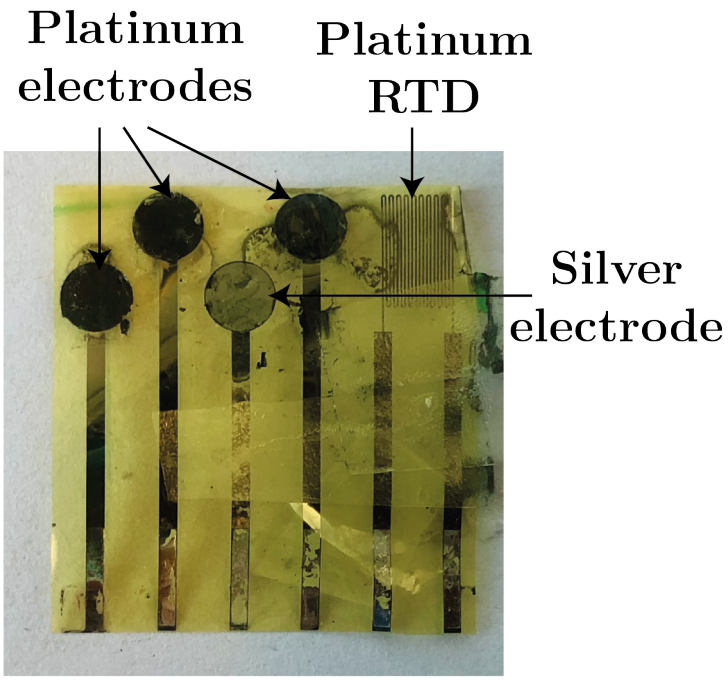

Figure 4.2 – Fully-integrated multi-sensing platform including three platinum sensing electrodes, one silver shared-RE, and a platinum RTD.

First, the silver electrode was chlorinated in 50 mM of $FeCl_3$ for 3 min. Then 10 µL of a membrane cocktail containing 0.1% of 1-Dodecyl-3-methylimidazolium chloride, 33% of PVC powder, and 66% of Bis(2-ethylhexyl) sebacate in 0.5 mL of THF was drop-cast on top of the electrode. After that, the RE was left to dry.

Resistive thermal device

A temperature sensor was included in the multi-sensor panel enabling in situ temperature monitoring. Namely, a RTD was micro-fabricated on the polyimide substrate by patterning a platinum serpentine-shaped wire of 20 foldings, with a width of 130 µM, as illustrated in Fig. 4.2. The resistance of the RTD can be computed from the material resistivity and geometry as

$$\mathrm{R(T)} = \rho_{\mathrm{Pt}}(\mathrm{T}) \frac{\text{total length}}{\text{width} \cdot \text{thickness}}, \tag{4.1}$$

where the material resistivity linearly varies with temperature [**?**]. The theoretical resistance of the device was estimated to be of 1.2 kΩ at 37 °C.

4.3 Electronic front-end interface

The electronic front-end interface enabling a remote potentiometric readout of the developed ion-sensors and in situ temperature monitoring is described in this section.

4.3.1 Hardware front-end

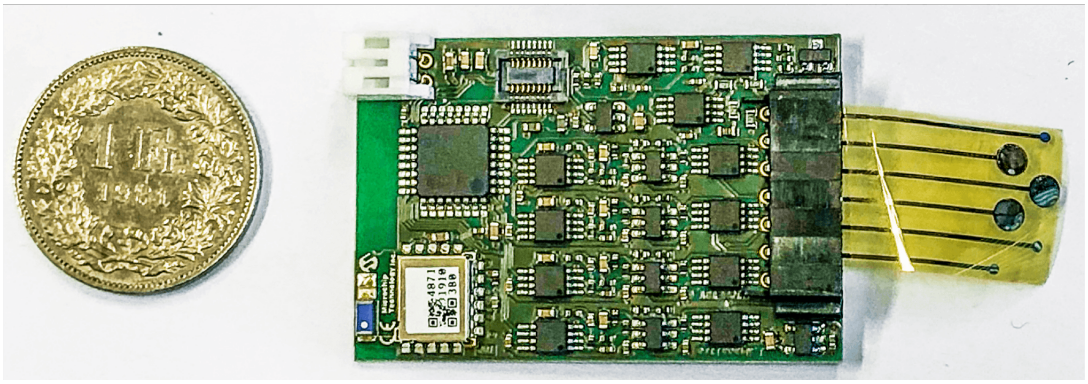

Figure 4.3 – Hardware front-end enabling four-channel ion-sensing and in situ temperature measurement.

The hardware front-end is displayed in Fig. 4.3. It was manufactured on a 1.6 mm FR4 rigid substrate, with dimensions of 30 × 45 mm that are compliant for an integration onto a wearable system. A seven-position flat-flex type edge connector was soldered to interface the hardware to a fully-integrated sensing platform, as illustrated in Fig. 4.3. Micro USB-B connectors were soldered instead, for prototyping and for the measurements performed with SPEs. The analog front-end comprised four separate ion-sensing channels where the RE was shared between the four ISEs. A temperature readout circuit was designed to sense the resistance of the RTD.

A low-power ATxMega32E5 MCU operating at 32.768 kHz, with a 8/16-bit AVR RISC CPU, is the core processing unit. It embeds a 12-bit resolution sample-and-hold ADC. Oversampling and decimation were implemented in order to achieve 16-bit resolution. In multi-sensing mode, the four potentiometric channels were scanned and sampled at 4.096 kHz, where conversions were triggered successively.

The hardware features a RN4871 BLE 4.2 module, providing a wireless link to a remote display. A GUI developed in PyQt5 was executed on a personal laptop in the vicinity of the sensing front-end. The GUI enables sensor panel configuration and real-time data visualization, with a protocol similar to the one described in Section 3.2.3. The personal laptop acts as a central device that scans service advertisements, while the BLE module on the hardware acts as a peripheral device that advertises so as to show its connectable status. The BLE module features a *Received Signal Strength Indicator* (RSSI) of –51 dBm at 1 m. Once connected and bonded, the security related keys were saved as long as the

connection is maintained. The RN4871 BLE supports Transparent UART GATT private service that handles data streaming function. The GATT server was configured by ASCII commands sent over a serial UART interface of the MCU, upon firmware initialization.

Moreover, the hardware was powered by a 3.7 V lithium ion rechargeable battery with a capacity of 2 Ah. MCP1801, low quiescent current, low dropout voltage regulators were used to supply stable 3.3 V to the analog blocks, to the MCU, and to the on-board Bluetooth module.

4.3.2 Readout circuit

Ion-sensing was accomplished by a potentiometric readout circuit similar to the one presented in Section 3.3.2. Namely, MAX44242 voltage buffers with 500 pA input bias current were used to ensure open circuit conditions and electrically isolate the sensors. Then, a single-ended differential amplifier was used to resolve the OCP sensed between the ISE and the grounded shared-RE. An amplification gain of 3.96 was implemented so as to use the whole dynamic range of the ADC. Besides, a fourth-order Butterworth LPF was implemented with a Sallen-Key topology. A corner frequency of 1.37 Hz was chosen considering that the cell potentials are DC signals.

Regarding in situ temperature measurements, the resistance of the RTD varies in a predictable way with temperature [**?**]. A straightforward solution to sense the thermistor temperature is the use of a voltage divider like in [**?**, **?**]. However, the measurements are non linear and loading effects might degrade measurement accuracy. Therefore, a resistance-to-voltage converter was implemented in this work, where the RTD was polarized by a DC current source, and the voltage across the device was measured. The current source should be designed carefully so as to avoid over-heating the RTD. An improved Howland current source with a boosted output impedance was designed [**?**]. The proposed circuit is displayed in Fig. 4.4.

The OpAmp *OA1* is sensing the input and the feedback signal differentially, setting a voltage drop of V_{in} across R_{ref}. As a result, the current source outputs a current $I_{out} = \frac{V_{in}}{R_{ref}}$. The output impedance of the current source is computed as:

$$Z_{out} = -\frac{V_{out}}{I_{out}}\bigg|_{V_{in}=0} . \tag{4.2}$$

Considering finite OpAmp open-loop gains A_1 and A_2, a nodal voltage analysis at the summing nodes of *OA1* yields

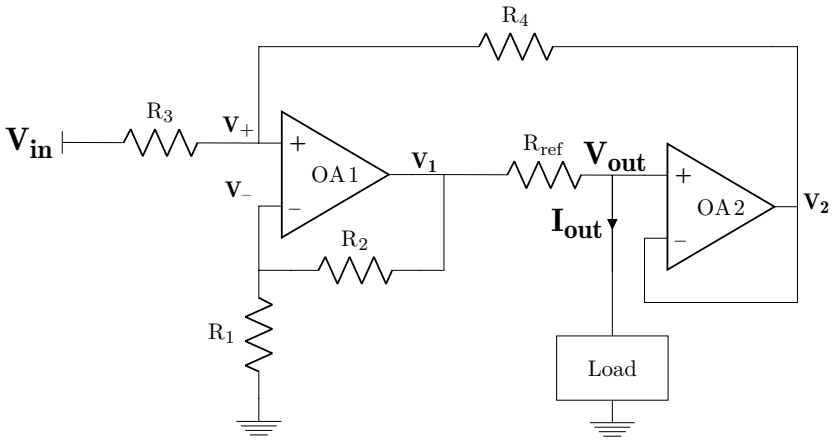

Figure 4.4 – Improved Howland current source.

$$\begin{cases} \mathrm{V}_+ &= \frac{\mathrm{R}_3}{\mathrm{R}_3+\mathrm{R}_4}\frac{\mathrm{A}_2}{1+\mathrm{A}_2}\mathrm{V}_{\mathrm{out}}\,, \\ \mathrm{V}_- &= \frac{\mathrm{R}_1}{\mathrm{R}_1+\mathrm{R}_2+\mathrm{A}_1\mathrm{R}_1}\mathrm{A}_1\mathrm{V}_+\,. \end{cases} \tag{4.3}$$

By combining equations in (4.3) with $\mathrm{V}_1 = \mathrm{A}_1(\mathrm{V}_+ - \mathrm{V}_-)$,

$$\mathrm{V}_1 = \mathrm{A}_1\frac{\mathrm{A}_2}{1+\mathrm{A}_2}\frac{\mathrm{R}_3}{\mathrm{R}_3+\mathrm{R}_4}\frac{\mathrm{R}_1+\mathrm{R}_2}{\mathrm{R}_1+\mathrm{A}_1\mathrm{R}_1+\mathrm{R}_2}\mathrm{V}_{\mathrm{out}}\,. \tag{4.4}$$

The output current is $\mathrm{I}_{\mathrm{out}} = \frac{\mathrm{V}_1-\mathrm{V}_{\mathrm{out}}}{\mathrm{R}_{\mathrm{ref}}}$. Therefore, the output impedance is obtained as

$$\begin{gathered} \mathrm{Z}_{\mathrm{out}} = \frac{\mathrm{R}_{\mathrm{ref}}}{1-\alpha}\,, \\ \text{with } \alpha = \mathrm{A}_1\frac{\mathrm{A}_2}{1+\mathrm{A}_2}\frac{\mathrm{R}_3}{\mathrm{R}_3+\mathrm{R}_4}\frac{\mathrm{R}_1+\mathrm{R}_2}{\mathrm{R}_1+\mathrm{A}_1\mathrm{R}_1+\mathrm{R}_2}\,. \end{gathered} \tag{4.5}$$

If we assume that $\mathrm{R}_1 = \mathrm{R}_2 = \mathrm{R}_3 = \mathrm{R}_4 = \mathrm{R}$, and with equal open-loop gains $\mathrm{A}_1 = \mathrm{A}_2 = \mathrm{A}$, the output impedance is

$$\mathrm{Z}_{\mathrm{out}} = \frac{\mathrm{R}_{\mathrm{ref}}}{1-\frac{\mathrm{A}^2}{\mathrm{A}^2+3\mathrm{A}+2}}\,. \tag{4.6}$$

We are only interested in the DC characteristics of the current source, where a high-precision shunt-mode voltage reference $\mathrm{V}_{\mathrm{in}} = 1\,\mathrm{V}$ is the controlling input. A bias current

of $I_{out} = 1\,mA$ was output with $R_{ref} = 1\,k\Omega$, taking into account the load $R_{RTD} \sim 1.2\,k\Omega$. Besides, the MAX44242 OpAmps used have a DC open-loop gain typically of 145 dB, yielding a DC output impedance $\mathbf{Z_{out} = 5.93\,G\Omega}$.

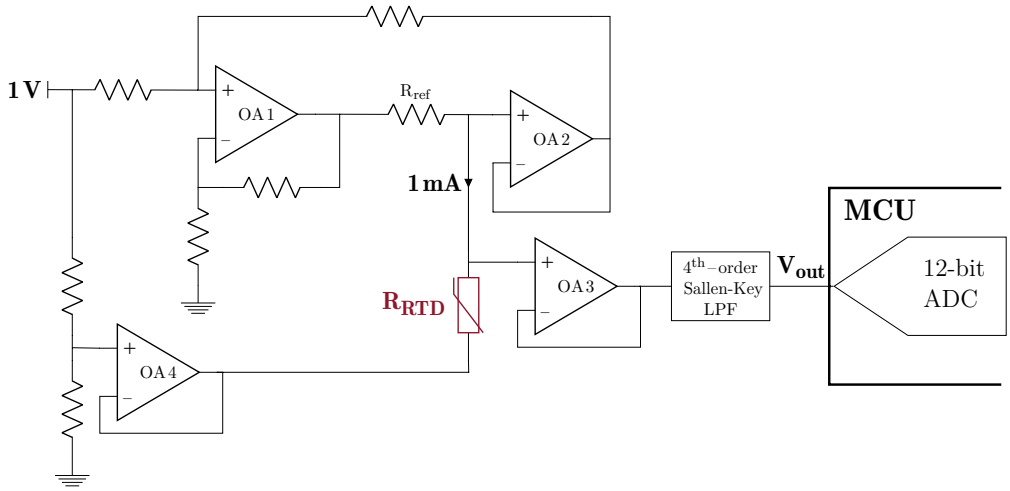

Figure 4.5 – Readout circuit for temperature sensing.

The complete RTD readout circuit is displayed in Fig. 4.5, where the improved Howland current pump is biasing the device with a DC polarization current 1 mA. The voltage across the thermistor is sensed by *OA3*, and a fourth-order Sallen-Key LPF with 1.37 Hz corner frequency is added to attenuate high-frequency noise.

4.3.3 Electrical characterization

This section presents the characterization of the readout circuitry of the front-end interface. First, a DC voltage between 0 mV and 540 mV was applied between the potentiometric channel input and the grounded-RE terminal. The output voltage was measured and plotted in Fig. 4.6.a. A voltage gain of 3.96 was obtained for the four channels, that corresponds to the gain of the amplification stage of the differential amplifier. An excellent linearity is observed, with an input range of $[20; 520]$ mV. An integrated input-referred voltage noise of 0.2286 mV was computed in the range [1 mHz; 1.4 Hz]. Besides, a resolution of 31.47 µV was achieved with the oversampling technique implemented.

Likewise, the resistance-to-voltage converter implemented for temperature measurement was characterized by sampling the output voltage while different high-precision value resistors ranging from 120 Ω to 1.9 kΩ were applied at the input of the readout circuit. The results are displayed in Fig. 4.6.b, showing a sensitivity of 1.0032 mV/Ω, and an excellent linearity with an input range of $[120; 1800]\,\Omega$. For both potentiometric and resistance readout, the results of the PSpice model simulations of the circuit blocks are displayed in Fig. 4.6, highlighting an excellent electrical behavior of the readout circuitry.

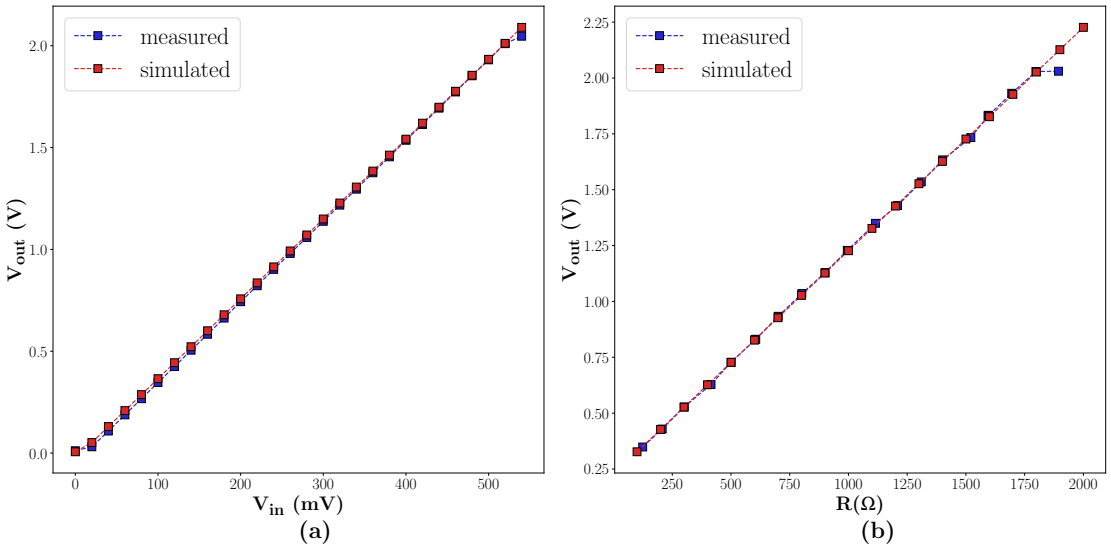

Figure 4.6 – Electrical characterization of analog front-end sensing channels: **(a)** potentiometric readout circuit for ion-sensing, **(b)** resistance readout circuit for temperature sensing.

As for BLE transactions, they were performed over Transparent UART GATT private service, emulating an end-to-end data pipe between the hardware front-end and the personal computer. Namely, in data transmission mode, the GATT client (personal computer) reads the values of the Transparent TX characteristic hosted by the GATT server (on-board RN40871 BLE), while during the configuration of the sensor panel, the GATT client performs a write operation on the Transparent RX characteristic. The specifications of BLE transactions are reported in Table 4.4. The connection interval and data throughput could be further optimized in order to reduce the power budget.

Table 4.4 – Specifications of BLE transactions

BLE packets	265 bytes
Connection interval	70 ms
Data throughput	2.65 kBps
RX/TX average current	2.86 mA

The power budget of the hardware front-end is shown in Fig. 4.7. In multi-sensing active mode, the average power consumed was of 135 mW, where 67% was absorbed by the analog circuitry, 26% was consumed by LDOs and the MCU, and 7% was owing to BLE transactions. With the 3.7 V and 2 Ah capacity lithium ion battery used, the front-end interface supports 54 h of continuous multi-sensing measurements, largely sufficient for remote physiology monitoring.

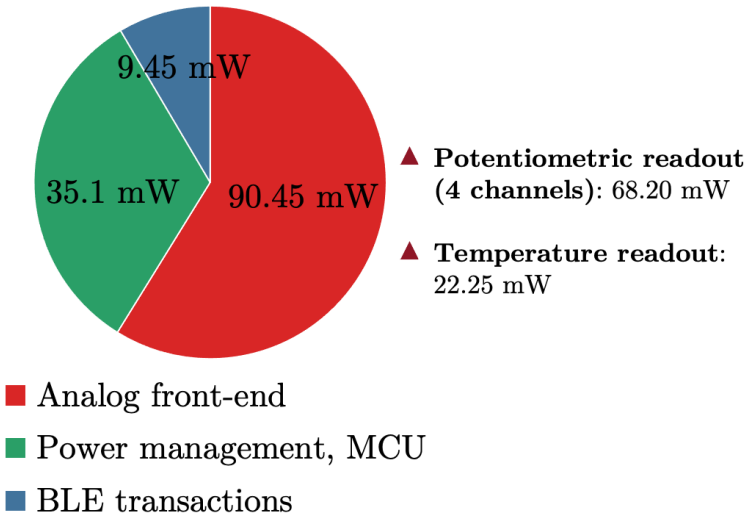

Figure 4.7 – Power budget of multi-ion-sensing front-end.

4.4 Electrochemical characterization

In this section, the results of the electrochemical characterization of the multi-channel ion-sensing interface with sodium, potassium, ammonium, and calcium solid-contact ISEs, built on SPEs, and on a fully-integrated polyimide platform are described. The characterization of the temperature readout circuit with the micro-fabricated platinum RTD is reported as well.

4.4.1 Solid-contact ISEs built on SPE substrates

First, the hardware front-end was characterized with solid-contact ISEs built on commercial SPEs. The latter technology is robust and enables an objective assessment of the sensing performances of the potentiometric readout circuit, by comparing the results obtained with an EMF6 Lawson Labs precision electrode interface. A double junction Ag/AgCl/KCl (3 M)/LiOAc (1 M) RE from Metrohm (Switzerland) was used.

Sensor calibration

Each ion-sensor was conditioned in a solution containing the target electrolyte at least 24 h before the measurement. The solid-contact ISEs were calibrated separately, in pure water samples, in order to assess their Nernstian sensitivity. Sensor calibrations were performed with target ion concentrations ranging from 10^{-9} M to $10^{-0.5}$ M, for sodium, potassium, ammonium, and calcium ions. Typical calibration curves acquired with the hardware front-end and the laboratory potentiometer are displayed in Fig. 4.8 for sodium-ISE. The calibration curves show flat OCP responses in diluted analyte,

and a detection regime where the sensor response increases with a Nernstian sensitivity (theoretically, 59.18 mV/decade and 29.59 mV/decade at 25 °C, for monovalent and divalent ions, respectively). The lower LOD is computed as the intersection of the two linear portions of the calibration curve. We notice that the upper LOD is not reached since the OCP responses do not lose sensitivity at high analyte concentration.

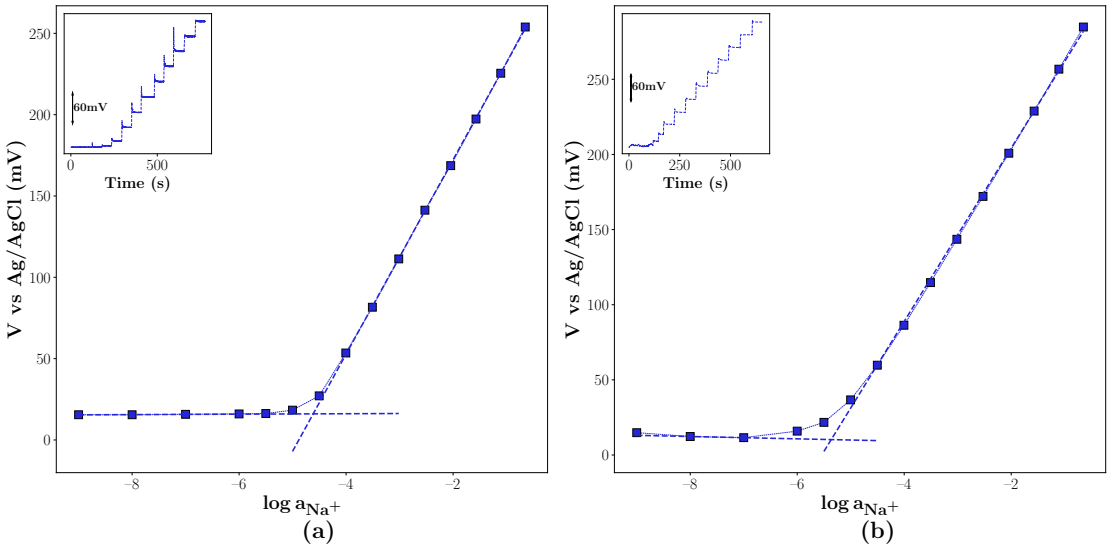

Figure 4.8 – Sodium-ISE calibration in a pure water sample performed **(a)** with the proposed hardware front-end, **(b)** with an EMF6 Lawson Labs potentiometer. The time traces acquired during measurements are displayed in the top left insight.

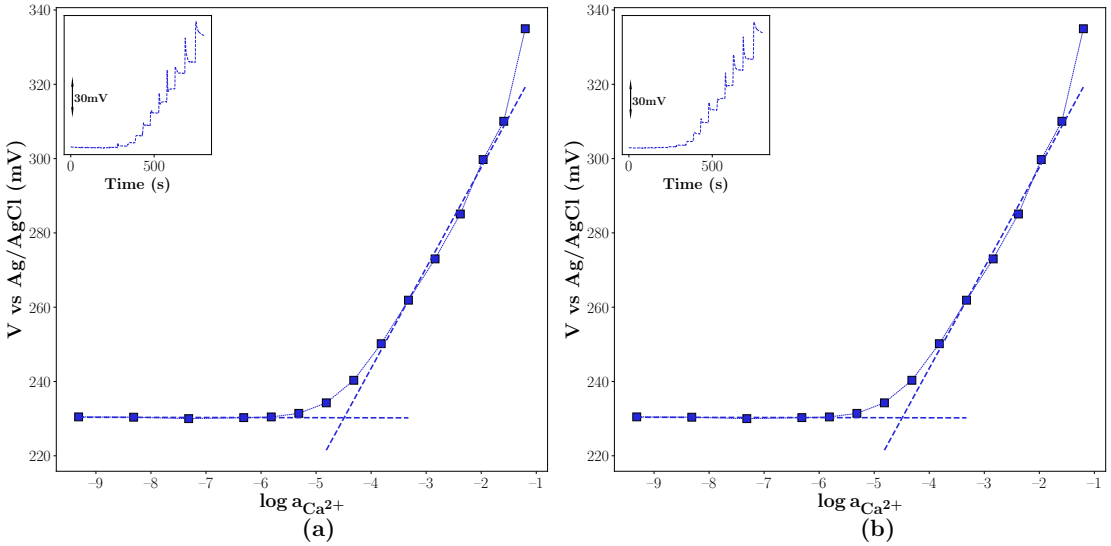

Figure 4.9 – Calcium-ISE calibration in an artificial sweat sample performed **(a)** with the proposed hardware front-end, **(b)** with an EMF6 Lawson Labs potentiometer. The time traces acquired during measurements are displayed in the top left insight.

Then, the solid-contact ISEs were calibrated in artificial sweat samples. Typical cali-

bration curves are displayed in Fig. 4.9 for calcium ion-sensors characterized with both hardware front-end and EMF6 potentiometer. Identical flat OCP response and Nernstian regime, as in pure water samples are obtained. Nevertheless, the electrolytes present in the artificial sweat sample add a large background offset potential that shifts the elbow of the calibration curve towards higher ion activity. In other terms, the background electrolytes considerably increase the sensor lower LOD.

The results of ion-sensor calibrations in pure water samples and artificial sweat, obtained with both hardware and EMF6 potentiometer, are summarized in Table 4.5, where five sensors were built for each type of ISE for statistical significance. We observe that all solid-contact ISEs exhibit Nernstian responses in both pure water and artificial sweat. Sensor sensitivity is slightly lower in artificial sweat background due to ion interference. Besides, the sensitivity obtained with the hardware front-end are comparable with the ones obtained with the high-precision EMF6 Lawson Labs potentiometer. The sensor lower LODs are reported as well, confirming the aforementioned observation that the interfering background electrolytes in artificial sweat shift the elbow of the calibration curves towards higher ion activity, thus worsening sensor LOD. Nevertheless, the lower LODs remain several factors of magnitude below the lower bound of range of interest of the target ions (see Table 4.1). Moreover, a slightly higher sensor LOD is measured with the hardware, compared to the EMF6 potentiometer. This is explained by the background potential noise induced by the front-end interface (cabling).

Table 4.5 – Calibration of sodium, potassium, ammonium, and calcium ions solid-contact ISEs in pure water and artificial sweat background

SC-ISE		**Sensitivity (mV/decade)**		**Limit of detection (μM)**	
		Hardware	**EMF6**[1]	**Hardware**	**EMF6**[1]
Na^+	Water	59.59 ± 0.21	59.69 ± 0.58	25.90 ± 3.19	7.23 ± 3.51
	AS[2]	59.75 ± 3.83	59.54 ± 2.89	382.20 ± 144.72	258.27 ± 50.75
K^+	Water	61.02 ± 3.32	60.55 ± 2.39	63.06 ± 12.95	58.44 ± 12.53
	AS[2]	57.70 ± 4.21	59.00 ± 3.24	119.47 ± 20.30	135.97 ± 40.24
NH_4^+	Water	62.22 ± 1.11	59.23 ± 1.02	5.09 ± 1.92	3.31 ± 2.30
	AS[2]	57.12 ± 0.42	54.74 ± 3.90	754.44 ± 311.94	537.94 ± 215.19
Ca^{2+}	Water	30.75 ± 0.90	29.39 ± 1.47	14.01 ± 10.21	4.15 ± 0.79
	AS[2]	28.35 ± 0.30	28.97 ± 0.47	46.08 ± 4.98	12.18 ± 2.04

[1] EMF6 Lawson Labs electrode interface [2] Artificial Sweat

Sensor selectivity

The selectivity coefficient $K_{I,J}^{pot}$ quantifies the selectivity of the ISE towards a target ion I with respect to an interfering ion J. It is usually comprised between 0 and 1, where $K_{I,J}^{pot} \rightarrow 0$ for highly-selective sensors. The extreme case $K_{I,J}^{pot} = 1$ is observed when the ISE can not distinguish ions I and J, and produces identical response in presence of both

electrolytes. The selectivity coefficients are determined experimentally, in pure water samples, with **SSM** and **FIM**.

First, SSM consists in separate ISE calibrations with samples containing a single ion at a time. The procedure described in [**?**] was carried out in order to achieve unbiased values. The solid-contact ISEs were conditioned 48 h beforehand, at 3 mM with the lowest interfering ion. Then, sensor calibrations were performed for each interfering ion in order of increasing interference. The ISE calibration order for each target ion is reported in Table 4.6. Eventually, a calibration with the target electrolyte was carried out.

Table 4.6 – ISE calibration order with SSM method

ISE	Interfering ions
Sodium-selective electrode	Mg^{2+} | Ca^{2+} | NH_4^+ | K^+
Potassium-selective electrode	Mg^{2+} | Ca^{2+} | Na^+ | NH_4^+
Ammonium-selective electrode	Mg^{2+} | Ca^{2+} | Na^+ | K^+
Calcium-selective electrode	NH_4^+ | K^+ | Na^+ | Mg^{2+}

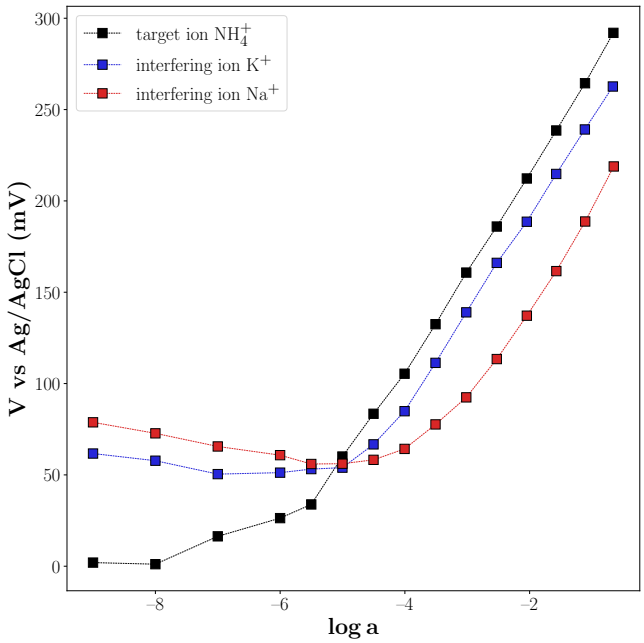

Figure 4.10 – Typical calibration curves with SSM method.

Typical calibration curves are displayed in Fig. 4.10, where the selectivity of an ammonium-selective electrode was characterized with respect to potassium and sodium interfering ions. The selectivity coefficients are extracted from the calibration curves, assuming that a Nernstian slope is observed for both target electrolyte and interfering ions. The selectivity coefficients are computed as

$$\log K_{I,J}^{pot} = \frac{z_I}{s}(E_J - E_I) + \log\left(\frac{a_I}{a_J^{z_I/z_J}}\right), \tag{4.7}$$

where s is the sensitivity of the ISE, and the potentials E_I and E_J are excerpted at an activity a_I and a_J in the Nernstian portion of the curves. The calibration curves were extrapolated to $a_I = 1$ and $a_J = 1$, yielding $\log K_{I,J}^{pot} = \frac{z_I}{s}(E_J - E_I)$. As a result, the OCP difference observed between two calibration curves, in their Nernstian range, indicates the selectivity of the sensor towards the interfering ion, where a small potential gap is obtained for a poorly-selective sensor. As a matter of fact, the developed ammonium-ISEs were poorly selective with respect to potassium ions, with selectivity $\log K_{NH_4^+,K^+}^{pot} = -1.00 \pm 0.20$, and better selectivity for sodium ions, $\log K_{NH_4^+,Na^+}^{pot} = -3.15 \pm 0.15$.

The results obtained with SSM might not always be consistent and depend on sensor potential stability. Indeed, coefficients $K_{I,J}^{pot} > 1$ where computed when the calibration curve obtained with the interfering ion exhibits OCP offset larger than with the primary ion. Therefore, FIM method was carried out for a comprehensive selectivity study. It consists in sensor calibration in presence of an interfering electrolyte at a known constant activity in the sample. If the resulting calibration curve is Nernstian, the selectivity coefficient is computed as

$$K_{I,J}^{pot} = \frac{a_I(LOD)}{a_J^{z_I/z_J}}, \tag{4.8}$$

where $a_I(LOD)$ is the lower LOD extracted from the calibration curve in presence of the interfering ion at the activity a_J. The computed selectivity coefficients for sodium, potassium, ammonium, and calcium-ISEs, with both SSM and FIM are reported in Table 4.7, where values obtained in literature are shown for comparison. We observe consistent results where monovalent cation ISEs are more selective towards divalent cations, with both SSM and FIM methods, and vice-versa. Besides, we notice that the developed potassium ion-sensors are poorly-selective towards sodium and ammonium ions. The selectivity coefficients obtained with SSM method are generally more optimistic, but also less reliable than FIM, since the calibration curves with the interfering ions were not always thoroughly Nernstian. However, the latter is a necessary condition to extract correct values. Therefore, the selectivity coefficients measured with FIM will be used in the sequel of this thesis.

Table 4.7 – Selectivity coefficients of the developed ISEs with SSM and FIM methods

	$\log K^{pot}_{I,J}$					Ref.
I \ J	Na^+	K^+	NH_4^+	Ca^{2+}	Mg^{2+}	
Na^+	–	-2.14 ± 0.2	-2.46 ± 0.33	-2.42 ± 0.75	-3.21 ± 0.36	
	–	-2.29	n.a.	-3.39	-4.32	[?]
	–	-2.91 ± 0.06	-4.20 ± 0.23	-4.23 ± 0.91	-2.82 ± 0.39	
	–	-4.74	-4.76	-3.23	-3.35	[?]
K^+	-0.66 ± 0.04	–	-0.28 ± 0.10	-2.53 ± 0.11	-2.93 ± 0.29	
	-4.1	–	n.a.	-5.7	n.a.	[?]
	-0.38 ± 0.27	–	n.a.	n.a.	-2.52 ± 0.30	
	-4.67	–	-2.00	-6.70	-7.84	[?]
NH_4^+	-1.79 ± 0.13	-1.37 ± 0.28	–	-2.99 ± 0.61	-3.15 ± 0.26	
	-3.11	-1.48	–	n.a.	n.a.	[?]
	-3.15 ± 0.15	-1.00 ± 0.20	–	-4.46 ± 0.55	-4.08 ± 0.47	
	-2.42	-1.41	–	n.a.	n.a.	[?]
Ca^{2+}	-2.77 ± 0.12	-2.87 ± 0.56	-3.03 ± 0.04	–	-1.94 ± 0.56	
	n.a.	n.a.	n.a.	–	n.a.	
	-7.30 ± 1.02	-5.44 ± 0.95	-7.47 ± 0.46	–	-5.50 ± 1.20	
	-5.9	-7.5	n.a.	–	-4.4	[?]

FIM (this work) – FIM (literature) – SSM (this work) – SSM (literature)

Sensor stability

Sensor response stability and reversibility was assessed in [?], where current reversal chronopotentiometry experiments were carried out with a lithium-ISE functionalized with and without platinum nanostructures. Potential drifts of $3 \cdot 10^{-2} \pm 2 \cdot 10^{-2}\,\mathrm{mV \cdot s^{-1}}$ and $1.80 \pm 0.29\,\mathrm{mV \cdot s^{-1}}$ were obtained respectively, highlighting the impact of platinum nanostructures on increasing sensor response stability and reversibility. Sensor stability was assessed also when no potential was applied, resulting in a stable potential response over 2 h of OCP measurement.

4.4.2 Fully-integrated sensing platform

After validating the functionality of the potentiometric readout channels, the hardware front-end was then characterized with a fully-integrated sensing platform manufactured on a flexible polyimide substrate. A thin rigid support was attached at the back of the sensing platform to facilitate its interfacing to the flat-flex type edge connector of the hardware front-end.

All-solid-state reference electrode

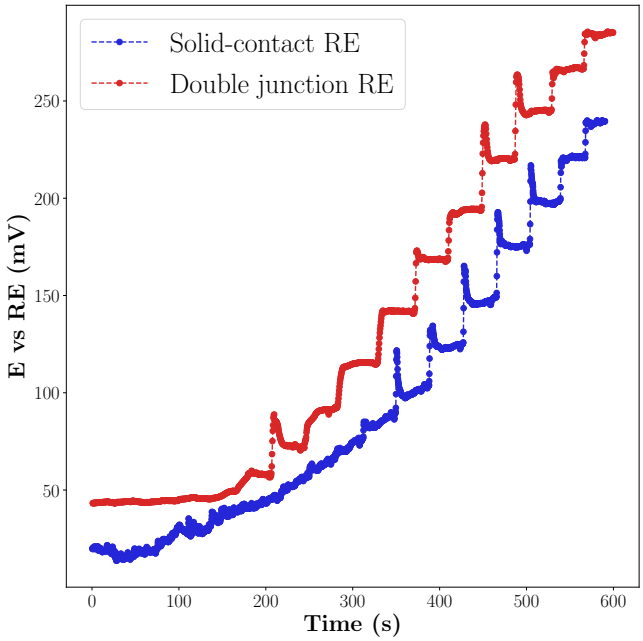

Figure 4.11 – Calibration time traces of potassium-ISE built on a SPE against an all-solid-state RE and a double junction RE, in a pure water sample.

A stable RE is paramount to ensure accurate measurements since the acquired OCP depends on the potentials at each interface of the electrochemical cell (see Fig. 2.5). A Ag/AgCl RE was obtained by chlorinating the micro-fabricated silver electrode. Then, an ionic liquid-doped PVC membrane was coated on top of the RE in order to increase potential stability, as described in Section 4.2.2. The produced Ag/AgCl RE was characterized by a calibration in a pure water sample, with a potassium-ISE built on a SPE substrate. The sensor calibration was done against a double junction Ag/AgCl RE as well for comparison. The calibration time traces are displayed in Fig. 4.11. The all-solid-state RE exhibits potential drift and noise at lower concentration compared to the double junction RE. Nevertheless, potential steps of similar values are observed at higher concentration, in the Nernstian regime of the potassium-ISE.

Potassium ion-sensor calibration

Next, the solid-contact ISEs built on the fully-integrated platform were characterized with the hardware front-end. Potassium-ISEs were fabricated with a similar functionalization procedure as with SPEs, and the measurements were carried out against the all-solid state RE. The calibration curves obtained in a pure water sample, with both hardware front-end and EMF6 Lawson Labs precision electrode interface are shown in Fig. 4.12. A relatively flat, but with some OCP response drift, is observed at diluted analyte concentration, and a sub-Nernstian regime is highlighted beyond the sensor LOD. The

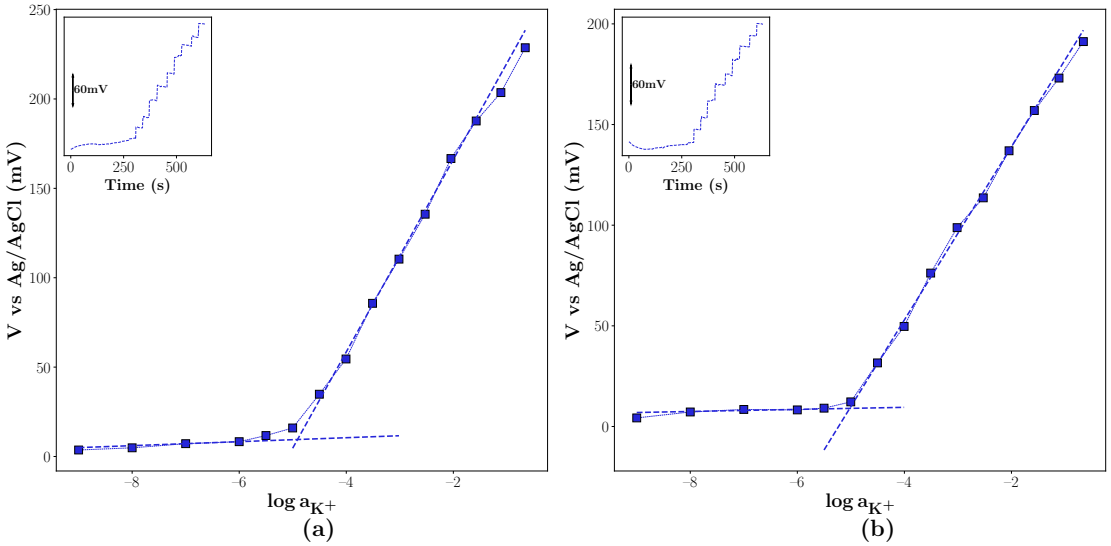

Figure 4.12 – Fully-integrated potassium-ISE calibration in pure water sample performed **(a)** with the proposed hardware front-end, **(b)** with an EMF6 Lawson Labs potentiometer. The time traces acquired during measurements are displayed in the top left insight.

Table 4.8 – Calibration of potassium solid-contact ISEs built on SPE and flexible substrate, in pure water sample

SC-ISE	**Sensitivity (mV/decade)**		**Limit of detection (μM)**	
	Hardware	**EMF6**[1]	**Hardware**	**EMF6**[1]
built on SPE substrate	61.02 ± 3.32	60.55 ± 2.39	63.06 ± 12.95	58.44 ± 12.53
built on flexible substrate	53.82 ± 2.52	53.04 ± 2.59	12.28 ± 2.50	9.53 ± 2.37

[1] EMF6 Lawson Labs electrode interface

results of the calibration of potassium-ISEs built on a SPE and on a flexible substrate are reported in Table 4.8. The ion-sensors built on the flexible substrate exhibit sub-Nernstian slopes of 53 mV/decade with both hardware and laboratory potentiometer. This is lower than the sensitivity obtained in [**?**], where the sensing platform has been optimized by placing electrode wells to avoid the spreading of the ISM when the latter was drop-cast on top of the electrode. Besides, we note that the Nernstian sensitivity achieved with SPEs outperforms the sensitivity of ion-sensors built on micro-fabricated flexible platforms since SPE technology is more robust. The larger sensor lower LOD observed with SPEs is due to sensor conditioning at 10 mM. Namely, a conditioning at lower concentration (typically 1 mM) usually yields lower LODs.

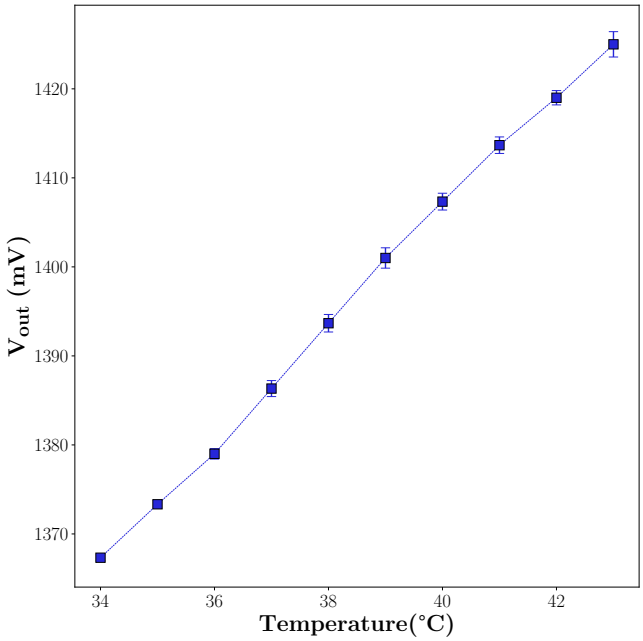

Figure 4.13 – Resistive thermal device calibration with the hardware front-end.

Integrated temperature sensor

Furthermore, the RTD sensors were characterized with the hardware front-end. The sensors patterned on the flexible polyimide substrate were directly interfaced to the edge connector of the hardware, thus, reducing contact resistances. Then, the flexible platform was placed on top of a hotplate, and the output voltage of the temperature readout circuit was acquired at each temperature step increase. The temperature was controlled by a VWR® Professional Hotplate in the range $[34; 43]$°C. The calibration curve is displayed in Fig. 4.13, exhibiting a sensitivity of $6.56\,\text{mV}/°\text{C}$, and an excellent linearity ($R^2 = 0.9983$, RMSE $= 0.7719\,\text{mV}$). Therefore, the readout circuit was correctly designed, around the operating point of the RTD, theoretically at $1.2\,\text{k}\Omega$.

4.5 Summary and main contributions

In this chapter, the design of a multi-ion-sensing front-end aiming at remote monitoring of relevant electrolytes for physiology is presented. This work addresses physical activity practice, sport applications, and medical care for persons suffering from physiological dysfunctions. The main contributions are summarized hereunder.

- An **electronic front-end interface** was designed, enabling a continuous and concurrent monitoring of four target electrolytes through separate potentiometric readout channels. Besides, in situ temperature is essential for sensor calibration. Thus, the front-end circuit includes a resistance-to-voltage converter, where an

improved Howland current source with a boosted output impedance is biasing the RTD with a stable DC current of 1 mA. The readout circuits exhibit excellent linearity and sensitivity in the dynamic range of the sensors. Namely, for OCPs in $[20; 520]$ mV, and for an RTD featuring a nominal value of 1.2 kΩ at body temperature. The dimensions of the hardware, its wireless connectivity through a BLE module, and its power budget enable a seamless integration into wearable systems for on-body measurements through biological fluids such as sweat.

- A **multi-ion-sensing array** was fabricated on commercial SPEs to demonstrate the ability of the electronic front-end to monitor typical ions constituting sweat samples. Sodium, potassium, ammonium, and calcium-ISEs were fabricated and successfully characterized in terms of sensitivity, selectivity, and LOD, in pure water and artificial sweat samples. Measurements were performed with both proposed hardware and a high-precision laboratory potentiometer, showing comparable results, with slightly higher background potential noise and LODs with the custom electronic front-end.

- The proposed hardware was characterized with a **flexible fully-integrated multi-sensing platform**, where solid-contact ISEs and all-solid-state RE were built for integrated measurements. The hardware was successfully validated through potassium ions calibration, and for in situ temperature measurements with the micro-fabricated RTD.

The proposed multi-ion-sensing front-end addresses the lack of multi-sensing capabilities in current ion-sensing platforms developed for biomedical applications. Moreover, it provides the sensing interface for an electronic tongue system performing a multivariate analysis of complex samples such as sweat, where ion interference significantly distorts sensor response.

5 Ion interference modeling in multi-ion-sensing

Multi-ion-sensing in complex samples is hindered by ion interference that considerably affect sensor responses, hence reducing sensing performance. Therefore, this chapter is dedicated to the modeling of ion interference in multi-electrolyte samples such as artificial sweat. A compact model of the transduction mechanism through polymeric ISEs is derived and implemented at the core of an ion-sensing emulator. The latter provides both qualitative and quantitative interpretation of ion interference in mixed-ion samples. Moreover, the ion-sensing model is used to generate emulated synthetic datasets that will be used to train and optimize non-linear multivariate calibration models.

5.1 Motivation

Ion-sensors are ubiquitous in many fields, leveraging progress in all-solid-state sensing and technology to perform measurements on real samples [**?**]. Namely, they are widely used for monitoring pollutants in environmental applications [**?**], for agricultural soil analysis [**?**], for water quality control [**?**], or for biomedical applications like physiology and healthcare monitoring [**?**, **?**]. Ion-sensors usually consist in ISEs coated with a polymeric selective membrane that entraps exclusively the target electrolyte. Latest research is driven towards the improvement of sensing technology and transduction mechanisms [**?**], but ion-sensing performance is hampered by ion interference, mostly in complex samples, where intrinsic selectivity bounds are reached [**?**]. Indeed, interference arises from the electrolytes inherently constituting the sample, that are hindering the selective detection of the analyte. The effect is even more severe when the concentration of the interfering molecule is much higher than the target ion. For example, this is the case of the detection of trace of toxic heavy metals such as lead or arsenic in sweat (µM concentration) [**?**]. The sensor lower LOD is strongly deteriorated by the interfering ions, and the ion-monitoring accuracy is degraded if the sensor LOD is of the same order of magnitude as the concentration of the analyte. Besides, the concentration of the interfering ions could vary in a non-predictable way in the sample, making the

management of this phenomenon even more intricate.

The coupling of low-selective ion-sensing arrays and advanced chemometric tools has been implemented for the analysis of the multivariate sensor response in electronic tongue systems [**?**]. Several works has been reported in literature, involving ANN architectures for the simultaneous determination of multiple analytes in synthetic and/or real samples [**?**,**?**,**?**,**?**,**?**,**?**,**?**,**?**,**?**]. The prediction capability of such data-driven models depends on the quality and representativeness of the training dataset. Unfortunately, the acquisition of big data is time and resource consuming in practice, entailing high labor costs of chemical assays. Indeed, the datasets in the cited works count from 15 up to 100 samples only, that is restrictive for achieving good generalization performance. Some approaches have been proposed to cope with this dataset scarcity, and have been discussed in Section 2.3.3.

In this thesis, an analytical modeling of the multivariate response from polymeric ISEs is implemented, first, to get a thorough understanding of the parameters influencing ion interference, and then to automatically generate emulated multi-ion-sensor responses in complex mixed-ion samples such as artificial sweat.

5.2 Modeling polymeric ion-selective electrodes

In potentiometric measurements, the OCP signal observed between an ISE selective for a primary ion I against a RE is

$$E_I(a_I(aq)) = K_{cell} + E_{PB}(a_I(aq)), \tag{5.1}$$

where K_{cell} accounts for all potential drops at the interfaces of the electrochemical cell (metal electrode contacts, liquid junction potential of the RE), that should be independent of sample composition. E_{PB} is the potential built up at the sample/ISM interface when the target electrolyte is entrapped by the polymeric membrane. Ion activity a_I describes the ability of the analyte I to interact with other ions, and is related to its concentration in the sample by the activity coefficient γ_I, as discussed in Section 2.1.2. In the sequel of this chapter, the target ion activity in the sample $a_I(aq)$ refers to the chemical property of interest in ion-sensor modeling. ISE responses are usually described by the following semi-empirical Nicolsky-Eisenman equation, extended from Nernst equation,

$$E_{PB} = E_I^0 + \frac{s}{z_I} \log \left(a_I(aq) + \sum_{j \neq I} K_{I,j}^{pot} a_j(aq)^{\frac{z_I}{z_j}} \right) [**?**], \tag{5.2}$$

where E_I^0 is an apparent standard potential depending on the ISM properties, $s = \ln 10 \cdot \frac{RT}{F}$ is the Nernst slope, $K_{I,j}^{pot}$ is the sensor selectivity coefficient towards any ion j in the sample, and z is the ion valence. ISE responses have been mostly explained with the Nicolsky-Eisenman formalism [**?**], but (5.2) is not very accurate when ions of different charges are present in the sample. Indeed, large deviations from experimental data were observed in mixed-ion samples [**?**]. Therefore, the phase-boundary potential model, or so-called Nicolsky-Bakker model, is used to explain the response of polymeric ISEs in complex ion mixtures. A comprehensive description of the model was presented in [**?**, **?**]. The hereunder analytical derivation is carried out to get a compact ion-sensing model, highlighting the key parameters accounting for sensor output distortion due to ion interference.

5.2.1 Phase-boundary potential

The phase-boundary potential model is based on ion-exchange considerations at the sample/ISM interface, neglecting transmembrane ion fluxes (assuming zero current ion distribution). The electrochemical potential of any ion j in either membrane or solution phase is

$$\overline{\mu_j}(\text{phase}) = \mu_j^0(\text{phase}) + RT \ln a_j(\text{phase}) + z_j F \Phi(\text{phase}), \tag{5.3}$$

where μ_j^0 is the standard chemical potential, and Φ is the electrical potential. At electrochemical equilibrium, there is an ion partition equilibrium between both membrane and sample phase, leading to $\overline{\mu_j}(m) = \overline{\mu_j}(aq)$. An electrical potential is built up to counter-balance the ion fluxes resulting from the concentration gradient of the ion j from the solution to the ISM, thus ensuring the membrane electroneutrality, yielding

$$E_{PB} = \Phi(m) - \Phi(aq) = \frac{\mu_j^0(aq) - \mu_j^0(m)}{z_j F} + \frac{RT}{z_j F} \ln \left(\frac{a_j(aq)}{a_j(m)} \right). \tag{5.4}$$

The standard potential is defined as $\varepsilon_j^0 = \frac{\mu_j^0(aq) - \mu_j^0(m)}{z_j F}$. If we assume that $a_j(m)$ is constant and independent of sample composition, a Nernstian sensor response is obtained

$$E_{PB} = E_j^0 + \frac{s}{z_j} \log \left(a_j(aq) \right), \tag{5.5}$$

where the apparent standard potential E_j^0 includes the standard potential ε_j^0 and $a_j(m)$. The role of sensor conditioning (ISE exposed to the target electrolyte for an extended time) prior to any measurement is crucial to maintain the activity of the free ions in the membrane constant.

5.2.2 Ion-exchanges at the phase-boundary

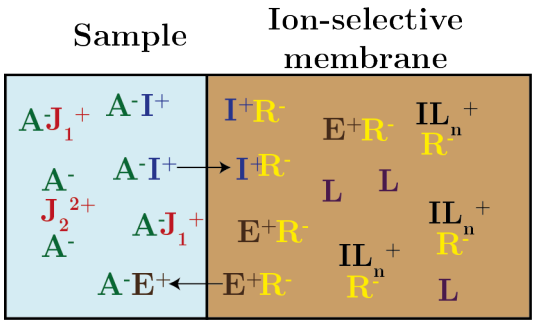

Figure 5.1 – Ion-exchange equilibrium at the sample/ISM interface: I^+ is the target ion and A^- is its counter ion, while J_1^+ and J_2^{2+} are interfering ions. The ISM contains the neutral ionophore L, complex IL_n^+ formed by entrapment of the primary ion, free ions I^+, the ion-exchanger R^- and its counter ion E^+.

The ion-exchanges at the sample/ISM phase-boundary are pictured in Fig. 5.1, for a monovalent cation I^+, where the interfering ions J_1^+ and J_2^{2+} are not interacting with the ISM. Let us consider a general case where the ISM phase comprises the **ionophore** L (valence z_L). It is a lipophilic compound that selectively binds to the primary ion, forming complexes IL_n (n is the complex stoichiometry), following

$$I(m) + nL(m) \xrightarrow{\beta_n} IL_n(m)\,, \tag{5.6}$$

where $\beta_n = \frac{a_{IL_n}(m)}{a_L(m)^n \cdot a_I(m)}$ is the complex formation constant. The electroneutrality of the ISM is ensured by an **ion-exchanger** R (valence z_R) that is the counter ion of the formed complex. The ionophore and ion-exchanger are lipophilic compounds so that they could be retained in the hydrophobic membrane phase. Besides, during the primary ion detection, the hydrophilic counter ion of the ion-exchanger, E (valence z_E), is transferred to the sample phase. Lastly, the membrane contains free ions I (valence z_I). As a result, the electroneutrality of the ISM imposes the charge balance

$$z_L c_L(m) + \sum_n (nz_L + z_I) c_{IL_n}(m) + z_I c_I(m) + z_R c_R(m) = 0\,, \tag{5.7}$$

where c refers the concentration of each respective compound.

5.2.3 Selectivity coefficient

A paramount parameter in ion-sensor modeling is the selectivity coefficient of the polymeric ISM. It indicates the ability of the membrane to be permeable to the target ion and impermeable to interfering ions. If we assume a Nernstian sensor response caused by the interfering ion J solely in the sample, the measured cell potential is obtained leveraging (5.1) and (5.5),

$$\mathrm{E} = \mathrm{K_{cell}} + \mathrm{E_J^0} + \frac{\mathrm{s}}{\mathrm{z_J}} \log \left(\mathrm{a_J(aq)} \right). \tag{5.8}$$

Besides, the Nicolsky-Eisenman equation (5.2) provides

$$\mathrm{E} = \mathrm{K_{cell}} + \mathrm{E_I^0} + \frac{\mathrm{s}}{\mathrm{z_I}} \log \left(\mathrm{K_{I,J}^{pot}} \mathrm{a_J^{\frac{z_I}{z_J}}(aq)} \right), \tag{5.9}$$

that introduces the selectivity coefficient. By subtracting (5.8) and (5.9),

$$\mathbf{\log\, K_{I,J}^{pot} = \frac{z_I}{s}(E_J^0 - E_I^0)}, \tag{5.10}$$

which allows us to compute the selectivity coefficient with apparent Nernstian standard potentials.

5.2.4 Ion-selective electrode response in mixed-ion samples

With the aforementioned equations, we can compute the phase-boundary potential in complex samples containing ions of different charges, and taking into account ion interference. We will restrict the analysis to monovalent and divalent cations, but the approach could be generalized for trivalent ions or anions.

First, the ISM electroneutrality condition from (5.7) is generalized for any ion j (z_j, c_j), an ionophore L (z_L, c_L), and an ion-exchanger R (z_R, c_R). Ion activity and complex formation constant β_n are inserted as well, yielding

$$\mathrm{z_R c_R} + \mathrm{z_L} \frac{\mathrm{a_L}}{\gamma_\mathrm{L}} + \mathrm{z_j} \frac{\mathrm{a_j(m)}}{\gamma_\mathrm{j}(\mathrm{m})} \left(1 + \sum_\mathrm{n} \frac{\mathrm{n z_L} + \mathrm{z_j}}{\mathrm{z_j}} \frac{\gamma_\mathrm{j}(\mathrm{m})}{\gamma_{\mathrm{jL_n}}} \beta_\mathrm{n} \mathrm{a_L^n} \right) = 0\,. \tag{5.11}$$

The labels (m) has been dropped for clarity, except for ion I that is present in both membrane and aqueous phase. Then, let us consider that multiple ions from the sample

phase, including interfering ions, could interact with the ISM. It is assumed that the activity of the uncomplexed ionophore and the activity coefficient of the extracted ions remain unaltered during ion-exchanges. This is valid for an ISM with an ionophore in excess with respect to the ion-exchanger, and considering that the membrane ionic strength is not changing during ion-exchange. Equation (5.11) is summed over the ions exchanged at the phase-boundary, yielding

$$\sum_{j} z_j \frac{a_j(m)}{\gamma_j(m)} \left(1 + \sum_{n} \frac{n z_L + z_j}{z_j} \frac{\gamma_j(m)}{\gamma_{jL_n}} \beta_n a_L^n\right) = -z_R c_R - z_L \frac{a_L}{\gamma_L} \,. \tag{5.12}$$

The apparent standard potential E_j^0 is by definition from (5.5), $E_j^0 = \varepsilon_j^0 + \frac{s}{z_j} \log\left(\frac{1}{a_j(m)}\right)$. It is substituting $a_j(m)$ in (5.12), giving

$$z_j \frac{k_j}{\gamma_j(m)} \left(1 + \sum_{n} \frac{n z_L + z_j}{z_j} \frac{\gamma_j(m)}{\gamma_{jL_n}} \beta_n a_L^n\right) 10^{-z_j E_j^0/s} = -z_R c_R - z_L \frac{a_L}{\gamma_L} \,, \tag{5.13}$$

where the free energy of ion transfer is defined as $\varepsilon_j^0 = \frac{s}{z_j} \log(k_j)$. Moreover, $a_j(m)$ is extracted from (5.4), and substituted in (5.12), yielding

$$\sum_{j} z_j \frac{k_j}{\gamma_j(m)} \left(1 + \sum_{n} \frac{n z_L + z_j}{z_j} \frac{\gamma_j(m)}{\gamma_{jL_n}} \beta_n a_L^n\right) 10^{-z_j E_{PB}/s} a_j(aq) = -z_R c_R - z_L \frac{a_L}{\gamma_L} \,. \tag{5.14}$$

By subtracting (5.13) and (5.14), one finds

$$10^{-z_j E_{PB}/s} \sum_{j} a_j(aq) 10^{z_j E_j^0/s} = 1 \,. \tag{5.15}$$

Furthermore, the selectivity coefficient in (5.10) is inserted in (5.15), providing the compact expression

$$10^{z_I(E_I^0-E_{PB})/s}a_I(aq) + 10^{(E_I^0-E_{PB})/s}\sum_{j\ \text{s.t.}\ z_j=1}(K_{I,j}^{pot})^{\frac{1}{z_I}}a_j(aq) + 10^{2(E_I^0-E_{PB})/s}\sum_{j\ \text{s.t.}\ z_j=2}(K_{I,j}^{pot})^{\frac{2}{z_I}}a_j(aq) = 1\,, \quad (5.16)$$

where each term corresponds to the contribution in the sensor response from the primary ions, the monovalent interfering ions, and the divalent interfering ions, respectively. Equation (5.16) is solved for E_{PB}, with a second-order polynomial equation, with the unknown $X = 10^{(E_{PB}-E_I^0)/s}$. The cases where $z_I = 1$, and $z_I = 2$, are treated separately, and the positive roots in both equations are

$$\mathbf{E_{PB}} = E_I^0 + s\log\left(\frac{1}{2}\left(\mathbf{a_I(aq)} + \sum_{j\ \text{s.t.}\ z_j=1}K_{I,j}^{pot}a_j(aq)\right) + \sqrt{\frac{1}{4}\left(\mathbf{a_I(aq)} + \sum_{j\ \text{s.t.}\ z_j=1}K_{I,j}^{pot}a_j(aq)\right)^2 + \sum_{j\ \text{s.t.}\ z_j=2}(K_{I,j}^{pot})^2a_j(aq)}\right), \quad (5.17)$$

$$\mathbf{E_{PB}} = E_I^0 + s\log\left(\frac{1}{2}\sum_{j\ \text{s.t.}\ z_j=1}(K_{I,j}^{pot})^{\frac{1}{2}}a_j(aq) + \sqrt{\frac{1}{4}\left(\sum_{j\ \text{s.t.}\ z_j=1}(K_{I,j}^{pot})^{\frac{1}{2}}a_j(aq)\right)^2 + \mathbf{a_I(aq)} + \sum_{j\ \text{s.t.}\ z_j=2}K_{I,j}^{pot}a_j(aq)}\right), \quad (5.18)$$

for $z_I = 1$, and $z_I = 2$, respectively. If we establish by convention $K_{I,I}^{pot} = 1$, then (5.17) and (5.18) could be merged in

$$E_{PB} = E_I^0 + s\log\left(\frac{1}{2}\sum_{j\ \text{s.t.}\ z_j=1}(K_{I,j}^{pot})^{\frac{1}{z_I}}a_j(aq) + \sqrt{\left(\frac{1}{2}\sum_{j\ \text{s.t.}\ z_j=1}(K_{I,j}^{pot})^{\frac{1}{z_I}}a_j(aq)\right)^2 + \sum_{j\ \text{s.t.}\ z_j=2}(K_{I,j}^{pot})^{\frac{2}{z_I}}a_j(aq)}\right). \quad (5.19)$$

5.3 Design of an ion-sensing emulator

The sensing model of polymeric ISEs previously described was then implemented to emulate ion-sensor responses in different sample compositions. An ion-sensing emulator was built in order to get a qualitative and quantitative estimation of the effect of sensor parameters on the distortion of calibration curves subject to ion interference. The accuracy of the emulator was assessed by comparing simulated sensor responses to experimental curves.

5.3.1 Compact ion-sensing model

A compact formulation of the response of a polymeric ISE could be written as

$$\mathrm{E_I} = \mathrm{K_{cell}} + \mathrm{E_I^0} + \mathrm{s}\log\Big(\mathrm{f}(\mathrm{a_I}, \{(\mathrm{a_{J_1}}, \mathrm{K_{I,J_1}^{pot}}), \cdots, (\mathrm{a_{J_l}}, \mathrm{K_{I,J_l}^{pot}})\}_{\mathrm{z_J}=1}, \{(\mathrm{a_{J_1}}, \mathrm{K_{I,J_1}^{pot}}), \cdots, (\mathrm{a_{J_m}}, \mathrm{K_{I,J_m}^{pot}})\}_{\mathrm{z_J}=2}) + \mathrm{lod}\Big), \quad (5.20)$$

where the model parameters are:

- $\mathbf{K_{cell}}$: it accounts for the potential drops at each interface of the two-electrodes electrochemical cell (metal contacts, RE junction potential). It is assumed to be constant and independent of sample composition.
- $\mathbf{E_I^0}$: the apparent standard potential is formally defined as $\mathrm{E_I^0} = \varepsilon_\mathrm{I}^0 + \frac{\mathrm{s}}{\mathrm{z_I}}\log\left(\frac{1}{\mathrm{a_I(m)}}\right)$. It mainly depends on the properties of the analyte (standard potential), and on the activity of the primary ion in the membrane. The latter is assumed to be large, constant, and independent of sample composition, by performing sensor conditioning prior to the measurement.
- **s**: the sensor sensitivity depends on in situ temperature, and is a parameter assessing sensing performance of the ion-sensor. It is set to 59.16 mV/decade by default. The latter is the theoretical Nernstian sensitivity at room temperature (25 °C).
- **f**: it is a non-linear function depending on sample composition (activity of ions constituting the sample), and on the selectivity coefficient of each ion towards the primary ion, considering monovalent and divalent electrolytes. $\mathrm{K_{I,j}^{pot}}$ could be seen as weight factors of the activity $\mathrm{a_j(aq)}$ that are summed.
- **lod**: it is a parameter accounting for the non-linear distortion observed in pure water samples. It is approximated to the sensor lower LOD. It is set to zero by

default.

5.3.2 Ion-sensing emulator

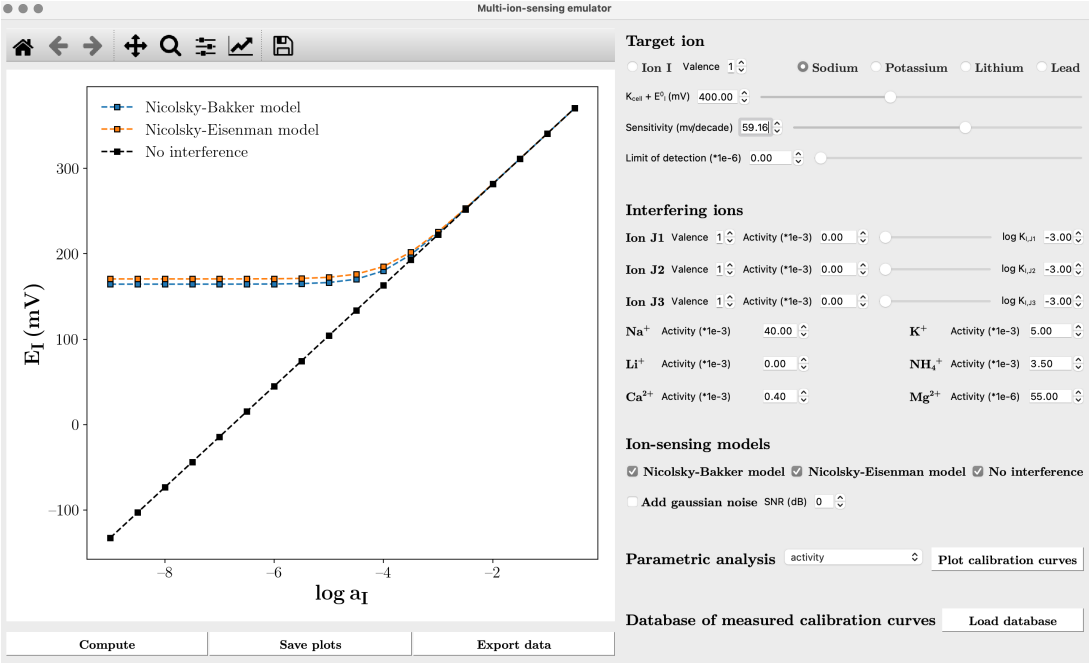

Figure 5.2 – Ion-sensing emulator implemented on a GUI.

The compact ion-sensing model was then implemented at the core of an emulator of calibration curves for which the model parameters were extracted from experimental calibration curves. A GUI was built in PyQt5 [**?**], and the user interface is displayed in Fig. 5.2. The main features of the GUI are detailed hereunder:

- **Target ion**: I ∈ {sodium, potassium, lithium, lead} is selected. These electrolytes are typical analytes in physiology and healthcare monitoring (see Section 5.4.1). Besides, monovalent or divalent ion I can be selected for a standard ion-sensing simulation.
- $\mathbf{K_{cell} + E_I^0}$ is modeled as an offset potential. It is fitted from experimental data.
- **Sensitivity**: is extracted from experimental calibration curves. It corresponds to the Nernst slope s.
- **Limit of detection**: is extracted from experimental calibration curves.
- **Interfering ions**: multi-ion sensing in artificial sweat involves sodium, potassium, lithium, ammonium, calcium, and magnesium ions as main electrolytes. The physiological activity of these ions in sweat are used by default. The cross-selectivity coefficients are obtained from FIM characterization of platinum-nanostructured

ISEs for sodium, potassium, lithium, and lead ions. The coefficients are reported in Table 5.1. For standard simulation with target ion I, ions J_1, J_2, J_3, with selectable valence, activity, and selectivity coefficient, are the interfering electrolytes.

Table 5.1 – Selectivity coefficients of platinum-nanostructured solid-contact ISEs obtained from fixed-interference method

	$\log K^{pot}_{I,J}$					
I \ J	Na^+	K^+	Li^+	NH_4^+	Ca^{2+}	Mg^{2+}
Na^+	–	-2.2	-2.58	-1.89	-2.57	-3.56
K^+	-1.8	–	-1.91	-1.68	-4.6	-3.32
Li^+	-2.55	-2.56	–	-3.08	-4.01	n.a.
Pb^{2+}	-2.89	-1.64	-2.9	-2.76	-4.28	-3.76

- **Ion-sensing models**: Nicolsky-Bakker and Nicolsky-Eisenman models are available to simulate ISE responses with the ion mixture designed. The compact phase-boundary potential model was used by default, unless otherwise stated. The ideal full-Nernstian response can be plotted to visualize the amount of potential distortion due to interference. A Gaussian noise defined as an equivalent sensor SNR can be added to the emulated response.

- **Parametric analysis**: a parametric sweep of the activity of the interfering ion J_1, or the selectivity coefficient $\log K^{pot}_{I,J_1}$ can be performed.

- **Compute, save plots, export data**: after selecting the primary ion, the interfering ions, and defining the sample composition and sensor parameters, the calibration curves are computed, and plotted with a target ion activity ranging from 10^{-9} to $10^{-0.5}$, with two points per decade. The plots can be saved, and the emulated data can be exported as text files.

- **Load database of calibration curves**: calibration curves obtained from in vitro measurements can be loaded to compare emulated and experimental calibration curves.

5.3.3 Ion interference analysis

The ion-sensing emulator was used as an investigation tool to assess the effect of ion interference on OCP distortion. Fig. 5.3 illustrates the impact of the interfering ion activity a_{J_1}, and the selectivity of the ISE towards the interfering ion $\log K^{pot}_{I,J_1}$, on sensor calibration curve, for monovalent primary and interfering ion. Namely, in Fig. 5.3.a, a_{J_1} was swept from $1e-5$ to $1e-1$ at a fixed selectivity coefficient $\log K^{pot}_{I,J_1} = -3$, and in Fig. 5.3.b, $\log K^{pot}_{I,J_1}$ was swept from –5 to –0.5 at a fixed activity $a_{J_1} = 1e-2$. In

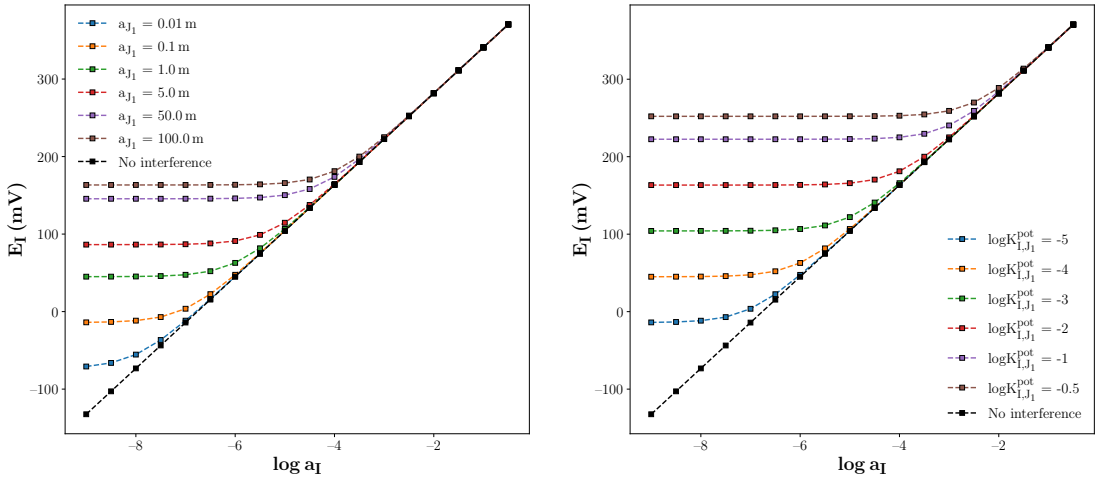

(a) (b)

Figure 5.3 – Parametric analysis of OCP distortion induced by ion interference: **(a) interfering ion activity** a_{J_1} swept from 1e – 5 to 1e – 1, with $z_I = 1$, $z_{J_1} = 1$, and $\log K^{pot}_{I,J_1} = -3$; **(b) ISE selectivity** $\log K^{pot}_{I,J_1}$ swept from –5 to –0.5, with $z_I = 1$, $z_{J_1} = 1$, and $a_{J_1} = 1e-2$.

both parametric analysis, the offset $K_{cell} + E^0_I = 400\,mV$, $s = 59.16\,mV/decade$, and $lod = 0$. The ideal sensor response is plotted as well in order to visualize the impact of ion interference on the non-linear distortion of the calibration curves. We observe that the background potential offset in diluted analyte ($\log a_I \to -\infty$) increases with the activity of the interfering ion, and this effect is enhanced for a poorly-selective sensor. Moreover, the sensor lower LOD rises with ion interference since the elbow of the calibration curve is shifted towards higher target ion activity.

Table 5.2 – Sensor parameters for the analysis of the impact of primary and interfering ion valence on calibration curve distortion

SC-ISE	s (mV/decade)	LOD (×1e – 6)	$\log K^{pot}_{I,Na^+}$	$\log K^{pot}_{I,Ca^{2+}}$
K^+	56.1	3.83	-1.8	-4.6
Pb^{2+}	58.6	0.93	-2.89	-4.28

Next, the impact of primary and interfering ion valence on the distortion of calibration curves was evaluated. The sensor parameters of the simulation were extracted from experimental calibration curves of platinum-nanostructured ISEs, and are reported in Table 5.2. First, the calibration curve of a potassium-ISE (monovalent target ion) was simulated in presence of sodium ions (monovalent ions), with $a_J = \{1e\text{-}5, 1e\text{-}4, 1e\text{-}3, 5e\text{-}3, 5e\text{-}2, 1e\text{-}1\}$. The *Root Mean-Squared Deviation* (RMSD) between the emulated sensor response and the full-Nernstian response (same sensitivity was used so as to take into account only

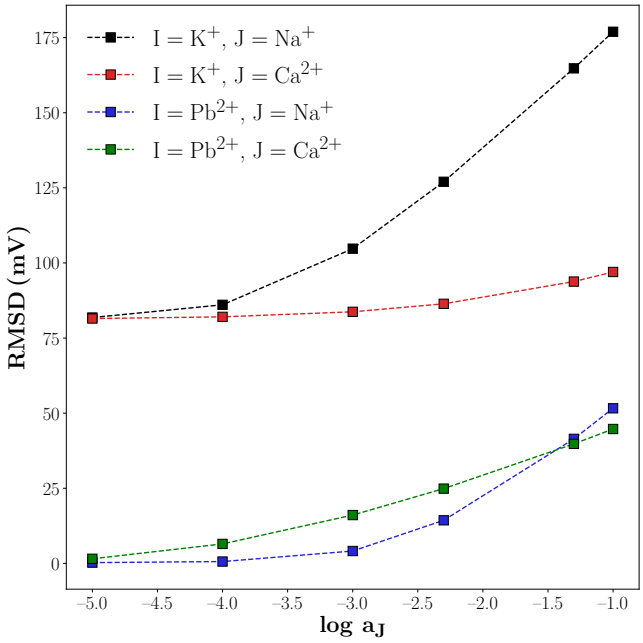

Figure 5.4 – Impact of primary and interfering ion valence on the distortion of calibration curves, for different interfering ion activity. The RMSD between emulated calibration curve and ideal full-Nernstian response is computed for each a_J.

the non-linear distortion in the calibration curve) was computed, for each a_J, and the results are displayed in Fig. 5.4. We observe, as expected, that sensor response distortion increases with a_J. Likewise, potassium-ISE response was simulated in presence of calcium ions (divalent ions). We observe that sensor response distortion increases at a smaller rate than with a monovalent interfering ion. Indeed, $K^{pot}_{K^+,Na^+} > K^{pot}_{K^+,Ca^{2+}}$ since K^+ and Na^+ are both spherical alkali cations with the same charge, similar ionic radii, and comparable chemical and physical properties [**?**]. Thus, ion interference is expected to be more severe between K^+ and Na^+, than with Ca^{2+}. Moreover, similar experiments were carried out with lead ions as target electrolytes (divalent ions). We notice in Fig. 5.4 that sensor distortion is smaller with the divalent target ion. Besides, the deviation from the full-Nernstian sensor response is larger for primary and interfering ion of the same valence. However, at very large a_J, the RMSD in presence of Na^+ is higher than with Ca^{2+}. Indeed, the selectivity of the lead-ISE towards Na^+ is lower than with Ca^{2+} (see Table 5.1), and this effect is dominant at high a_J.

5.3.4 Comparison with experimental calibration curves

After that, the calibration curves output by the ion-sensing emulator were compared with experimental calibration curves acquired from polymeric solid-contact ISEs in artificial sweat [**?**]. The results are displayed in Fig. 5.5, where the measured calibration

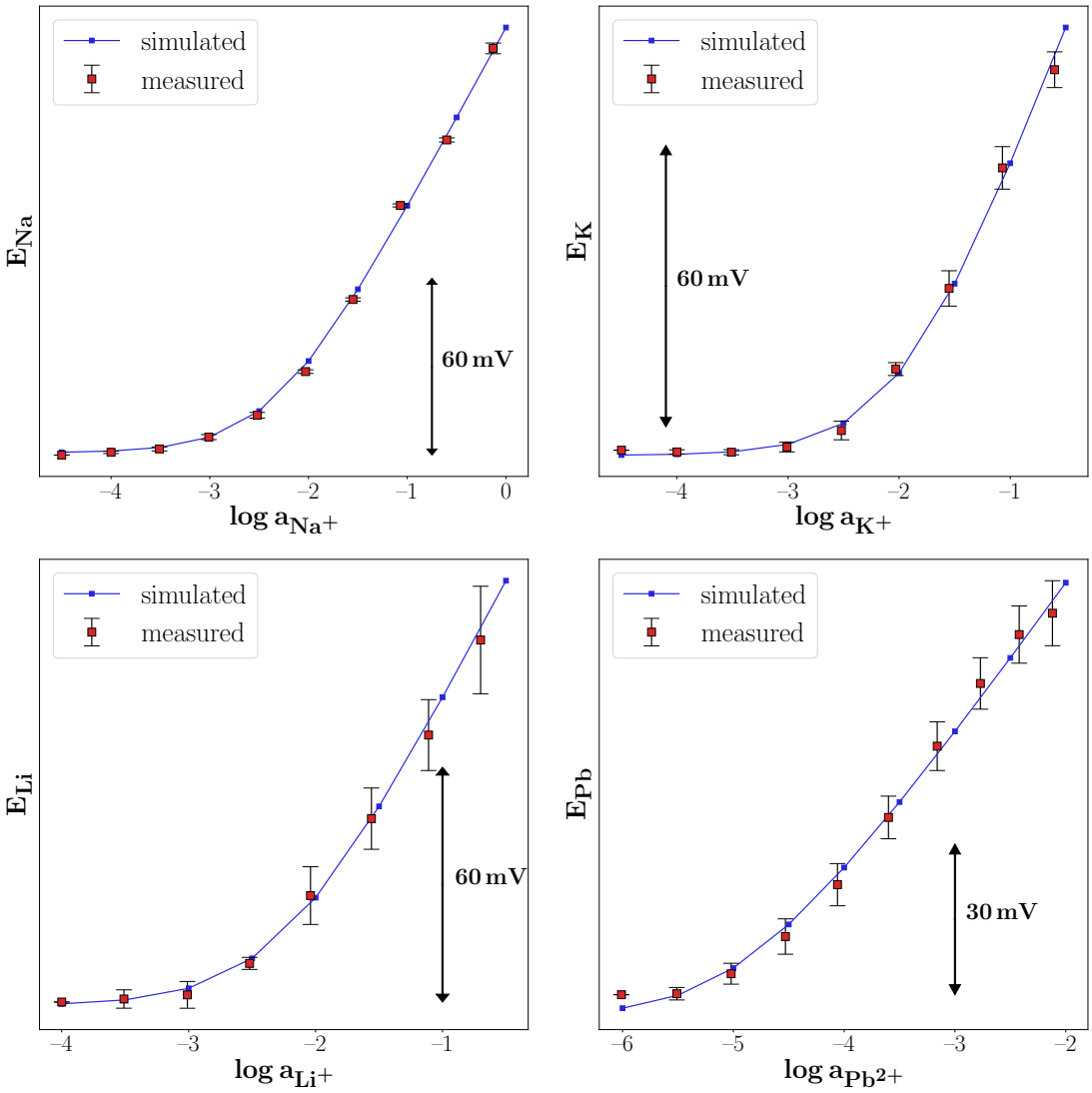

Figure 5.5 – Comparison between the calibration curves output by the ion-sensing emulator and the calibration curves acquired from batch of polymeric solid-contact ISEs in artificial sweat (adapted from [**?**]).

curves exhibit inter-sensor variability, especially for lithium and lead-ISEs. The ion-sensing emulator was configured with identical background electrolyte composition as the artificial sweat composition used for sensor calibration. Besides, the parameter $K_{cell} + E_I^0$ was fitted to the measured data so as to have zero potential offset in both measurements and simulations, and the sensitivity and LOD parameters were extracted from the experimental calibration curves. Then, the RMSD between the modeled and the measured data was computed, and yields, 1.37, 1.44, 1.78, 2 mV, for Na^+, K^+, Li^+, Pb^{2+} sensors, respectively. As a result, the compact phase-boundary potential model explains accurately the response of polymeric ISEs subject to ion interference from artificial sweat background electrolytes.

5.4 Generation of emulated synthetic datasets

The ion-sensing emulator has been demonstrated to accurately model the response of solid-contact ISEs in artificial sweat samples. Therefore, in this section, the compact ion-sensing model was used to generate emulated synthetic datasets, enabling the training and optimization of the multivariate calibration models presented in Chapter 6.

5.4.1 Case study

The multivariate calibration framework considered involves the concurrent monitoring of sodium, potassium, lithium, and lead ions, in an environment representative of sweat samples. These compounds are relevant analytes for physiology, TDM, and heavy metal contamination. Namely, the main minerals present in perspiration include sodium, potassium, ammonium, and calcium ions [**?**]. During intense physical exercise, a depletion of sodium and potassium ions is observed [**?**], and an excessive loss of these ions could lead to severe physiological dysfunctions or physical trauma, as discussed in Chapter 4. Moreover, TDM could be achieved through sweat ion-sensing. For instance, lithium salts are administrated to people suffering from bipolar disorder, as discussed in Chapter 3. The therapeutic window of this compound is very narrow ($0.5 - 1.5\,\text{mM}$ [**?**]), hence, requiring a continuous and accurate follow-up care. Furthermore, trace of heavy metals such as lead are present in sweat, but in diluted amount (below $1.4\,\mu\text{M}$). Nevertheless, persons exposed to lead through food poisoning, dust, gasoline products, or contamination from the environment, could have a sweat lead level around $85\,\mu\text{M}$ [**?**]. Such toxic ingestion might result in memory trouble, pain, numbness, or behavioral problems, thus requiring an accurate lead ions monitoring system at these low electrolyte concentrations where ion interference is stronger.

The training and optimization of a multivariate calibration model enabling a concurrent and accurate estimation of the activity of the four target ions in artificial sweat samples necessitates a big dataset that captures the complexity of multi-ion-sensing subject to ion interference, and that explains the variance of sensor response in different sample composition. The methodology implemented to design synthetic training, validation, and test sets is described in the sequel of this section.

5.4.2 Design of synthetic sample compositions

A design of experiments procedure is needed to create synthetic datasets. The term "synthetic" means that the samples correspond to ion-sensor responses in an ion activity or concentration-controlled environment. Thus, synthetic datasets could be obtained from in vitro experimental measurements with solid-contact ISEs, or from the ion-sensing emulator described in Section 5.3. The design of mixed-ion sample compositions for the case study is detailed hereunder.

Table 5.3 – OA_{18} ($6^1 \times 3^6$)

	$\mathbf{C_0}$	$\mathbf{C_1}$	$\mathbf{C_2}$	$\mathbf{C_3}$	$\mathbf{C_4}$	$\mathbf{C_5}$	$\mathbf{C_6}$
$\mathbf{R_0}$	0	0	0	0	0	0	0
$\mathbf{R_1}$	0	1	1	1	1	1	1
$\mathbf{R_2}$	0	2	2	2	2	2	2
$\mathbf{R_3}$	1	0	0	1	1	2	2
$\mathbf{R_4}$	1	1	1	2	2	0	0
$\mathbf{R_5}$	1	2	2	0	0	1	1
$\mathbf{R_6}$	2	0	1	0	2	1	2
$\mathbf{R_7}$	2	1	2	1	0	2	0
$\mathbf{R_8}$	2	2	0	2	1	0	1
$\mathbf{R_9}$	3	0	2	2	1	1	0
$\mathbf{R_{10}}$	3	1	0	0	2	2	1
$\mathbf{R_{11}}$	3	2	1	1	0	0	2
$\mathbf{R_{12}}$	4	0	1	2	0	2	1
$\mathbf{R_{13}}$	4	1	2	0	1	0	2
$\mathbf{R_{14}}$	4	2	0	1	2	1	0
$\mathbf{R_{15}}$	5	0	2	1	2	0	1
$\mathbf{R_{16}}$	5	1	0	2	0	1	2
$\mathbf{R_{17}}$	5	2	1	0	1	2	0

The electrolytes constituting the samples are the four analytes Na^+, K^+, Li^+, Pb^{2+}, plus NH_4^+, Ca^{2+}, and Mg^{2+}, that are the prevalent ions present in sweat [**?**, **?**]. The determination of mixed-ion activity requires a multi-factorial design of synthetic samples. A full-factorial design involves n_{level}^7 ion activity combinations, where n_{level} is the number of quantized ion activity levels. It is chosen as a trade-off between capturing enough variability in the activity of the ions, and avoiding exponential number of samples. Indeed, with $n_{level} = 3$, 2187 sample compositions are created, which is already a numerical burden. Moreover, the produced dataset would be redundant. Therefore, the **training set** was designed through Taguchi method [**?**]. The latter was implemented in order to create a representative and independent subset of mixed-ion activity combinations by leveraging orthogonal arrays [**?**]. The orthogonal array $OA_{18}(6^1 \times 3^6)$ reported in Table 5.3 was used. The factors C_i represent each of the seven constituting ions, while the rows R_i are the independent samples. The first factor C_0 comprises six levels, while the other factors have three levels. The columns of the table are orthogonal, and orthogonality is preserved through column permutation. Therefore, C_0 was permuted over the four primary ions. Besides, R_0 is redundant while permuting columns, so this row was removed. As a result $17 \cdot 4 = 68$ sample compositions are obtained with the generic orthogonal array.

The typical physiological range of activity of each electrolyte was subdivided into $n_{level} = 6$ levels. The discrete ion activity levels are reported in Table 5.4, where they span the

detection range of the analytes. The quantized ion activity, normalized to the upper and lower bound of the range of interest of the compound, are displayed in Fig. 5.6. The nominal activity of the electrolyte in sweat is highlighted in red.

Table 5.4 – Discrete ion activity levels of the constituents (activity × 1e – 3)

Ions	Na^+ [?]	K^+ [?]	Li^+ [?]	Pb^{2+} [?]	NH_4^+ [?]	Ca^{2+} [?]	Mg^{2+} [?]
Detection range	[7; 95] mM	[3; 8] mM	[0.5; 4.5] mM	[1.4; 85.4] µM	–	–	–
Nominal conc.[1]	39.1 mM	5.12 mM	0.1 mM	0.24 µM	3.4 mM	0.37 mM	53.5 µM
$\mathbf{L_0}$	1	0.1	0.1	1e-3	0.1	1e-2	1e-3
$\mathbf{L_1}$	5	0.5	0.25	5e-3	0.5	5e-2	5e-3
$\mathbf{L_2}$	10	1	0.5	1e-2	1	0.1	1e-2
$\mathbf{L_3}$	25	2.5	1.25	2.5e-2	2.5	0.25	2.5e-3
$\mathbf{L_4}$	50	5	2.5	5e-2	5	0.5	5e-2
$\mathbf{L_5}$	100	10	5	0.1	10	1	0.1

[1] Nominal concentration

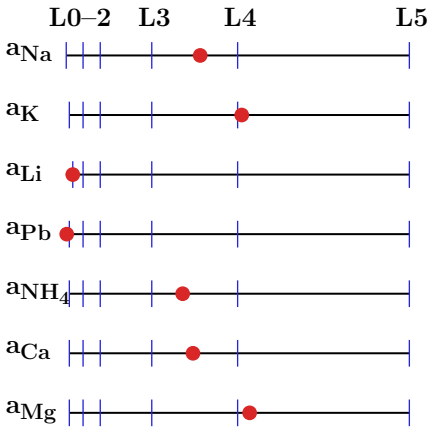

Figure 5.6 – Quantized ion activity of the electrolytes, normalized to the range of interest. The nominal activity of the ion in sweat is plotted in red.

Besides, training sets of different size were designed in order to assess the effect of dataset scarcity on the accuracy and robustness of the multivariate calibration models presented in Chapter 6. Therefore, different ion activity combinations were used for the 3-level factors of the orthogonal array. Namely, if the highest level L_5 is discarded, 10 different 3-level factors can be obtained from the 5 remaining levels. Fig. 5.7 illustrates the 10 3-level factors that were used to design 10 orthogonal training sample compositions of size $68 \cdot n_{comb}$ each, from the generic orthogonal array of size 68, where $n_{comb} = \{1, 2, \cdots, 10\}$ aggregates the 3-level factors.

The entire orthogonal training set is needed to train the multivariate calibration models since it includes all the variance in the data that the regressor should learn. As a result, standard cross-validation procedure or splitting of the training set is not recommended.

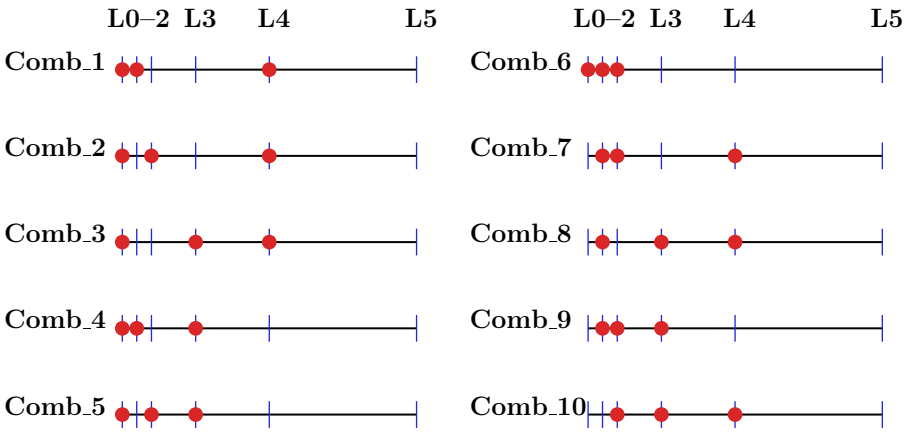

Figure 5.7 – 3-level factors used in the generic orthogonal array.

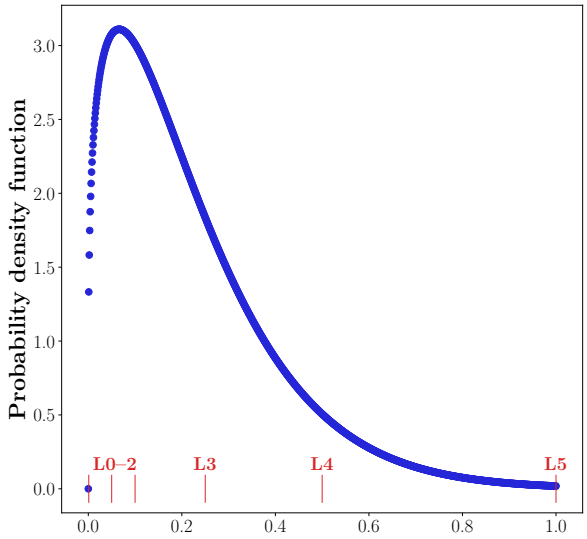

Figure 5.8 – Weibull distribution ($k = 1.25, b = 6$) (blue), and discrete levels of each constituent scaled to its respective activity range(red) (reprinted from [**?**]).

Consequently, the validation and test sets were designed independently. Random sampling in the activity range of the ions of interest is the usual approach adopted [**?**, **?**]. In this work, the Weibull distribution, which probability distribution function is plotted in Fig. 5.8 was used. It is defined as

$$f(x; k, b) = \begin{cases} b\,k\,x^{k-1}\exp(-b\,x^{k}), & x \geq 0\,, \\ 0, & x < 0\,, \end{cases} \tag{5.21}$$

where the scale and shape of the distribution are $\lambda = b^{-1/k}$, and k, respectively. This

random distribution was utilized to generate independent and identically distributed ion mixtures representative of sweat samples, for which the activity of each constituent was around its nominal value, or rather in excess in the sample (e.g. due to physical exercise for physiology). This parametric distribution allows us to tune the position and width of the bell shape of the random distribution, compared to commonly used Gaussian or Poisson probability distributions. Therefore, five **validation sets**, of one-fifth of the size of the training set each, were designed with random sample composition. This increases the robustness of the comparison between different multivariate regressors. A final external **test set** was randomly designed as well, with a size of one-fifth of the training set.

5.4.3 Automatic generation of synthetic datasets

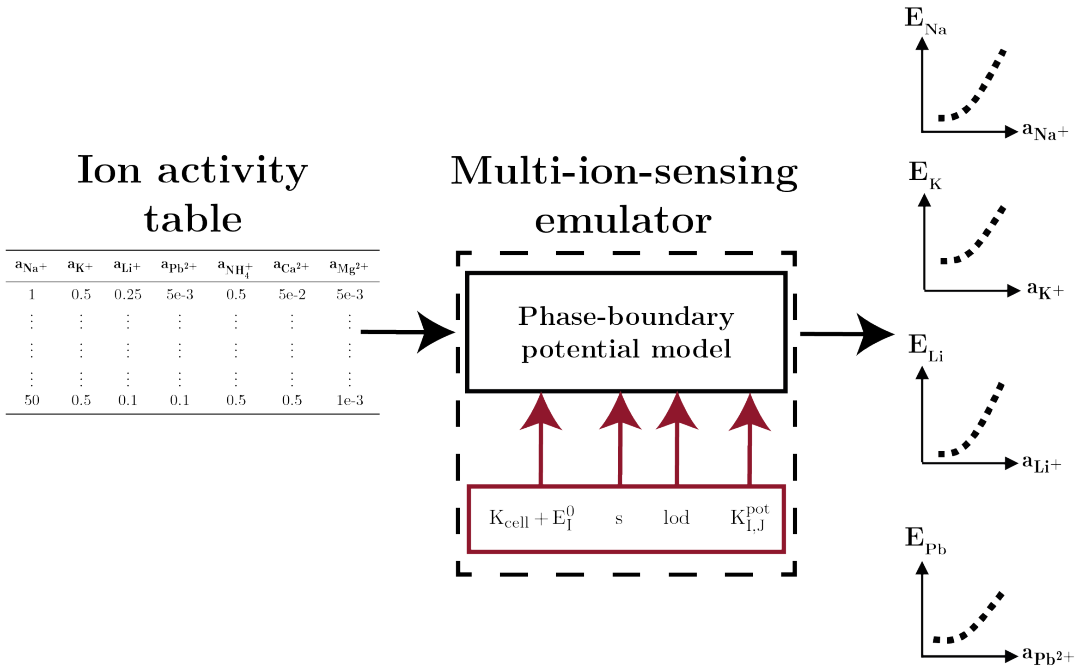

a_{Na^+}	a_{K^+}	a_{Li^+}	$a_{Pb^{2+}}$	$a_{NH_4^+}$	$a_{Ca^{2+}}$	$a_{Mg^{2+}}$
1	0.5	0.25	5e-3	0.5	5e-2	5e-3
⋮	⋮	⋮	⋮	⋮	⋮	⋮
⋮	⋮	⋮	⋮	⋮	⋮	⋮
⋮	⋮	⋮	⋮	⋮	⋮	⋮
50	0.5	0.1	0.1	0.5	0.5	1e-3

Figure 5.9 – Design flow for the generation of synthetic datasets.

The design flow for the automatic generation of synthetic datasets is displayed in Fig. 5.9. The synthetic ion activity table of the seven constituting electrolytes was generated either through an orthogonal design (for training set), or through a random design (for validation and test sets). The table was then fed to the multi-ion-sensing emulator, where the phase-boundary potential model was implemented. The model parameters $K_{cell} + E_I^0$, s, and lod were fitted from experimental calibration curves acquired with platinum-nanostructured ISEs, while the selectivity coefficients $K_{I,J}^{pot}$ were obtained through FIM experiments (see Table 5.1). Eventually, the emulated multivariate sensor responses were output.

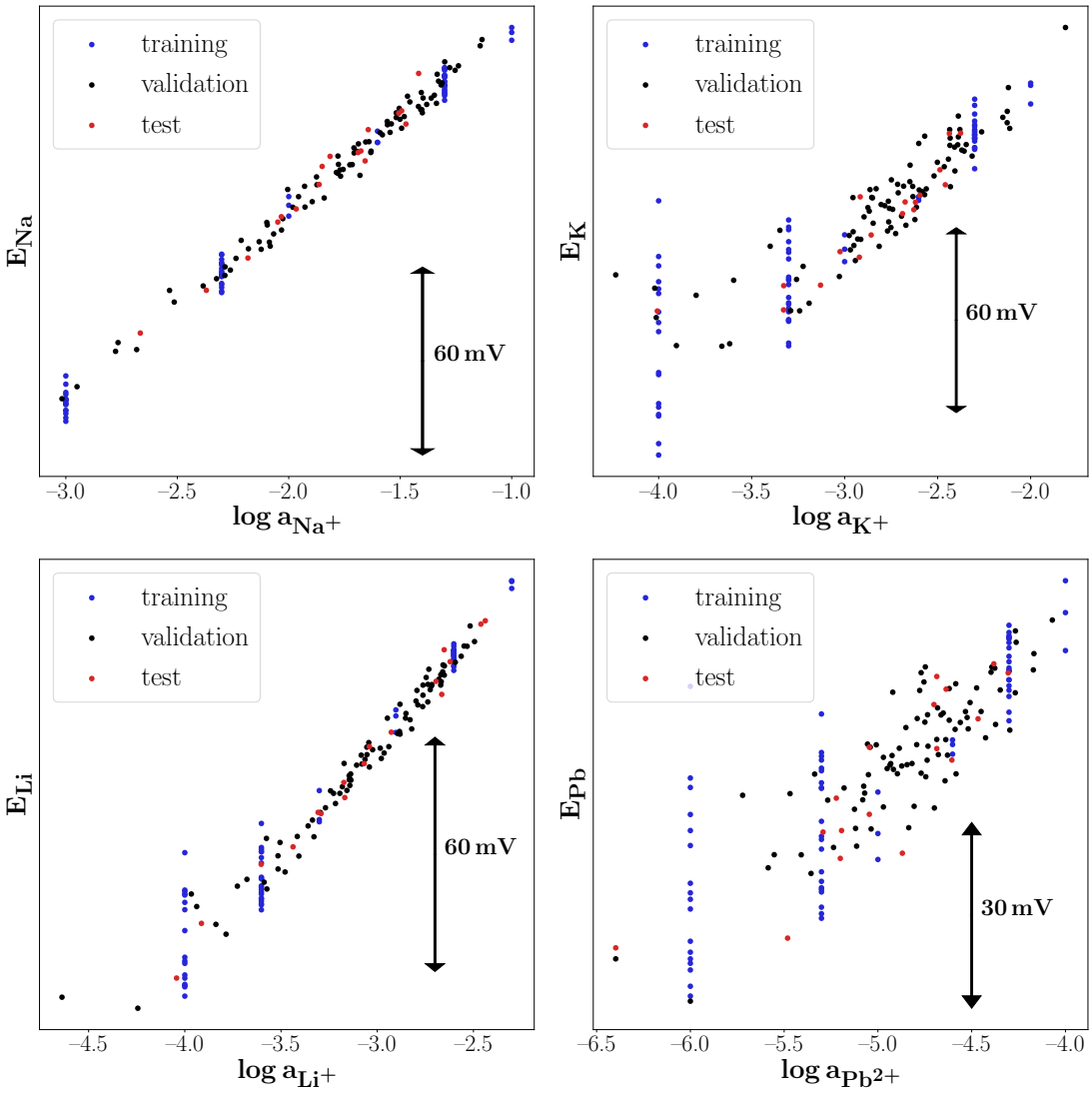

Figure 5.10 – Typical emulated synthetic dataset: $N_{train} = 68$, $N_{val,1} = 17$, $N_{test} = 17$ (reprinted from [?]).

The smaller synthetic dataset ($N_{train} = 68$, $N_{val,1} = N_{test} = 17$) is shown in Fig. 5.10. For the training set, we clearly observe the six activity levels of each target ion, while the samples are intermingled in between the factor levels for the validation and test sets that have been randomly designed in the same activity range as the training set. Besides, sodium sensor exhibits a Nernstian response. This is due to the higher ion activity range where the sensor operates. Indeed, the nominal concentration of sodium in sweat samples is in the order of tens of mM, well beyond sensor lower LOD, so it is less exposed to ion interference. Conversely, lead ions are toxic compounds detected as metal traces (tens of µM). We observe larger potential dispersion that is due to ion interference. As for lithium sensor, the ISE features good selectivity towards the constituents (see Table 5.1), so it is less affected by ion interference. It is not the case of potassium sensor that is

poorly selective, mainly towards sodium ions, that is the prevalent ion in the sample mixtures. As a result, a greater OCP dispersion is observed, and the interference is accentuated at lower a_{K^+}.

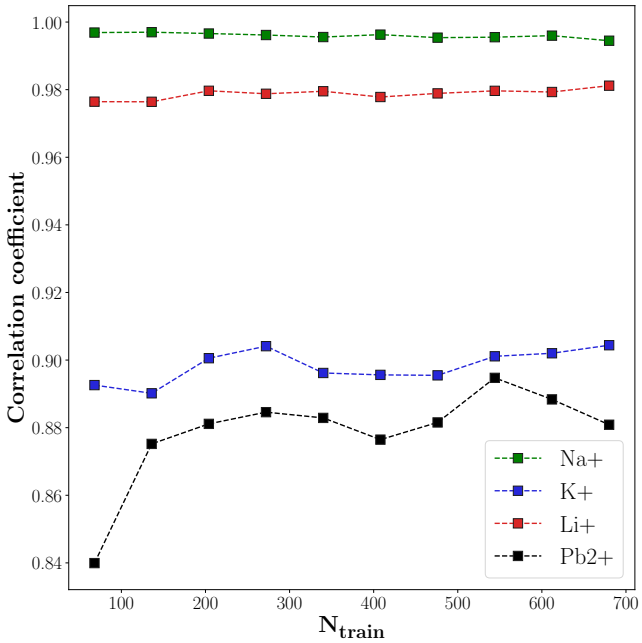

Figure 5.11 – Pearson correlation coefficient of the calibration curves (adapted from [**?**]).

The same results were observed with larger datasets. The linear correlation between the emulated sensor response and the activity of the target ion was then computed to assess the level of non-linearity introduced by interference for each sensing channel. The training sets were considered for this analysis, and the results are displayed in Fig. 5.11. The lower correlation with potassium and lead sensors is due to ion interference that is explained by the greater OCP dispersion, mainly in diluted analyte. The correlation between the emulated sensor response and the target ion activity tends to increase with larger datasets. Besides, the weaker interference exhibited by sodium sensor is reflected by the higher correlation coefficients for all datasets ($\rho_{E_{Na},a_{Na^+}} > 0.99$).

5.5 Summary and main contributions

In this chapter, the impact of ion interference on multi-ion-sensor response was studied from an analytical perspective, and validated through comparison with experimental data. The main contributions are summarized hereunder.

- A **compact model of polymeric ISEs** was derived from the phase-boundary potential model. The latter relies on ion-exchange considerations at the sample/ISM interface. The phase-boundary potential is built up to counter-act the entrapment

of the target ion in the sample by the selective ionophore present in the polymeric membrane, thus ensuring the electrochemical transduction of the analyte. Moreover, the response of a polymeric ISE in mixed-ion samples is computed, for monovalent and divalent cations. The resulting compact model includes sensor parameters that are extracted from experimental calibration curves. Namely, sensor sensitivity, sensor lower LOD, and background offset OCP were excerpted from calibration of platinum-nanostructured sodium, potassium, lithium, and lead ISEs. The selectivity coefficients of the fabricated ISEs were obtained from FIM experiments. The compact model takes as input the mixed-ion activity composition of the sample, and outputs the modeled sensor response.

- The compact model was implemented at the core of an **ion-sensing emulator** featuring utmost flexibility for the simulation of ion-sensor calibration curves in different mixed-ion samples. Namely, simulations can be performed for a standard monovalent/divalent target cation, or for sodium, potassium, lithium, or lead sensor. Sensor parameters, properties of the interfering ions constituting the sample, and ion-sensing model can be selected/tuned on the user interface. The investigation tool provides both quantitative and qualitative estimation of the impact of sensor properties and sample composition on the distortion of the calibration curves through ion interference. The latter is shown to be more severe for monovalent analytes in presence of interfering electrolytes of the same charge and similar size as the primary ion. This is the case of potassium sensors in presence of sodium ions, for instance.

- Moreover, the ion-sensing emulator enabled an **automatic generation of emulated synthetic datasets** for sodium, potassium, lithium, and lead ions. These electrolytes are monitored for physiology, TDM, and toxic compound identification applications. The tool takes as input an ion activity table of the electrolytes constituting the sample, and outputs the emulated multivariate sensor responses. A design of experiment was carried out in order to generate synthetic mixed-ion samples that are representative of artificial sweat composition during the experiments. Namely, an orthogonal design was performed for the generation of an independent training set that should include all the variability in ion activity, while a random design was implemented for the generation of synthetic samples for the validation and test sets. The emulated synthetic datasets will be used for the training and optimization of multivariate calibration models developed to cope with ion interference in complex mixed-ion samples, as presented in the subsequent chapter.

6 Multivariate calibration optimization by machine learning models

The sensing performance of multi-ion-sensors is considerably degraded by ion interference that distorts sensor response. Therefore, in this chapter, machine learning models are proposed to improve the multivariate calibration accuracy of low-selective ion sensors in complex samples such as artificial sweat. The emulated synthetic datasets obtained in Section 5.4 are used to train, optimize, and evaluate linear and non-linear regressors implemented for the multivariate calibration task.

6.1 Multivariate calibration problem

A theoretical background on multivariate calibration in multi-ion-sensing systems was provided in Section 2.3.2. The multivariate calibration problem applied to the case study involving the concurrent monitoring of sodium, potassium, lithium, and lead ions in artificial sweat samples is described hereunder. The inverse calibration problem can be formulated as

$$\mathbf{Y} = (\mathbf{X}\mathbf{W} + \mathbf{b}) + \mathbf{E}\,, \tag{6.1}$$

for N observations, where $\mathbf{Y} = \{\mathbf{y_n}\}_{\mathrm{n}=1,\cdots,\mathrm{N}}$, with $\mathbf{y_n} \in \mathbb{R}^4$, denotes the matrix of activity of the four primary ions; $\mathbf{X} = \{\mathbf{x_n}\}_{\mathrm{n}=1,\cdots,\mathrm{N}}$, with $\mathbf{x_n} \in \mathbb{R}^4$, is the matrix of emulated OCP signals from the four sensors; $(\mathbf{W}, \mathbf{b})$ is the regressor model including the regression coefficients and the bias term; and $\mathbf{E}$ is the matrix of prediction error. The input matrix $\mathbf{X}$ can be raw OCP signals, normalized OCP signals, or PCA scores of the multivariate sensor response. The label $\mathbf{Y}$ refers to the log-activity of the primary ions, given that ion-sensors theoretically exhibit a Nernstian response $\mathrm{E_I} \propto \log \mathrm{a_I}$ in absence of ion interference. The calibration problem is a multivariate multiple regression task since both $\mathbf{X}$ and $\mathbf{Y}$ are multivariate ($(\mathbf{x_n}, \mathbf{y_n}) \in \mathbb{R}^4$). Moreover, the metrics used to assess the accuracy of the multivariate regressors are the *Normalized Root Mean-Squared*

Error (NRMSE) and the *Mean Relative Error* (MRE). They are defined as

$$\mathrm{NRMSE} = \frac{100}{\overline{\mathrm{y}}}\sqrt{\frac{1}{\mathrm{N_{test}}}\sum_{\mathrm{n=1}}^{\mathrm{N_{test}}}\left(\mathrm{y_n}-\hat{\mathrm{y}}_\mathrm{n}\right)^2}\,, \tag{6.2}$$

$$\mathrm{MRE} = \frac{100}{\mathrm{N_{test}}}\sum_{\mathrm{n=1}}^{\mathrm{N_{test}}}\frac{\left|\mathrm{y_n}-\hat{\mathrm{y}}_\mathrm{n}\right|}{\mathrm{y_n}}\,, \tag{6.3}$$

where $\overline{\mathrm{y}}$ is the mean of the test set labels, $\mathrm{y_n}$ and $\hat{\mathrm{y}}_\mathrm{n}$ are the ground truth and predicted log-activity of the primary ions, respectively. Normalized metrics are required to balance error contributions from analytes that have a large activity (e.g. sodium ions), and diluted analytes in the sample (e.g. lead ions). In addition, the two metrics do not over-penalize outliers. Compact metrics are obtained by summing the NRMSE and MRE of the four channels, yielding Total NRMSE and Total MRE.

6.2 Multivariate calibration models

The multivariate calibration models implemented in this thesis are described in this section. To avoid confusion in the notation, let us consider the multivariate matrices $\mathbf{X} = \{\mathbf{x_n}\}_{\mathrm{n}=1,\cdots,\mathrm{N}}$ with $\mathbf{x_n} \in \mathbb{R}^\mathrm{P}$, and $\mathbf{Y} = \{\mathbf{y_n}\}_{\mathrm{n}=1,\cdots,\mathrm{N}}$ with $\mathbf{x_n} \in \mathbb{R}^\mathrm{M}$.

6.2.1 Linear regression models

Linear regressors are commonly used for the calibration of ion-sensors since a Nernstian response is expected in the detection range of the target ion.

Multiple linear regression

Inverse least-squares regression is the simplest model implemented for sensor calibration. It maps the multivariate response $\mathbf{X}$ to each ion activity $\mathbf{y}_{:,\mathrm{m}}$, through multiple independent OLS regressions, referred as MLR. $\widehat{\mathbf{W}}$ can be computed in a closed-form with the normal equation $\widehat{\mathbf{W}} = (\mathbf{X}^\mathrm{T}\mathbf{X})^{-1}\mathbf{X}^\mathrm{T}\mathbf{Y}$, where $\mathbf{X}$ needs to be a full-rank matrix so that $\mathbf{X}^\mathrm{T}\mathbf{X}$ could be invertible. The main advantage of inverse least-squares regression, compared to a classical least-squares regression $\mathbf{X} = \mathbf{YK} + \mathbf{E}$, arises from the fact that the knowledge of the exact composition of the sample (primary and interfering ions) is not required during the training phase. Nevertheless, the calibration set needs to be representative of typical samples (it should include interfering ions) given that such model cannot predict reliably instances out of the calibration set.

Principal components regression

When $\mathbf{X}$ is highly colinear, it is usually transformed through PCA, an unsupervised factorial decomposition of the input matrix in *Principal Component*s (PCs), that accumulate the maximum amount of variance within the data into orthogonal factors. Namely, the columns of $\mathbf{X}$ are standardized to zero-mean and unit-variance. Then, the matrix is decomposed through *Single Value Decomposition* (SVD), yielding $\mathbf{X} = \mathbf{USV}^{\mathrm{T}}$, where $\mathbf{U}$ and $\mathbf{V}$ are the eigenvectors of $\mathbf{XX}^{\mathrm{T}}$ and $\mathbf{X}^{\mathrm{T}}\mathbf{X}$, and $\mathbf{S}$ is a diagonal matrix containing the eigenvalues. Next, the multivariate least-squares regression is implemented between $\mathbf{T} = \mathbf{XP}$ and each column $\mathbf{Y}_{:,\mathrm{m}}$, where the score matrix $\mathbf{T}$ is the projection of $\mathbf{X}$ in the latent space defined by the loading vectors $\mathbf{P}$. In addition, $\mathbf{T}$ and $\mathbf{P}$ could be truncated to the first A columns that aggregate most of the variance observed in sensor response. This is relevant, especially when data is collected from a large amount of ion-sensors. The combination of PCA on $\mathbf{X}$ and MLR refers to PCR.

Partial least-squares regression

Moreover, PLS is another popular chemometric model, where latent variables from both $\mathbf{X}$ and $\mathbf{Y}$ are constructed by explaining both the maximum amount of variance in $\mathbf{X}$, and the maximum correlation between $\mathbf{X}$ and $\mathbf{Y}$ [**?**]. Thus, the PLS model is built by projecting the matrix $\mathbf{X}$ into an A-dimensional hyperplane ($\mathrm{A} \leq \min(\mathrm{N}-1, \mathrm{P}, \mathrm{M})$) that approximates well the original matrix $\mathbf{X}$, and the projection of the observations $\mathbf{x_n}$ on this hyperplane are related to $\mathbf{Y}$ (the covariance of X-scores and Y-scores is maximum). Therefore, the latent variables depend on both OCP signals and the activity of the analytes, contrary to the latent variables in PCR that only depend on $\mathbf{X}$. PLS is commonly implemented with the *Non-linear Iterative Partial Least-Squares* (NIPALS) algorithm, where the factors for both $\mathbf{X}$ and $\mathbf{Y}$ are computed iteratively by projections onto the optimal hyperplane. An exhaustive description of the NIPALS-PLS algorithm can be found in [**?**]. The pseudo-code of the NIPALS implementation in this work is detailed hereunder.

PLS is a more compact model than PCR since fewer PCs are usually needed to achieve the same performance [**?**]. It is quicker to converge with high-dimension datasets given that NIPALS involves only simple matrix multiplications and no eigenvalue/eigenvector decomposition or matrix inversions. This chemometric tool is also more robust than PCR when the columns of $\mathbf{Y}$ are correlated.

The aforementioned linear regressors are usually efficient for univariate calibrations. However, the non-linearity induced by ion interference in the calibration curves suggests to consider non-linear regressors in order to improve the multivariate calibration accuracy.

Algorithm: NIPALS-PLS algorithm

Input : OCP signal $\mathbf{X}$, ions log-activity $\mathbf{Y}$, number of factors to compute A, convergence tolerance *tol*

Output : PLS regression coefficients $\widehat{\mathbf{W_{PLS}}}$, factors $\mathbf{W}, \mathbf{T}, \mathbf{U}, \mathbf{P}, \mathbf{C}$

/* Initialization */

$\mathbf{X} \leftarrow \mathbf{X} - \frac{1}{\mathrm{N}}\mathbf{1}_{\mathrm{N}}^{\mathrm{T}}\mathbf{X}$; $\mathbf{X} \leftarrow \mathbf{X} \cdot \mathrm{diag}(\frac{1}{\mathrm{std}(\mathbf{X})})$; // column centering and scaling of $\mathbf{X}$

$\mathbf{Y} \leftarrow \mathbf{Y} - \frac{1}{\mathrm{N}}\mathbf{1}_{\mathrm{N}}^{\mathrm{T}}\mathbf{Y}$; $\mathbf{Y} \leftarrow \mathbf{Y} \cdot \mathrm{diag}(\frac{1}{\mathrm{std}(\mathbf{Y})})$; // column centering and scaling of $\mathbf{Y}$

$\mathbf{U} \leftarrow \mathbf{0_A}$; $\mathbf{W} \leftarrow \mathbf{0_A}$; $\mathbf{T} \leftarrow \mathbf{0_A}$; $\mathbf{C} \leftarrow \mathbf{0_A}$; $\mathbf{P} \leftarrow \mathbf{0_A}$;

/* Iterative projections through latent vectors */

for *a=1 to A*

  $\mathrm{k} \leftarrow 0$; // iterator of amount of projections onto the latent space

  /* Computation of each factor */

  $\mathbf{u} \leftarrow \mathbf{Y}_{:,\mathrm{a}}$; // $\mathbf{Y}$ factor scores

  $\mathbf{w} \leftarrow \mathbf{X}^{\mathrm{T}}\frac{\mathbf{u}}{\mathbf{u}^{\mathrm{T}}\mathbf{u}}$; $\mathbf{w} \leftarrow \frac{\mathbf{w}}{\|\mathbf{w}\|}$; // $\mathbf{X}$ factor weights

  $\mathbf{t} \leftarrow \mathbf{X}\mathbf{w}$; $\mathbf{t}^{\mathrm{k}} \leftarrow \mathbf{t}$; // $\mathbf{X}$ factor scores

  $\mathbf{c} \leftarrow \mathbf{Y}^{\mathrm{T}}\frac{\mathbf{t}}{\mathbf{t}^{\mathrm{T}}\mathbf{t}}$; // $\mathbf{Y}$ factor weights

  $\mathbf{u} \leftarrow \mathbf{Y}\frac{\mathbf{c}}{\mathbf{c}^{\mathrm{T}}\mathbf{c}}$;

  $\mathbf{w} \leftarrow \mathbf{X}^{\mathrm{T}}\frac{\mathbf{u}}{\mathbf{u}^{\mathrm{T}}\mathbf{u}}$; $\mathbf{w} \leftarrow \frac{\mathbf{w}}{\|\mathbf{w}\|}$;

  $\mathbf{t} \leftarrow \mathbf{X}\mathbf{w}$; $\mathbf{t}^{\mathrm{k+1}} \leftarrow \mathbf{t}$;

  while $\frac{\|\mathbf{t}^{\mathrm{k}} - \mathbf{t}^{\mathrm{k+1}}\|}{\|\mathbf{t}^{\mathrm{k}}\|} > \mathrm{tol}$ **do**

    $\mathrm{k} \leftarrow \mathrm{k} + 1$;

    $\mathbf{w} \leftarrow \mathbf{X}^{\mathrm{T}}\frac{\mathbf{u}}{\mathbf{u}^{\mathrm{T}}\mathbf{u}}$; $\mathbf{w} \leftarrow \frac{\mathbf{w}}{\|\mathbf{w}\|}$;

    $\mathbf{t} \leftarrow \mathbf{X}\mathbf{w}$; $\mathbf{t}^{\mathrm{k}} \leftarrow \mathbf{t}$;

    $\mathbf{c} \leftarrow \mathbf{Y}^{\mathrm{T}}\frac{\mathbf{t}}{\mathbf{t}^{\mathrm{T}}\mathbf{t}}$;

    $\mathbf{u} \leftarrow \mathbf{Y}\frac{\mathbf{c}}{\mathbf{c}^{\mathrm{T}}\mathbf{c}}$;

    $\mathbf{w} \leftarrow \mathbf{X}^{\mathrm{T}}\frac{\mathbf{u}}{\mathbf{u}^{\mathrm{T}}\mathbf{u}}$; $\mathbf{w} \leftarrow \frac{\mathbf{w}}{\|\mathbf{w}\|}$;

    $\mathbf{t} \leftarrow \mathbf{X}\mathbf{w}$; $\mathbf{t}^{\mathrm{k+1}} \leftarrow \mathbf{t}$;

  $\mathbf{p} \leftarrow \mathbf{X}^{\mathrm{T}}\frac{\mathbf{t}}{\mathbf{t}^{\mathrm{T}}\mathbf{t}}$; // Loading matrix

  /* Deflation of the residual matrices */

  $\mathbf{X} \leftarrow \mathbf{X} - \mathbf{t}\mathbf{p}^{\mathrm{T}}$;

  $\mathbf{Y} \leftarrow \mathbf{Y} - \mathbf{t}\mathbf{c}^{\mathrm{T}}$;

  /* Aggregation of each factor to the corresponding matrix */

  $\mathbf{U}_{:,\mathrm{a}} \leftarrow \mathbf{u}$; $\mathbf{W}_{:,\mathrm{a}} \leftarrow \mathbf{w}$; $\mathbf{T}_{:,\mathrm{a}} \leftarrow \mathbf{t}$; $\mathbf{C}_{:,\mathrm{a}} \leftarrow \mathbf{c}$; $\mathbf{P}_{:,\mathrm{a}} \leftarrow \mathbf{p}$;

/* PLS regression coefficients */

$\widehat{\mathbf{W_{PLS}}} \leftarrow \mathbf{W}(\mathbf{P}^{\mathrm{T}}\mathbf{W})^{-1}\mathbf{C}^{\mathrm{T}}$

6.2.2 Support vector regressor

SVMs are efficient tools for linear and non-linear input/output modeling [**?**], as it is the case of multivariate calibration hindered by ion interference. Standard SVR models perform unidimensional regression of the input matrix $\mathbf{X}$ to each output channel $\mathbf{y}_{:,\mathrm{m}}$. Non-linear SVR models are obtained by implicitly mapping $\mathbf{X}$ to a higher dimensional feature space through a kernel function [**?**]. Thus, the model learns a linear function in the space induced by the kernel. Gaussian *Radial Basis Function* (RBF) is a common non-linear kernel for which $\mathbf{X}$ is mapped to an infinite dimensional Hilbert space [**?**]. The primal formulation of the SVR minimization objective is

$$\begin{aligned} &\forall\ \mathrm{m} \in [\![1;\mathrm{M}]\!], \quad \min_{\mathbf{W}_{:,\mathrm{m}},\mathrm{b_m}} \frac{1}{2}\left\|\mathbf{W}_{:,\mathrm{m}}\right\|^2 + \mathrm{C}\sum_{\mathrm{n}=1}^{\mathrm{N}} \mathrm{L}_\varepsilon(\mathrm{u_{n,m}}), \\ &\text{with} \quad \mathrm{u_{n,m}} = \mathbf{y}_{\mathrm{n,m}} - (\Phi(\mathbf{x_n})^{\mathrm{T}}\mathbf{W}_{:,\mathrm{m}} + \mathrm{b_m}). \end{aligned} \tag{6.4}$$

L_ε is the Vapnik ε-insensitive loss function defined as $\mathrm{L}_\varepsilon(\mathrm{u}) = \max\{0, |\mathrm{u}| - \varepsilon\}$, with $\mathrm{u} \in \mathbb{R}$. Φ is the non-linear function defining the kernel function $\varkappa(\mathbf{x}_\mathrm{i}, \mathbf{x}_\mathrm{j}) \equiv \Phi(\mathbf{x}_\mathrm{i})^{\mathrm{T}} \cdot \Phi(\mathbf{x}_\mathrm{j})$. $\mathrm{C} > 0$ is a hyper-parameter trading-off margin violations and minimization of the distance ε from the support vectors to the SVR model hyperplane. In practice, a dual SVR minimization is used, where quadratic programming leveraging the kernel formulation yields a problem faster to solve.

In (6.4), the residual error between the predicted ion activity and the ground truth is computed one channel at a time, leading to M independent minimization objectives. As a result, the solution complexity of multiple SVRs grows linearly with M. Moreover, such unidimensional model does not consider correlations between the output columns. Hence, it is less robust to noise, dataset scarcity, and to the non-linearity present in the dataset.

6.2.3 Proposed multi-output support vector regressor

In this thesis, a multivariate multi-output SVR, referred as M-SVR, is proposed and implemented to consider correlations and non-linear cross-relations between $\mathbf{X}$ and $\mathbf{Y}$, enabling a concurrent optimization of the predicted ion activity of the $\mathrm{M} = 4$ primary ions. The objective function to minimize is

$$\begin{aligned} &\mathcal{L}(\mathbf{W}, \mathbf{b}) = \frac{1}{2}\sum_{\mathrm{m}=1}^{\mathrm{M}} \left\|\mathbf{W}_{:,\mathrm{m}}\right\|^2 + \mathrm{C}\sum_{\mathrm{n}=1}^{\mathrm{N}} \mathrm{L}(\mathrm{u_n}), \\ &\text{with} \quad \mathrm{u_n} = \|\mathbf{e}_\mathrm{n}\|_2 \text{ s.t. } \mathbf{e}_\mathrm{n} = \mathbf{y}_\mathrm{n} - (\mathbf{W}^{\mathrm{T}}\Phi(\mathbf{x}_\mathrm{n}) + \mathbf{b}). \end{aligned} \tag{6.5}$$

Iterative Reweighted Least-Squares (IRWLS) procedures enable the use of arbitrary cost functions L. L_2-based norm cost functions are appealing since the constraints for all M output dimensions can be aggregated into a single error vector, contrary to L_1-based Vapnik loss function described previously, that needs to take into account of all M dimensions separately. In this thesis, an IRWLS procedure was implemented with the quadratic and differentiable cost function

$$L(u) = \begin{cases} 0, & u < \varepsilon. \\ u^2 - 2u\varepsilon + \varepsilon^2, & u \geq \varepsilon. \end{cases} \tag{6.6}$$

The convergence of such SVM was demonstrated in [**?**]. The IRWLS procedure is constructed by performing a first-order Taylor approximation of the error function (6.5) over the previous solution ($\mathbf{W}$,$\mathbf{b}$). A quadratic approximation of the resulting expansion yields the weighted least-squares minimization problem

$$\mathcal{L}'(\mathbf{W}, \mathbf{b}) = \frac{1}{2} \sum_{m=1}^{M} \|\mathbf{W}_{:,m}\|^2 + \frac{1}{2} \sum_{n=1}^{N} a_n u_n^2 + \text{cste}, \tag{6.7}$$

$$\text{where} \quad a_n = \frac{C}{u_n^k} \frac{dL(u)}{du}\Big|_{u_n^k} = \begin{cases} 0, & u_n^k < \varepsilon. \\ \frac{2C(u_n^k - \varepsilon)}{u_n^k}, & u_n^k \geq \varepsilon. \end{cases}$$

The latter function $\mathcal{L}'$ is then minimized with respect to $(\mathbf{W}, \mathbf{b})$. It yields a linear system represented in matrix form as

$$\forall m \in [\![1; M]\!], \underbrace{\begin{bmatrix} \mathbf{K} + \mathbf{D}_a^{-1} & \mathbf{1} \\ \mathbf{a}^T\mathbf{K} & \mathbf{1}^T\mathbf{a} \end{bmatrix}}_{\mathbf{H}} \begin{bmatrix} \mathbf{W}_{*,m}^{sol} \\ b_m^{sol} \end{bmatrix} = \begin{bmatrix} \mathbf{Y}_{:,m} \\ \mathbf{a}^T\mathbf{Y}_{:,m} \end{bmatrix}, \tag{6.8}$$

where $(\mathbf{K})_{ij} = \varkappa(\mathbf{x}_i, \mathbf{x}_j)$, $\mathbf{a} = [a_1, \cdots, a_n]^T$, $(\mathbf{D}_a)_{ij} = a_i\delta(i-j)$. It is important to notice that the matrix $\mathbf{H}$ is independent of m, so it does not depend on the output channel. The kernel function used was the Gaussian RBF. The pseudo-code of the IRWLS procedure

is reported hereunder.

Algorithm: Iterative reweighted least-squares procedure

Input : OCP signal $\mathbf{X}$, ions log-activity $\mathbf{Y}$,
kernel function Φ, kernel parameters *param*,
convergence tolerance *tol*,
maximum number of iterations *max_iter*

Output : M-SVR model $(\mathbf{W}, \mathbf{b})$, number of iterations k

/* Initialization */

$(\mathbf{W}, \mathbf{b}) \leftarrow (\mathbf{0}, \mathbf{0})$; $k \leftarrow 0$;

$\mathbf{K} \leftarrow \mathbf{X}$ mapped to non-linear kernel Φ;

/* Compute error vector */

for *n=1 to N*

  $\mathbf{e_n} \leftarrow \mathbf{y}_n - (\mathbf{W}^T \mathbf{K}_{:,n} + \mathbf{b})$;

  $u_n^k \leftarrow \|\mathbf{e_n}\|$;

/* Identify support vectors */

$\{i\} \leftarrow \{n \text{ s.t. } u_n^k \geq \varepsilon\}$;

/* Compute objective function $\mathcal{L}$ and $\mathcal{L}'$ */

foreach *i* **do**

  $L(u_i^k) \leftarrow {u_i^k}^2 - 2u_i^k\varepsilon + \varepsilon^2$;

  $a_i \leftarrow \frac{2C(u_i^k - \varepsilon)}{u_i^k}$;

/* Iterative procedure */

while *convergence tolerance is not reached* ***and*** $k \leq$ max_iter ***and*** $\{i\} \neq \{\emptyset\}$ **do**

  /* Save variables of previous iteration */

  $(\mathbf{W}^k, \mathbf{b}^k) \leftarrow (\mathbf{W}, \mathbf{b})$; $\mathbf{u}^k \leftarrow \mathbf{u}$; $\{i\}^k \leftarrow \{i\}$;

  /* Minimize $\mathcal{L}'(\mathbf{W}, \mathbf{b})$ */

  for *m=1 to M*

    Solve $\begin{cases} \nabla_{\mathbf{W}_{:,m}} \mathcal{L}'(\mathbf{W}, \mathbf{b}) = 0 \\ \nabla_{b_m} \mathcal{L}'(\mathbf{W}, \mathbf{b}) = 0 \end{cases}$ yields $(\mathbf{W}^{sol}, \mathbf{b}^{sol})$

  /* Minimize $\mathcal{L}$ with descending direction $\begin{bmatrix} \mathbf{W}^{sol} - \mathbf{W}^k \\ (\mathbf{b}^{sol} - \mathbf{b}^k)^T \end{bmatrix}$ */

  $\begin{bmatrix} \mathbf{W}^{k+1} \\ (\mathbf{b}^{k+1})^T \end{bmatrix} = \begin{bmatrix} \mathbf{W}^k \\ (\mathbf{b}^k)^T \end{bmatrix} + \eta^k \begin{bmatrix} \mathbf{W}^{sol} - \mathbf{W}^k \\ (\mathbf{b}^{sol} - \mathbf{b}^k)^T \end{bmatrix}$;

  /* Update variables */

  recompute $\mathbf{u}$, $\{i\}$, a_i;

  $k \leftarrow k + 1$;

The IRWLS procedure was implemented in a quasi-Newton approach, where the norm of the residual errors (u_n^k), and the coefficients (a_n) and solution ($\mathbf{W}^{sol}, \mathbf{b}^{sol}$) of the reweighted least-squares problem were recomputed at each iteration k. Each iteration has the complexity of M OLS minimizations (solving of reweighted least-squares problem).

The IRWLS procedure was stopped when either:

- a local minimum of $\mathcal{L}$ was reached,
- $\mathcal{L}$ could not be further improved (tuned by convergence tolerance parameter *tol*),
- no support vector was found,
- the number of iterations k reached *max_iter*.

6.2.4 Multi-layer perceptrons model

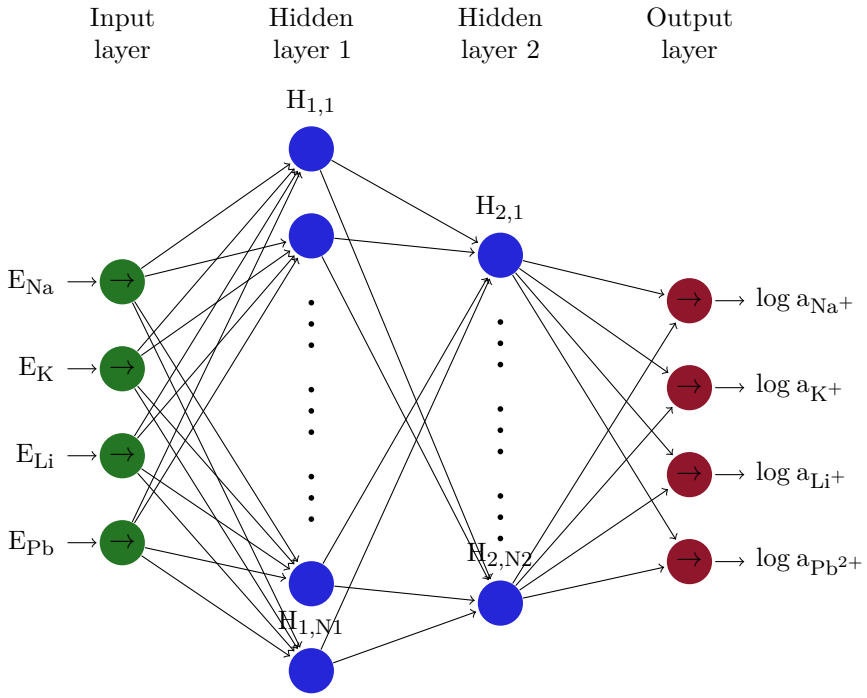

Figure 6.1 – FFNN enabling a simultaneous monitoring of sodium, potassium, lithium, and lead ions: the input features (OCP signals or their PC scores) are fed to the pass-through neurons of the input layer, then conveyed to two fully-connected hidden layers of N1 and N2 number of units, respectively. The output layer consists of four neurons with linear activation function, providing the log-activity of the four target ions.

MLP models are commonly used in complex multivariate calibration systems [**?**, **?**, **?**, **?**, **?**, **?**, **?**, **?**, **?**, **?**]. Neural networks were built for the multivariate calibration of ion-sensors hindered by ion interference, as a benchmark for the proposed M-SVR algorithm. The FFNN architecture implemented is illustrated in Fig. 6.1. The input layer consists of four pass-through neurons that relay the input features $\mathbf{x}_n$ to the subsequent layers. The features are either the OCP signals of the four ion-sensors, or their PC scores after applying PCA. Two hidden layers of N1 and N2 units produce non-linear transformations of the dataset through the *Exponential Linear Unit* (ELU) function, and the output layer predicts the activity of the four target ions with a linear activation function. The

model parameters (weights and bias) were optimized with a back-propagation training algorithm minimizing the mean-squared error loss function [**?**]. The configuration and hyper-parameters of the MLP models are reported in Table 6.1. The parameters in bold were optimized through a grid-search procedure.

Table 6.1 – Configuration and hyper-parameters of MLP model, optimizer, and training procedure

MLP model	Input layer: 4 pass-through neurons Hidden layer 1: **N1** neurons (σ = ELU) Hidden layer 2: **N2** neurons (σ = ELU) Output layer: 4 neurons Weights initializer: Glorot (normal distribution) [**?**] Regularizer: L_2 regularizer ($\alpha = 10^{-3}$)
Loss function	Mean-squared error
Optimizer	Type: stochastic gradient descent with momentum optimization Learning rate scheduling: $\eta(t) = \frac{\eta_0}{1+10^{-5}t}$
Training	Number of epochs: 500 (early-stopping) Batch size: 32

6.2.5 Hardware and software

The data pre-processing pipeline and multivariate models were implemented within a Python 3.7 environment. PCA algorithm was implemented through SVD where LAPACK routine [**?**] was used. The OCP matrices were standardized to zero-mean and unit-variance before applying PCA. Moreover, MLR and OLS minimization problems were solved using SVD with LAPACK routine [**?**], while PLS was implemented with the NIPALS algorithm previously described. Single-output SVRs were constructed leveraging LIBSVM library that supports quadratic programming [**?**]. As for MLP models, they were implemented through Keras high-level API [**?**], with TensorFlow 2.0 deep learning library as computational back-end. All experiments were run on a 2x Intel(R) Xeon(R) CPU E5-2690 v4 @ 2.60 GHz with 256 GB RAM.

6.3 Results and discussion

The training and optimization of machine learning models implemented for the multivariate calibration of emulated synthetic datasets for sodium, potassium, lithium, and lead ions in artificial sweat samples are presented in this section. In particular, the performance achieved by the proposed M-SVR model, on ten datasets of different size, is compared to linear and non-linear multivariate regressors.

6.3.1 Linear regression models

The training datasets were analyzed through a factorial decomposition of the matrix of emulated OCP signals **X**. Then MLR, PCR, and PLS were applied for the multivariate calibration of the four target ions.

Factorial decomposition of OCP signals

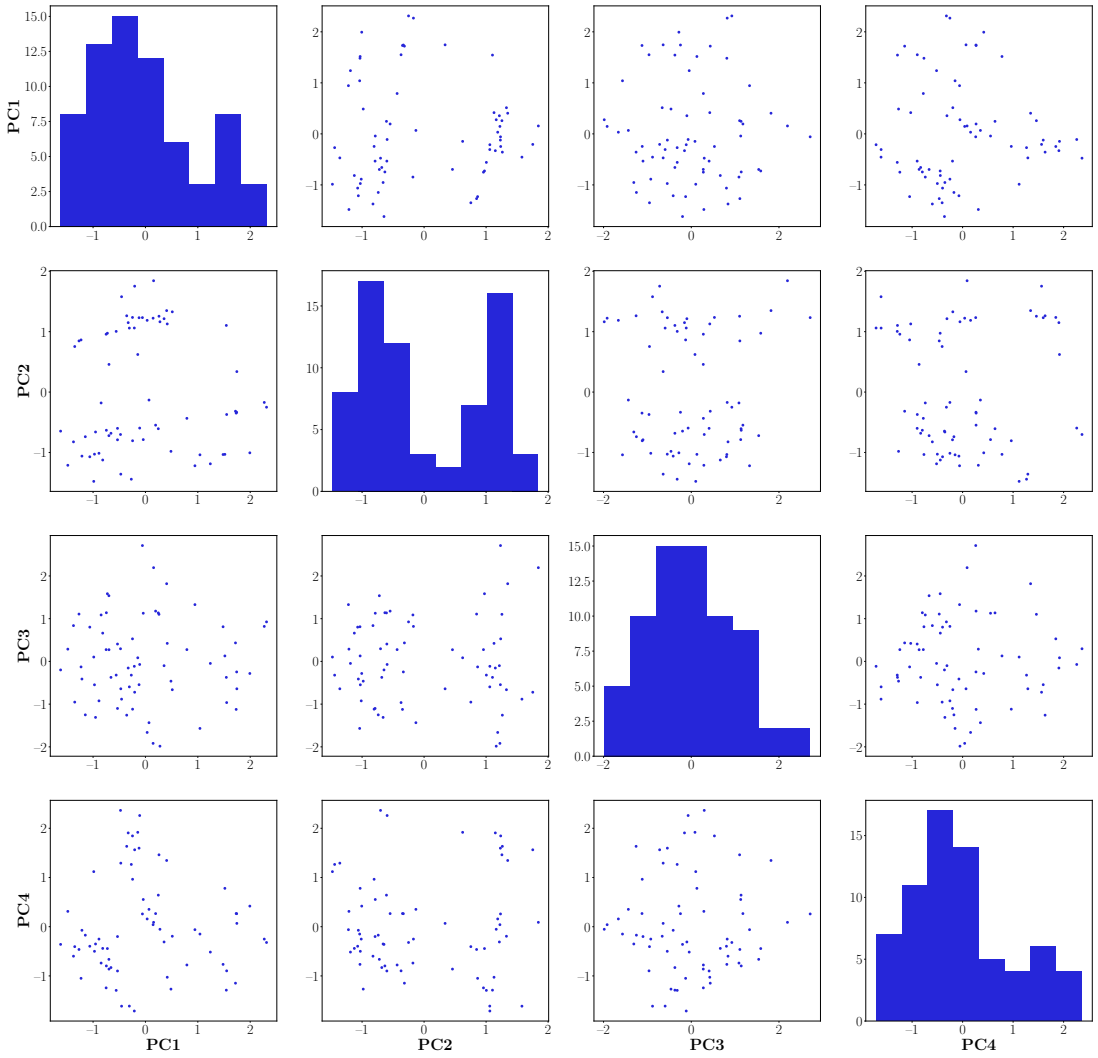

Figure 6.2 – PC scores of the OCP signals for Dataset_1 (reprinted from [**?**]).

First, the matrix of OCP responses **X** was transformed through PCA. The resulting PCs were sorted in decreasing order, according to the amount of explained variance in **X**. The scatter plots of the PC scores are shown in Fig. 6.2 for the smallest training set Dataset_1. We observe that the whitened PC scores are uncorrelated and do not present higher order dependence. Moreover, the explained variance per PC yields 34.23%, 24.51%, 21.39%,

and 19.87%, for PC1 to PC4, respectively. This indicates that the four PCs explain a significant amount of variance in the data, and should all be considered. Therefore, PCA is expected to be employed as a pre-processing step in order to remove higher order correlations in OCP signals, rather than a dimensionality reduction technique (the matrix dimension is not large, P = 4).

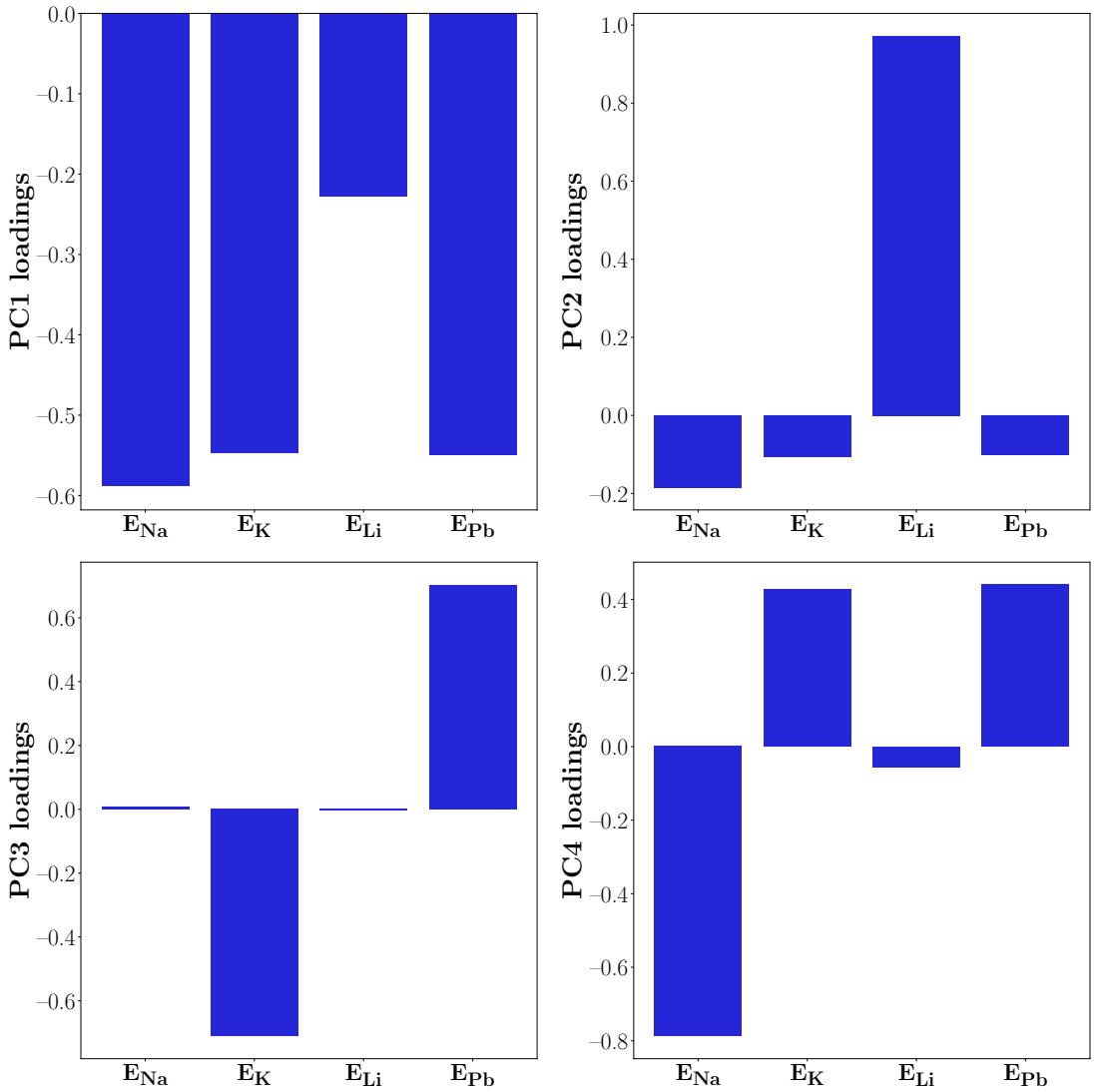

Figure 6.3 – Principal component loading vectors of the OCP signals for Dataset_1.

Next, the loading vectors on which the data was projected are shown in Fig. 6.3, for the OCP signals of Dataset_1. They indicate the contribution of the OCP signals to each PC. We observe that all features have significant loading weight on the first PC, then the contributions are more disparate for the other PCs. This suggests that the four PCs need to be considered to avoid losing information from the multivariate signals. Besides, the accuracy of the PCA model was assessed by computing the residual distance between the samples from the original matrix **X**, and their projection on the PC loadings.

Indeed, the PCA hyperplane was built as a best-fit of the original matrix. The matrix of residual error is merely $\mathbf{E} = \mathbf{X} - \mathbf{T} \cdot \mathbf{P}^{\mathrm{T}}$, where $\mathbf{T}$ and $\mathbf{P}$ are the PC scores and loadings, respectively. The residual error for each sample is

$$\mathrm{pca\_res_i} = \sqrt{(\mathbf{x_i} - \mathbf{t_i} \cdot \mathbf{p_i}^{\mathrm{T}})^{\mathrm{T}} \cdot (\mathbf{x_i} - \mathbf{t_i} \cdot \mathbf{p_i}^{\mathrm{T}})}\,, \tag{6.9}$$

where $\mathbf{T}$ and $\mathbf{P}$ are matrices of dimensions (N × A) and (P × A), respectively, where A is the number of PCs considered. An analysis was carried out, evaluating the effect of A on the accuracy of the PCA model. The results are displayed in Fig. 6.4.

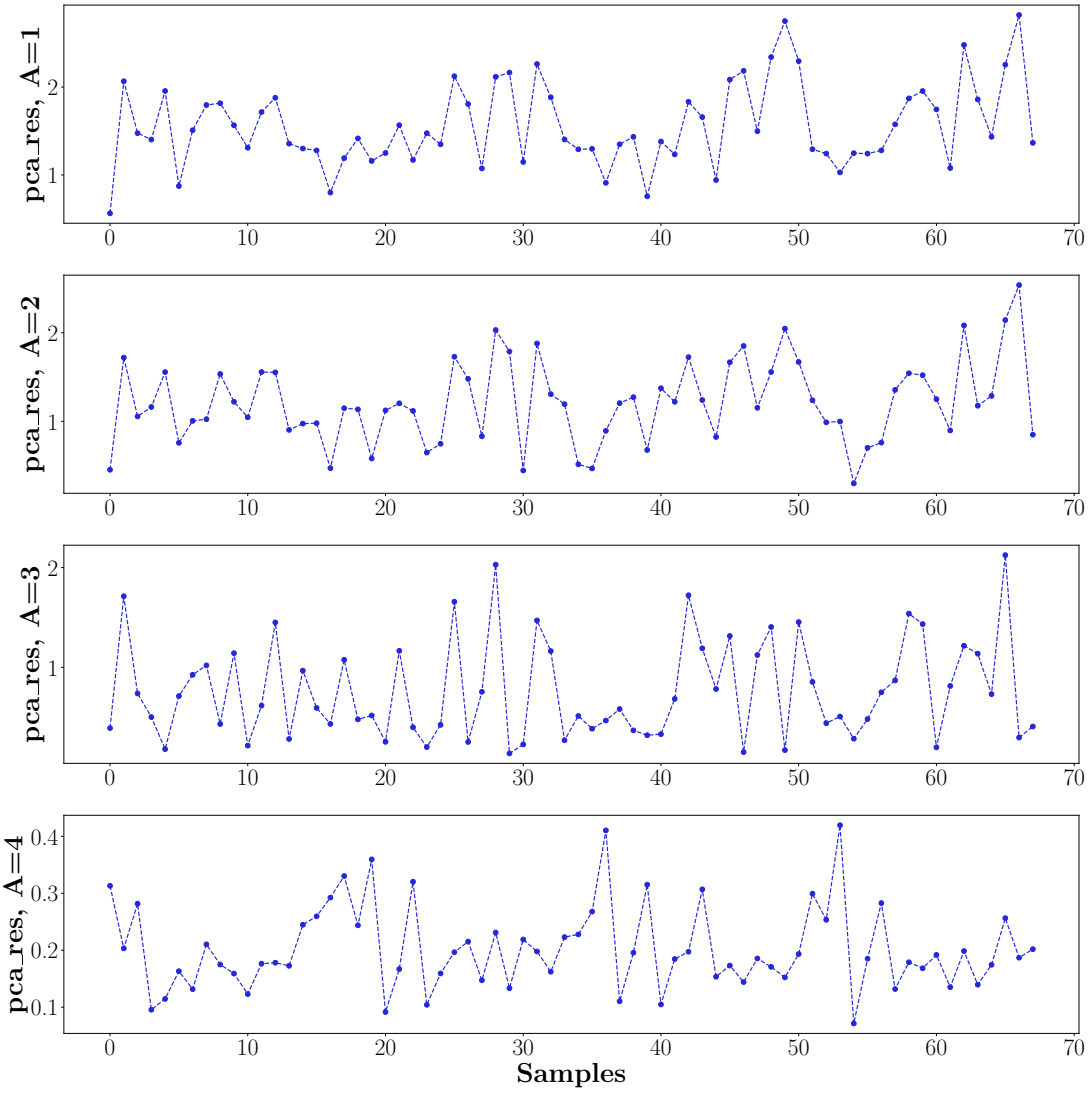

Figure 6.4 – Effect of the number of principal components on the accuracy of the PCA model.

We observe that the residual error for each sample is large for A < 4, and is greatly

reduced when all PCs are considered in the model, enhancing the importance of keeping the four PCs. The amount of variance explained by the PCA model over the variance already present in $\mathbf{X}$, defined as

$$R^2_{pca} = 1 - \frac{\text{var}(\mathbf{X} - \mathbf{T} \cdot \mathbf{P}^T)}{\text{var}(\mathbf{X})}, \tag{6.10}$$

was also computed, and yields 0.33, 0.58, 0.79, and 0.99, in the four cases. Moreover, similar conclusions were observed for the factorial decomposition of $\mathbf{X}$ with all ten datasets.

Multiple linear regression

The multivariate calibration of the four primary ions was implemented with MLR. The regressor was fitted to the training set, and the metrics defined in (6.1) and (6.2) were computed with the external test set. The results are reported in Table 6.2.

Table 6.2 – Prediction accuracy obtained by applying MLR to datasets of different size

Dataset	log a_{Na^+}		log a_{K^+}		log a_{Li^+}		log $a_{Pb^{2+}}$		**Total**	
	NRMSE	MRE	NRMSE	MRE	NRMSE	MRE	NRMSE	MRE	**NRMSE**	**MRE**
Dataset_1	3.64	3.04	9.72	8.19	3.11	2.76	6.68	5.82	**23.15**	**19.81**
Dataset_2	4.32	3.61	8.22	7.23	2.84	2.61	6.33	4.96	**21.71**	**18.41**
Dataset_3	3.76	3.40	8.74	7.15	3.00	2.52	5.44	4.36	**20.94**	**17.43**
Dataset_4	3.72	3.07	7.33	6.56	3.18	2.47	5.66	4.71	**19.88**	**16.81**
Dataset_5	3.17	2.59	8.92	7.85	2.60	2.21	5.17	3.85	**19.86**	**16.49**
Dataset_6	3.02	2.47	8.24	6.81	2.72	2.28	5.31	4.11	**19.29**	**15.68**
Dataset_7	3.55	2.99	7.21	5.95	3.68	2.20	4.98	4.10	**19.41**	**15.23**
Dataset_8	3.51	2.94	8.21	5.31	2.21	1.80	5.08	4.11	**19.02**	**14.16**
Dataset_9	3.14	2.63	6.98	5.15	3.36	1.98	5.04	4.11	**18.52**	**13.87**
Dataset_10	3.35	2.87	7.16	5.30	3.42	1.77	4.13	3.46	**18.06**	**13.40**

It is highlighted that potassium and lead ions calibrations are less accurate, due to the non-linear distortion added by severe ion interference in the emulated samples. Besides, the metrics are improving steadily with larger datasets, for the four target ions. The metrics obtained with MLR were used as benchmark for the subsequent multivariate regressors implemented.

Linear regression leveraging factorial decomposition

Then, multivariate calibration was implemented with PCR and PLS, that involve a factorial decomposition of the input matrix $\mathbf{X}$ for PCR, and both $\mathbf{X}$ and $\mathbf{Y}$ for PLS regression. An analysis of the impact of A (the amount of PCs constructed) on the accuracy of the multivariate regressors was implemented with a pseudo cross-validation procedure. Namely, the linear models were fitted to the orthogonal training set, then

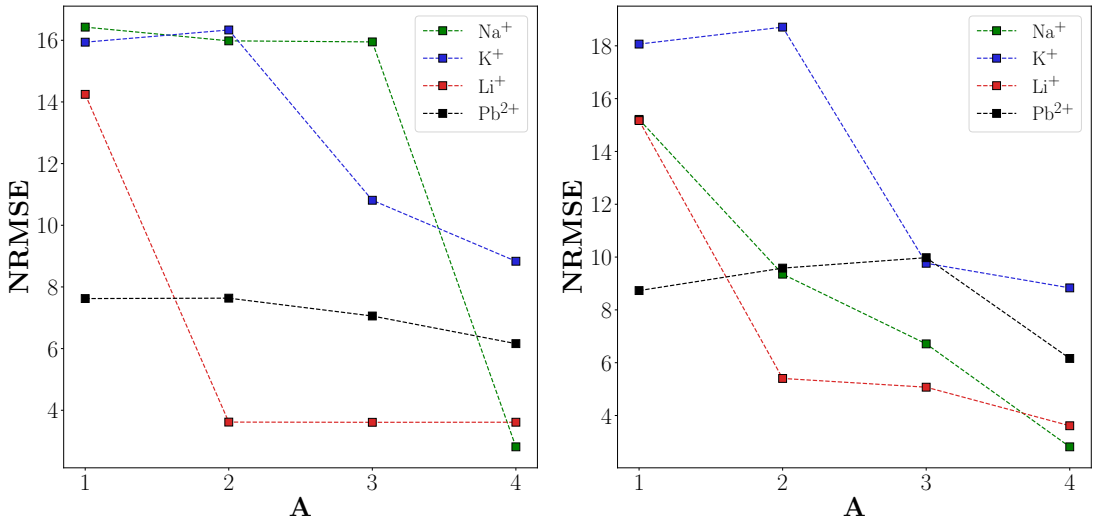

(a) Effect of the number of PCs on the accuracy of PCR (left) and PLS (right) for each primary ion.

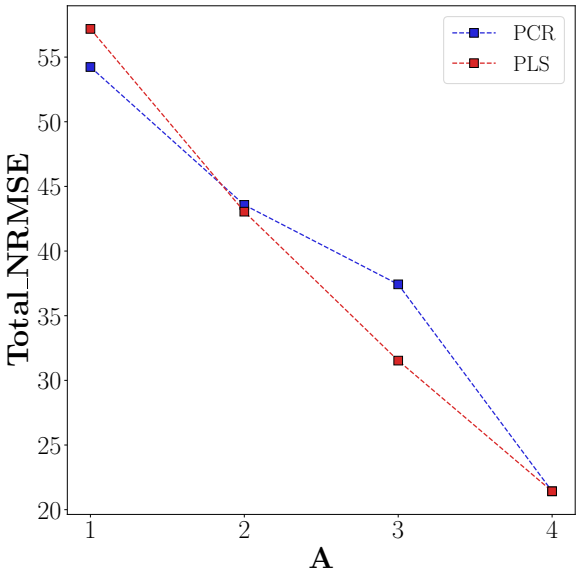

(b) Comparison between PCR and PLS.

Figure 6.5 – Effect of the number of principal components on the accuracy of PCR and PLS regressors.

they were evaluated on five validation sets of one-fifth of size of the training set each. The mean NRMSE and MRE were computed for each primary ion. The results are shown in Fig. 6.5, where the NRMSE is plotted for each primary ion in Fig. 6.5.a, and the Total NRMSE is reported for comparison in Fig. 6.5.b. The NRMSE obtained by both PCR and PLS decrease with A. In particular, for PCR, the impact of the loading weights is highlighted for each primary ion. For instance, the PC loading plots of Fig. 6.3 show that the variance in sodium OCP signals is explained mostly by the fourth PC. The NRMSE observed while performing PCR with the three first PCs is around 16, and

it drops to 2.8 when the fourth PC is considered. Likewise, lithium OCP signals are explained by the two first PCs. Thus, the NRMSE drops when A = 2. This remark is not applicable to PLS regression, because the latent variables were constructed by taking into account the variance explained by **X**, but also the correlation between **X** and **Y**. The correlations between the latent variables are shown in Fig. 6.6, for the training and test set of Dataset_1. The correlation coefficients are also reported, indicating that the correlation between **X** and **Y** scores tends to decrease with less important factors.

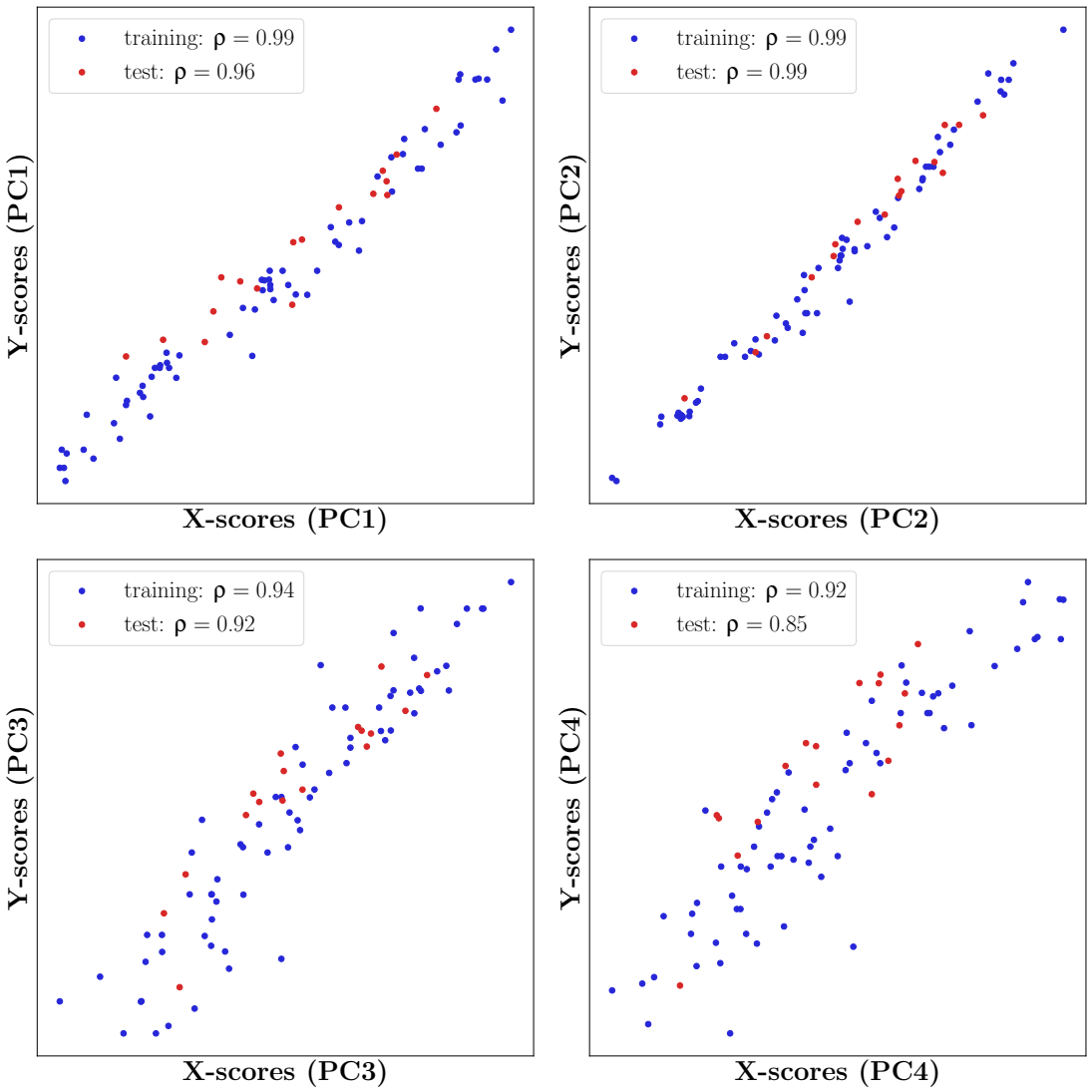

Figure 6.6 – Correlation between X-scores and Y-scores using PLS on Dataset_1.

Moreover, Fig. 6.5.b shows that PLS regressor is more compact than PCR. The Total NRMSE linearly decreases with A, and PLS usually performs better than PCR with fewer PCs. However, same metrics are obtained when the maximum amount of PCs were built. Indeed, the columns of **Y** are uncorrelated since they have been created with an orthogonal design of experiments. Therefore, the main advantages of PLS, that is,

better accuracy and robustness when the columns of **Y** are strongly correlated, are not exploited in this case study. Identical conclusions were drawn with the other datasets.

6.3.2 Non-linear regression models

Next, the multivariate calibration of the four primary ions was optimized by using the machine learning models presented in Section 6.2. Namely, the accuracy achieved by the proposed M-SVR on the ten emulated synthetic datasets was compared with single-output SVRs, MLP model, and traditional MLR. A cross-validation grid-search on the model hyper-parameters was carried out for the optimization of the calibration models, while limiting overfitting. Namely, for each set of model hyper-parameters, the multivariate regressors were trained with the entire orthogonal training set, and evaluated on the validation set that comprises five splits of one-fifth of size of the training set each. Then, the metrics (6.1) and (6.2) were computed and averaged. The ten best models were then evaluated independently on the external set, yielding the metrics Total NRMSE and Total MRE. For MLP models, the hyper-parameter space being wide, a coarse search was done before refining the grid-search on the relevant hyper-parameter space. The results of multivariate calibration on the datasets of different size are displayed in Fig. 6.7.

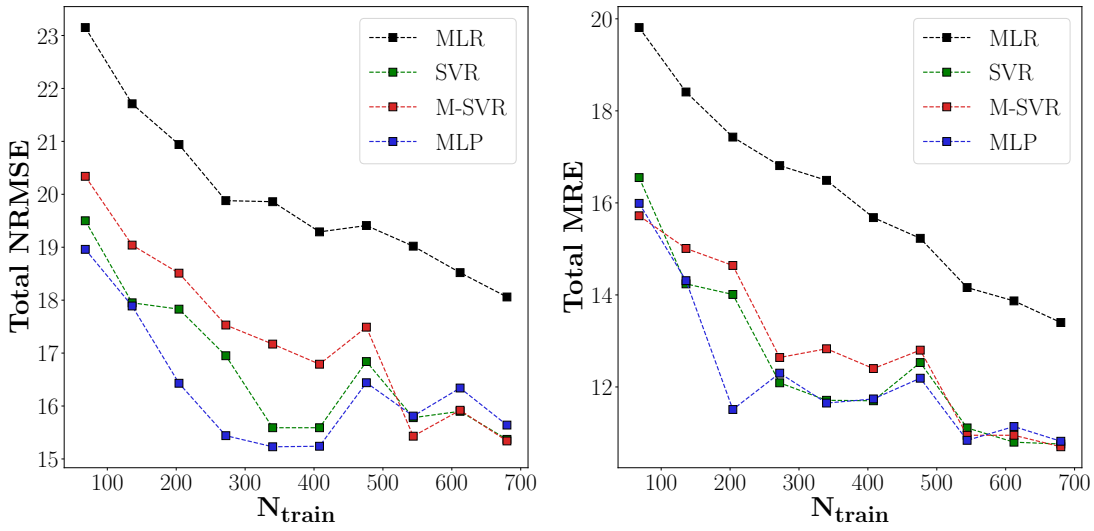

Figure 6.7 – Total NRMSE and Total MRE obtained by evaluating the best multivariate calibration models on the external test set of the ten emulated synthetic datasets (reprinted from [**?**]).

We observe a net improvement between linear and non-linear regressors. For Total NRMSE, there is an average improvement of 16.27%, 13.22%, and 18.12%, and for Total MRE, an amelioration of 22.23%, 20.29%, and 23.92%, for SVR, M-SVR, and MLP model, respectively. The accuracy enhancement achieved by the proposed M-SVR is satisfactory given the lower complexity of the proposed model. Namely, M-SVR optimizes concurrently the calibration of the four target ions with four-dimension support vectors.

Conversely, single-output SVRs optimize independently one ion calibration at a time with one-dimension support vectors. Hence, with four times more support vectors than with M-SVR. Besides, M-SVR is more robust to noise and correlation in the dataset since it considers the four ion activity when constructing the model regression hyperplane. We also observe that with large datasets (more than 540 training samples), M-SVR performs better than SVR and MLP regressors.

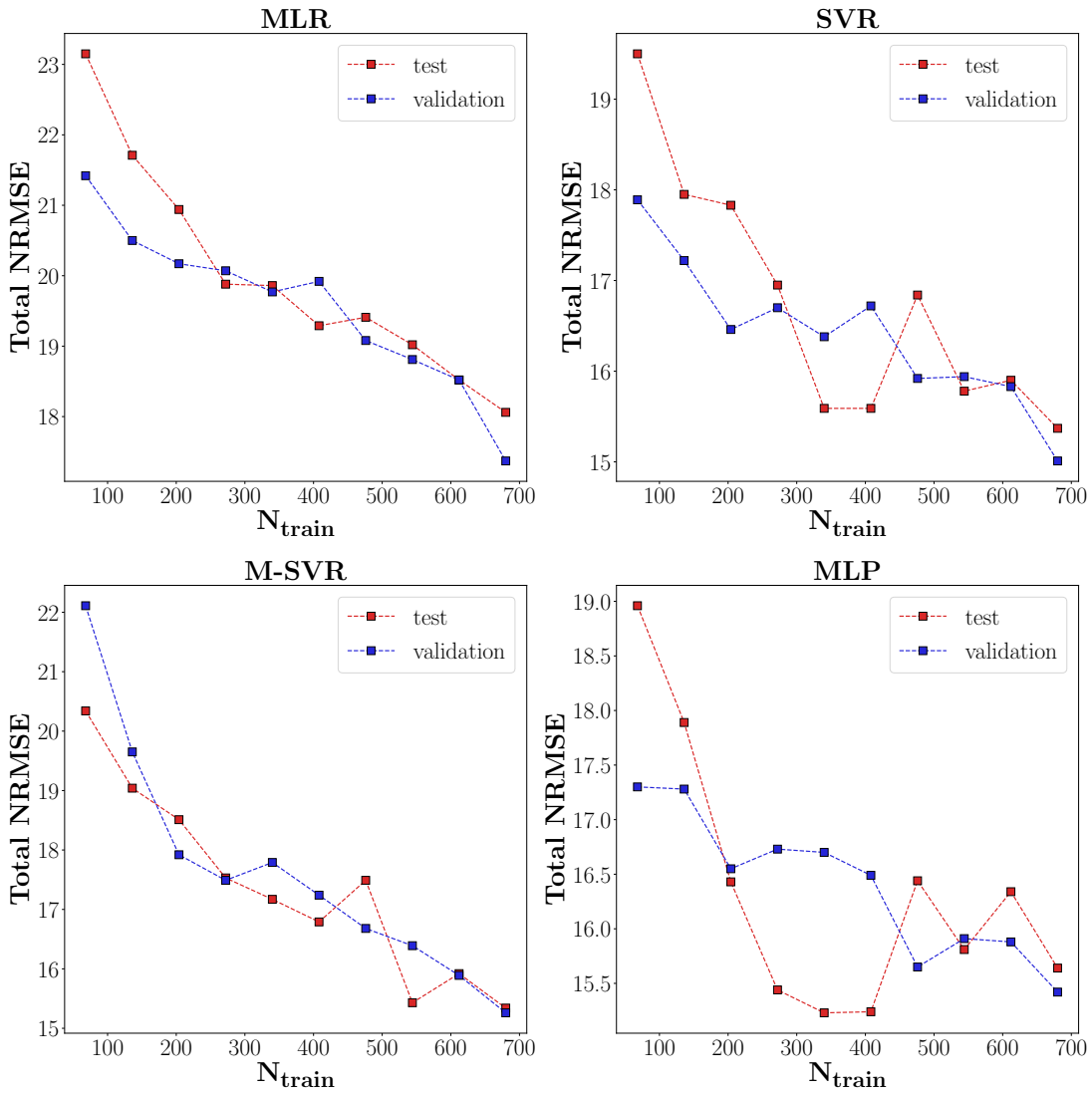

Figure 6.8 – Total NRMSE achieved during the validation phase and during inference (reprinted from [**?**]).

Next, the generalization error of the multivariate regressors was assessed by comparing the metrics obtained during the validation phase (metrics computed on five validation splits of randomly distributed samples), and during inference (metrics computed with the external test set). The results are displayed in Fig. 6.8, highlighting a large generalization error with scarce datasets, for which the models are more likely subject to overfitting.

Overall, the generalization error is the smallest for M-SVR, with an average of 3.22%, while it is of 4.43% and 4.79%, for SVR and MLP models, respectively.

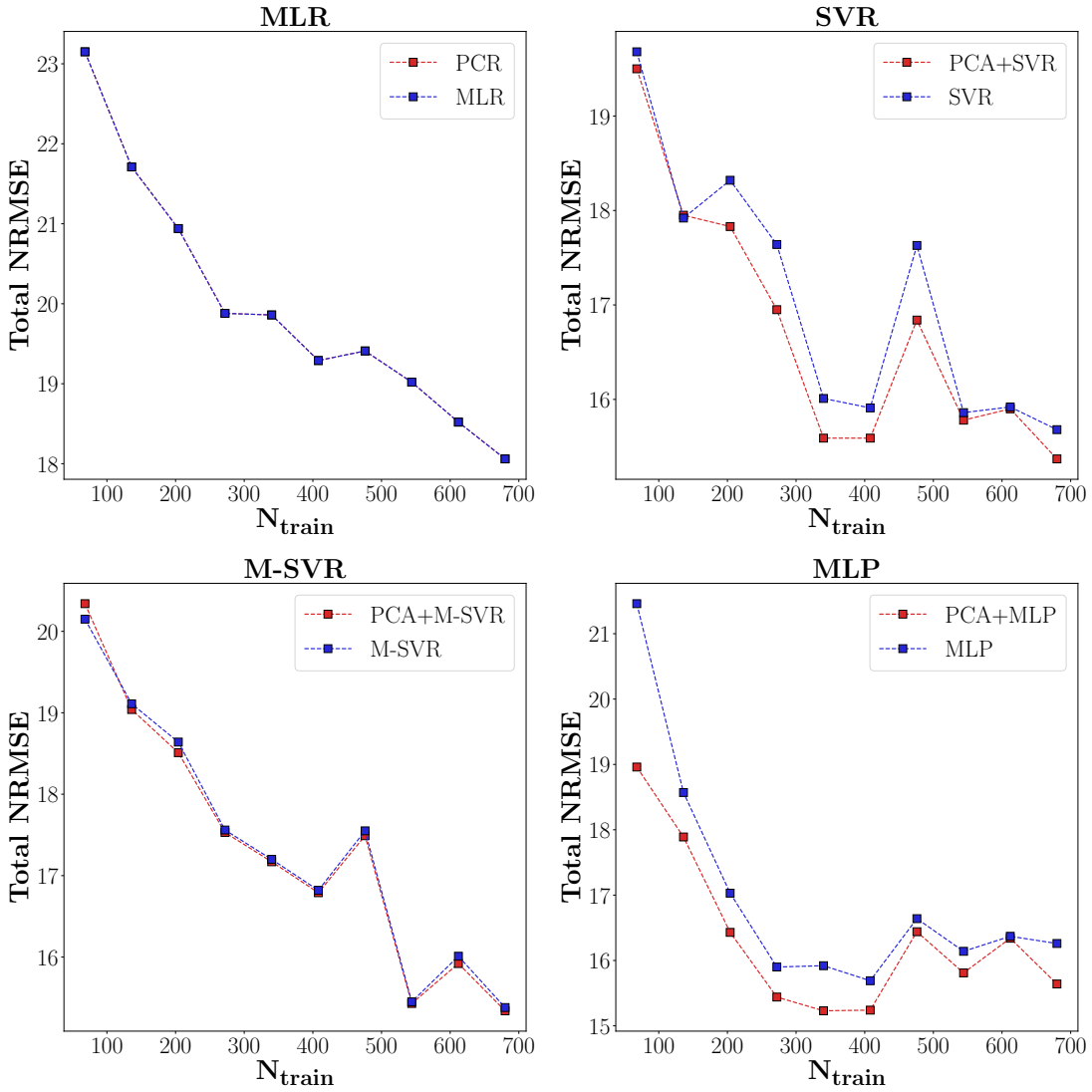

Figure 6.9 – Total NRMSE achieved with and without PCA pre-processing (reprinted from [**?**]).

Furthermore, the importance of transforming the input OCP signals through PCA prior to the multivariate calibration was evaluated. The metrics obtained with and without factorial decomposition of $\mathbf{X}$ are reported in Fig. 6.9. The raw matrix $\mathbf{X}$ was standardized to zero-mean and unit-variance in both experiments. We observe that PCA does not influence the calibration accuracy for both MLR and M-SVR that rely on OLS regressions. Instead, an improvement is observed with SVR and MLP models. Indeed, MLP regressors are feature-based models, so the pre-processing of the input matrix is paramount in order to feed uncorrelated data to the FFNN model. SVR models are distance-based models, so scaling the input matrix is the essential pre-processing step.

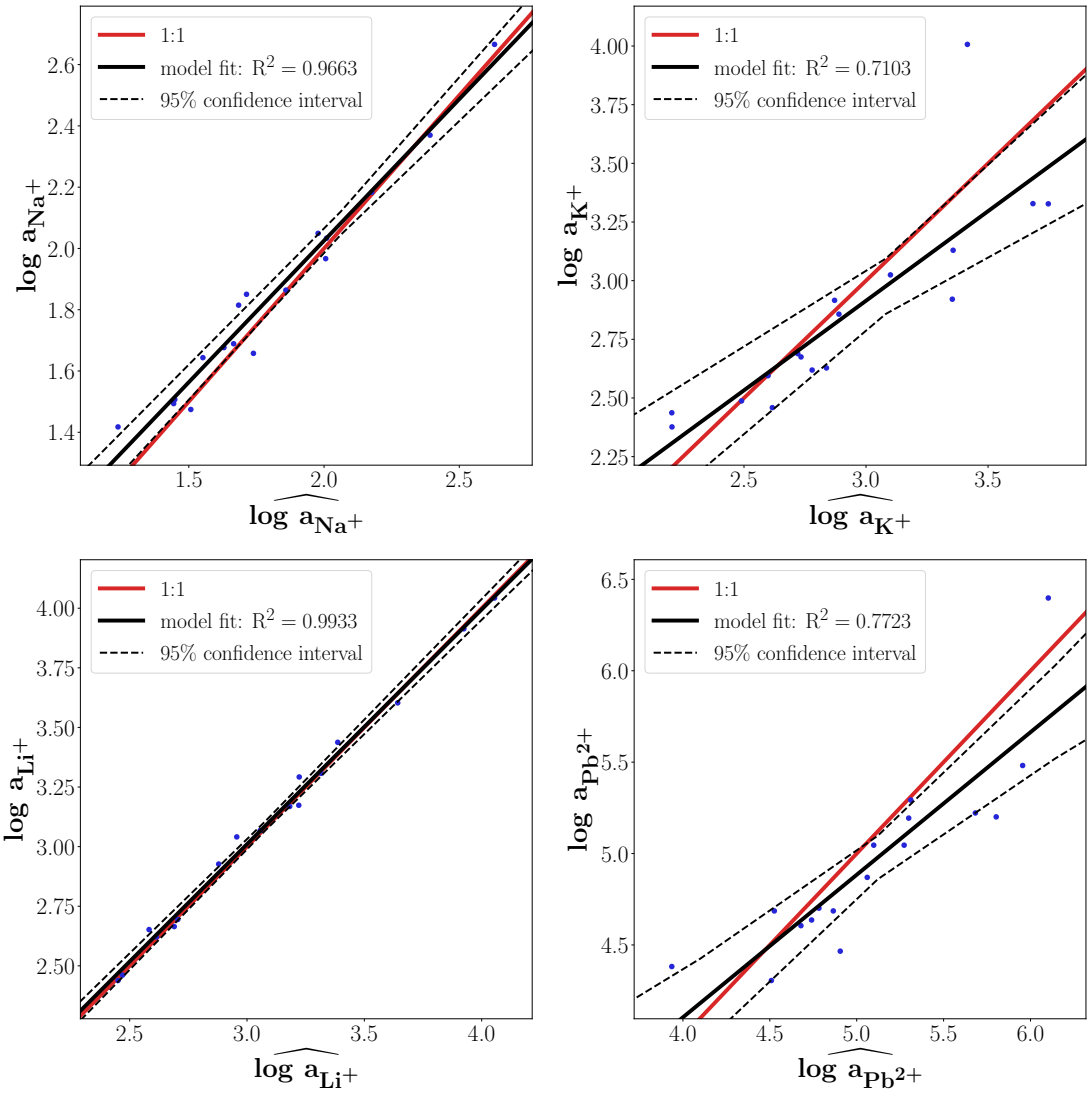

Figure 6.10 – Predicted ion activity and ground truth by applying M-SVR on Dataset_1. The model fit and its 95% confidence interval are plotted, where R^2 is the coefficient of determination. The red plot is the 1:1 line (reprinted from [**?**]).

Moreover, the goodness-of-fit and consistency of the proposed M-SVR model was evaluated. Namely, the ground truth ion activity is plotted against the values predicted by the multivariate regressor, on Dataset_1 and Dataset_10, in Fig. 6.10 and 6.11, respectively. The linear fitting of the scatter points was performed, and the 95% confidence interval of the model fit was computed. The coefficient of determination of the linear fit was calculated as well. The scatter points fall along the 1:1 lines, with more dispersion for potassium and lead ions calibration that are hindered by ion interference. For Dataset_1, the 95% confidence interval on the slopes of the model fit contains 1 for both calibration of lithium and lead ions, and all intercepts contain 0 except for lead ions. These results are consistent with the aforementioned conclusion that M-SVR models are less accurate with

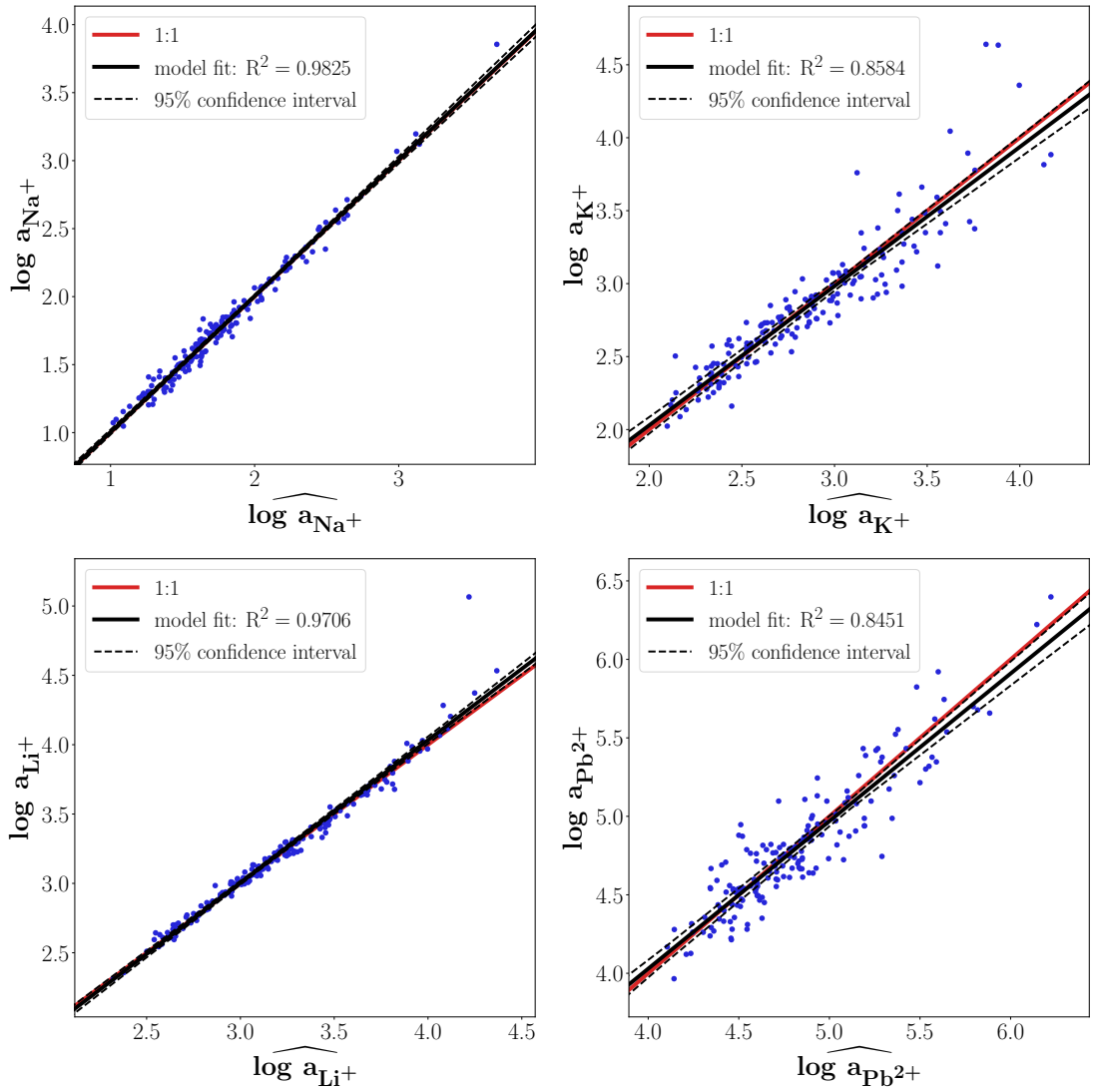

Figure 6.11 – Predicted ion activity and ground truth by applying M-SVR on Dataset_10. The model fit and its 95% confidence interval are plotted, where R^2 is the coefficient of determination. The red plot is the 1:1 line (reprinted from [**?**]).

scarce datasets since the models are biased. Regarding the largest dataset Dataset_10, the 95% confidence interval on the slopes of the model fit contains 1, and the intercepts contain 0 for the calibrations of the four primary ions. Therefore, M-SVR is an accurate and unbiased estimator for larger datasets. Besides, the coefficient of determination of the linear fit provides reliable information about the variance in target ion activity that is explained by the multivariate calibration model.

Table 6.3 – Training parameters of the multivariate calibration models

N_{train}	**MLR** # train. param.[1]	**SVR** # supp. vect.[2]	**M-SVR** # supp. vect.[2]	**M-SVR** # IRWLS iterations	**MLP** # train. param.[1]	**MLP** # train. epochs[3]
68	16	251	68	5	1329	96
136	16	543	125	5	3004	365
204	16	814	204	12	1604	187
272	16	1024	272	9	2179	235
340	16	1360	340	4	2579	177
408	16	1632	408	10	1904	221
476	16	1904	476	17	1229	192
544	16	2176	544	5	1104	203
612	16	2446	612	17	3179	223
680	16	2720	680	4	3179	209

[1] trainable parameters [2] support vectors [3] training epochs

6.3.3 Analysis of model complexity

The complexity of the multivariate calibration models is an essential feature to consider prior to deploying the model onto energy-constrained edge devices, for online training and real-time ion monitoring. The trainable parameters of the multivariate calibration models implemented are reported in Table 6.3. MLR models has $M \cdot P = 16$ trainable weights, independently of the size of the training set, and OLS minimization has a complexity of $\mathcal{O}(NM^2)$. The complexity of single-output SVRs is reflected by the number of support vectors needed to build the regression hyperplane. More accurate models were obtained with small ε hyperplane margin tolerance. As a result, most of the training instances were used as support vectors. Besides, four independent regressors are constructed by single-output SVRs, justifying the linear growth of the amount of support vectors used with larger training sets. Conversely, M-SVR provides four-dimension support vectors, for each training instance, since the activity of the four primary ions are considered simultaneously. Moreover, the complexity of an IRWLS procedure is equivalent to an OLS minimization per iteration. The number of iterations performed to reach a converging solution is reasonable (less than 20 with the 10 datasets). As for MLP models, the model complexity is set by the number of neurons in the neural network architecture. The amount of trainable parameters (weights and bias) that are optimized during the training phase is quite large, and tends to grow with larger datasets. The number of epochs before early-stopping (training is stopped when the mean-squared loss function does not improve, up to a certain tolerance) is also reported. It does not exceed 365 epochs for a training batch size of 32 samples.

Moreover, the training runtime of the different models was measured in order to compare the model complexity quantitatively. Namely, the multivariate regressors were trained 100

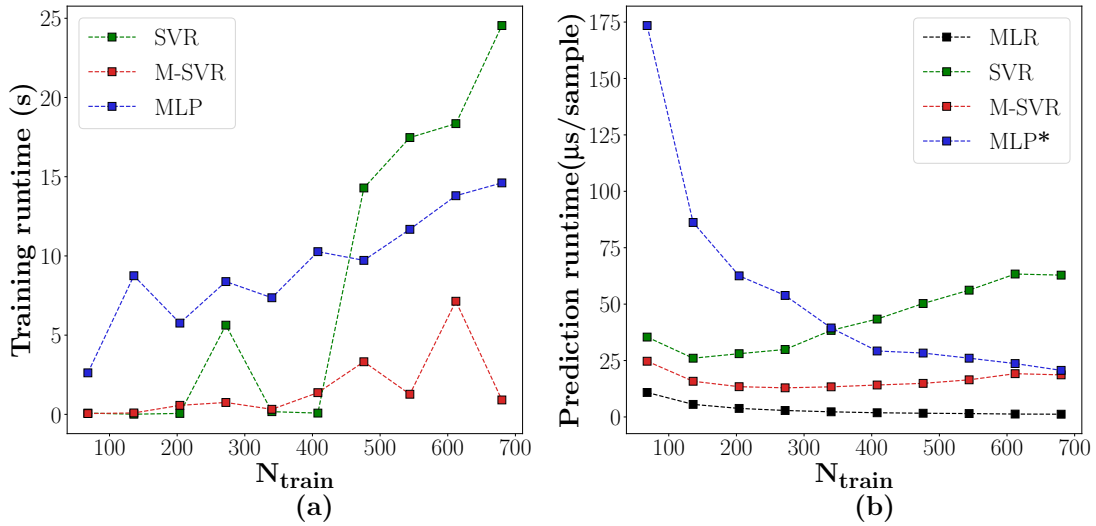

Figure 6.12 – Analysis of multivariate calibration model complexity: training runtime **(a)**, and prediction latency **(b)** (reprinted from [**?**]). * values divided by 10

times, on the 10 datasets, with the best hyper-parameters found during the grid-search procedure. The results are displayed in Fig. 6.12.a. The training runtime of MLR models is not reported since it is constantly between 300 and 450 µs. We observe that the training runtime of SVR models is relatively fast for scarce datasets, but it increases geometrically with the number of training samples, beyond 400 samples. Instead, the training runtime of M-SVR models does not grow excessively and remains below 8 s. As for MLP models, they are the longest to train for scarce datasets, and the runtime grows steadily with the training set size. In addition, the prediction latency of each model was measured for 100 runs, and normalized by the number of samples constituting the test set. The results are reported in Fig. 6.12.b. The prediction latency is obviously the shortest for MLR models. M-SVRs are compact models, so the prediction latency is inferior to 20 µs/sample. On the other hand, single-output SVRs embed M dense models, explaining the larger latency. Neural network models have the largest prediction latency (scale divided by 10 in Fig. 6.12.b), making these models the less suitable for real-time monitoring applications.

6.4 Summary and main contributions

The machine learning models implemented to improve the multivariate calibration accuracy of multi-ion-sensors hindered by severe ion interference was presented in this chapter. A case study was performed for the analysis of emulated synthetic datasets of sodium, potassium, lithium, and lead ions in artificial sweat sample compositions, with datasets of 68 to 680 training instances. The main contributions are summarized hereunder:

- **Multivariate linear regressors** were built as independent multiple linear estimators of each primary ion activity. Such MLR models are traditionally employed in sensor calibration, thus they were used as baseline to assess the accuracy improvement of the proposed calibration models. The prediction accuracy of the linear calibration model increases with the size of the dataset.

- The **factorial decomposition** of the emulated OCP signals was studied. Such processing method yields uncorrelated input matrices that are prominent for feature-based regressors such as neural network models. It can also be useful with a large sensor array, since it accumulates the variance explained in the original matrix in few orthogonal PCs, hence reducing the dimensionality of the multivariate calibration problem. This feature was not exploited in the case study involving four primary ions. Indeed, the variance in the OCP signals of the emulated datasets was explained by the maximum number of PCs (A = 4). Moreover, multivariate regression leveraging latent variables was investigated through PCR and PLS models. The latter was implemented with a common NIPALS-PLS algorithm that does not involve matrix inversion and singular/eigenvalue decomposition, as in typical OLS methods. The advantages of PLS, i.e. robustness and model compactness, could not be exploited thoroughly since the ion activity in the synthetic datasets were uncorrelated (designed with orthogonal arrays).

- A **M-SVR** model was proposed as an **accurate**, **robust**, and **low-complexity** solution for the multivariate calibration task. Indeed, it achieves NRMSE improvement of 13.22%, and MRE improvement of 20.29%, with respect to the baseline MLR model. The generalization error is quite small, being of 3.22%, in average for the ten datasets, and the regressor is statistically unbiased for medium to large datasets. Moreover, the proposed regressor is more compact and more robust than a standard SVR that constructs four independent regressors for the estimation of the activity of the four primary ions. Such single-output SVRs do not consider the correlations between ion activity, and above all, its computational complexity increases geometrically with the training set size. Instead, M-SVR is a multivariate multi-output regressor that is constructed with both multivariate matrices $\mathbf{X}$ and $\mathbf{Y}$. This enables the consideration of cross-dependence between the columns of both matrices, which is especially effective with scarce or noisy datasets. M-SVR involves an IRWLS procedure implemented in a quasi-Newton method, where each iteration has the complexity of an OLS minimization. The algorithm converges in typically less than 20 iterations with all dataset size. In addition, the use of a squared loss function provides a compact model with four-dimension support vectors. Its training runtime and prediction latency are much lower than neural network models and standard SVR models. Therefore, the presented M-SVR model is an accurate, robust, and low-complexity solution, appealing for memory and energy-constrained embedded devices used for continuous and real-time multi-ion monitoring.

7 Real-time multi-ion-monitoring front-end interface for accurate physiology

A continuous and real-time physiological status insight is critical for intensive physical activity applications, where the monitoring of relevant ions enables the assessment of the level of dehydration, muscle fatigue, aerobic performance, and electrolyte balance [**?**]. Sodium, potassium, ammonium, and calcium ions are the biomarkers considered for these purposes. Unfortunately, multi-ion-sensing in complex samples such as artificial sweat is hindered by ion interference that greatly degrades sensing accuracy. Therefore, an electronic tongue system is proposed, where a multi-ion-sensing front-end interface is coupled to an edge node, on which a multivariate calibration model is deployed in order to increase the prediction accuracy of the ion activity of the analytes. The embedded device enables the real-time monitoring of the target ions, and the sharing of the data onto cloud platforms, in an IoT context.

7.1 System overview

The electronic tongue system proposed for real-time multi-ion-monitoring is illustrated in Fig. 7.1. The several building blocks are discussed in the sequel of this section.

7.1.1 Multi-ion-sensor panel

The multi-ion-sensor panel consists of four solid-contact ISEs built on SPEs, enabling the monitoring of sodium, potassium, ammonium, and calcium ions. The fabrication and characterization (sensitivity, LOD, selectivity) of the developed sensors in pure water and artificial sweat samples was thoroughly described in Chapter 4. A double-junction Ag/AgCl/KCl (3 M)/LiOAc (1 M) RE from Metrohm (Switzerland) was used in all subsequent experiments. These sensors were chosen for such in vitro multi-ion-monitoring task in artificial sweat samples because of their robustness that enables massive experimental data acquisition.

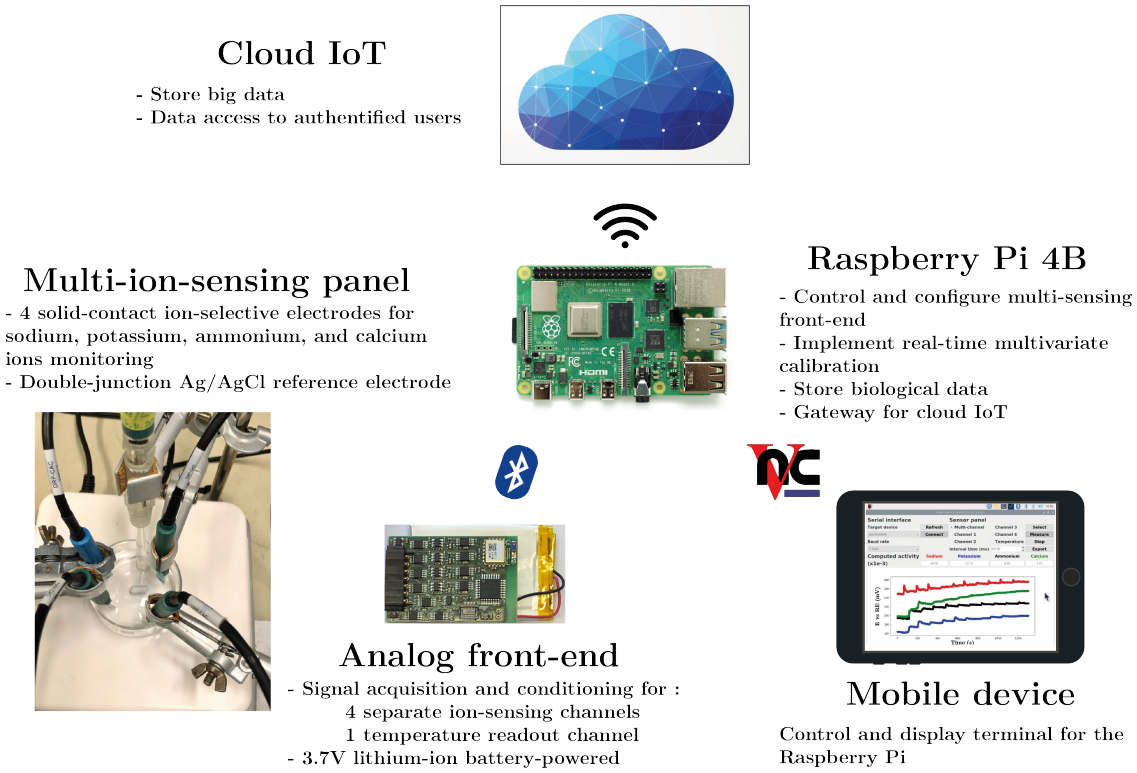

Figure 7.1 – Multi-ion-monitoring front-end for accurate and real-time physiology.

7.1.2 Analog front-end

The sensing array was interfaced to an analog front-end carrying out OCP acquisition and signal conditioning. The description of the readout circuit and its characterization with the fabricated ion-sensors was thoroughly presented in Chapter 4. Micro USB-B connectors were soldered for the measurements performed with the SPEs. The hardware was powered by a 3.7 V 2 Ah lithium ion battery.

7.1.3 Edge node

A Raspberry Pi 4B was used as an edge node to configure the front-end readout circuit, and to perform the real-time determination of the ion activity of the four analytes through the M-SVR model deployed on the device. The hardware supports a 64 – bit quad core Cortex-A72 processor (armv71 architecture), with 4 GB LPDDR4 RAM. It features Bluetooth® 5.0 BLE, and 2.4 GHz and 5.0 GHz IEEE 802.11ac wireless connectivity. An external 32 GB micro-SD card was used to store the Raspbian operating system image, open source software libraries, drivers, and applications. The measured data was locally saved into the memory card as well. A smartphone was used as display and control terminal of the *Raspberry Pi* (RPi) through a *Virtual Network Computing* (VNC) session. A GUI developed in PyQt5 was executed on the edge node, enabling the user

configuration of sensor measurements, and the continuous and real-time visualization of sensor OCPs and target ions activity.

Moreover, the RPi was used as gateway enabling the sharing of the measured multivariate OCPs to *Amazon Web Services* (AWS) Cloud. Namely, the gateway software AWS Greengrass core was installed and configured with temporary security credentials from an Identity and Acces Management role created on a AWS personal account. Then, the stream manager component was deployed to the edge node, and configured so as to export data streams to Amazon Simple Storage Service, where the collected data was stored and could be retrieved at anytime by authenticated users. Data streams exported by stream manager to the AWS Cloud leverage standard AWS service client encryption with Transport Layer Security.

7.2 Design and acquisition of synthetic datasets

First, a synthetic dataset was acquired in order to train, optimize, and evaluate the multivariate calibration models implemented.

7.2.1 Design of synthetic datasets

Table 7.1 – $OA_{16}(4^5)$

	$\mathbf{C_0}$	$\mathbf{C_1}$	$\mathbf{C_2}$	$\mathbf{C_3}$	$\mathbf{C_4}$
$\mathbf{R_0}$	0	0	0	0	0
$\mathbf{R_1}$	0	1	1	1	1
$\mathbf{R_2}$	0	2	2	2	2
$\mathbf{R_3}$	0	3	3	3	3
$\mathbf{R_4}$	1	0	1	2	3
$\mathbf{R_5}$	1	1	0	3	2
$\mathbf{R_6}$	1	2	3	0	1
$\mathbf{R_7}$	1	3	2	1	0
$\mathbf{R_8}$	2	0	2	3	1
$\mathbf{R_9}$	2	1	3	2	0
$\mathbf{R_{10}}$	2	2	0	1	3
$\mathbf{R_{11}}$	2	3	1	0	2
$\mathbf{R_{12}}$	3	0	3	1	2
$\mathbf{R_{13}}$	3	1	2	0	3
$\mathbf{R_{14}}$	3	2	1	3	0
$\mathbf{R_{15}}$	3	3	0	2	1

The training dataset should be representative of sweat compositions observed during intensive physical exercise, but acquiring big data is extremely expensive in terms of chemical resources and labor time. In this chapter, synthetic datasets were obtained both

Table 7.2 – Discrete levels of ion activity of the five constituting ions ($\times$1e – 3)

Ions	Na^+	K^+	NH_4^+	Ca^{2+}	Mg^{2+}
Det. range[1] ($\times$**1e – 3**)[**?**]	[20; 100]	[4; 24]	[0.5; 8]	[0.5; 3]	[0.04; 0.70]
Nom. act.[2] ($\times$**1e – 3**)	40	5	3.5	0.4	55e-3
L0	10	1	0.50	0.50	0.04
L1	25	5	2.12	1.25	0.16
L2	40	10	3.75	2.00	0.29
L3	55	15	5.37	2.75	0.41
L4	70	20	7.00	3.5	0.54
L5	85	25	8.62	4.25	0.66
L6	100	30	10.00	5.00	0.80

[1] Detection range [2] Nominal activity

experimentally with the aforementioned ion-sensing array, and through an ion-sensing emulator similar to the one described in Section 5.3.2, for comparison purposes. As a result, a factorial design of experiments was implemented with Taguchi method, in order to generate a subset of independent artificial sweat electrolyte compositions, leveraging the orthogonal array $OA_{16}(4^5)$ shown in Table 7.1. Namely, the five factors $C_0 - C_4$ represent the five constituting electrolytes, sodium, potassium, ammonium, calcium, and magnesium ions. The four levels in the orthogonal array correspond to quantized values of ion activity. Indeed, the detection range of each ion was subdivided into seven discrete activity, as reported in Table 7.2. The normalized quantized levels are displayed in Fig. 7.2.a, where the nominal activity in sweat is highlighted in red.

Moreover, eight four-level factors where used to design a synthetic dataset of $16 \cdot 8 = 128$ samples, that is large enough to train the M-SVR model accurately [**?**]. The selected factor combinations are shown in Fig. 7.2.b. As for the validation and test set, artificial sweat compositions were designed through random sampling over the range of activity of the constituting ions. A Weibull distribution (scale = 0.5, shape = 2) was used, yielding 32 random validation, and 32 random test samples.

7.2.2 Experimental synthetic datasets

The experimental dataset was obtained by acquiring ion-sensor responses in the synthetic samples previously designed. Namely, artificial sweat samples were prepared with the following background composition: urea (5 mM), L-Lactic acid (5 mM), D-glucose (100 µM), L-Ascorbic acid (10 µM), according to Table 4.3. The OCP of sodium, potassium, ammonium, and calcium sensors were measured in the blank sample. Then, the constituting ions were added successively in order to obtain the designed ion activity,

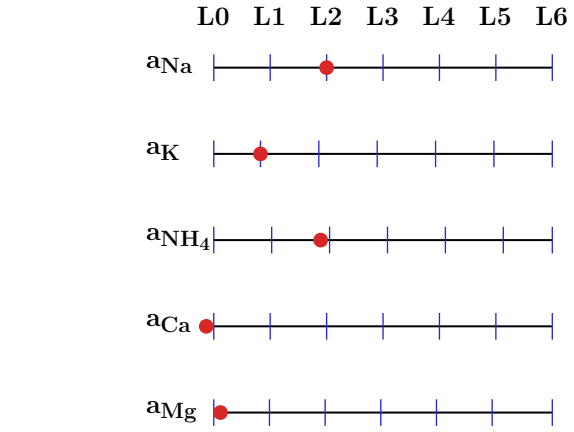

(a) Subdivision of the detection range of each constituting ion in seven levels.

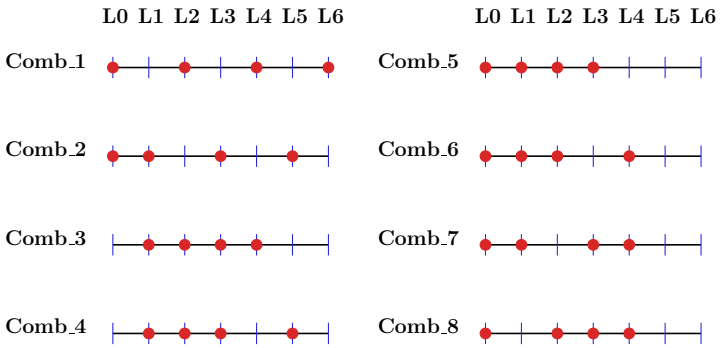

(b) four-level factors used for the design of the training set composition.

Figure 7.2 – Discrete levels of the activity of the ions constituting the orthogonal training set samples.

while measuring the OCPs of the sensors (magnesium ions were added in the sample, but only as interfering agents, since they were not monitored). The final multivariate sensor response was computed as the difference between the steady OCP in the synthetic sample, and the steady OCP in the blank. Such differential measurement reduces the impact of sensor drifts from one measurement to another (inter-sensor and inter-sample variability). The measurements were repeated three times with different sensors, for statistical significance. A typical time trace of sodium, potassium, ammonium, and calcium OCPs, while successively adding the constituting ions (sodium, potassium, ammonium, calcium, and magnesium ions, in this order) is displayed in Fig. 7.3. The addition of each electrolyte induces a large potential step for the corresponding sensor. Moreover, the impact of ion interference is highlighted by the potential steps observed when adding an interfering ion into the sample. Indeed, all ion-sensors react to the addition of sodium ions, that are prevalent in the sample ($a_{Na^+} = 29.20\,e-3$). The potential step is large for sodium-ISE, but the other polymeric ISEs exhibit a potential response as well. The

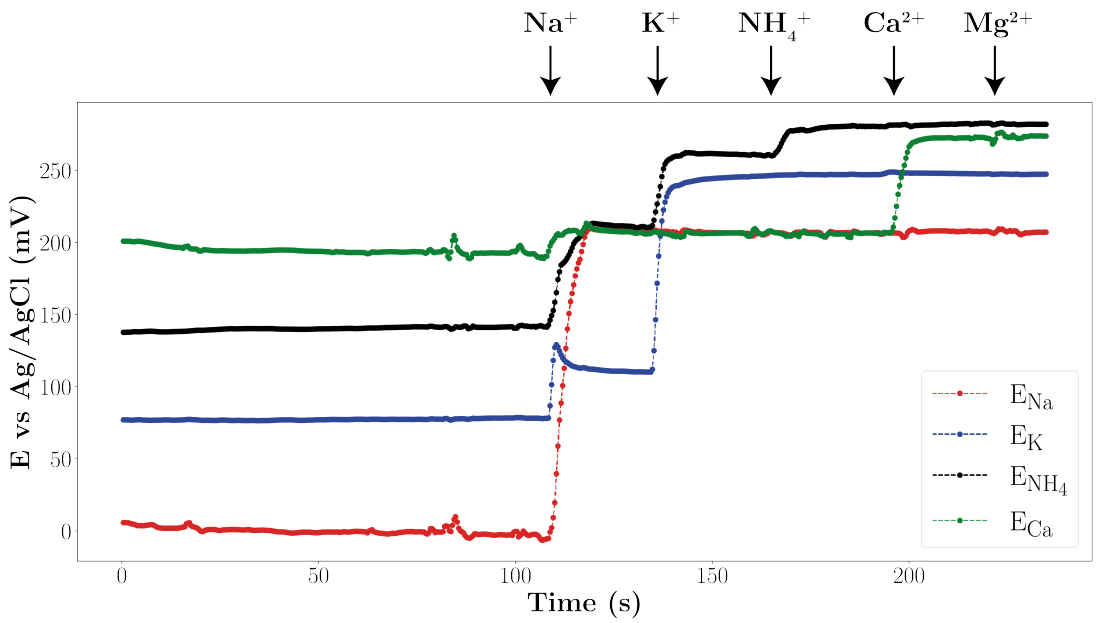

Figure 7.3 – Typical time trace of sodium, potassium, ammonium, and calcium OCPs while successively adding the constituting ions: $a_{Na^+} = 29.20\,e-3$, $a_{K^+} = 5.53\,e-3$, $a_{NH_4^+} = 1.71\,e-3$, $a_{Ca^{2+}} = 1.52\,e-3$, $a_{Mg^{2+}} = 70.0\,e-6$.

latter artifact is weighted by the selectivity coefficients of the developed ion-sensors.

Next, the correlation in the multivariate OCP response was investigated. The scatter plots of sensor responses, for the orthogonal training set, are displayed in Fig. 7.4. The Pearson correlation coefficients are reported as well, indicating that the OCP signals are uncorrelated. Therefore, no factorial decomposition of OCP signals was implemented. The application of PCA pre-processing did not improve the accuracy of the multivariate models, except for FFNNs.

The resulting experimental synthetic dataset is displayed in Fig. 7.5. The 128 training samples were designed with an orthogonal array, explaining the grouping of sensor responses around the seven discrete ion activity of each analyte. The Pearson correlation coefficients between the measured OCP signal and the ion activity, for the training set, are reported in Table 7.3. They reflect the non-linearity in the sensing channels caused by ion interference, that is highlighted by the potential dispersion in y-axis, in Fig. 7.5. The non-linear effect is enhanced at lower ion activity, as expected. Moreover, the potential response of potassium and ammonium sensors is greatly distorted by ion interference due to lower sensor cross-selectivity. Namely, selectivity coefficients $\log K^{pot}_{K^+,Na^+} = -0.66$, $\log K^{pot}_{K^+,NH_4^+} = -0.28$, $\log K^{pot}_{NH_4^+,Na^+} = -1.79$, and $\log K^{pot}_{NH_4^+,K^+} = -1.37$ were measured with FIM method, suggesting that the interfering ions have a higher contribution to the potential observed at these ISEs. As for the 32 validation and 32 test samples, they were

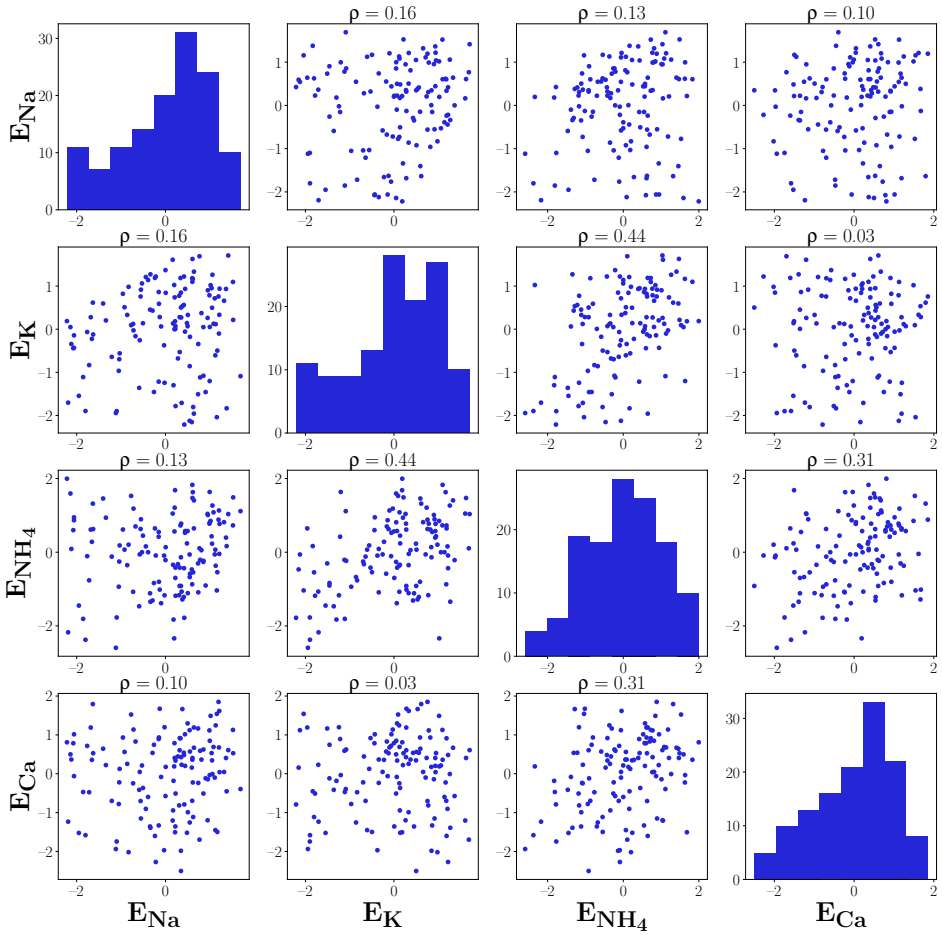

Figure 7.4 – Correlation in the multivariate OCP responses.

acquired with random sample composition, thus, the activity of the analytes span the whole detection range of the four target ions.

Table 7.3 – Pearson correlation coefficients between measured OCPs and ion activity for the orthogonal training set

ρ	log a_{Na^+}	log a_{K^+}	log $a_{NH_4^+}$	log $a_{Ca^{2+}}$
E_{Na}	**0.8993**	-0.0505	0.0270	-0.0719
E_{K}	0.2370	**0.8528**	0.0065	-0.1072
E_{NH_4}	0.1163	0.4728	**0.6504**	0.1088
E_{Ca}	0.0583	0.0733	0.1021	**0.8308**

7.2.3 Emulated synthetic dataset

Moreover, the emulator of synthetic datasets presented in Section 5.3.2 was adapted to the current case study aiming at physiology, in order to compare the automatically generated

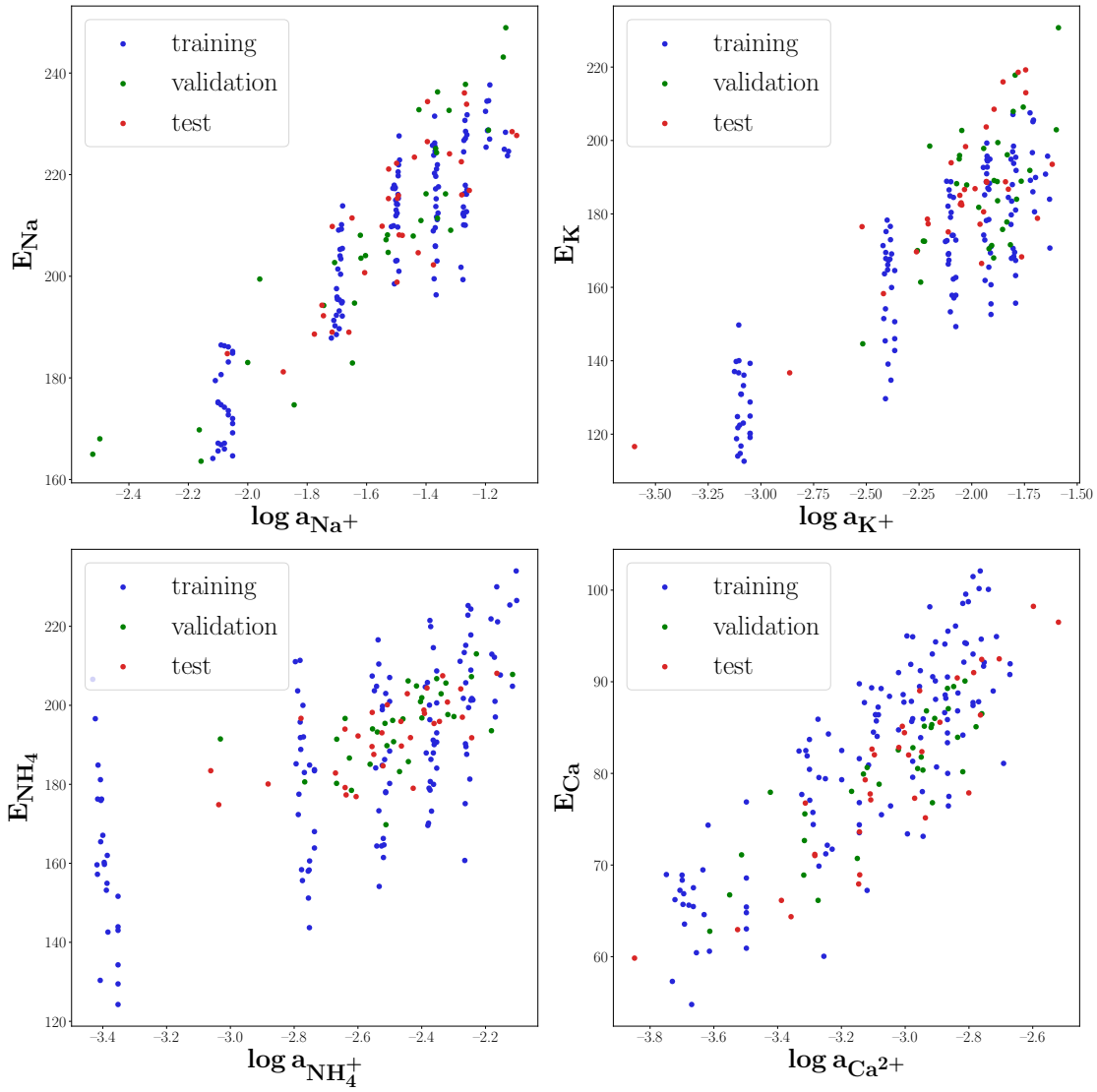

Figure 7.5 – Experimental synthetic dataset acquired to train, optimize, and evaluate the multivariate calibration models.

dataset to the experimental dataset presented above. Thus, the sensor parameters (sensitivity, LOD, selectivity) obtained through the characterization of the polymeric ISEs in Chapter 4 were used to fit the phase-boundary potential model.

First, the calibration curves output by the ion-sensing model were compared to experimental calibration curves. The results are displayed in Fig. 7.6 for sensor calibration in pure water samples. The simulated OCP responses exhibit similar sensitivity and LOD as the measured responses, and the RMSD between the modeled and measured data yields 0.70, 2.63, 0.97, and 2.08 mV, for sodium, potassium, ammonium, and calcium ions, respectively. As a result, the compact ion-sensing model explains accurately the

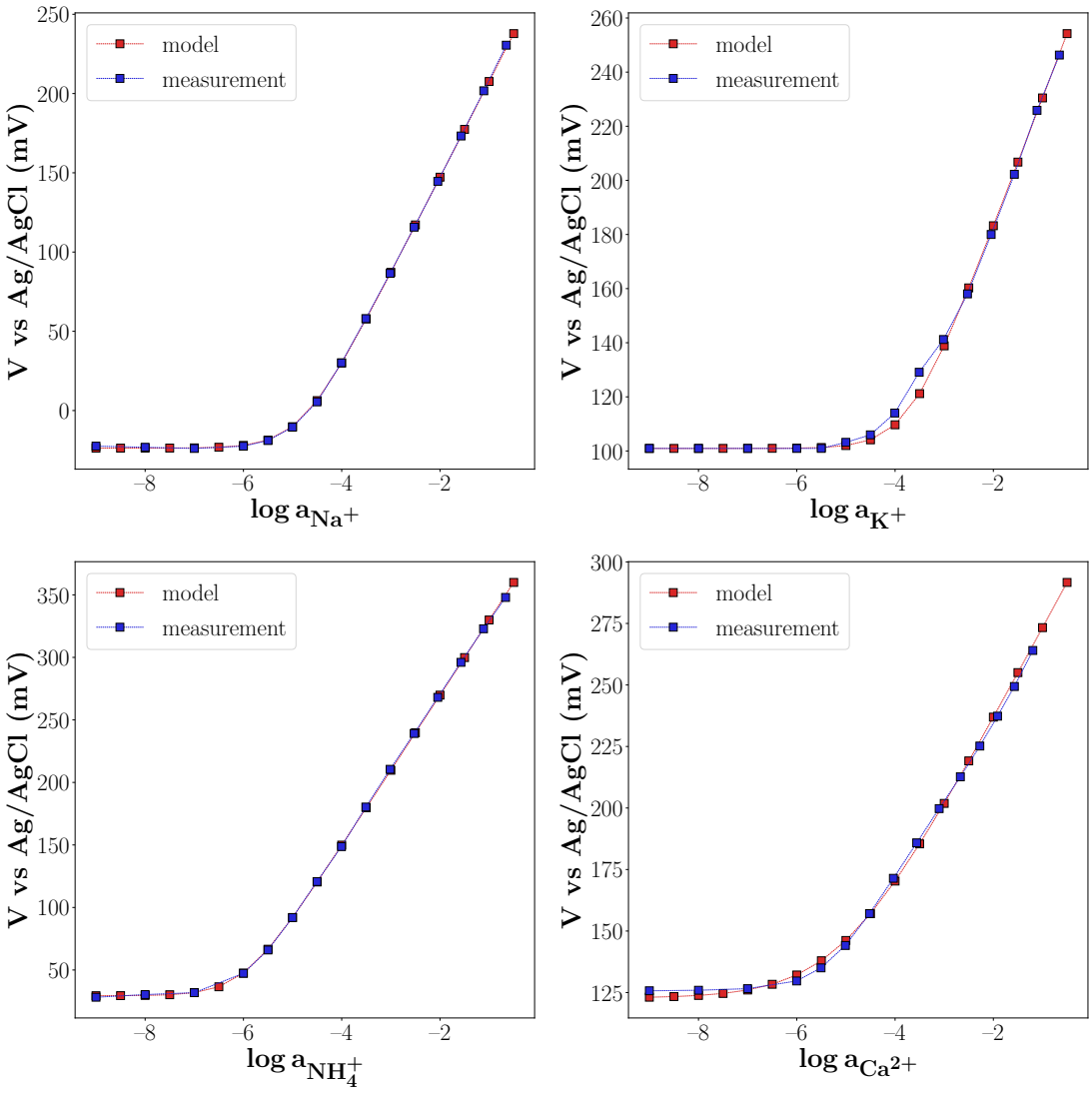

Figure 7.6 – Comparison between emulated and experimental calibration curves obtained in pure water.

measured response from the polymeric ISEs used.

Then, an emulated synthetic dataset was generated using the electrolyte sample compositions designed in Section 7.2.1. The emulated orthogonal training set is displayed in Fig. 7.7, where the measured dataset is shown for comparison. As a result, the grouping of potential responses around the activity levels of each target ion reflects the factorial design. Moreover, the OCP dispersion is the signature of ion interference, explained by both modeled and experimental data. The similarity between the datasets was evaluated by computing the mean relative OCP deviation for each primary ion. Mean relative OCP deviations of 3.47%, 7.93%, 7.10%, and 6.78% were obtained with the raw signals. Lower OCP deviations are observed with sodium sensors that are less affected by ion

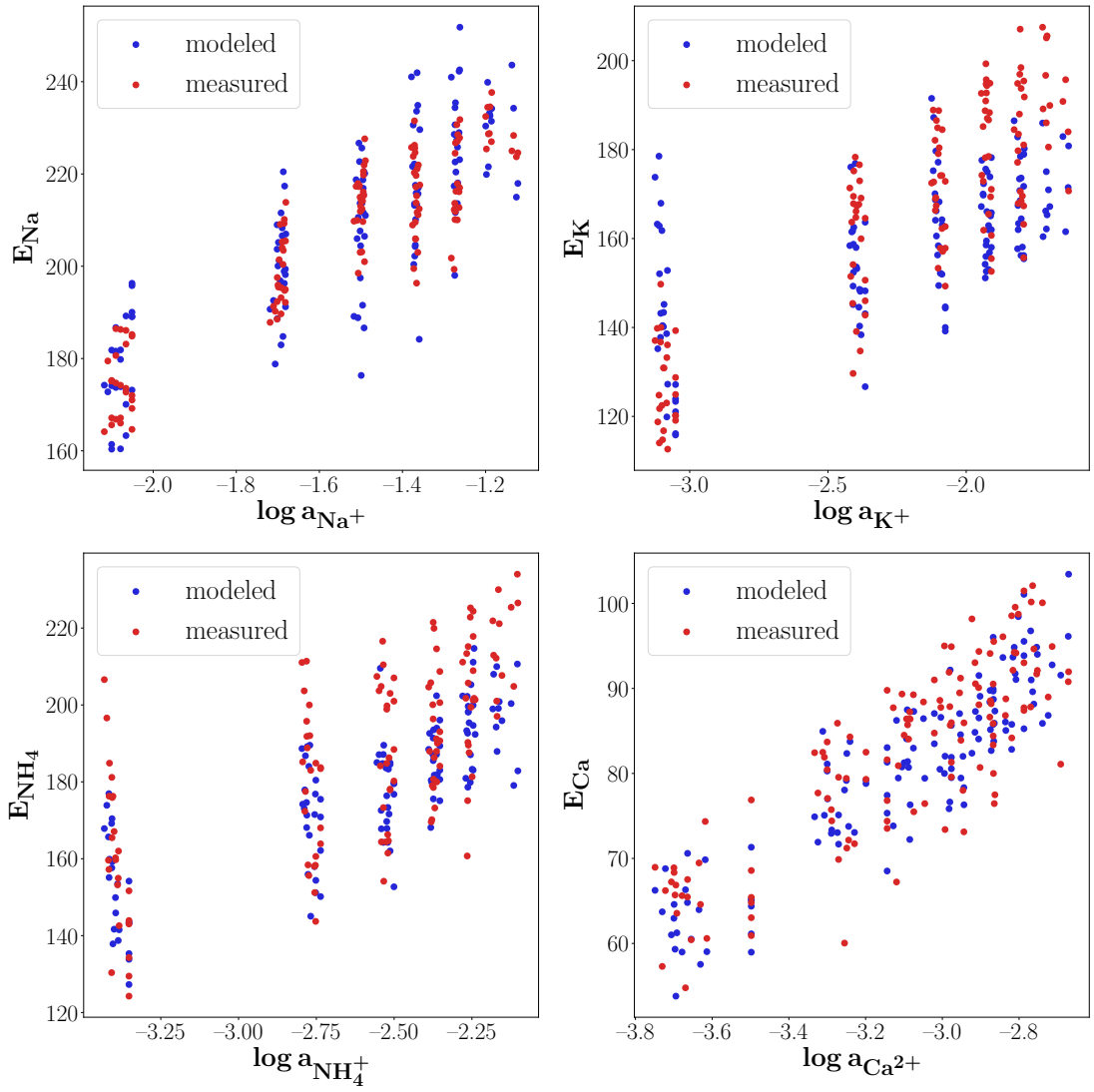

Figure 7.7 – Comparison between emulated and experimental training set.

interference (activity of sodium ions is high in the synthetic samples). Larger deviations are observed for the other primary ions, which is due to non-predictable sensor response distortion caused by ion interference.

7.3 Training and optimization of multivariate calibration model

The experimental synthetic dataset was then used to train and optimize the M-SVR model presented in Section 6.2.3. The prediction performance achieved by M-SVR was compared to linear and non-linear regression models. Furthermore, an automatic training of the multivariate calibration model is proposed as an alternative to avoid re-calibrating

the multivariate regressor before each inference phase.

7.3.1 M-SVR training, optimization, and testing

The M-SVR model was trained and optimized with the acquired experimental synthetic dataset. The input matrix was standardized to zero-mean and unit-variance. The labels were the log-activity of the primary ions. Non-linear kernel functions were used to cope with the non-linearity introduced by ion interference in the dataset. Therefore, polynomial kernel $\varkappa^{\text{poly}}(\mathbf{x}_i, \mathbf{x}_j) = (\gamma\langle \mathbf{x}_i, \mathbf{x}_j^T\rangle + b)^d$, and Gaussian RBF $\varkappa^{\text{rbf}}(\mathbf{x}_i, \mathbf{x}_j) = \exp(-\gamma||\mathbf{x}_i - \mathbf{x}_j||^2)$ were implemented. The model hyper-parameters (C and ε), and the kernel hyper-parameters were optimized through a grid-search procedure. Namely, for each set of hyper-parameters, the M-SVR model was trained and evaluated with the validation set. The NRMSE and MRE defined in (6.2) were the metrics computed to assess model accuracy.

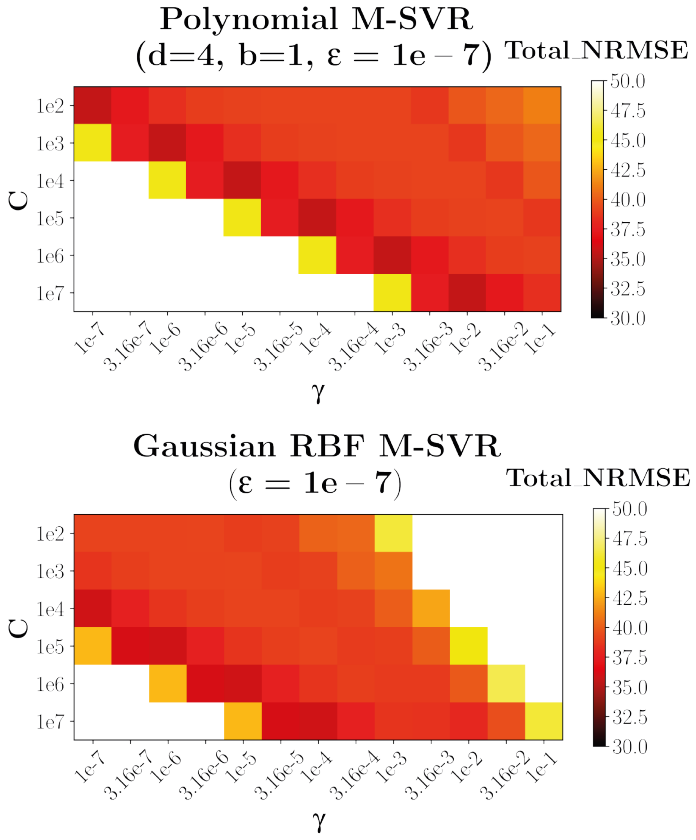

Figure 7.8 – M-SVR optimization with polynomial and Gaussian RBF kernels.

The heatmaps displayed in Fig. 7.8 show the Total NRMSE obtained with a polynomial and Gaussian RBF kernel, for different hyper-parameters C and γ. For visualization purposes, the hyper-parameters d, b, and ε were fixed. C and γ were selected by trading-off model generalization capability, and risk of overfitting to the training dataset. For

identical accuracy achieved, lower values of C were chosen to under-constrain the model, hence limiting overfitting. The best M-SVR model was then evaluated on an external test set. Polynomial M-SVRs yield slightly better results than Gaussian RBF. The metrics obtained with such kernelized-M-SVR are reported in Table 7.4.

Table 7.4 – Metrics obtained during training and evaluation of a polynomial M-SVR (d = 4, b = 1, $\gamma = 1e-3$, C = 1e3, $\varepsilon = 1e-7$)

	$\log a_{Na^+}$	$\log a_{K^+}$	$\log a_{NH_4^+}$	$\log a_{Ca^{2+}}$
NRMSE_val	11.44	10.27	7.94	5.86
NRMSE_test	8.20	11.27	6.91	6.20
MRE_val	7.34	8.90	6.87	5.23
MRE_test	6.88	7.90	6.13	5.41

Larger prediction errors were obtained with potassium and ammonium sensors, that are hindered by ion interference due to lower sensor cross-selectivity. Calcium-ISEs seem to be predicted more accurately since they exhibit a higher selectivity with respect to monovalent cations, and magnesium ions are rather diluted in artificial sweat. As for sodium ion-sensors, they exhibit a rather good linearity in the training dataset of Fig. 7.5. The larger NRMSE and MRE observed suggests that a linear M-SVR would be suitable for predicting the activity of this analyte.

Moreover, the goodness-of-fit and accuracy of the M-SVR model was evaluated by plotting the ground truth log-activity against the values predicted by the multivariate regressor, for the four target ions. The results are displayed in Fig. 7.9. The scatter plots are dispersed along the 1:1 line for both sodium and potassium ions, where the 95% confidence interval of the slope and intercept of the fitted model contain one and zero, respectively. As a result, the implemented M-SVR model is an unbiased estimator of sodium and potassium ion activity. However, with ammonium and calcium ions, the model predictions are not consistent. This is due to dataset scarcity and/or to the severity of ion interference for these sensors.

7.3.2 Benchmarking with other multivariate regressors

Different multivariate calibration models were used as benchmark for the proposed M-SVR model. Namely, a simple MLR, single-output SVRs, and MLP models were deployed on the RPi. A Gaussian RBF kernel was used for the kernelized-SVR. The configuration of the MLP models was reported in Table 6.1. An hyper-parameters grid-search similar to the one detailed for M-SVR was performed. The metrics achieved during the training and test phase are displayed in Fig. 7.10. We observe that non-linear regressors improve prediction accuracy compared to a simple linear model. NRMSE improvements of 9.14%, 6.97%, 7.85%, and MRE improvements of 18.45%, 10.26%, 12.31% were achieved with

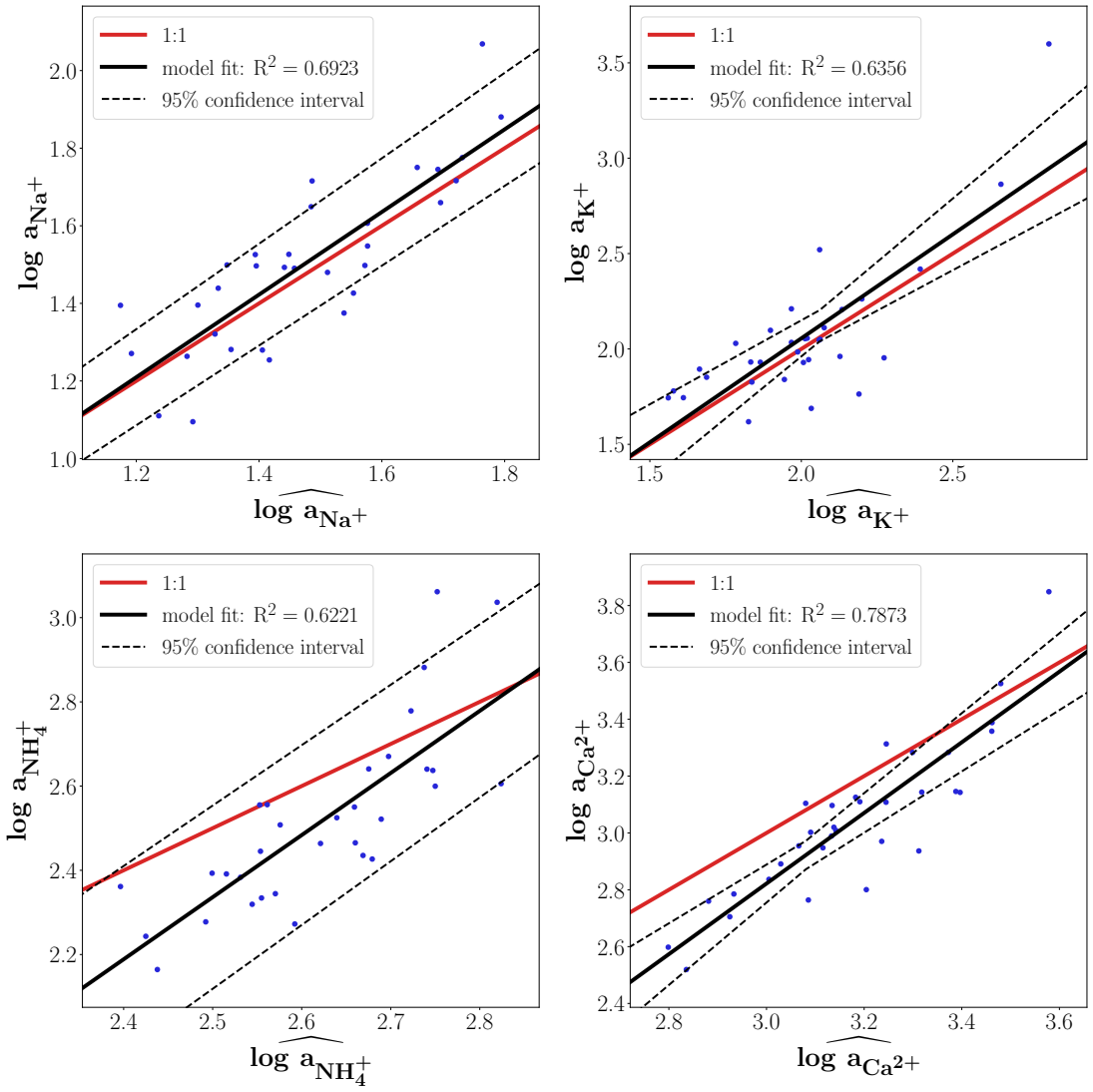

Figure 7.9 – Ground truth and predicted ion activity by evaluating the M-SVR on the test set. The model fit and its 95% confidence interval are plotted, where R^2 is the coefficient of determination. The red plot is the 1:1 line.

single-output SVRs, M-SVR, and MLP model, respectively. The multivariate calibration models generalize well with unseen data since the metrics obtained during test phase are better than in training phase. Single-output SVRs provide the lowest prediction error. However, recall that the latter consists of four uncorrelated regressors that optimize the prediction of the four target ion activity independently. Hence, a regressor closer to a linear-SVR was obtained for the prediction of sodium ions activity, and a non-linear SVR was more suitable for ammonium ions. Conversely, M-SVR and MLP models are multivariate input/output models. They are built by taking into account correlations in the multidimensional output, namely, the activity of the four analytes.

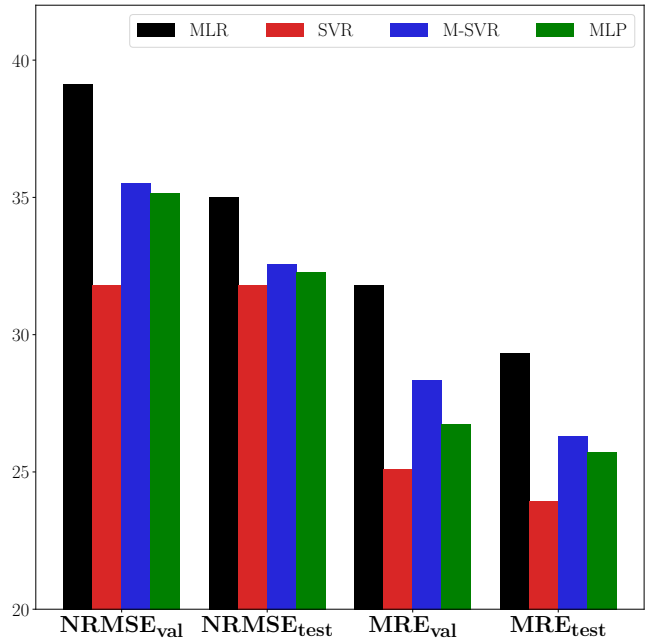

Figure 7.10 – Training and optimization of different multivariate calibration models. The total metrics are reported.

Moreover, the accuracy of the multivariate models was evaluated by a linear fit of the ground truth log-activity of the target ions against the values predicted by the regressors. The slope and intercept of the fitted model with a 95% confidence interval, the RMSD of the predicted ion activity against the 1:1 line, and the Theil's partial inequality coefficients are reported in Table 7.5. The latter are the decomposition of the sum of squared of predicted errors into the proportion associated with mean difference between log a_X and $\widehat{\log a_X}$ (U_{bias}), the proportion associated with the slope of the linear fit and the 1:1 line (U_{slope}), and the proportion associated with the variance in log a_X unexplained by $\widehat{\log a_X}$ (U_{error}). The coefficients provide an assessment of the goodness-of-fit of the model [**?**]. It results that a simple MLR model is an inconsistent estimator of the activity of sodium and potassium ions, and a biased estimator of ammonium and calcium ions. The large prediction errors, for all ions, reflects its inability to cope with ion interference. The SVR model is an unbiased and accurate estimator for the prediction of sodium ions only. M-SVR and MLP models are unbiased estimators of sodium and potassium ions, but they are inconsistent for the prediction of ammonium and calcium ions. We notice that the prediction of the activity of ammonium and calcium ions is more intricate due to the larger prediction error reflected by bias and slope misleading.

Furthermore, the computational complexity of the multivariate models was compared. An average training runtime of 1.81 ms, 13.97 ms, 8.18 ms, and 14.01 s was obtained with MLR, SVR, M-SVR, and MLP models, respectively. The IRWLS procedure implemented in M-SVR converges quickly, typically in 11 iterations. Each iteration has the complexity

Table 7.5 – Benchmarking of model accuracy

		$\log a_{Na^+}$	$\log a_{K^+}$	$\log a_{NH_4^+}$	$\log a_{Ca^{2+}}$
MLR	Slope	0.84 ± 0.10	0.84 ± 0.11	0.86 ± 0.14	0.94 ± 0.09
	Intercept	0.28 ± 0.15	0.43 ± 0.23	0.20 ± 0.40	0.03 ± 0.29
	RMSD	0.1344	0.2588	0.1870	0.2019
	U_{bias}[1]	11.14	18.50	44.07	59.32
	U_{slope}[1]	6.97	5.13	1.93	0.55
	U_{error}[1]	81.89	76.37	54.00	40.13
SVR	Slope	0.98 ± 0.12	1.26 ± 0.17	1.77 ± 0.26	1.18 ± 0.11
	Intercept	0.04 ± 0.18	-0.44 ± 0.35	-1.90 ± 0.60	-0.70 ± 0.40
	RMSD	0.1227	0.2473	0.1495	0.1892
	U_{bias}[1]	1.56	8.97	0.27	51.17
	U_{slope}[1]	0.08	6.22	23.07	3.80
	U_{error}[1]	98.36	84.81	76.66	45.03
M-SVR	Slope	1.06 ± 0.13	1.09 ± 0.15	1.47 ± 0.21	1.24 ± 0.12
	Intercept	-0.07 ± 0.19	-0.13 ± 0.30	-1.40 ± 0.60	-0.90 ± 0.40
	RMSD	0.1250	0.2360	0.1767	0.1918
	U_{bias}[1]	4.93	5.82	37.28	50.71
	U_{slope}[1]	0.79	1.11	9.14	6.08
	U_{error}[1]	94.28	93.07	53.58	43.21
MLP	Slope	0.95 ± 0.11	1.00 ± 0.12	0.52 ± 0.15	0.87 ± 0.09
	Intercept	0.11 ± 0.16	0.03 ± 0.24	1.20 ± 0.40	0.30 ± 0.29
	RMSD	0.1241	0.2042	0.2112	0.1892
	U_{bias}[1]	7.88	2.76	4.99	44.63
	U_{slope}[1]	0.70	0	25.38	3.79
	U_{error}[1]	91.42	97.24	69.63	51.58

[1] Theil's partial inequality coefficients

of an OLS minimization. Moreover, the single-output SVRs embed four times more support vectors than M-SVR since four independent regressors are constructed. Lastly, the extremely slow training of the neural network model, with 1079 trainable parameters and 228 training epochs, highlights the larger complexity of such multivariate regressor.

7.3.3 Automatic training of multivariate calibration models

Furthermore, an automatic training of the M-SVR model deployed on the RPi is proposed as an alternative to avoid re-calibrating the multivariate regressor before model inference to unknown samples, thus avoiding the acquisition of large training sets, that is extremely expensive in terms of chemical resources and experimental time. Namely, the emulated synthetic training set presented in Section 7.2.3 was used to calibrate the multivariate regressor, and the experimental random validation and test sets were used to assess

the performance of the resulting model. Polynomial and Gaussian RBF-M-SVRs were implemented, and they were optimized through a grid-search procedure similar to the one detailed in Section 7.3.1.

Table 7.6 – Accuracy achieved by M-SVR trained on emulated and experimental synthetic dataset

		log a_{Na^+}	log a_{K^+}	log $a_{NH_4^+}$	log $a_{Ca^{2+}}$	Total
M-SVR_emulated	NRMSE_val	10.37	11.49	6.66	4.29	**32.81**
	NRMSE_test	8.21	10.92	6.23	4.51	**29.86**
	MRE_val	7.13	10.26	4.71	3.45	**25.56**
	MRE_test	6.98	8.70	5.17	3.40	**24.24**
	Slope	0.95 ± 0.12	0.92 ± 0.13	0.99 ± 0.17	1.069 ± 0.098	
	Intercept	0.08 ± 0.18	0.15 ± 0.26	-0.04 ± 0.45	-0.28 ± 0.31	
	RMSD	0.13	0.23	0.16	0.14	
	U_{bias}[1]	0.33	0.92	15.76	21.13	
	U_{slope}[1]	0.54	1.41	0	1.29	
	U_{error}[1]	99.12	97.68	84.24	77.58	
M-SVR_experimental	NRMSE_val	11.44	10.27	7.94	5.86	**35.51**
	NRMSE_test	8.20	11.27	6.91	6.20	**32.58**
	MRE_val	7.34	8.90	6.87	5.23	**28.35**
	MRE_test	6.88	7.90	6.13	5.41	**26.32**
	Slope	1.06 ± 0.13	1.09 ± 0.15	1.47 ± 0.21	1.24 ± 0.12	
	Intercept	-0.07 ± 0.19	-0.13 ± 0.30	-1.40 ± 0.60	-0.90 ± 0.40	
	RMSD	0.1250	0.2360	0.1767	0.1918	
	U_{bias}[1]	4.93	5.82	37.28	50.71	
	U_{slope}[1]	0.79	1.11	9.14	6.08	
	U_{error}[1]	94.28	93.07	53.58	43.21	

[1] Theil's partial inequality coefficients

Polynomial M-SVRs yield slightly better results, like in Section 7.3.1. The accuracy achieved by training the polynomial M-SVRs with the emulated dataset, and with the experimental dataset is reported in Table 7.6. The metrics computed during validation and test phase highlight that the M-SVR trained with the emulated dataset has good generalization performance. Slightly better metrics are achieved, indicating that the emulated training set explains well the variance contained in the evaluation datasets. In particular, major improvements are observed for the prediction of calcium ions, which response is hindered by the other interfering ions that are present at higher concentrations in artificial sweat samples. Besides, the M-SVR model yields 14% NRMSE, and 15% MRE improvement with respect to a MLR model trained with the same emulated dataset. The consistency and goodness-of-fit of the model was evaluated by performing a linear fit of the ground truth log-activity and the predicted values. The results are reported in Fig. 7.11. Thus, the M-SVR model is an unbiased estimator of the activity of the four primary ions. Most of the residual error arises from the variance of log a_X that is

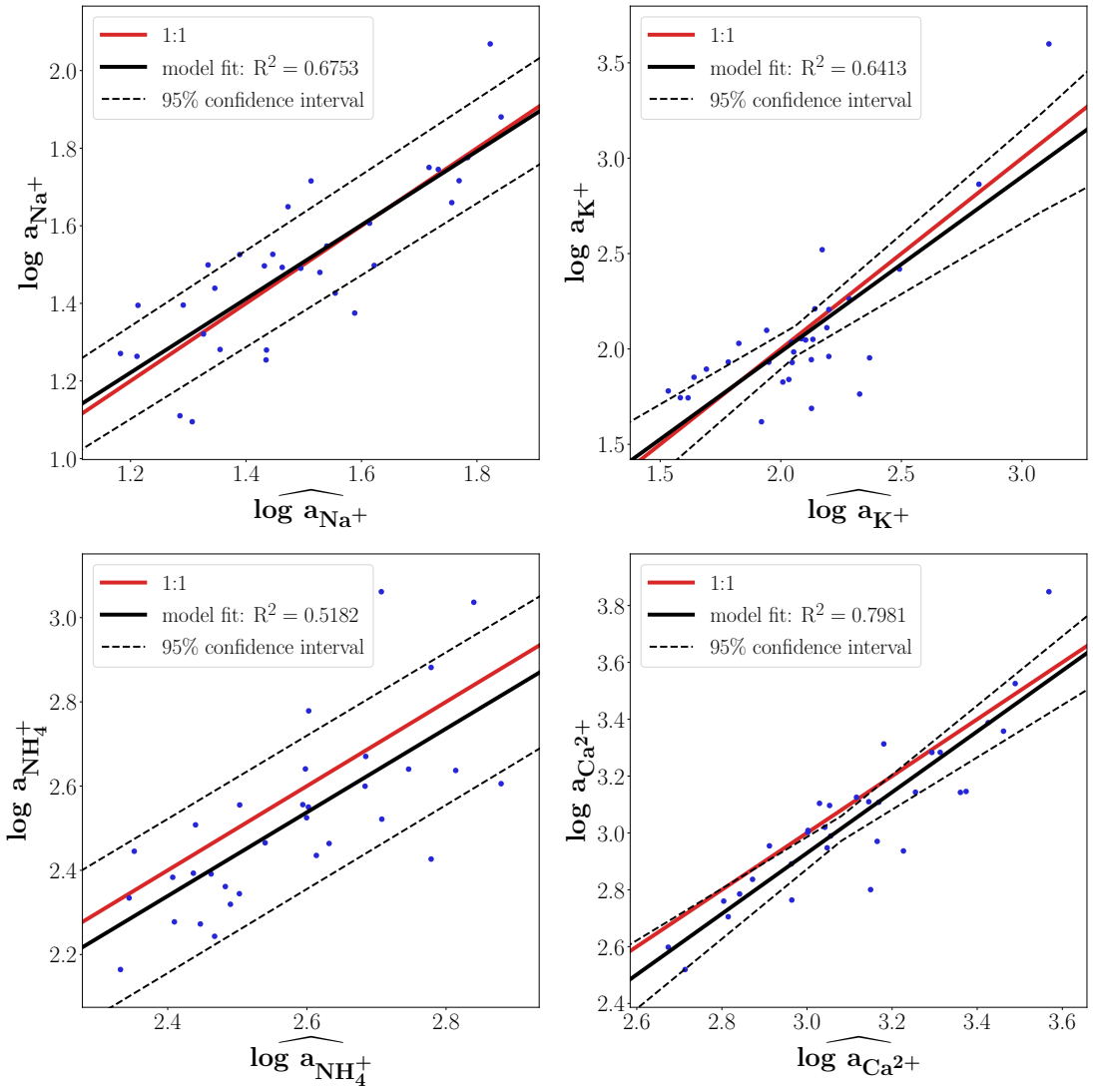

Figure 7.11 – Accuracy of M-SVR trained with the emulated dataset.

unexplained by $\widehat{\log a_X}$, reflected by the low coefficient of determination of the linear fit. Therefore, the automatic calibration of the M-SVR with an emulated synthetic dataset provides a fast and accurate solution for precise multi-ion-monitoring, avoiding the re-calibration of the M-SVR model. This method is valid as long as the sensor parameters (sensitivity, LOD, selectivity) are correctly extracted. This is achieved through a couple of sensor calibrations before model inference to unknown samples.

7.4 Real-time multi-ion-monitoring

After optimizing and characterizing the ion-sensors, the analog front-end interface, and the embedded multivariate calibration model, the overall electronic tongue system is now

evaluated for a real-time multi-ion-monitoring task.

7.4.1 Validation setup

Before the measurement, the solid-contact sodium, potassium, ammonium, and calcium ISEs were calibrated in pure water samples. These calibration curves will be used to estimate the activity of the four primary ions with a traditional MLR model, and will set a baseline for evaluating the accuracy of the M-SVR model. Then, the four ISEs were interfaced to the analog front-end powered by a 3.7 V lithium ion battery. The different on-board modules were configured during firmware initialization (system clock, sleep manager module, ADC module, UART interface, Bluetooth module). Next, the RPi was powered-on, and a VNC session was initiated on a smartphone. A GUI was executed on the edge node in order to control the sensing platform, configure the measurements, and visualize the acquired data. Thus, a wireless link was created between the edge device and the sensing interface. Namely, the BLE module of the RPi was advertising neighboring devices, acting as a GATT server. After pairing, bonding, and connecting to the BLE module of the analog front-end, a private Transparent UART GATT service was used to send serial data streams from one device to another. In particular, the ion-sensing panel was configured through the user interface (channels to be measured, sampling time interval), and the measured data was visualized in real-time on the smartphone. Moreover, the M-SVR model trained with the experimental synthetic dataset was deployed on the edge node. It was implemented for inference of the activity of the four primary ions. The measured data was saved locally on the RPi, enabling further post-processing. In addition, the sensor data streams were stored onto Amazon Simple Storage Service. Namely, a stream was created in a software component run on the edge device, and it was configured so as to export the measured OCP to the aforementioned location whenever the Stream Manager was called.

Table 7.7 – Activity of the constituting ions for the real-time multi-ion-monitoring task

Time	**Activity** ($\times$ **1e** $-$ **3**)				
(min)	$\mathbf{Na^+}$	$\mathbf{K^+}$	$\mathbf{NH_4^+}$	$\mathbf{Ca^{2+}}$	$\mathbf{Mg^{2+}}$
0	17.16	3.43	0.43	0.28	0.02
2	21.51	5.75	1.23	0.49	0.05
4	25.68	7.96	1.98	0.68	0.06
6	29.71	10.08	2.70	0.85	0.08
8	33.61	12.11	3.38	1.00	0.10
10	37.39	14.07	4.05	1.14	0.11
12	41.06	15.97	4.69	1.28	0.13
14	44.63	17.82	5.31	1.40	0.14
16	48.10	19.61	5.91	1.51	0.15
18	51.49	21.35	6.49	1.62	0.17
20	54.80	23.04	7.05	1.73	0.18

Real-time multi-ion-monitoring in artificial sweat was performed emulating an intense physical activity that leads to a steady increase of the activity of the five constituting ions. Therefore, the initial sample was the nominal activity of the electrolytes in sweat. Then, sodium, potassium, ammonium, calcium, and magnesium ions were added successively in the sample, every time stamp of 2 min. The sample was homogenized with a constant stirring at 120 rpm throughout the experiment. The activity of the ions at each time stamp are reported in Table 7.7. Such experimental design enables a quantitative assessment of the accuracy of the M-SVR model deployed on the edge device, where the sample composition is known at each time stamp.

7.4.2 Results and discussion

The real-time monitoring task started upon request on the GUI displayed on the smartphone. The multivariate sensor response was continuously acquired, processed, and plotted in real-time on the user interface, leveraging three concurrent threads. A default sampling interval of five samples per second was used. Every 30 samples acquired, the OCP signals were averaged on that time frame, and the activity of the four target ions was estimated by the calibrated M-SVR model. The ion activity was then updated on the GUI, and the raw OCP streams were exported to the AWS cloud by calling the Stream Manager.

The screenshot of the smartphone at the end of the experiment is displayed in Fig. 7.12. The peaks in the OCP time traces highlight the increase of ion activity at each time stamp. The peak potential amplitudes decay throughout the experiment. It is emphasized that the activity of the constituting ions was linearly increased during the experiment so as to cover the physiological range of the primary ions. Therefore in this narrow range of activity, the ISEs exhibit a logarithmic Nernstian response. Besides, calcium ions are diluted analytes in the sample, explaining the steady sensor response increase due to interference from the other ions.

In a post-processing phase, the sensor response time series were fed to different multivariate calibration models in order to assess the prediction performance of the deployed M-SVR. Namely, the multivariate OCP at the end of each time stamp was extracted, and fed to the linear regression model constructed from the prior sensor calibration, to the single-output SVRs and MLP models trained with the experimental synthetic dataset, and to the M-SVR models trained with the experimental and emulated synthetic dataset. Then, the NRMSE was computed, assuming that the activity of the primary ions at the end of each time stamp was constant and equal to the values in Table 7.7. The Total NRMSE computed at each time stamp are displayed in Fig. 7.13. The non-linear multivariate regressors considerably improve the accuracy of the predicted ion activity, compared to a traditional sensor calibration performed prior to the measurement. Improvements of 50.93%, 54%, and 51.75%, are obtained with single-output

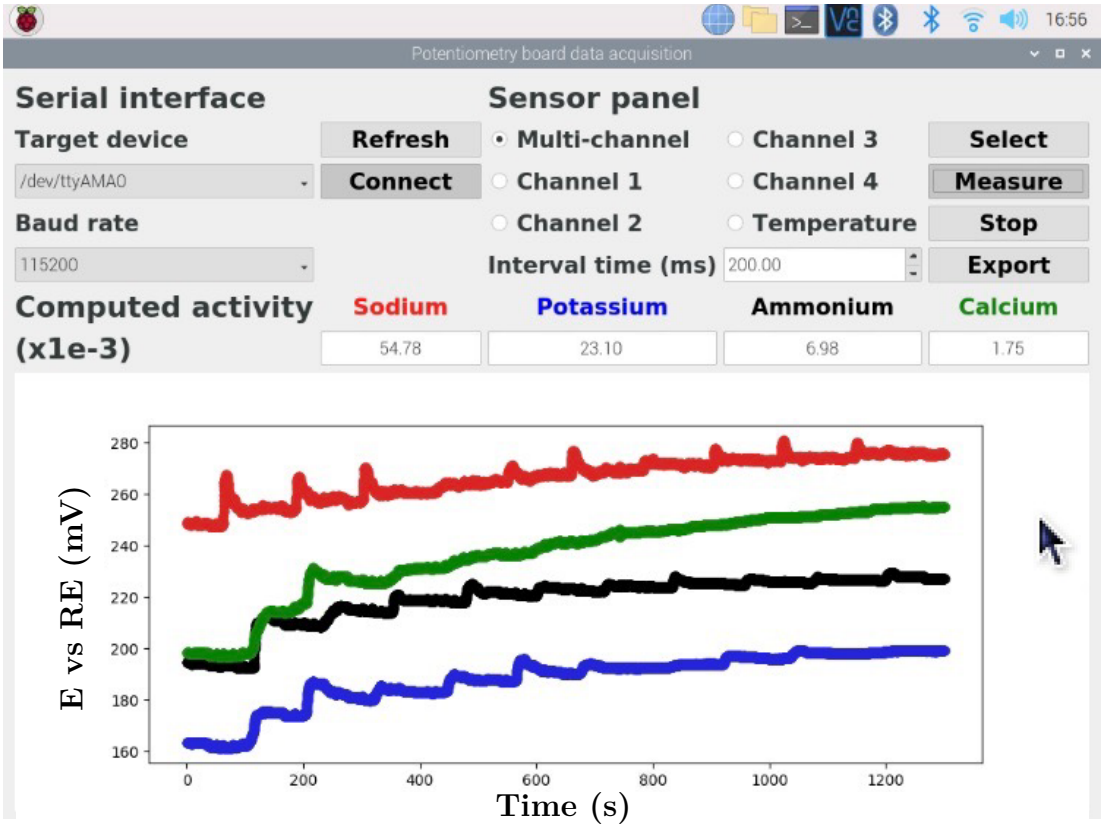

Figure 7.12 – Screenshot of the smartphone serving as display terminal for the GUI executed on the Raspberry Pi.

SVRs, M-SVR, and MLP model, respectively. The steady increase of the prediction error for all multivariate calibration models arises from the calcium ISE, which response was greatly distorted by the interfering ions. The small amount of calcium ions injected in the sample should induce tiny peak sensor response (see Table 7.7), but the constant increase of the calcium OCP observed in Fig. 7.12 highlights a non-specific response due to the interfering electrolytes. As for the M-SVR model automatically trained with the emulated synthetic dataset, the prediction performance is more homogeneous throughout the multi-ion-monitoring task.

Furthermore, the prediction latency of the multivariate regressors was evaluated. The tasks needed for the ion activity prediction include the column averaging of the 30 last samples of the multivariate OCP matrix, the standardization of the resulting input vector with the column-mean and column-standard deviation taken from the training set, and the ion activity prediction with the trained regressor model. Latency of $18.34 \pm 4.74\,\mu s$, $39.07 \pm 1.8\,\mu s$, $22.68 \pm 1.73\,\mu s$, and $3.89 \pm 1.33\,ms$ are obtained with MLR, single-output SVRs, M-SVR, and MLP model, respectively. Therefore, the proposed M-SVR model is suitable for accurate real-time multi-ion-sensing applications, providing a low latency and a greatly meliorated ion activity prediction accuracy compared to a simple and

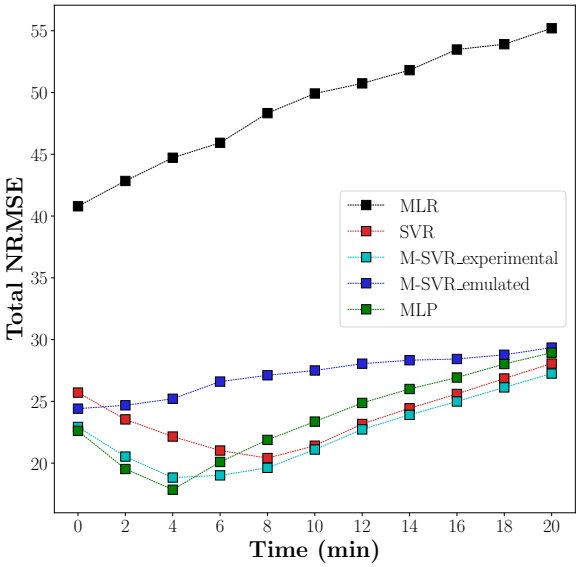

Figure 7.13 – Accuracy of the multivariate calibration models throughout the real-time multi-ion-monitoring task.

traditional linear calibration model.

7.5 Summary and main contributions

A complete electronic tongue system implemented for accurate and real-time physiology withing an IoT framework was presented in this chapter. The main contributions are summarized hereunder:

- An **electronic tongue system** was proposed for continuous and real-time monitoring of sodium, potassium, ammonium, and calcium ions, that are relevant analytes for physiology in sweat. The ion-sensors were fabricated on SPEs, and interfaced to a battery-powered analog front-end, enabling the acquisition and conditioning of OCP responses. The sensing platform was coupled to a wireless edge node, on which a trained M-SVR model was deployed in order to provide an accurate estimation of the activity of the primary ions. A VNC session of the RPi was launched on a smartphone, enabling sensor configuration and real-time visualization of the measured data through a GUI executed on the edge device. Moreover, the raw sensor responses were exported to AWS Cloud services for storage, where authenticated users could access and post-process the data.

- The M-SVR model was trained, optimized, and evaluated with **experimental synthetic datasets** acquired with solid-contact ISEs. An orthogonal training set of 128 samples, and random validation and test set of 32 samples each, were acquired in artificial sweat samples, where the activity of the electrolytes was designed in

their physiological range in sweat. A polynomial M-SVR model meliorates the multivariate calibration accuracy in presence of ion interference, with NRMSE improvement of 6.97%, and MRE improvement of 10.26%, with respect to a simple linear calibration model. The multivariate input/output regressor exhibits good generalization performance, and is an unbiased estimator of sodium and potassium ions. The prediction of ammonium and calcium ions activity is more intricate due to ion interference.

- An **automatic training of the M-SVR model** was proposed to avoid re-calibration before each inference phase. An emulated synthetic training set was created leveraging sensor parameters (sensitivity, LOD, and selectivity). The obtained dataset accurately explains the multivariate sensor response, with OCP deviations of 3.47%, 7.93%, 7.10%, and 6.78%, with respect to experimental sodium, potassium, ammonium, and calcium sensor response, respectively. The M-SVR model trained with the emulated synthetic dataset is an unbiased estimator of the four primary ions, with improved prediction capability of unknown measured samples. The automatic re-calibration approach is valid as long as the sensor parameters are extracted accurately before each measurement, through a couple of sensor calibrations.

- The electronic tongue system was validated through a **real-time multi-ion monitoring task** emulating an intense physical exercise, where the activity of the electrolytes constituting sweat samples steadily increases throughout the experiment. The analytic composition of the artificial sweat samples was designed so as to cover the physiological range of the constituting ions. The M-SVR deployed on the edge node improves the prediction accuracy of the activity of the four primary ions by 54%, with respect to a linear regressor typically constructed prior to the measurement. A latency of $22.68 \pm 1.73\,\mu s$ was achieved with the compact, accurate, and low-complexity M-SVR model.

8 Conclusions and future works

Remote healthcare monitoring is fostered by advancements in **sensing technology**, where improvements in microfabrication techniques provide miniaturized sensors that can be integrated into wearable systems. Research is driven towards the amelioration of sensitivity, selectivity, and response stability of electrochemical sensors, that enable a fast and continuous detection of relevant biomarkers in biological fluids such as sweat. Moreover, a careful design of **hardware electronic interfaces** is needed to control and implement different analytical techniques, and ensure an accurate acquisition and conditioning of the electrical signals transduced by the sensing electrodes. Furthermore, advanced **software processing pipelines** are required to analyze the multivariate sensor response in complex samples, in order to obtain a precise interpretation of the chemical proprieties of the analytes. Besides, the development of wireless sensor networks and IoT frameworks sustains **data decentralization**, yielding a continuous and real-time diagnosis and insight on the health and physiological status of the patient, that is not constrained to be in medical facilities. Likewise, these technological improvements and developments are applied to remote physiology monitoring in athletes, or for sport applications.

The main contributions of this thesis are summarized below:

- **The design and realization of a multi-mode hardware front-end enabling voltammetric and potentiometric multi-analyte measurements**. Voltammetric sensing was implemented with a potentiostat and a DDS circuit, providing programmable electrochemical cell potential waveforms. Namely, potential steps, linear potential scans, and pulsed potentials, were generated to enable CA, CV, and DPV measurements, respectively. In addition, a resistive-feedback circuit and signal conditioning circuits ensure a simple and accurate acquisition and processing of the Faradaic cell current, in the detection range of the analytes of interest. As for potentiometry, buffered and differential circuitry with an amplification gain were implemented for monitoring sensor OCPs. The electronic interface was mounted

on both flexible and rigid substrates, with size compliant for an integration into portable systems. The power consumption of the overall hardware front-end enables continuous measurements for 27 h, with a 1.1 Ah 3.7 V lithium ion battery. The hardware front-end was successfully characterized through lactate, paracetamol, and lithium ion sensing, that are relevant examples of endogenous metabolite, exogenous drug, and electrolyte, monitored for physiology and/or TDM applications. The biosensors were fabricated on SPEs, and sensitivity and LOD comparable to the results obtained with a bulky laboratory Autolab potentiostat were achieved by the proposed hardware, with an excellent linearity in the detection or therapeutical range of the analytes.

Analyte	Lactate	Paracetamol		Lithium ions
Det. technique[1]	CA	CV	DPV	potentiometry
Sample	PBS + HMF	PBS	PBS	pure water
Sensitivity	1.2 ± 0.3 $\mu A \cdot mM^{-1}$	52.4 ± 0.2 $nA \cdot \mu M^{-1}$	69.6 ± 2.0 $nA \cdot \mu M^{-1}$	55.6 ± 1.2 mV/decade
LOD (µM)	37.0 ± 8.0	2.6 ± 0.5	2.1 ± 1.2	11.0 ± 3.5

[1] Detection technique

- **The design and realization of a multi-sensing front-end enabling a concurrent and continuous monitoring of four electrolytes and in situ temperature**. This hardware interface addresses the lack of multi-sensing capabilities in ion-sensing platforms, which is prominent for a comprehensive physiology, and because of correlations between the measured electrolytes. The electronic front-end was interfaced to sodium, potassium, ammonium, and calcium-ISEs, that were developed on SPEs, and successfully characterized in terms of sensitivity, selectivity, and LOD, in pure water and artificial sweat samples. The proposed hardware achieves comparable sensing performances as a high precision laboratory potentiometer, and has dimension and power budget that are compliant for continuous wearable sensing.

Target ion	Sodium	Potassium	Ammonium	Calcium
Sample	Artificial sweat			
Sensitivity (mV/decade)	59.8 ± 3.8	57.7 ± 4.2	57.1 ± 0.4	28.4 ± 0.3
LOD (µM)	382.2 ± 144.7	119.5 ± 20.3	754.4 ± 311.9	46.1 ± 5.0

Moreover, the electronic front-end was interfaced to a flexible fully-integrated sensing platform embedding a microfabricated electrode array, and a RTD for temperature measurements. Ion-sensing was validated through potassium measurement against an all-solid-state Ag/AgCl RE. Besides, the temperature readout circuit was implemented with an improved Howland current source yielding a boosted output impedance. Temperatures between 34 and 43 °C were measured, with an excellent

linearity ($R^2 = 0.9983$, RMSE = 0.7719 mV), and a sensitivity of 6.56 mV/°C.

- **The derivation of a compact analytical model of ion-sensing through polymeric ISEs** provides both quantitative and qualitative interpretation of the impact of ion interference in the distortion of ion-sensor signals. The model was implemented at the core of an **emulator of synthetic datasets** of sodium, potassium, lithium, and lead ions, that are relevant electrolytes for physiology, TDM, and toxic compound detection, through perspiration analysis. The sensing performances of fabricated ISEs (sensitivity, LOD, selectivity) were parameters added to the model in order to produce datasets explaining accurately the experimental response of polymeric ion-sensors. OCP RMSD of 1.37, 1.44, 1.78, 2 mV were obtained between the modeled and experimental calibration curves for Na^+, K^+, Li^+, Pb^{2+} sensors, respectively. Such emulator addresses the expensive time and chemical resources needed to obtain large database for training complex multivariate calibration algorithms.

- **The optimization of the multivariate calibration accuracy of ion-sensor arrays hindered by ion interference through M-SVR**. The latter was proposed as an accurate, unbiased, robust, compact, low-complexity, and low-latency multivariate input/output regressor, leveraging an IRWLS procedure implemented in a quasi-Newton method, where each iteration has the complexity of an OLS minimization. The proposed model was trained and evaluated on emulated synthetic datasets of sodium, potassium, lithium, and lead ions, and achieved NRMSE improvement of 13.22%, and MRE improvement of 20.29%, with respect to a traditional MLR model.

- **The implementation of a complete electronic tongue system enabling an accurate, continuous, and real-time multi-ion-monitoring for physiology, within an IoT framework**. The different modules (ion-sensor array, analog front-end interface, embedded multivariate calibration model, edge node, and cloud storage service) were co-integrated for the real-time monitoring of sodium, potassium, ammonium, and calcium ions in artificial sweat. The M-SVR deployed on the RPi improves the prediction accuracy of the activity of the four primary ions by 54%, with respect to a linear regressor typically constructed prior to the measurement. The multivariate regressor deployed on the edge device can be re-calibrated with emulated synthetic datasets, thus avoiding expensive and time-consuming acquisition of synthetic datasets prior to each inference phase.

This thesis presents tools and solutions for a seamless design and co-integration of hardware and software interfaces for multi-analyte-sensors, with particular emphasis on ion-sensing in sweat. This thesis combines engineering and technological efforts in sensor development and modeling, analog front-end design and realization, embedded system design, optimization algorithms design and implementation, in order to build innovative

and accurate remote healthcare systems. Some possible works to further broaden this research are reported hereunder:

- **The co-integration of the electronic tongue system for wearable multi-ion-sensing in sweat on human volunteers, for physiology during intense physical activity**. A preliminary qualitative study has been carried out for the monitoring of sodium and potassium ions with a wearable system embedded on the forehead of volunteers performing exercise on a stationary bike. A quantitative analysis of the accuracy of the electronic tongue during inference phase necessitates laboratory instruments to provide the exact activity/concentration of the ions in the sample. This could be done by ex situ measurements with inductively coupled plasma-optical emission spectrometry, for instance.

- **The study of the correlation between relevant biomarkers for physiology in sweat**. The concentration of lactate, potassium, and ammonium ions are indicators of muscle fatigue. A thorough study of the correlation between the concentration/activity of these compounds and the physiological status of the subject would ameliorate the interpretation of the results acquired during real-time-monitoring tasks. Moreover, this analysis could be completed by the integration of electromyography sensors, enabling an accurate assessment of muscle activity.

- **The development of a sweat stimulation system**. A very intense physical activity is needed to produce a small amount of sweat. However, at least $10-30\,\mu L$ of sweat is required to ensure a stable and accurate potentiometric readout. An iontophoresis system is commonly proposed to stimulate sweat excretion from the eccrine glands, by applying a current between iontophoresis electrodes placed on the skin. This external sweat stimulation system is crucial for wearable sweat sensing carried out for stationary healthcare monitoring.

- **The implementation of the remote electronic tongue system to other fields than biomedical applications**. Indeed, an accurate, continuous and real-time multi-ion-monitoring is desired in several area such as food and water quality monitoring, agriculture soil analysis, environmental pollution monitoring.

Remote multi-analyte monitoring is a great area of research and development. We hope that the findings presented in this thesis will contribute to open up new paradigms in the design of hardware and software interfaces developed for multi-target electrochemical sensing, providing more robust and accurate healthcare monitoring systems.

[1] N. Bui and M. Zorzi, "Health care applications: A solution based on the internet of things." New York, NY, USA: Association for Computing Machinery, 2011.

[2] M. C. Domingo, "An overview of the internet of things for people with disabilities," *Journal of Network and Computer Applications*, vol. 35, no. 2, pp. 584–596, 2012, simulation and Testbeds.

[3] B. J. Drew, R. M. Califf, M. Funk, E. S. Kaufman, M. W. Krucoff, M. M. Laks, P. W. Macfarlane, C. Sommargren, S. Swiryn, and G. F. V. Hare, "Practice standards for electrocardiographic monitoring in hospital settings," *Circulation*, vol. 110, no. 17, pp. 2721–2746, 2004.

[4] K. Lorincz, D. Malan, T. Fulford-Jones, A. Nawoj, A. Clavel, V. Shnayder, G. Mainland, M. Welsh, and S. Moulton, "Sensor networks for emergency response: challenges and opportunities," *IEEE Pervasive Computing*, vol. 3, no. 4, pp. 16–23, 2004.

[5] M. Chen, S. Gonzalez, A. Vasilakos, H. Cao, and V. C. Leung, "Body area networks: A survey," *Mobile Networks and Applications*, vol. 16, no. 2, pp. 171–193, 2011.

[6] H. Mamaghanian, N. Khaled, D. Atienza, and P. Vandergheynst, "Compressed sensing for real-time energy-efficient ecg compression on wireless body sensor nodes," *IEEE Transactions on Biomedical Engineering*, vol. 58, no. 9, pp. 2456–2466, 2011.

[7] J.-W. Jeong, M. K. Kim, H. Cheng, W.-H. Yeo, X. Huang, Y. Liu, Y. Zhang, Y. Huang, and J. A. Rogers, "Capacitive epidermal electronics for electrically safe, long-term electrophysiological measurements," *Advanced Healthcare Materials*, vol. 3, no. 5, pp. 642–648, 2014.

[8] D. Son, J. Lee, S. Qiao, R. Ghaffari, J. Kim, J. E. Lee, C. Song, S. J. Kim, D. J. Lee, S. W. Jun, S. Yang, M. Park, J. Shin, K. Do, M. Lee, K. Kang, C. S. Hwang, N. Lu, T. Hyeon, and D.-H. Kim, "Multifunctional wearable devices for diagnosis and therapy of movement disorders," *Nature Nanotechnology*, vol. 9, no. 5, pp. 397–404, 2014.

[9] E. Bakker, "Electrochemical sensors," *Analytical Chemistry*, vol. 76, no. 12, pp. 3285–3298, 06 2004.

[10] M. Bariya, H. Y. Y. Nyein, and A. Javey, "Wearable sweat sensors," *Nature Electronics*, vol. 1, no. 3, pp. 160–171, 2018.

[11] J. Kim, A. S. Campbell, B. E.-F. de Ávila, and J. Wang, "Wearable biosensors for healthcare monitoring," *Nature Biotechnology*, 2019.

[12] W. Jia, A. J. Bandodkar, G. Valdés-Ramírez, J. R. Windmiller, Z. Yang, J. Ramírez, G. Chan, and J. Wang, "Electrochemical tattoo biosensors for real-time noninvasive lactate monitoring in human perspiration," *Analytical Chemistry*, vol. 85, no. 14, pp. 6553–6560, 2013.

[13] J. Kim, G. Valdés-Ramírez, A. J. Bandodkar, W. Jia, A. G. Martinez, J. Ramírez, P. Mercier, and J. Wang, "Non-invasive mouthguard biosensor for continuous salivary monitoring of metabolites," *Analyst*, vol. 139, no. 7, pp. 1632–1638, 2014.

[14] M. Parrilla, R. Cánovas, I. Jeerapan, F. J. Andrade, and J. Wang, "A textile-based stretchable multi-ion potentiometric sensor," *Advanced Healthcare Materials*, vol. 5, no. 9, pp. 996–1001, 2016.

[15] R. W. Licht, "Lithium: Still a major option in the management of bipolar disorder," *CNS Neuroscience & Therapeutics*, vol. 18, no. 3, pp. 219–226, 2012.

[16] J. Kim, W. R. de Araujo, I. A. Samek, A. J. Bandodkar, W. Jia, B. Brunetti, T. R. Paixão, and J. Wang, "Wearable temporary tattoo sensor for real-time trace metal monitoring in human sweat," *Electrochemistry Communications*, vol. 51, pp. 41–45, 2015.

[17] T. Seesaard, P. Lorwongtragool, and T. Kerdcharoen, "Development of fabric-based chemical gas sensors for use as wearable electronic noses," *Sensors (Basel, Switzerland)*, vol. 15, no. 1, pp. 1885–1902, 2015.

[18] J. Wang, "Electrochemical glucose biosensors," *Chemical Reviews*, vol. 108, no. 2, pp. 814–825, 2008.

[19] C. Wang, D. Hwang, Z. Yu, K. Takei, J. Park, T. Chen, B. Ma, and A. Javey, "User-interactive electronic skin for instantaneous pressure visualization," *Nature Materials*, vol. 12, no. 10, pp. 899–904, 2013.

[20] F. Criscuolo, F. Cantù, I. Taurino, S. Carrara, and G. De Micheli, "Flexible sweat sensors for non-invasive optimization of lithium dose in psychiatric disorders," in *2019 IEEE SENSORS*, 2019, pp. 1–4.

[21] H. Lee, C. Song, Y. S. Hong, M. S. Kim, H. R. Cho, T. Kang, K. Shin, S. H. Choi, T. Hyeon, and D.-H. Kim, "Wearable/disposable sweat-based glucose monitoring

device with multistage transdermal drug delivery module," *Science Advances*, vol. 3, no. 3, 2017.

[22] J. Hu, A. Stein, and P. Buhlmann, "Rational design of all-solid-state ion-selective electrodes and reference electrodes," *TrAC - Trends in Analytical Chemistry*, vol. 76, pp. 102–114, 2016.

[23] M. Parrilla, M. Cuartero, and G. A. Crespo, "Wearable potentiometric ion sensors," *TrAC - Trends in Analytical Chemistry*, vol. 110, pp. 303–320, 2019.

[24] N. A. Taylor and C. A. Machado-Moreira, "Regional variations in transepidermal water loss, eccrine sweat gland density, sweat secretion rates and electrolyte composition in resting and exercising humans," *Extreme Physiology & Medicine*, vol. 2, no. 1, p. 4, 2013.

[25] J. Heikenfeld, "Non-invasive analyte access and sensing through eccrine sweat: Challenges and outlook circa 2016," *Electroanalysis*, vol. 28, no. 6, pp. 1242–1249, 2016.

[26] P. Pirovano, M. Dorrian, A. Shinde, A. Donohoe, A. J. Brady, N. M. Moyna, G. Wallace, D. Diamond, and M. McCaul, "A wearable sensor for the detection of sodium and potassium in human sweat during exercise," *Talanta*, vol. 219, no. May, p. 121145, 2020.

[27] D. Ma, Y. Chen, S. S. Ghoreishizadeh, and P. Georgiou, "Spaceman: Wireless soc for concurrent potentiometry and amperometry," in *2021 IEEE International Symposium on Circuits and Systems (ISCAS)*, 2021, pp. 1–5.

[28] C. Baj-Rossi, E. G. Kilinc, S. S. Ghoreishizadeh, D. Casarino, T. R. Jost, C. Dehollain, F. Grassi, L. Pastorino, G. De Micheli, and S. Carrara, "Full fabrication and packaging of an implantable multi-panel device for monitoring of metabolites in small animals," *IEEE Transactions on Biomedical Circuits and Systems*, vol. 8, no. 5, pp. 636–647, 2014.

[29] W. Gao, S. Emaminejad, H. Y. Y. Nyein, S. Challa, K. Chen, A. Peck, H. M. Fahad, H. Ota, H. Shiraki, D. Kiriya, D.-H. Lien, G. A. Brooks, R. W. Davis, and A. Javey, "Fully integrated wearable sensor arrays for multiplexed in situ perspiration analysis," *Nature*, vol. 529, no. 7587, pp. 509–514, 2016.

[30] J. Kim, I. Jeerapan, S. Imani, T. N. Cho, A. Bandodkar, S. Cinti, P. P. Mercier, and J. Wang, "Noninvasive alcohol monitoring using a wearable tattoo-based iontophoretic-biosensing system," *ACS Sensors*, vol. 1, no. 8, pp. 1011–1019, 2016.

[31] A. Brueck, T. Iftekhar, A. B. Stannard, K. Yelamarthi, and T. Kaya, "A real-time wireless sweat rate measurement system for physical activity monitoring," *Sensors (Switzerland)*, vol. 18, no. 2, 2018.

[32] A. J. Bandodkar and J. Wang, "Wearable biofuel cells: A review," *Electroanalysis*, vol. 28, no. 6, pp. 1188–1200, 2016.

[33] J.-H. Bahk, H. Fang, K. Yazawa, and A. Shakouri, "Flexible thermoelectric materials and device optimization for wearable energy harvesting," *J. Mater. Chem. C*, vol. 3, pp. 10 362–10 374, 2015.

[34] D. P. Rose, M. E. Ratterman, D. K. Griffin, L. Hou, N. Kelley-Loughnane, R. R. Naik, J. A. Hagen, I. Papautsky, and J. C. Heikenfeld, "Adhesive rfid sensor patch for monitoring of sweat electrolytes," *IEEE Transactions on Biomedical Engineering*, vol. 62, no. 6, pp. 1457–1465, 2015.

[35] S. Imani, A. J. Bandodkar, A. M. Mohan, R. Kumar, S. Yu, J. Wang, and P. P. Mercier, "A wearable chemical-electrophysiological hybrid biosensing system for real-time health and fitness monitoring," *Nature Communications*, vol. 7, pp. 1–7, 2016.

[36] S. Emaminejad, W. Gao, E. Wu, Z. A. Davies, H. Yin Yin Nyein, S. Challa, S. P. Ryan, H. M. Fahad, K. Chen, Z. Shahpar, S. Talebi, C. Milla, A. Javey, and R. W. Davis, "Autonomous sweat extraction and analysis applied to cystic fibrosis and glucose monitoring using a fully integrated wearable platform." *Proceedings of the National Academy of Sciences of the United States of America*, vol. 114, no. 18, pp. 4625–4630, may 2017.

[37] Y. Lee, C. Howe, S. Mishra, D. S. Lee, M. Mahmood, M. Piper, Y. Kim, K. Tieu, H.-S. Byun, J. P. Coffey, M. Shayan, Y. Chun, R. M. Costanzo, and W.-H. Yeo, "Wireless, intraoral hybrid electronics for real-time quantification of sodium intake toward hypertension management," *Proceedings of the National Academy of Sciences*, vol. 115, no. 21, pp. 5377–5382, 2018.

[38] A. J. Bard and L. R. Faulkner, *Electrochemical Methods: Fundamentals and Applications*, 2nd ed., J. Wiley, Ed., 2001.

[39] F. Stradolini, A. Tuoheti, T. Kilic, D. Demarchi, and S. Carrara, "Raspberry-pi based system for propofol monitoring," *Integration*, vol. 63, pp. 213–219, 2018.

[40] G. Dimeski, T. Badrick, and A. S. John, "Ion Selective Electrodes (ISEs) and interferences-A review," *Clinica Chimica Acta*, vol. 411, no. 5-6, pp. 309–317, 2010.

[41] J. Cohn and E. Emmett, "The excretion of trace metals in human sweat," *Annals of Clinical and Laboratory Science*, vol. 8, no. 4, 1978.

[42] M. Schirmer, F. Stradolini, S. Carrara, and E. Chicca, "FPGA-based approach for automatic peak detection in cyclic voltammetry," *2016 IEEE International Conference on Electronics, Circuits and Systems, ICECS 2016*, pp. 65–68, 2017.

[43] X. Li, J. Dunn, D. Salins, G. Zhou, W. Zhou, S. M. Schüssler-Fiorenza Rose, D. Perelman, E. Colbert, R. Runge, S. Rego, R. Sonecha, S. Datta, T. McLaughlin, and M. P. Snyder, "Digital health: Tracking physiomes and activity using wearable biosensors reveals useful health-related information," *PLOS Biology*, vol. 15, no. 1, pp. 1–30, 01 2017.

[44] F. Stradolini, A. Tuoheti, T. Kilic, S. L. Ntella, N. Tamburrano, Z. Huang, G. De Micheli, D. Demarchi, and S. Carrara, "An iot solution for online monitoring of anesthetics in human serum based on an integrated fluidic bioelectronic system," *IEEE Transactions on Biomedical Circuits and Systems*, vol. 12, no. 5, pp. 1056–1064, 2018.

[45] Y.-L. Zheng, X.-R. Ding, C. C. Y. Poon, B. P. L. Lo, H. Zhang, X.-L. Zhou, G.-Z. Yang, N. Zhao, and Y.-T. Zhang, "Unobtrusive sensing and wearable devices for health informatics," *IEEE Transactions on Biomedical Engineering*, vol. 61, no. 5, pp. 1538–1554, 2014.

[46] J. Andreu-Perez, C. C. Y. Poon, R. D. Merrifield, S. T. C. Wong, and G.-Z. Yang, "Big data for health," *IEEE Journal of Biomedical and Health Informatics*, vol. 19, no. 4, pp. 1193–1208, 2015.

[47] W. You, A. Simalatsar, N. Widmer, and G. De Micheli, *Personalized drug administrations using support vector machine.* Springer US, 2013, vol. 3, no. 4, pp. 378–393.

[48] P. Kassal, M. D. Steinberg, and I. M. Steinberg, "Wireless chemical sensors and biosensors: A review," *Sensors and Actuators, B: Chemical*, vol. 266, pp. 228–245, 2018.

[49] M. Chen, S. Gonzalez, A. Vasilakos, H. Cao, and V. C. M. Leung, "Body area networks: A survey," *Mobile Networks and Applications*, vol. 16, no. 2, pp. 171–193, 2011.

[50] A. J. Bandodkar, W. J. Jeang, R. Ghaffari, and J. A. Rogers, "Wearable Sensors for Biochemical Sweat Analysis," *Annual Review of Analytical Chemistry*, vol. 12, pp. 1–22, 2019.

[51] A. McLister, J. McHugh, J. Cundell, and J. Davis, "New developments in smart bandage technologies for wound diagnostics," *Advanced Materials*, vol. 28, no. 27, pp. 5732–5737, 2016.

[52] E. Scurati-Manzoni, E. F. Fossali, C. Agostoni, E. Riva, G. D. Simonetti, M. Zanolari-Calderari, M. G. Bianchetti, and S. A. G. Lava, "Electrolyte abnormalities in cystic fibrosis: systematic review of the literature," *Pediatric Nephrology*, vol. 29, no. 6, pp. 1015–1023, 2014.

[53] L. Li, X. Liu, W. A. Qureshi, and A. J. Mason, "CMOS amperometric instrumentation and packaging for biosensor array applications," *IEEE Transactions on Biomedical Circuits and Systems*, vol. 5, no. 5, pp. 439–448, 2011.

[54] H. Li, X. Liu, L. Li, X. Mu, R. Genov, and A. J. Mason, "CMOS Electrochemical Instrumentation for Biosensor Microsystems: A Review," *Sensors*, 2016.

[55] W. E. Morf, "The Principles of ion-selective electrodes and of membrane transport," in *Volume 2*. Elsevier science Ltd, 1981.

[56] P. C. Meier, "Two-parameter debye-hückel approximation for the evaluation of mean activity coefficients of 109 electrolytes," *Analytica Chimica Acta*, vol. 136, pp. 363–368, 1982.

[57] G. L. Long and J. D. Winefordner, "Limit of detection a closer look at the iupac definition," *Analytical Chemistry*, vol. 55, no. 07, pp. 712A–724A, 1983.

[58] E. Lindner and R. E. Gyurcsányi, "Quality control criteria for solid-contact , solvent polymeric membrane ion-selective electrodes," *J. Solid State Electrochem.*, vol. 13, pp. 51–68, 2009.

[59] R. P. Buck and E. Lindner, "Recomendations for nomenclature of ion-selective electrodes (IUPAC recommendations 1994)," *Pur & Appl. Chem*, vol. 66, no. 12, pp. 2527–2536, 1994.

[60] F. Criscuolo, I. Taurino, F. Stradolini, S. Carrara, and G. De Micheli, "Highly-stable Li + ion-selective electrode based on noble metal nanostructures as solid-contacts," *Anal. Chim. Acta*, vol. 1027, pp. 22–32, 2018.

[61] A. Shvarev and E. Bakker, "Reversible electrochemical detection of nonelectroactive polyions," *Journal of the American Chemical Society*, vol. 125, no. 37, pp. 11 192–11 193, 2003.

[62] A. Sun, A. G. Venkatesh, and D. A. Hall, "A multi-technique reconfigurable electrochemical biosensor: Enabling personal health monitoring in mobile devices," *IEEE Transactions on Biomedical Circuits and Systems*, vol. 10, no. 5, pp. 945–954, 2016.

[63] J. E. B. Randles, "Kinetics of rapid electrode reactions," *Discuss. Faraday Soc.*, vol. 1, pp. 11–19, 1947.

[64] S. Kochowski and K. Nitsch, "Description of the frequency behaviour of metal–sio2–gaas structure characteristics by electrical equivalent circuit with constant phase element," *Thin Solid Films*, vol. 415, no. 1, pp. 133–137, 2002.

[65] S. S. Ghoreishizadeh, C. Baj-rossi, A. Cavallini, S. Carrara, and G. De Micheli, "An Integrated Control and Readout Circuit for Implantable Multi-Target Electrochemical Biosensing," *IEEE Transactions on Biomedical Circuits and Systems*, vol. 8, no. 6, pp. 1–8, 2014.

[66] F. Stradolini, A. Tuoheti, P. M. Ros, D. Demarchi, and S. Carrara, "Raspberry Pi Based System for Portable and Simultaneous Monitoring of Anesthetics and Therapeutic Compounds," pp. 237–240, 2017.

[67] D. Ma, S. S. Ghoreishizadeh, and P. Georgiou, "Dapper: A low power, dual amperometric and potentiometric single-channel front end," in *2020 IEEE International Symposium on Circuits and Systems (ISCAS)*, 2020, pp. 1–5.

[68] C. Yang, Y. Huang, B. L. Hassler, R. M. Worden, and A. J. Mason, "Amperometric electrochemical microsystem for a miniaturized protein biosensor array," *IEEE Transactions on Biomedical Circuits and Systems*, vol. 3, no. 3, pp. 160–168, 2009.

[69] K.-L. Lee and R. Mayer, "Low-distortion switched-capacitor filter design techniques," *IEEE Journal of Solid-State Circuits*, vol. 20, no. 6, pp. 1103–1113, 1985.

[70] C. Enz and G. Temes, "Circuit techniques for reducing the effects of op-amp imperfections: autozeroing, correlated double sampling, and chopper stabilization," *Proceedings of the IEEE*, vol. 84, no. 11, pp. 1584–1614, 1996.

[71] M. M. Ahmadi and G. A. Jullien, "Current-mirror-based potentiostats for three-electrode amperometric electrochemical sensors," *IEEE Transactions on Circuits and Systems I: Regular Papers*, vol. 56, no. 7, pp. 1339–1348, 2009.

[72] S. Aiassa, F. Stradolini, A. Tuoheti, S. Carrara, and D. Demarchi, "Quasi-digital biosensor-interface for a portable pen to monitor anaesthetics delivery," in *2019 15th Conference on Ph.D Research in Microelectronics and Electronics (PRIME)*, 2019, pp. 265–268.

[73] S. Wold, "Chemometrics; what do we mean with it, and what do we want from it?" *Chemometrics and Intelligent Laboratory Systems*, vol. 30, no. 1, pp. 109–115, 1995.

[74] Y. Vlasov, A. Legin, A. Rudnitskaya, C. Di Natale, and A. D'Amico, "Nonspecific sensor arrays ("electronic tongue") for chemical analysis of liquids (IUPAC Technical Report)," *Pure and Applied Chemistry*, vol. 77, no. 11, pp. 1965 – 1983, 2005.

[75] M. del Valle, "Sensor Arrays and Electronic Tongue Systems," *International Journal of Electrochemistry*, vol. 2012, pp. 1–11, 2012.

[76] J. Zeravik, A. Hlavacek, K. Lacina, and P. Skládal, "State of the art in the field of electronic and bioelectronic tongues – towards the analysis of wines," *Electroanalysis*, vol. 21, no. 23, pp. 2509–2520, 2009.

[77] L. Moreno i Codinachs, J. P. Kloock, M. J. Schöning, A. Baldi, A. Ipatov, A. Bratov, and C. Jiménez-Jorquera, "Electronic integrated multisensor tongue applied to grape juice and wine analysis," *Analyst*, vol. 133, pp. 1440–1448, 2008.

[78] A. Mimendia, J. M. Gutiérrez, J. M. Alcañiz, and M. del Valle, "Discrimination of Soils and Assessment of Soil Fertility Using Information from an Ion Selective Electrodes Array and Artificial Neural Networks," *Clean - Soil, Air, Water*, vol. 42, no. 12, pp. 1808–1815, 2014.

[79] A. C. Olivieri, *Introduction to Multivariate Calibration.* Springer, 2018.

[80] L. Wang, Y. Cheng, D. Lamb, M. Megharaj, and R. Naidu, "Application of Ion Selective Electrode array to simultaneously determinate multi-free ions in solution," *Environmental Technology and Innovation*, vol. 15, p. 100424, 2019.

[81] R. Bro, "Parafac. tutorial and applications," *Chemometrics and Intelligent Laboratory Systems*, vol. 38, no. 2, pp. 149–171, 1997.

[82] S. Aiassa, I. Ny Hanitra, G. Sandri, T. Totu, F. Grassi, F. Criscuolo, G. De Micheli, S. Carrara, and D. Demarchi, "Continuous monitoring of propofol in human serum with fouling compensation by support vector classifier," *Biosensors and Bioelectronics*, vol. 171, p. 112666, 2021.

[83] C. Legner, U. Kalwa, V. Patel, A. Chesmore, and S. Pandey, "Sweat sensing in the smart wearables era: Towards integrative, multifunctional and body-compliant perspiration analysis," *Sensors and Actuators, A: Physical*, vol. 296, pp. 200–221, 2019.

[84] S. Wold, M. Sjöström, and L. Eriksson, "PLS-regression: A basic tool of chemometrics," *Chemometrics and Intelligent Laboratory Systems*, vol. 58, no. 2, pp. 109–130, 2001.

[85] R. Rosipal, "Nonlinear Partial Least Squares An Overview," in *Chemoinformatics and Advanced Machine Learning Perspectives.* IGI Global, 2011, pp. 169–189.

[86] V. Vapnik, S. E. Golowich, and A. Smola, "Support vector method for function approximation, regression estimation and signal processing," in *Proceedings of the 9th International Conference on Neural Information Processing Systems*, ser. NIPS'96. Cambridge, MA, USA: MIT Press, 1996, p. 281–287.

[87] V. N. Vapnik, *Statistical Learning Theory.* Wiley-Interscience, 1998.

[88] D. E. Rumelhart and J. L. McClelland, *Learning Internal Representations by Error Propagation*, 1987, pp. 318–362.

[89] A. Mimendia, J. M. Gutiérrez, L. Leija, P. R. Hernández, L. Favari, R. Muñoz, and M. del Valle, "A review of the use of the potentiometric electronic tongue in

the monitoring of environmental systems," *Environmental Modelling and Software*, vol. 25, no. 9, pp. 1023–1030, 2010.

[90] D. Wilson, M. N. Abbas, A. L. A. Radwan, and M. del Valle, "Potentiometric electronic tongue to resolve mixtures of sulfide and perchlorate anions," *Sensors*, vol. 11, no. 3, pp. 3214–3226, 2011.

[91] L. Wang, D. Yang, C. Fang, Z. Chen, P. J. Lesniewski, M. Mallavarapu, and R. Naidu, "Application of neural networks with novel independent component analysis methodologies to a Prussian blue modified glassy carbon electrode array," *Talanta*, vol. 131, pp. 395–403, 2015.

[92] A. V. Mueller and H. F. Hemond, "Extended artificial neural networks: Incorporation of a priori chemical knowledge enables use of ion selective electrodes for in-situ measurement of ions at environmentally relevant levels," *Talanta*, vol. 117, pp. 112–118, 2013.

[93] L. Wang, Y. Cheng, D. Lamb, Z. Chen, P. J. Lesniewski, M. Megharaj, and R. Naidu, "Simultaneously determining multi-metal ions using an ion selective electrode array system," *Environmental Technology and Innovation*, vol. 6, pp. 165–176, 2016.

[94] J. Gallardo, S. Alegret, M. A. De Román, R. Muñoz, P. R. Hernández, L. Leija, and M. Del Valle, "Determination of Ammonium Ion Employing an Electronic Tongue Based on Potentiometric Sensors," *Analytical Letters*, vol. 36, no. 14, pp. 2893–2908, 2003.

[95] A. M. Snauffer, U. Chauhan, K. Cogert, M. K. H. Winkler, and A. V. Mueller, "Data Fusion for Environmental Process Control: Maximizing Useful Information Recovery under Data Limited Constraints," *IEEE Sensors Letters*, vol. 3, no. 1, pp. 1–4, 2018.

[96] R. Baronas, F. Ivanauskas, R. Maslovskis, and P. Vaitkus, "An Analysis of Mixtures Using Amperometric Biosensors and Artificial Neural Networks," *Journal of Mathematical Chemistry*, vol. 36, no. 3, pp. 281–297, 2004.

[97] A. J. Bandodkar and J. Wang, "Non-invasive wearable electrochemical sensors: a review," *Trends in Biotechnology*, vol. 32, no. 7, pp. 363–371, 2014.

[98] P. Düking, C. Stammel, B. Sperlich, S. Sutehall, B. Muniz-Pardos, G. Lima, L. Kilduff, I. Keramitsoglou, G. Li, F. Pigozzi, and Y. P. Pitsiladis, "Necessary Steps to Accelerate the Integration of Wearable Sensors Into Recreation and Competitive Sports," *Current Sports Medicine Reports*, vol. 17, no. 6, pp. 178–182, 2018.

[99] K. Mitsubayashi, M. Suzuki, E. Tamiya, and I. Karube, "Analysis of metabolites in sweat as a measure of physical condition," *Analytica chimica acta*, vol. 289, no. 1, pp. 27–34, 1994.

[100] W. N. Fishbein, J. W. Foellmer, and J. I. Davis, "Medical implications of the lactate and ammonia relationship in anaerobic exercise," *International journal of sports medicine*, 1990.

[101] D. Gruson, A. Lallali, V. Furlan, A. M. Taburet, A. Legrand, and M. Conti, "Evaluation of a new lithium colorimetric assay performed on the dade behring dimension® x-pand™ system," *Clinical Chemistry and Laboratory Medicine (CCLM)*, vol. 42, no. 9, pp. 1066–1068, 2004.

[102] C. Donohue, B. Hobson, and R. C. Stephens, "An introduction to anaesthesia," *British Journal of Hospital Medicine*, vol. 74, no. Sup5, pp. C71–C75, 2013.

[103] P. Tonner, "Balanced anaesthesia today," *Best Practice and Research Clinical Anaesthesiology*, vol. 19, no. 3, pp. 475–484, 2005, renaissance of Inhalational Anaesthesia.

[104] F. Shihana, D. Dissanayake, P. Dargan, and A. Dawson, "A modified low-cost colorimetric method for paracetamol (acetaminophen) measurement in plasma," *Clinical Toxicology*, vol. 48, no. 1, pp. 42–46, 2010.

[105] L. Rassaei, W. Olthuis, S. Tsujimura, E. J. Sudhölter, and A. Van Den Berg, "Lactate biosensors: Current status and outlook," *Analytical and Bioanalytical Chemistry*, vol. 406, no. 1, pp. 123–137, 2014.

[106] O.-W. Lau, S.-F. Luk, and Y.-M. Cheung, "Simultaneous determination of ascorbic acid, caffeine and paracetamol in drug formulations by differential-pulse voltammetry using a glassy carbon electrode," *Analyst*, vol. 114, pp. 1047–1051, 1989.

[107] P. Fanjul-Bolado, P. J. Lamas-Ardisana, D. Hernández-Santos, and A. Costa-García, "Electrochemical study and flow injection analysis of paracetamol in pharmaceutical formulations based on screen-printed electrodes and carbon nanotubes," *Analytica Chimica Acta*, vol. 638, no. 2, pp. 133–138, 2009.

[108] W. S. Wang, H. Y. Huang, S. C. Chen, K. C. Ho, C. Y. Lin, T. C. Chou, C. H. Hu, W. F. Wang, C. F. Wu, and C. H. Luo, "Real-time telemetry system for amperometric and potentiometric electrochemical sensors," *Sensors*, vol. 11, no. 9, pp. 8593–8610, 2011.

[109] A. Parra, E. Casero, L. Vázquez, F. Pariente, and E. Lorenzo, "Design and characterization of a lactate biosensor based on immobilized lactate oxidase onto gold surfaces," *Analytica Chimica Acta*, vol. 555, no. 2, pp. 308–315, 2006.

[110] J. Lawrence, A. Patel, and J. Brisson, "The thermal conductivity of kapton hn between 0.5 and 5 k," *Cryogenics*, vol. 40, no. 3, pp. 203–207, 2000.

[111] M. I. Ny Hanitra, F. Criscuolo, N. Pankratova, S. Carrara, and G. De Micheli, "Multichannel front-end for electrochemical sensing of metabolites, drugs, and electrolytes," *IEEE Sensors Journal*, vol. 20, no. 7, pp. 3636–3645, 2020.

[112] M. I. Ny Hanitra, L. Lobello, F. Stradolini, A. Tuoheti, F. Criscuolo, T. Kilic, D. Demarchi, S. Carrara, and G. De Micheli, "A Flexible Front-End for Wearable Electrochemical Sensing," in *IEEE International Symposium on Medical Measurements and Applications, Proceedings*, 2018.

[113] R. P. Sallen and E. L. Key, "A practical method of designing rc active filters," *IRE Transactions on Circuit Theory*, vol. 2, no. 1, pp. 74–85, 1955.

[114] M. D. Rawlins, D. B. Henderson, and A. R. Hijab, "Pharmacokinetics of paracetamol (acetaminophen) after intravenous and oral administration," *European Journal of Clinical Pharmacology*, vol. 11, no. 4, pp. 283–286, 1977.

[115] S. Aiassa, S. Carrara, and D. Demarchi, "Optimized sampling rate for voltammetry-based electrochemical sensing in wearable and iot applications," *IEEE Sensors Letters*, vol. 3, no. 6, pp. 1–4, June 2019.

[116] F. Shihana, D. M. Dissanayake, P. I. Dargan, and A. H. Dawson, "A modified low cost coulorimetric method for paracetamol measurement in plasma," *Clinical Toxicology*, vol. 48, no. 1, pp. 42–46, 2011.

[117] D. B. Speedy, T. D. Noakes, and C. Schneider, "Exercise-associated hyponatremia: A review," *Emergency Medicine*, vol. 13, no. 1, pp. 17–27, 2001.

[118] J. V. Pagaduan, M. Ali, M. Dowlin, L. Suo, T. Ward, F. Ruiz, and S. Devaraj, "Revisiting sweat chloride test results based on recent guidelines for diagnosis of cystic fibrosis," *Practical Laboratory Medicine*, vol. 10, pp. 34 – 37, 2018.

[119] R. M. Morgan, M. J. Patterson, and M. A. Nimmo, "Acute effects of dehydration on sweat composition in men during prolonged exercise in the heat," *Acta Physiologica Scandinavica*, vol. 182, no. 1, pp. 37–43, 2004.

[120] L. B. Baker, J. R. Stofan, A. A. Hamilton, and C. A. Horswill, "Comparison of regional patch collection vs. whole body washdown for measuring sweat sodium and potassium loss during exercise," *Journal of Applied Physiology*, vol. 107, no. 3, pp. 887–895, 2009.

[121] D. Czarnowski, J. Langfort, W. Pilis, and J. Górski, "Effect of a low-carbohydrate diet on plasma and sweat ammonia concentrations during prolonged nonexhausting exercise," *European Journal of Applied Physiology and Occupational Physiology*, vol. 70, no. 1, pp. 70–74, 1995.

[122] R. Klesges, K. Ward, M. Shelton, and et al., "Changes in bone mineral content in male athletes: Mechanisms of action and intervention effects," *JAMA*, vol. 276, no. 3, pp. 226–230, 1996.

[123] F. Criscuolo, I. Ny Hanitra, S. Aiassa, I. Taurino, N. Oliva, S. Carrara, and G. De Micheli, "Wearable multifunctional sweat-sensing system for efficient healthcare monitoring," *Sensors and Actuators B: Chemical*, vol. 328, p. 129017, 2021.

[124] M. J. Patterson, S. D. R. Galloway, and M. A. Nimmo, "Variations in regional sweat composition in normal human males," *Experimental Physiology*, vol. 85, no. 6, pp. 869–875, 2000.

[125] A. J. Mccubbin and R. J. S. Costa, "The Impact of Dietary Sodium Intake on Sweat Sodium Concentration in Response to Endurance Exercise : A Systematic Review," *International Journal of Sports Science*, vol. 8, no. 1, pp. 25–37, 2018.

[126] J.-J. Wan, Z. Qin, P.-Y. Wang, Y. Sun, and X. Liu, "Muscle fatigue: general understanding and treatment," *Experimental & molecular medicine*, vol. 49, no. 10, pp. e384–e384, 2017.

[127] S. J. Montain, S. N. Cheuvront, and H. C. Lukaski, "Sweat mineral-element responses during 7 h of exercise-heat stress," *International Journal of Sport Nutrition and Exercise Metabolism*, vol. 17, no. 6, pp. 574 – 582, 2007.

[128] W. A. Latzka and S. J. Montain, "Water and electrolyte requirements for exercise," *Clinics in Sports Medicine*, vol. 18, no. 3, pp. 513–524, 1999.

[129] C. H. Bohl and S. L. Volpe, "Magnesium and exercise," *Critical Reviews in Food Science and Nutrition*, vol. 42, no. 6, pp. 533–563, 2002.

[130] M. Bariya, Z. Shahpar, H. Park, J. Sun, Y. Jung, W. Gao, H. Y. Y. Nyein, T. S. Liaw, L.-C. Tai, Q. P. Ngo, M. Chao, Y. Zhao, M. Hettick, G. Cho, and A. Javey, "Roll-to-roll gravure printed electrochemical sensors for wearable and medical devices," *ACS Nano*, vol. 12, no. 7, pp. 6978–6987, 2018.

[131] M. Parrilla, R. Cánovas, I. Jeerapan, F. J. Andrade, and J. Wang, "A textile-based stretchable multi-ion potentiometric sensor," *Advanced Healthcare Materials*, vol. 5, no. 9, pp. 996–1001, 2016.

[132] A. Alizadeh, A. Burns, R. Lenigk, R. Gettings, J. Ashe, A. Porter, M. McCaul, R. Barrett, D. Diamond, P. White, P. Skeath, and M. Tomczak, "A wearable patch for continuous monitoring of sweat electrolytes during exertion," *Lab Chip*, vol. 18, pp. 2632–2641, 2018.

[133] F. Criscuolo, M. Galfione, S. Carrara, and G. De Micheli, "All-solid-state reference electrodes for analytical applications," in *2019 IEEE 8th International Workshop on Advances in Sensors and Interfaces (IWASI)*, 2019, pp. 66–69.

[134] D. H. Dickey, "A Spreading Resistance Technique for Resistivity Measurements on Silicon," *Journal of the Electrochemical Society*, vol. 113, no. 3, pp. 255–259, 1966.

[135] P. Childs, J. Greenwood, and C. Long, "Review of temperature measurement," *Review of scientific instruments*, vol. 71, no. 8, pp. 2959–2978, 2000.

[136] M. A. Yokus, T. Songkakul, V. A. Pozdin, A. Bozkurt, and M. A. Daniele, "Wearable multiplexed biosensor system toward continuous monitoring of metabolites," *Biosensors and Bioelectronics*, vol. 153, p. 112038, 2020.

[137] K. F. Morcelles, V. G. Sirtoli, P. Bertemes-Filho, and V. C. Vincence, "Howland current source for high impedance load applications," *Review of Scientific Instruments*, vol. 88, no. 11, 2017.

[138] E. Bakker, "Selectivity of Liquid Membrane Ion-Selective Electrodes," *Electroanalysis*, vol. 9, no. 1, pp. 7–12, 1997.

[139] K. Wygladacz, M. Durnaś, P. Parzuchowski, Z. Brzózka, and E. Malinowska, "Miniaturized sodium-selective sensors based on silicon back-side contact structure with novel self-plasticizing ion-selective membranes," *Sensors and Actuators, B: Chemical*, vol. 95, no. 1-3, pp. 366–372, 2003.

[140] T. Ghosh, H. J. Chung, and J. Rieger, "All-solid-state sodium-selective electrode with a solid contact of chitosan/prussian blue nanocomposite," *Sensors (Switzerland)*, vol. 17, no. 11, 2017.

[141] D. M. Band, J. Kratochvil, P. A. P. Wilson, and T. Treasure, "Relationship Between Activity and Concentration Measurements of Plasma Potassium," *Analyst*, vol. 103, no. 246, pp. 246–251, 1978.

[142] T. Yin, D. Pan, and W. Qin, "All-solid-state polymeric membrane ion-selective miniaturized electrodes based on a nanoporous gold film as solid contact," *Anal. Chem.*, vol. 86, no. 22, pp. 11 038–11 044, 2014.

[143] Nien Hsuan Chou, Jung Chuan Chou, Tai Ping Sun, and Shen Kan Hsiung, "Measurement and comparison of potentiometric selectivity coefficients of urea biosensors based on ammonium ion-selective electrodes," *IEEE Sensors Journal*, vol. 5, no. 6, pp. 1362–1368, 2005.

[144] P. Gehrig, R. Rusterholz, and W. Simon, "Very lipophilic calcium ion-selective ionophore for chemical sensors of high life-time," *Chimia 43*, vol. 377, 1989.

[145] Ö. Isildak and O. Özbek, "Application of Potentiometric Sensors in Real Samples," *Critical Reviews in Analytical Chemistry*, vol. 0, no. 0, pp. 1–14, 2020.

[146] A. V. Mueller and H. F. Hemond, "Statistical generation of training sets for measuring NO3-, NH4+ and major ions in natural waters using an ion selective

electrode array," *Environmental Science: Processes and Impacts*, vol. 18, no. 5, pp. 590–599, 2016.

[147] A. Mena-Bravo and M. D. Luque de Castro, "Sweat: A sample with limited present applications and promising future in metabolomics," *Journal of Pharmaceutical and Biomedical Analysis*, vol. 90, pp. 139–147, 2014.

[148] L. Nuñez, X. Cetó, M. I. Pividori, M. V. Zanoni, and M. del Valle, "Development and application of an electronic tongue for detection and monitoring of nitrate, nitrite and ammonium levels in waters," *Microchemical Journal*, vol. 110, pp. 273–279, 2013.

[149] L. Z. Benet, "Glass electrodes for hydrogen and other cations. edited by george eisenman." *Journal of Pharmaceutical Sciences*, vol. 57, no. 7, pp. 1271–1271, 1968.

[150] M. Nägele, E. Bakker, and Pretsch, "General description of the simultaneous response of potentiometric ionophore-based sensors to ions of different charge," *Analytical Chemistry*, vol. 71, no. 5, pp. 1041–1048, 1999.

[151] E. Bakker, "Generalized Selectivity Description for Polymeric Ion-Selective Electrodes Based on the Phase Boundary Potential Model," *Journal of electroanalytical chemistry (Lausanne, Switzerland)*, pp. 1–20, 2011.

[152] M. I. Ny Hanitra, D. Demarchi, S. Carrara, and G. De Micheli, "Emulator design and generation of synthetic dataset in multi-ion sensing," in *2020 IEEE International Symposium on Circuits and Systems (ISCAS)*, 2020, pp. 1–5.

[153] C. Lim and T. Dudev, *Potassium Versus Sodium Selectivity in Monovalent Ion Channel Selectivity Filters*. Cham: Springer International Publishing, 2016, pp. 325–347.

[154] M. I. Ny Hanitra, F. Criscuolo, S. Carrara, and G. De Micheli, "Multi-ion-sensing emulator and multivariate calibration optimization by machine learning models," *IEEE Access*, vol. 9, pp. 46 821–46 836, 2021.

[155] M. Chung, G. Fortunato, and N. Radasci, "Wearable flexible sweat sensors for healthcare monitoring: a review," *Journal of The Royal Society Interface*, vol. 16, pp. 1–15, 2018.

[156] B. Lara, C. Gallo-Salazar, C. Puente, F. Areces, J. J. Salinero, and J. Del Coso, "nterindividual variability in sweat electrolyte concentration in marathoners," *Journal of International Society of Sports Nutrition*, vol. 13, 2016.

[157] M. E. Sears, K. J. Kerr, and R. I. Bray, "Arsenic, cadmium, lead, and mercury in sweat: A systematic review," *Journal of Environmental and Public Health*, vol. 2012, no. February 2012, 2012.

[158] R. N. Kackar, "Off-line quality control, parameter design, and the taguchi method," *Journal of Quality Technology*, vol. 17, no. 4, pp. 176–188, 1985.

[159] R. Kacker, E. Lagergren, and J. Filliben, "Taguchi's orthogonal arrays are classical designs of experiments," *Journal of Research of the National Institute of Standards and Technology*, vol. 96, no. 5, p. 577, 1991.

[160] W. Ament, J. R. Huizenga, G. A. Mook, C. H. Gips, and G. J. Verkerke, "Lactate and ammonia concentration in blood and sweat during incremental cycle ergometer exercise," *Int. J. Sports Med.*, vol. 18, pp. 35–39, 1997.

[161] S. Wold, A. Ruhe, H. Wold, and W. J. Dunn, III, "The collinearity problem in linear regression. the partial least squares (pls) approach to generalized inverses," *SIAM J. Sci. Stat. Comput.*, vol. 5, no. 3, p. 735–743, 1984.

[162] B. Scholkopf and A. J. Smola, *Learning with Kernels: Support Vector Machines, Regularization, Optimization, and Beyond.* Cambridge, MA, USA: MIT Press, 2001.

[163] M. Sánchez-Fernández, M. de Prado-Cumplido, J. Arenas-García, and F. Pérez-Cruz, "SVM Multiregression for Nonlinear Channel Estimation in Multiple-Input Multiple-Output Systems," *IEEE transactions on signal processing*, vol. 52, no. 8, pp. 2298–2307, 2004.

[164] X. Glorot and Y. Bengio, "Understanding the difficulty of training deep feedforward neural networks," in *In Proceedings of the International Conference on Artificial Intelligence and Statistics (AISTATS'10). Society for Artificial Intelligence and Statistics*, 2010.

[165] J. J. Dongarra, J. W. Demmel, and S. Ostrouchov, "Lapack: A linear algebra library for high-performance computers," in *Computational Statistics*, Y. Dodge and J. Whittaker, Eds. Heidelberg: Physica-Verlag HD, 1992, pp. 23–28.

[166] C. C. Chang and C. J. Lin, "LIBSVM: A Library for support vector machines," *ACM Transactions on Intelligent Systems and Technology*, vol. 2, no. 3, pp. 1–39, 2011.

[167] F. Chollet *et al.*, "Keras," https://keras.io, 2015.

[168] E. P. Smith and K. A. Rose, "Model goodness-of-fit analysis using regression and related techniques," *Ecological Modelling*, vol. 77, no. 1, pp. 49–64, 1995.

Ivan **Ny Hanitra**

Graduated Ph.D. in microelectronics and microsystems

Chemin de Renens 41, 1004 Lausanne, Switzerland
+41(0)786775875
ivan.nyhanitra@gmail.com
linkedin.com/in/ivan-ny-hanitra-13b7a185
github.com/IvanNH

Graduated Ph.D. researcher specialized in the **design of hardware and software interfaces** for electrochemical sensors. Expert in the design, realization, and characterization of **sensor readout front-end circuits**, development of **embedded software** and **machine learning** models. Published his research work in top-tier pier-reviewed international journals and conferences. Strong analytical and communication skills, very fast learner, team worker, and passionate about science and technology.

Core Experiences

October 2021 – April 2017 | **Ph.D. researcher in microelectronics and microsystems, EPFL, Switzerland**

Hardware and software interfaces design for multi-panel electrochemical sensors

- Fabricated and characterized enzymatic biosensors and solid-contact ion-sensors for healthcare monitoring and physiology
- Designed, realized, and characterized hardware front-end circuits for wearable electrochemical sensors (flexible and rigid printed circuit boards)
- Developed firmware code on microcontroller (C/C++) and designed graphical user interfaces (PyQt5, Matlab)
- Developed an ion-sensing emulator to study interference effect in multi-ion-sensing
- Developed and deployed machine learning models for multivariate calibration on a Raspberry Pi
- Published and reviewed manuscripts for top-tier international journal and conferences
- Technical program committee and Chair of session on Analog filters and Amplifiers for IEEE International Conference on Electronics Circuits and Systems (IEEE ICECS 2019)
- Teaching assistant for: Integrated circuits design I, Bio-nano-chip design, Analog circuits for biochips, Sciences et technologies de l'électricité
- Supervised and guided master students in their thesis works

March 2017 – October 2016 | **Researcher at Integrated Systems Laboratory, EPFL, Switzerland**

Design and realization of a multi-sensing electrochemical platform

- Optimized the design of three-electrode cell architectures for parallel sensing
- Designed and micro-fabricated a multi-electrode sensing platform (Lift-off process, E-beam evaporation, Atomic Layer Deposition, Ion Beam Etching, Wet bench processes)

August 2016 – February 2016 | **Researcher at Electronics Laboratory, EPFL, Switzerland**

Low-power strategy for continuous photoplethysmographic-based heart rate monitoring implemented in smart-watches

- Designed and realized a circuit front-end prototype for photoplethysmographic-based heart rate monitoring on the wrist
- Proposed a novel minimum variance algorithm for heart rate retrieval from low-frequency sampled photoplethysmographic signals
- Implemented a system-level simulation of the proposed algorithm (Matlab)
- Developed a graphical user interface investigation tool (Matlab)

August 2015 – July 2015 | **Researcher at Electronics Laboratory, EPFL, Switzerland**

Simulation of PPG heart-rate monitoring system based on FM demodulator with Phase Locked-Loop

- Performed optical and electrical characterization of a Dynamic Photodetector
- Proposed a system-level model of a Dynamic Photodetector (Matlab/Simulink)
- Proposed and implemented a system-level simulation of an FM demodulator with Phase Locked-Loop for low-power PPG heart-rate monitoring (Matlab/Simulink)

Software Skills

Programming	**Python**, **Matlab/Simulink**, **C**, **C++**, Wolfram
HW circuits design	**Altium Designer, OrCAD, PSpice**
EDA tools	Virtuoso, Assura, Spectre, Innovus
RTL design	Sigasi HDT, ModelSim, Design Compiler
Simulation	LabView, Comsol Multiphysics, Ansys
Other tools	**git**, **Jupyter**, **Unix/Linux**, **Raspbian**, **bash**, LaTeX, **Adobe creative suite**, **Microsoft Office suite**

Technical Skills

- Analog/Digital circuits design
- Printed circuits board design and prototyping
- Machine learning systems design and deployment
- IoT/Embedded systems design
- Electrochemical sensors design/fabrication/characterization
- Simulation and modeling
- Microfabrication processes

Education

October 2021 – April 2017 | **Ph.D. student in microelectronics and microsystems**
Swiss Federal Institute of Technology Lausanne (EPFL), Switzerland
- Analog circuits for biochips
- Design technologies for integrated systems
- Deep learning
- Design and optimization of IoT systems
- Advanced Engineering MEAD courses:

Advanced analog IC design, Low-power IC design, Mixed-signal IC design, Delta-sigma data converters, High performance data converters, Efficient machine learning for IoT

August 2016 – September 2014 | **M.Sc. in micro and nanotechnologies for integrated systems**
Swiss Federal Institute of Technology Lausanne (EPFL), Switzerland
Grenoble Institute of Technology, France **Politecnico di Torino, Italy**
- Microelectronics (analog/digital circuits design), VLSI design and testing
- Semiconductor physics and technology, Microsystems modeling and technology
- Nanophysics and nanostructures, Nanoelectronics
- Optoelectronics, Biomedical systems

June 2014 – September 2013 | **B.Sc. in physics and engineering, Grenoble Institute of Technology, France**
Matter physics, Solid state physics, Materials, Electronics, Thermodynamics, Fluid mechanics, Mechanics of continuous media, Crystallography, Physical-chemistry, Engineering sciences.

July 2013 – September 2011 | **Classes Préparatoires aux Grandes Écoles, Lycée Pierre de Fermat (Toulouse), France**
Intensive training in Mathematics, Physics, Chemistry, Spanish, and Philosophy

June 2011 | **Baccalauréat général scientifique, Lycée Français René Cassin (Fianarantsoa), Madagascar**
Specialization in Mathematics – *Grade: 17.43/20 (with distinction)*

Selected Publications

M. I. Ny Hanitra et al., **Real-time multi-ion-monitoring front-end with interference compensation by multi-output support vector regressor**. *IEEE Transactions on Biomedical Circuits and Systems*, Under publication (2021).

M. I. Ny Hanitra et al., **Multi-ion-sensing emulator and multivariate calibration optimization by machine learning models**. *IEEE Access*, vol. 9, pp. 46821-46836 (2021). Open access

S. Aiassa, M. I. Ny Hanitra et al., **Continuous monitoring of propofol in human serum with fouling compensation by support vector classifier**. *Biosensors & Bioelectronics*, vol. 171 (2021). Preprint

M. I. Ny Hanitra et al., **Multi-channel front-end for electrochemical sensing of metabolites, drugs, and electrolytes**. *IEEE Sensors Journal*, vol. 20, num. 7, pp. 3636-3645 (2020). Open access

Honors and Certifications

- **Selected in the Excellence-Major scholarship program from the Agency for French Education Abroad** (2011-2016)
- **LabView associate developer** (2016)
- **International English Level Testing System, B2 level** (2015)

Languages

English	● ● ● ● ●
French	● ● ● ● ●
Italian	● ● ● ● ●
Spanish	● ● ● ● ●
German	● ○ ○ ○ ○
Malagasy	● ● ● ○ ○

Personal Information

- Malagasy citizenship. Swiss residence permit (Type B)
- Born on February 1993
- Swiss driver's license (Type B)
- Extracurricular activities: Basketball, Soccer, Hiking

Volunteer Work

- Exam correction for 1^{st} year EPFL students (2018)
- RAID Grenoble INP organizer (2014)

Ivan Ny Hanitra

Graduated Ph.D. in microelectronics and microsystems

Chemin de Renens 41, 1004 Lausanne, Switzerland
+41(0)786775875
ivan.nyhanitra@gmail.com
linkedin.com/in/ivan-ny-hanitra-13b7a185
github.com/IvanNH

Peer-reviewed Journal Articles

M. I. Ny Hanitra et al., **Real-time multi-ion-monitoring front-end with interference compensation by multi-output support vector regressor**. *IEEE Transactions on Biomedical Circuits and Systems*, Under publication (2021).

F. Criscuolo and M. I. Ny Hanitra et al., **All-solid-state ion-selective electrodes: a tutorial for correct practice**. *IEEE Sensors Journal*, vol. 21, num. 20, pp. 22143-22154 (2021). Open access

S. Aiassa, P. Motto Ros, M. I. Ny Hanitra et al., **Smart portable pen for continuous monitoring of anaesthetics in human serum with machine learning**. *IEEE Transactions on Biomedical Circuits and Systems*, vol. 15, num. 2, pp. 294-302 (2021). Preprint

M. I. Ny Hanitra et al., **Multi-ion-sensing emulator and multivariate calibration optimization by machine learning models**. *IEEE Access*, vol. 9, pp. 46821-46836 (2021). Open access

F. Criscuolo, M. I. Ny Hanitra et al., **Wearable multifunctional sweat-sensing system for efficient healthcare monitoring**. *Sensors and Actuators B: Chemical*, vol. 328 (2021). Preprint

S. Aiassa, M. I. Ny Hanitra et al., **Continuous monitoring of propofol in human serum with fouling compensation by support vector classifier**. *Biosensors & Bioelectronics*, vol. 171 (2021). Preprint

M. I. Ny Hanitra et al., **Multi-channel front-end for electrochemical sensing of metabolites, drugs, and electrolytes**. *IEEE Sensors Journal*, vol. 20, num. 7, pp. 3636-3645 (2020). Open access

Peer-reviewed Conference Papers

M. I. Ny Hanitra et al., **Emulator design and generation of synthetic dataset in multi-ion sensing**. *Proceedings of 2020 IEEE International Symposium on Circuits and Systems (ISCAS)*, (2020).

M. I. Ny Hanitra et al., **Multi-target electrolyte sensing front-end for wearable physical monitoring**. *Proceedings of* 15^{th} *Conference on PhD Research in Microelectronics and Electronics (PRIME)*, (2019).

M. I. Ny Hanitra et al., **A flexible front-end for wearable electrochemical sensing**. *Proceedings of 2018 IEEE International Symposium on Medical Measurements and Applications (MEMEA)*, (2018).